UNIVERSITY OF CALGARY

Processing of DAS and geophone VSP data from the CaMI Field Research Station

by

Adriana Josefina Gordon Ferrebus

A THESIS

SUBMITTED TO THE FACULTY OF GRADUATE STUDIES

IN PARTIAL FULFILMENT OF THE REQUIREMENTS FOR THE

DEGREE OF MASTER OF SCIENCE

GRADUATE PROGRAM IN GEOLOGY AND GEOPHYSICS

CALGARY, ALBERTA

APRIL, 2019

Abstract

The monitoring program of CO_2 injection at the Field Research Station in Newell County Alberta includes diverse surveys and new technologies. The acquisition and processing of Vertical Seismic Profiles (VSP) were undertaken for this thesis. More specifically, the analysis of three different surveys: a walk around VSP for azimuthal anisotropy analysis, zero offset VSPs to test the emerging DAS technology and walk away VSP to obtain imaging results for straight and helical wounded fibre optic cables. From the azimuthal analysis, the fast direction was identified to the northeast with an epsilon value (0.02) indicative of weak anisotropy. For the DAS VSP processing, a calibration step was necessary to register the precise depth of DAS traces; two approaches were completed and yielded similar results. Additionally, DAS strain rate measurements were converted to strain to compare it with geophone data. The excellent correlation between the 3D seismic lines and VSP-CDP stacks and the imaging results shows that DAS is a promising technology for subsurface imaging and monitoring.

Acknowledgements

I would like to express my honest gratitude to my supervisor Dr. Don Lawton for his help, guidance and encouragement throughout my degree. His broad knowledge and experience combined with his sharp attention to details helped me engage positively the challenges I encountered during my research. I am also grateful for the opportunities he gave me to showcase my work and interact with other fellow students in international conferences and field trips.

Special thanks to Dr. Raul Cova for first letting me work on a research project with him during my undergraduate degree and secondly, for all the discussions and suggestions during my graduate degree. I appreciate all his help and friendship over the years.

I would like to thank the CREWES project sponsors, NSERC and CaMI FRS JIP partners for their continued support. I extend my gratitude to the CSEG Foundation for awarding me the 2016/2017 CSEG Scholarship sponsored by Arcis. Thanks to Schlumberger for providing the VISTA software and CGG for Hampson-Russell software. Many thanks to CREWES faculty and staff, their help and support made this a great journey. Further thanks to Dr. Kris Innanen and Dr. Roman Shor for being part of my examination committee. Thanks to Dr. Roy Lindseth, Dr. Larry Lines, Andreas Cordsen and Dr. Daniel Trad for the shared moments.

Special thanks to Laura Baird for her unconditional help and support but more importantly for becoming one of my dearest friends while teaching me interesting facts about Canadian history.

Thanks to all the friends I made during my degree, especially to the ladies in my office, Michelle Montano, Bona Wu and Jessica Dongas for the great company. My IBA family, Marco Venieri, Samantha Super, Sean Horner and Morgan Howrish for an amazing experience. Thanks to Marie Macquet, Marcelo Guarido, Junxiao Li, Sergio Romahn, Andy Iverson, Dennis Ellison and Carrie Youzwishen for their friendship. I also thank the Areperos group, Carlos Briceno, Gaby Gonzalez, Karen Sotelo, Carla Santiago and Nico Urrea for their friendship and good times. Thanks to Eric Rops, Andrew Mills, Tyler Spackman and Scott Keating for the fun moments. Thanks to Anton Biryukov, Alana Kent and Eric Motts for entertaining conversations.

I would like to thank my family, especially my parents Carmen Ferrebus and Hermes Gordon and my brother Hermes E. Gordon for their unconditional love and support. Their encouragement and guidance made me the person I am today. Last but not least, I would like to thank Volodymyr Vragov for his enthusiasm and support. His friendship and companionship during the culmination of my degree made it a cherished experience.

Dedication

To my parents, Carmen & Hermes and my brother Hermes E.
Thank you for always being there.
To my lovely grandma Carmen Rosa and my aunt Petrica.
I will always remember you.
To my family and friends scattered around the world.
We'll see each other again.

Table of Contents

List of Tables

List of Figures and Illustrations

List of Symbols, Abbreviations and Nomenclature

Symbol	Definition
GHG	Greenhouse gas
CCS	Carbon Capture and Storage
CO2	Carbon Dioxide
VSP	Vertical Seismic Profile
DAS	Distributed Acoustic Sensing
AVO	Amplitude versus Offset
3D	Three dimensions
2D	Two dimensions
S/N	Signal to noise ratio
P-wave	Compressional wave
S-wave	Shear wave
SV-wave	Shear wave that is polarized so that its particle motion and direction of propagation occur in a vertical plane
GPS	Global Positioning System
VP	Source point, Vibe point
3C	Three components
Vp	P-wave velocity
M	Meter
Ms	Millisecond
Hz	Hertz
Db	Decibels
AGC	Automatic Gain Control
NMO	Normal moveout
F-K	Frequency-wavenumber domain
CDP	Common depth point
CaMI	Containment and Monitoring Institute
VTI	Vertical Transverse Isotropy
HTI	Horizontal Transverse Isotropy
HWC	Helically Wound Cable
FRS	Field Research Station
TD	Total depth
MMV	Measurement, monitoring and verification
DTS	Distributed Temperature Sensing
ERT	Electrical resistivity cable
BBRS	Basal Belly River Sandstone
TWT	Two-way time
H1	Horizontal component 1
H2	Horizontal component 2
Z	Vertical component

Chapter One: **Introduction**

The increase of Greenhouse Gas (GHG) emissions and its probable contribution to global warming have been constantly mentioned and discussed in international meetings and scientific studies in recent years. As described in different reports, the greenhouse effect is mainly caused by the concentration of water vapour, carbon dioxide (CO_2), methane, nitrous oxide, ozone and other trace gases in the atmosphere (EPA, 2017; Lecomte et al., 2010). Among these gases, the CO_2 generated from fossil energies such as coal, oil and natural gas contributes significantly to the anthropogenic greenhouse effect (EPA, 2017; IPCC, 2014; Lecomte et al., 2010). Moreover, the increase of CO_2 emissions by 80% between 1970 and 2004 (Lecomte et al., 2010) raises the question on how can society address this issue and how to efficiently achieve the targets established by the Paris CDP 21 Agreement signed by 197 members of the United Nations Framework Convention on Climate Change in 2016. The Paris agreement demonstrates the commitment of the signing members to maintain the global average temperature increase to be below 2 °C by 2050. In order to achieve this target, global carbon dioxide emissions must be reduced by 40 to 70 % (IPCC, 2014). This type of commitment will require the implementation of low carbon technologies at industrial scales around the world.

There are several strategies for the reduction of CO_2 emissions that include the control of energy consumption, the development and increase usage of renewable energies and nuclear power, and the management of fossil fuels energies (Lecomte et al., 2010). The work shown in this thesis focuses on one of the key elements for managing CO_2 emissions from fossil fuel energies. A Carbon Capture and Storage (CCS) project that is being developed in Newell County, Alberta.

Containment and Monitoring Institutes (CaMI) has developed a Field Research Station (FRS) with the objective of executing advanced research while implementing new technologies to improve the understandings for geological containment and storage of CO_2 (Lawton et al., 2014). This thesis forms part of the FRS monitoring program which focusses on the study of borehole seismic surveys. The processing and interpretation of several vertical seismic profiles (VSP) datasets acquired at the FRS will be discussed. The datasets to be analyzed and processed in this work were acquired with two different recording systems; multicomponent geophone arrays and

Distributed Acoustic Sensing (DAS) technology. From which the processing of DAS datasets is one of the major scientific contributions of this thesis given the recent development of this technology and the interest in testing its applications for seismic imaging in monitoring projects.

1.1 Carbon Capture and Storage

Carbon Capture and Storage (CCS) is a process that confines atmospheric CO_2 emissions related to fossil fuel energies. This method consists of capturing CO_2 from industrial facilities such as oil refineries or factories and storing it in the subsurface at strategic geological formations that meet certain characteristics (Lecomte et al., 2010). This method is a promising solution to significantly reduce the CO_2 emissions associated with fossil fuels activities while the development of renewable energy continues to emerge.

The three main stages of the CCS process are the capture of CO_2 from an industrial facility, its transportation to a storage site and then its underground injection and storage. In the capture stage, three different methods can be used: post-combustion, pre-combustion and oxyfuel combustion (Rubin et al., 2005). Once the CO_2 is captured, it generally needs to be transported to the storage facility, with the most common methods to transport CO_2 being through pipelines, or by ships, road and railways (Rubin et al., 2005). For the storage phase, several geological conditions need to be analyzed; this entails the type of formation where the CO_2 will be injected, the characteristics of the seal that will trap the CO_2 in place as well as any potential migration paths through fractures present in the subsurface. Figure 1.1 shows a representation of the different geological formations that may be considered as suitable options for CO_2 injection. These options include depleted oil and gas fields, deep saline formations, unmined coal seams and the use of CO_2 to enhance oil recovery (EOR) at producing oil fields.

Other significant aspects of CCS projects are risk assessment and monitoring protocols. This crucial piece of the process is developed throughout the lifetime of the project as it involves several baseline surveys before injection starts and monitoring surveys during and after the injection is completed. Monitoring surveys generally include but are not limited to repeated surface seismic acquisitions, VSP surveys, electromagnetic methods, and hydrogeology analysis.

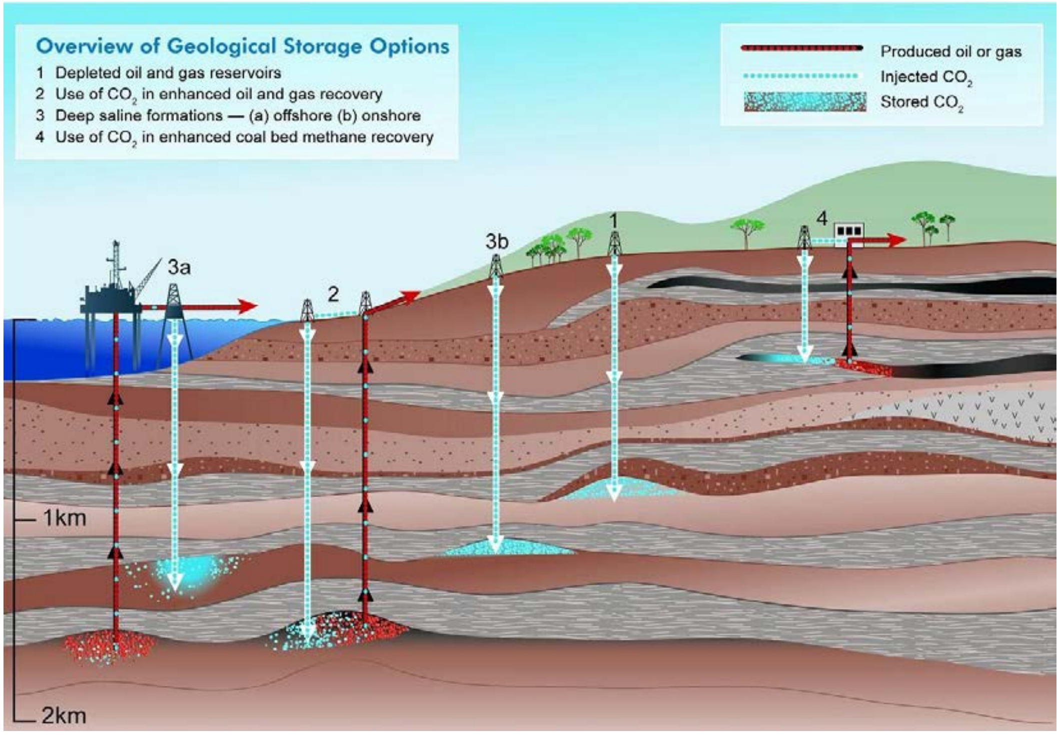

Figure 1.1. Subsurface geological options for CCS (Modified from Rubin et al., 2005).

1.2 Vertical Seismic Profile

The foundation of Vertical Seismic Profiles (VSP) is related to check-shots, which are a commonly used borehole technique to record the direct seismic travel time as a function of depth (Cassell, 1984). A VSP is a borehole seismic survey where the source is located on the surface near the wellhead and is recorded by geophones located in the well (Hardage, 1983). The primary difference between VSP surveys and borehole or surface seismic surveys is that VSP surveys are able to record both downgoing and upgoing wavefields by having surface sources and receivers in the well (5-20 m intervals). Surface seismic surveys only record upgoing wavefields, and check-shot surveys only record the time to depth relation, generally with larger receiver intervals (50-200 m) (Cassell, 1984; Hinds et al., 1996). Figure 1.2 represents the source and receivers configuration of surface seismic and VSP surveys.

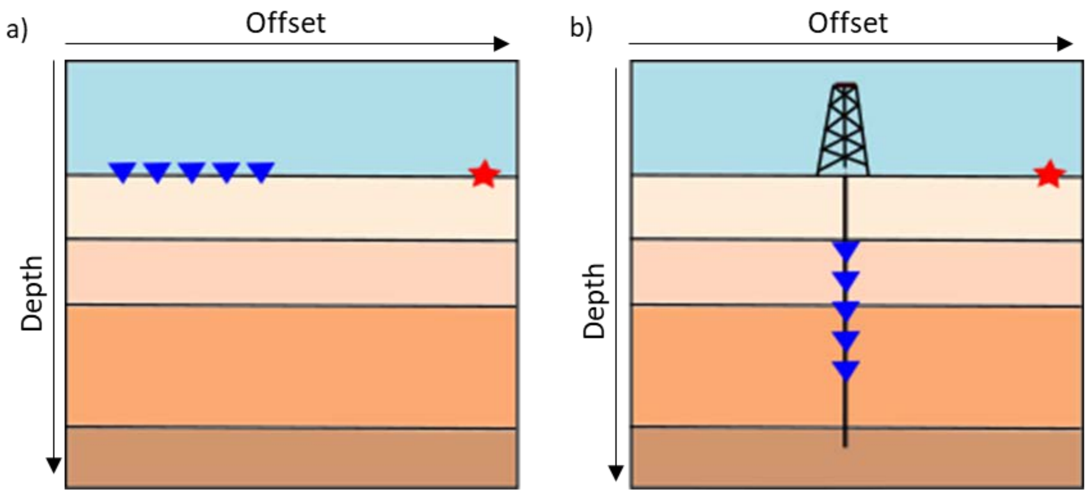

Figure 1.2. a) Scheme of surface seismic and b) vertical seismic profile. Sources are indicated by red stars and receivers by blue triangles.

1.3 Types of VSP surveys

A typical VSP survey consists of surface sources and an array of geophones down or along the well. Depending on the objectives of the survey as well as the configuration of the sources and receivers, and the borehole orientation, VSP surveys are categorized in different types (Pereira et al., 2010). The most common VSP configurations are explained in the following section.

1.3.1 Zero offset VSP

Zero offset VSP is the most common configuration where the source is located near the wellhead (100 m maximum offset), and the geophones are distributed at equally spaced intervals in the well. In this type of geometrical configuration, the source and receiver array are treated as vertically aligned during processing. (Hinds et al., 1996; Pereira et al., 2010). The downgoing wavefield can be easily affected by multiples as the wavelet changes with time. However, the upgoing wavefield captures the reflections from the subsurface in time and depth. From this, we obtain a corridor stack, which is the summation of the primary reflections and repeated on several traces for visual comparison with surface seismic data (Cassell, 1984; Pereira et al., 2010).

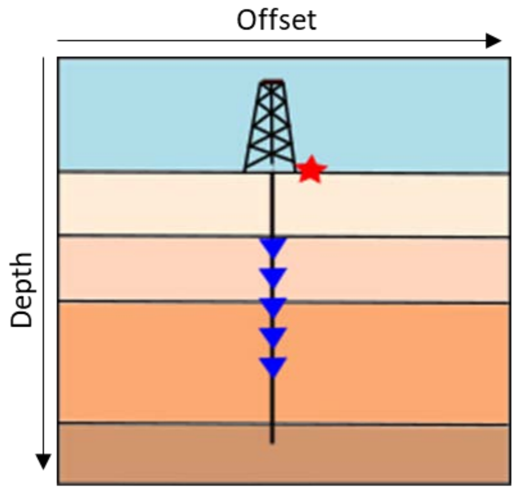

Figure 1.3. Zero offset VSP configuration. The source is represented by a red star close to the wellhead and the receivers in the well are represented by blue triangles.

1.3.2 Offset and walk away VSP

Offset VSPs consist of a geometrical configuration where the source is located at a distance from the wellhead and therefore, the source and receiver locations can no longer be treated as a vertical array for processing purposes (Hinds et al., 1996). By locating the source at an offset from the well, the area of the reflector illuminated by the seismic waves increases significantly. This provides more subsurface information that maps reflectors at a distance from the well and is also linked to the offset and velocity structure. In addition, the imaging results can be correlated with surface seismic data or used for fault and dip identification at a lateral distance from the well and can be used for azimuth versus offset (AVO) and anisotropy analysis (Pereira et al., 2010).

The walk-away VSP configuration is similar to an offset VSP as the source points are placed at increasing distances from the well, while the receivers remain fixed in the wellbore. This type of geometry can generate high-resolution P-waves and S-waves images; it is also used for AVO and anisotropy analysis (Pereira et al., 2010).

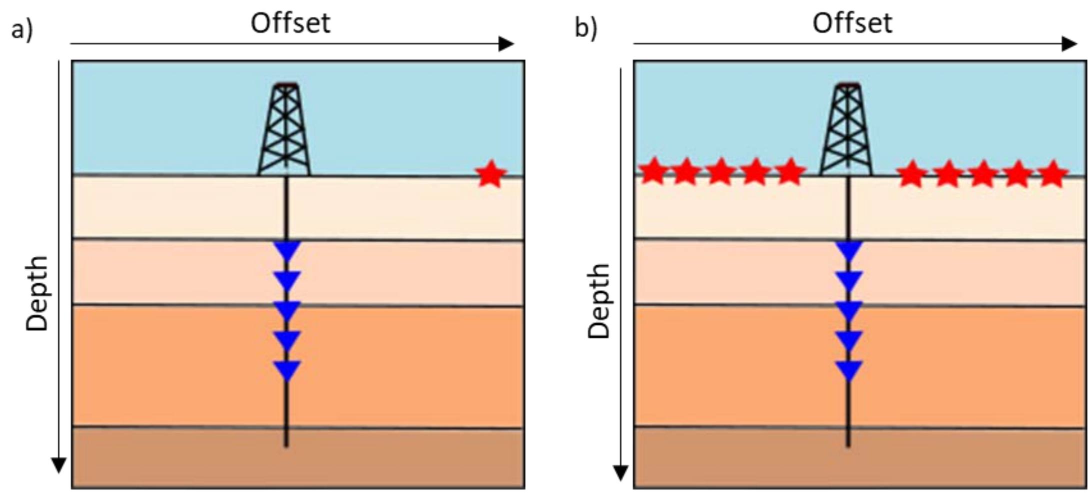

Figure 1.4. a) Offset VSP and b) Walk away VSP configuration. The sources are represented by red stars at a distance from the wellhead, and the receivers in the well are represented by blue triangles.

1.3.3 Walk around VSP

A walk around VSP survey consists of a number of source points located at an equal distance from the well spaced in a circular profile around the well, therefore its name. This configuration covers a broad range of azimuths and is generally used for anisotropy analysis caused by fractures present in the subsurface (Pereira et al., 2010).

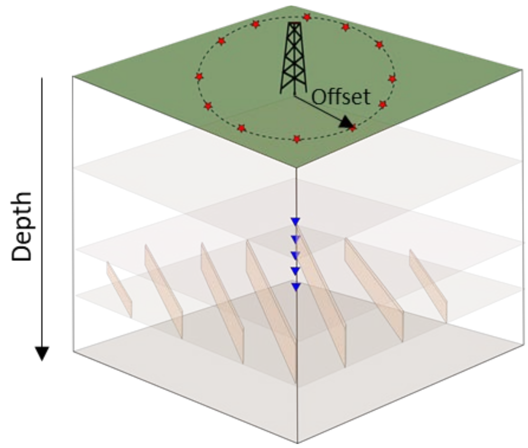

Figure 1.5. Walk around VSP configuration. Based on Pereira et al., 2010.

Anisotropy is defined as the "variation of a physical property depending on the direction in which it is measured" (Sheriff, 2002). Anisotropy is scale dependent, and its detection relies on the scale of the measurements. For this reason rocks can be anisotropic in different aspects depending on the characteristic measured, for example, elastic properties, permeability or resistivity (Pereira et al., 2010; Sheriff, 2002). Furthermore, seismic anisotropy refers to the directional variations of a material's response with the propagation of seismic waves (Liu et al., 2012). Likewise, since seismic wave propagation is dependent on the elastic properties of rocks, the changes with direction would affect the speed of the waves travelling through the material (Pereira et al., 2010). In 1986, Thomsen defined vertical transverse isotropy (VTI) as the simplest case of anisotropy because it has one distinct direction and it is generally the vertical direction whereas the horizontal directions are considered equivalent. In the VTI case, he defined three anisotropy parameters (ε, γ, and δ) which are considered an appropriate combination of elastic moduli, for cases of weak anisotropy. Anisotropy can be classified depending on the direction of the symmetry axis of a transverse isotropy media. If the symmetry axis is vertical, it is called vertical transverse isotropy (VTI) or polar anisotropy, as shown in Figure 1.6 (Liu et al., 2012). Fine layering is a good example of VTI media, and it is also the most common causes of elastic anisotropy. Even though there may be horizontal layers with different isotropic elastic properties, when a seismic wave with a wavelength larger than the thickness of the layers crosses the media, the effective response is dependent on the direction (Pereira et al., 2010).

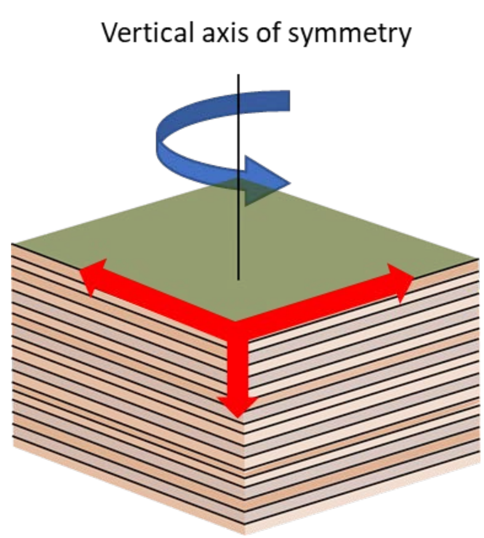

Figure 1.6 Vertical transverse isotropy (VTI) model (based on Pereira & Jones, 2010).

If the symmetry axis is horizontal, it is called horizontal transverse isotropy (HTI) or azimuthal anisotropy (Figure 1.7.) and is generally related to vertically aligned fractures present in the material (Liu et al., 2012). This type of anisotropy can also be described by Thomsen parameters by referencing the angles relative to the horizontal fracture normal direction (Pereira et al., 2010).

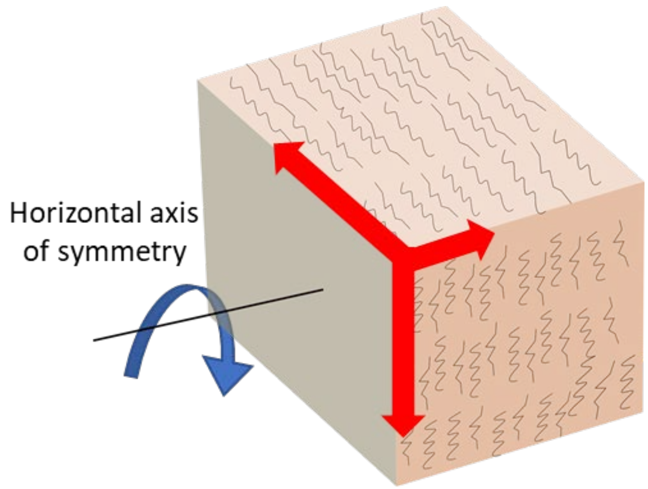

Figure 1.7. Horizontal transverse isotropy (HTI) model (based on Pereira & Jones, 2010).

Anisotropy is present in the majority of rocks, and some of the physical causes of seismic anisotropy include oriented minerals in thin layers and vertically aligned fractures. Even though different anisotropy models with greater complexity can be created and analyzed, VTI and HTI models are the most commonly used anisotropy models in the industry (Liu et al., 2012). Azimuthal anisotropy analysis can be completed by acquiring multi-azimuth walkaway VSP and walkaround VSP surveys (Pereira et al., 2010). Some of the applications of anisotropy analysis include the improvement of seismic imaging, velocity models and the extraction of fracture information (Liu et al., 2012).

1.4 Distributed Acoustic Sensing (DAS)

Distributed Acoustic Sensing is a new technology that has been gaining acceptance for seismic monitoring purposes including surface seismic and wellbore seismic surveys. DAS technology consists of the use of standard fibre optic cables for seismic sensing along a well or horizontal trench. The fibre optic cable is connected to a device called “Interrogation Unit” which measures the deformations generated by impinging seismic waves along the fibre optic cable (Mateeva et al., 2014). When the interrogator unit sends laser pulses along the fibre (Figure 1.8) in the well, a small part of the laser light is back-scattered due to the micro-heterogeneities present in the fibre, also known as Rayleigh scattering. Once the seismic waves travelling through the media reach the fibre, the Rayleigh back-scattered pattern is perturbated, and those variations are transformed into seismic measurements (Mateeva et al., 2014).

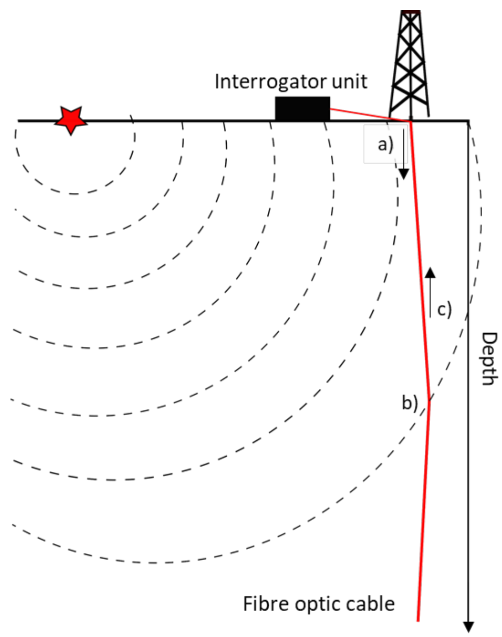

Figure 1.8. DAS schematic (based on Mateeva et al., 2014). a) Interrogator unit sends laser pulse. b) Impinging seismic wave deforms fibre optic cable. c) The perturbated laser pulse is backscattered.

Moreover, the location of those deformations can be determined by recording the arrival time of the returning light, resulting in a profile of the backscattered light. This is enhanced by looking at the phase of two pulses of light separated at a known distance referred to as gauge length or differentiation interval (Dean et al., 2015; Mateeva et al., 2014; Parker et al., 2014). Even though a fixed or variant value can be used for the gauge length, a fixed value of 10 m is commonly used in the literature (Dean et al., 2015; Hartog et al., 2014). The gauge length has an impact in the signal to noise ratio (SNR) such that a larger gauge length yields higher SNR although it also causes lower resolution and distortion at high frequencies. Nevertheless, SNR can be improved by stacking DAS traces of repeated shots (Daley et al., 2016; Mateeva et al., 2014).

Generally, the output measurement of DAS surveys is strain or strain rate. The interrogator unit used for the surveys processed in this thesis is a first generation Silixa iDAS and it measures the strain rate of the fibre. Other characteristics of this interrogator include a spatial resolution of 1 to 2 m and a sampling resolution down to 25 cm (Mondanos et al., 2015). To avoid confusion, DAS channel spacing also known as the spatial resolution is defined as the distance between fibre samples at which DAS measurements are taken over the gauge length (Hartog, 2017; Mateeva et al., 2014). Whereas the trace output spacing or sampling resolution is the interval at which the data is sampled and recorded. Knowing that geophones measure the particle velocity, it is important to understand the connection between DAS and geophone measurements. Daley et al. (2016) described the conversion from strain rate to strain with the integration of raw DAS signal with respect to time. Similarly, he also showed the relationship between the fibre strain and the fibre particle velocity, involving a ratio given by the apparent velocity or the propagation speed along the fibre cable, where the sign determines the direction of propagation (Daley et al., 2016). This conversion seems like a good approach to properly convert DAS signal to a geophone equivalent signal. Even though in this thesis we only show some examples of DAS signal conversion from strain rate to strain (Chapter 4 and 5), it would be interesting to convert the fibre strain to particle velocity and compare the results with the geophone data.

Another interesting aspect of DAS is its amplitude response dependence to cosine squared of the incidence angle. Compared to conventional geophones which have a response proportional to the cosine of the incidence angle. Kuvshinov (2016) described the relationship between DAS response and the cosine squared of the incidence angle as follows. When a P-wave propagates in a medium, the strain generated is parallel to the direction of the wave propagation. The strain is defined as a second rank tensor and its projections present a cosine squared dependence of the angle between the wave propagation vector and the fibre direction (Hornman et al., 2013; Innanen, 2016; Kuvshinov, 2016). This observation has been demonstrated in geometrical models (Eaid et al., 2017; Innanen, 2016, 2017) and proven with field data as shown by Mateeva et al. (2014) and Willis et al. (2016). Figure 1.9 illustrates a schematic of a straight fibre embedded in a cable, where the fibre is shown in blue and the cable in green with an incident wave at an angle θ with respect to the cable.

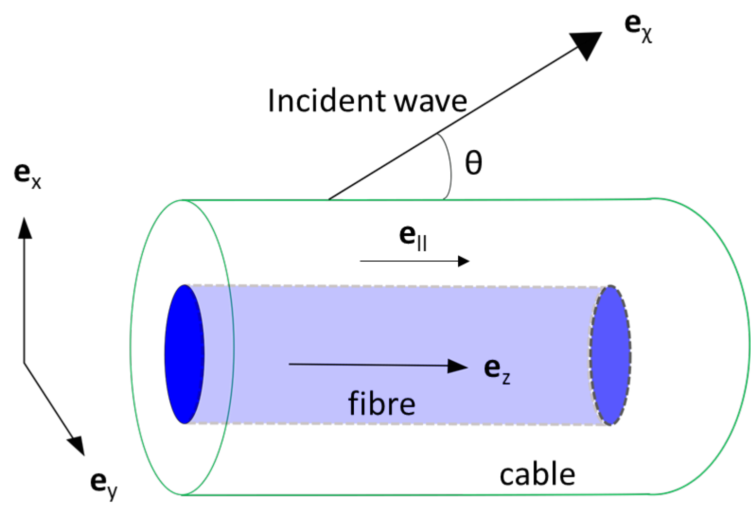

Figure 1.9 Schematic of straight fibre embedded in a cable (modified from Kuvshinov 2016).

Although DAS is considered a new technology, it has several advantages for monitoring purposes. The advantages include a low-cost for data acquisition once fibre optic cables are installed; it is non-intrusive, ideal for production monitoring; it has full vertical coverage in wells, and it is possible to use pre-installed fibre optic cables for DAS measurements. Nevertheless, some of the challenges entail the initial cost of the fibre optic cable installation, lower signal-to-noise ratio (S/N) compared to geophones, the uncertainty in the precise location of DAS channels in the well, and the broadside sensitivity limitation (Mateeva et al., 2014 and Wu et al., 2015). An alternative to mitigate the axial deformation limitation is utilizing different fibre optic configurations to increase the broadside sensitivity along the cable. One of the cables developed to increase the broadside sensitivity of DAS measurements is called Helically Wound Cable (HWC) (Hornman et al., 2013; Kuvshinov 2016; Lumens et al., 2013). HWC consists of shaping the fibre inside the cable as shown in Figure 1.10, where the response of the cable as a function of the incidence angle depends on the elastic properties of the cable, the wrapping angle α and the ground (Hornman et al., 2013; Kuvshinov, 2016; Mateeva et al., 2014). The value of the wrapping angle α equal to 30° is used frequently in the literature for HWC and the reason behind it is that it has a nearly isotropic sensitivity (Hornman et al., 2013; Mateeva et al., 2014).

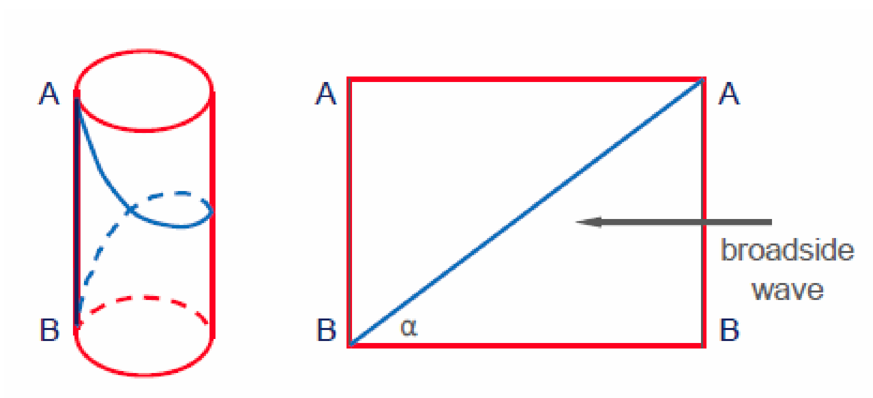

Figure 1.10. HWC representation (modified from Mateeva et al., 2014).

Innanen (2016) developed a geometrical model that considers the shape of the cable and the geometry of the fibre to analyze the response of the fibre and test different configurations that could be a potential solution to the broadside sensitivity of DAS. In this thesis, a variation of HWC consisting of two fibre helixes wrapped on a mandrel is discussed with field tests results from the FRS. An example of this type of HWC is shown in Figure 1.11 corresponding to the HWC deployed at the FRS.

Figure 1.11 Example of the HWC deployed at the FRS. a) axial view of the HWC cable b) image of the two fibre helixes wrapped on a mandrel. (Lawton et al., 2017).

1.5 Thesis objectives and overview

The main goal of this thesis is to process, interpret and analyze several Vertical Seismic Profile surveys acquired at the Field Research Station between 2015 and 2017 while testing and comparing new technologies such as fibre optic cables for Distributed Acoustic Sensing (DAS). Each chapter of this thesis explains the workflows used for each survey to achieve this goal.

Chapter 2 provides an overview of the Field Research Station. Including a geology background and the acquisition parameters of the datasets and software used in this thesis.

Chapter 3 covers the azimuthal traveltime analysis performed with the walk-around VSP dataset acquired at the Field Research Station.

Chapter 4 presents the comparison between geophone and DAS measurements by processing zero-offset VSP surveys acquired at the Field Research Station in May and July 2017. The depth estimation of DAS channels is also discussed as is one of the limitations of this new technology.

Chapter 5 is the continuation of the comparison carried out in the previous chapter. In this case by processing a walk-away line for both datasets, geophones, and fibre optic cables.

Chapter 6 provides the conclusions of this thesis and recommendations for the application of similar methods.

Chapter Two: **CaMI Field Research Station**

The Field Research Station (FRS) is a multidisciplinary project developed by the Containment and Monitoring Institute (CaMI) in collaboration with the University of Calgary. This project encourages the support and contribution of industry, research groups and universities, with the University of Calgary as one of the more involved contributors. The objective of the FRS is a small-scale CO_2 field site with new technologies and research approaches to improve monitoring technologies applicable to Carbon Capture and Storage (CCS) and its applicability in Canada. The FRS supports a broad range of experiments associated with the measurement, monitoring and verification (MMV) program, including: 3D surface seismic surveys, time-lapse seismic data analysis, borehole seismic measurements, cross-well seismic measurements, well logging analysis, microseismic monitoring, electromagnetic surveys, surface electrical resistivity tomography, geochemical sampling, hydrostratigraphic characterization, aquifer testing and analysis, among others (CaMI, 2013; Lawton et al. 2014).

The FRS is located in southern Alberta, approximately 189 km southeast of Calgary, near the town of Brooks in Newell County (Figure 2.1). The site covers a total of 200 hectares, leased courtesy of Torxen Energy. The field site consists of an injection well, two observation wells, several groundwater monitoring wells, a CO_2 tank and associated CO_2 piping and pump systems, as shown in Figure 2.2. (Lawton et al. 2014; Lawton et al., 2017). The injection well, CMCRI Countess 100/10-22-017-16W4/00 has a total depth (TD) of 550 m, the observation wells, CMCRI Countess 103/10-22-017-16W4/00 and CMCRI Countess 102/10-22-017-16W4/00, also called geochemical and geophysical wells, respectively, have a TD of 350 m.

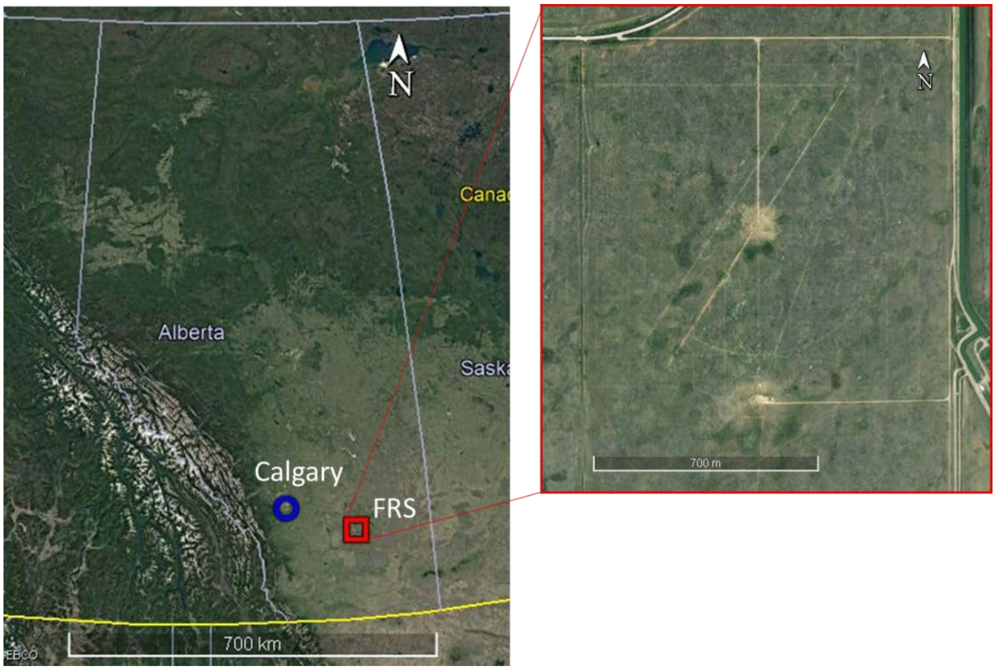

Figure 2.1 Field Research Station location highlighted with a red box (Google Earth, 2019).

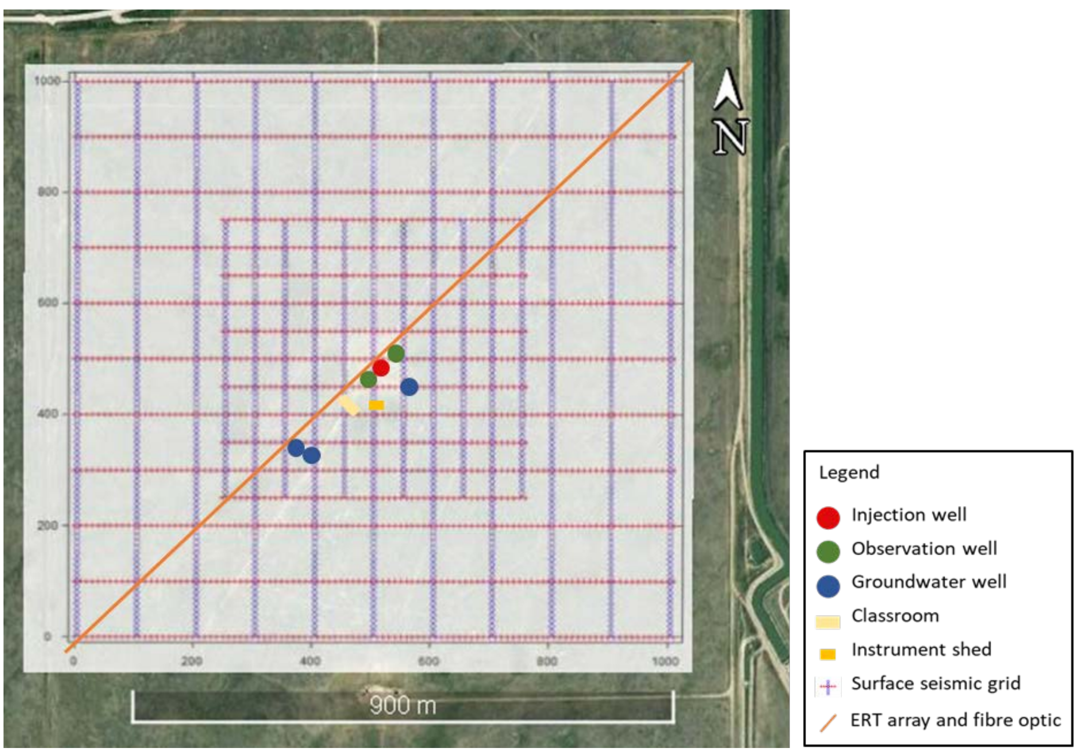

Figure 2.2 Infrastructure diagram of the FRS (Modified from Lawton et al., 2017; Google Earth, 2019).

Both observation wells have a set of equipment installed permanently for monitoring purposes. The geochemical well is completed with steel casing and has integrated fibre optic cables for Distributed Acoustic Sensing (DAS) and Distributed Temperature Sensing (DTS), a heat-pulse cable, stainless steel U-tube for fluid reservoir sampling, and an above zone pressure gauge (Lawton et al., 2017). In comparison, the geophysical well is completed with fibreglass casing and includes fibre optic cables for DAS and DTS measurements, a heat-pulse cable, a 16-level electrical resistivity cable (ERT), and a 24-level 3 component geophone array. The well is accessible for wireline tools (Lawton et al., 2017). As an example, Figure 2.3 shows a representation of the competition diagram of geophysical Observation Well 2 provided by Schlumberger. In addition to the observation wells, the FRS also has installed an ERT array of 112 electrodes and fibre optic cables deployed at a depth of 1.3 m in a horizontal trench of 1.1 km length crossing the field site from NE to SW direction (Figure 2.2).

The fibre optic cable installation at the FRS consisted of an encircled connection starting at the classroom, going through the geophysics observation well, in which straight and helical-wound (HWC) fibre optic cables were deployed. From there, the fibre continues to the geochemical well where only straight fibre optic cable was deployed in the well. The cable then continues to the NE-SW horizontal trench and buried at a depth of 1 m, as illustrated in Figure 2.4. Both fibre optic cables have a nominal gauge length of 10 m and output trace spacing of 0.25 m.

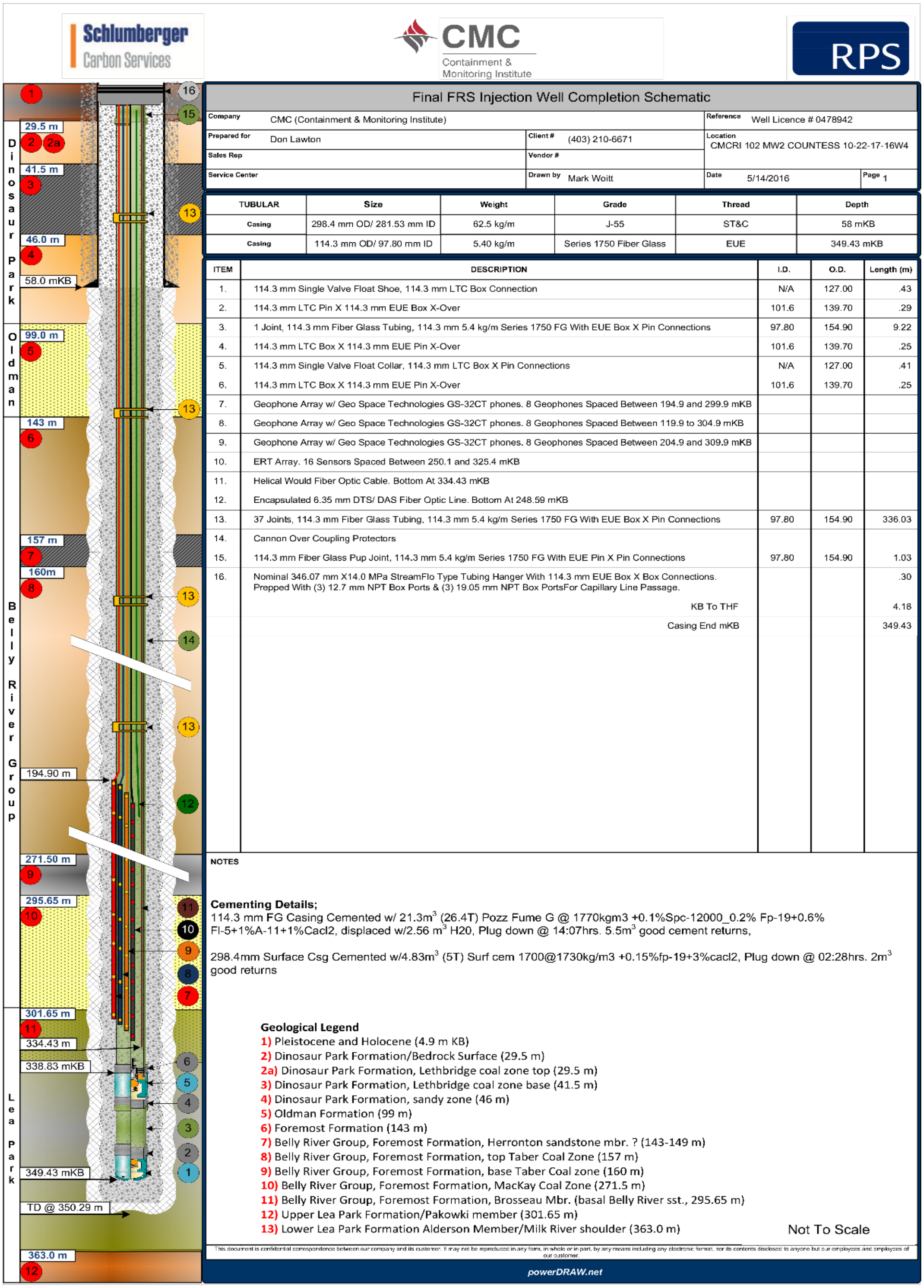

TUBULAR	Size	Weight	Grade	Thread	Depth
Casing	298.4 mm OD/ 281.53 mm ID	62.5 kg/m	J-55	ST&C	58 mKB
Casing	114.3 mm OD/ 97.80 mm ID	5.40 kg/m	Series 1750 Fiber Glass	EUE	349.43 mKB

ITEM	DESCRIPTION	I.D.	O.D.	Length (m)
1.	114.3 mm Single Valve Float Shoe, 114.3 mm LTC Box Connection	N/A	127.00	.43
2.	114.3 mm LTC Pin X 114.3 mm EUE Box X-Over	101.6	139.70	.29
3.	1 Joint, 114.3 mm Fiber Glass Tubing, 114.3 mm 5.4 kg/m Series 1750 FG With EUE Box X Pin Connections	97.80	154.90	9.22
4.	114.3 mm LTC Box X 114.3 mm EUE Pin X-Over	101.6	139.70	.25
5.	114.3 mm Single Valve Float Collar, 114.3 mm LTC Box X Pin Connections	N/A	127.00	.41
6.	114.3 mm LTC Box X 114.3 mm EUE Pin X-Over	101.6	139.70	.25
7.	Geophone Array w/ Geo Space Technologies GS-32CT phones. 8 Geophones Spaced Between 194.9 and 299.9 mKB			
8.	Geophone Array w/ Geo Space Technologies GS-32CT phones. 8 Geophones Spaced Between 119.9 to 304.9 mKB			
9.	Geophone Array w/ Geo Space Technologies GS-32CT phones. 8 Geophones Spaced Between 204.9 and 309.9 mKB			
10.	ERT Array. 16 Sensors Spaced Between 250.1 and 325.4 mKB			
11.	Helical Would Fiber Optic Cable. Bottom At 334.43 mKB			
12.	Encapsulated 6.35 mm DTS/ DAS Fiber Optic Line. Bottom At 248.59 mKB			
13.	37 Joints, 114.3 mm Fiber Glass Tubing, 114.3 mm 5.4 kg/m Series 1750 FG With EUE Box X Pin Connections	97.80	154.90	336.03
14.	Cannon Over Coupling Protectors			
15.	114.3 mm Fiber Glass Pup Joint, 114.3 mm 5.4 kg/m Series 1750 FG With EUE Pin X Pin Connections	97.80	154.90	1.03
16.	Nominal 346.07 mm X14.0 MPa StreamFlo Type Tubing Hanger With 114.3 mm EUE Box X Box Connections. Prepped With (3) 12.7 mm NPT Box Ports & (3) 19.05 mm NPT Box PortsFor Capillary Line Passage.			.30
	KB To THF			4.18
	Casing End mKB			349.43

NOTES

Cementing Details;
114.3 mm FG Casing Cemented w/ 21.3m^3 (26.4T) Pozz Fume G @ 1770kgm3 +0.1%Spc-12000_0.2% Fp-19+0.6% Fl-5+1%A-11+1%Cacl2, displaced w/2.56 m^3 H20, Plug down @ 14:07hrs. 5.5m^3 good cement returns,

298.4mm Surface Csg Cemented w/4.83m^3 (5T) Surf cem 1700@1730kg/m3 +0.15%fp-19+3%cacl2, Plug down @ 02:28hrs. 2m^3 good returns

Geological Legend
1) Pleistocene and Holocene (4.9 m KB)
2) Dinosaur Park Formation/Bedrock Surface (29.5 m)
2a) Dinosaur Park Formation, Lethbridge coal zone top (29.5 m)
3) Dinosaur Park Formation, Lethbridge coal zone base (41.5 m)
4) Dinosaur Park Formation, sandy zone (46 m)
5) Oldman Formation (99 m)
6) Foremost Formation (143 m)
7) Belly River Group, Foremost Formation, Herronton sandstone mbr. ? (143-149 m)
8) Belly River Group, Foremost Formation, top Taber Coal Zone (157 m)
9) Belly River Group, Foremost Formation, base Taber Coal zone (160 m)
10) Belly River Group, Foremost Formation, MacKay Coal Zone (271.5 m)
11) Belly River Group, Foremost Formation, Brosseau Mbr. (basal Belly River sst., 295.65 m)
12) Upper Lea Park Formation/Pakowki member (301.65 m)
13) Lower Lea Park Formation Alderson Member/Milk River shoulder (363.0 m)

Figure 2.3 Completion schematic of geophysical Observation Well 2.

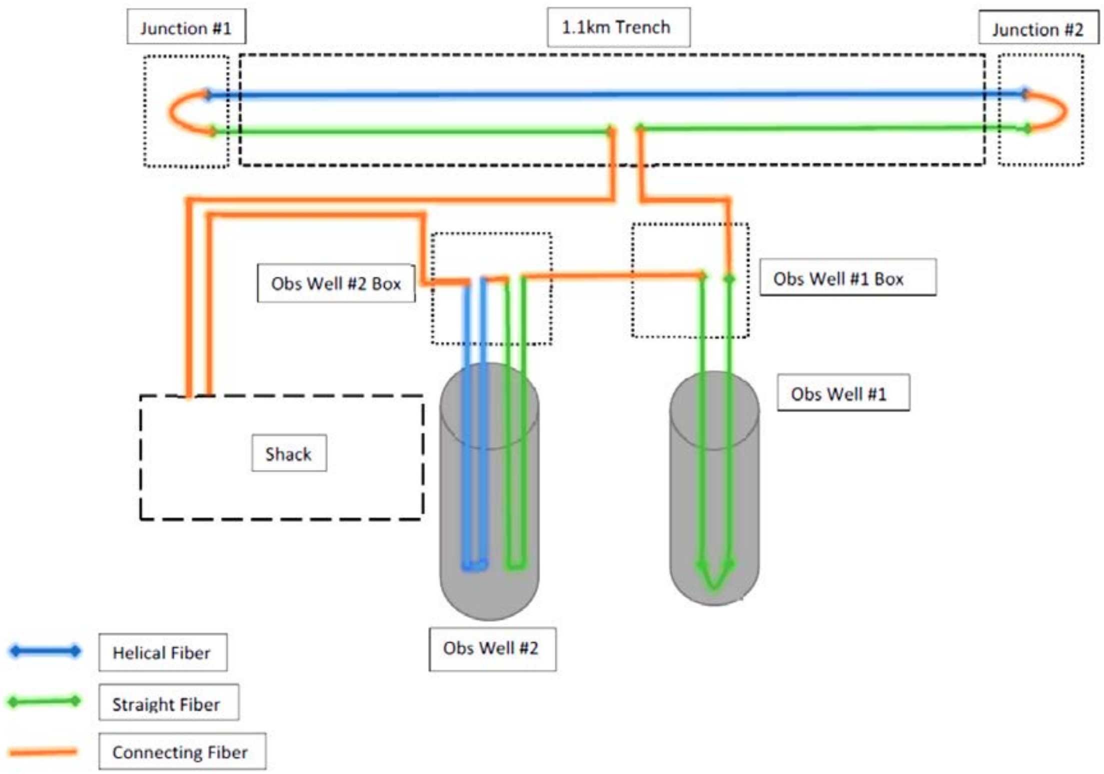

Figure 2.4 Fibre optic cable distribution at the FRS (from Lawton, 2017).

For visual reference, a DAS VSP source gather recorded in the observation wells is displayed in Figure 2.5. The source gather was recorded in July 2017 with a zero offset source location and a vertical stack of sixteen sweeps. The first thing to notice is a three-panel separation; each panel corresponds to the fibre loop in the wells. Figure 2.5a) is the HWC in the geophysics well; b) is the straight fibre in the geophysics well, and c) is the straight fibre of the geochemical well. An interesting remark is a horizontal noise visible across the panel in Figure 2.5c), more specifically in the shallow section from 0 ms to 50 ms. The noise seems to be associated with the interrogator unit or objects near it causing a perturbation during the acquisition of the dataset. Each panel displays a “V” shape, where each side of it corresponds to the data recorded as the fibre loops down and up in the well. The events recorded from each side are expected to generate similar results as they are recording the same energy. To verify this, a quality control step was performed between both sides of the fibre loop and it is described in Chapter four.

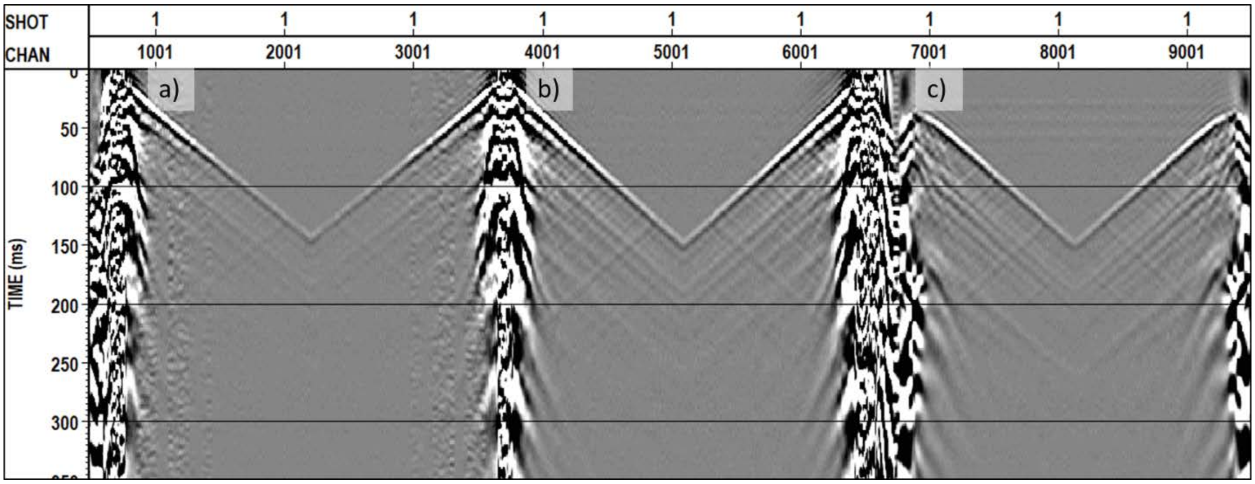

Figure 2.5 Example of a DAS record for a zero offset vibe location at the geophysical observation well. a) HWC in geophysical observation well, b) straight fibre in geophysical observation well and c) straight fibre in geochemical observation well.

2.1 Geology

The FRS is located within the Southern Alberta Plains, and a stratigraphic column of the Upper Cretaceous and Cenozoic strata is illustrated in Figure 2.6. There are two proposed intervals for the CO_2 injection that consist of sand reservoirs at 300 and 500 m deep approximately, corresponding to the Basal Belly River Sandstone (BBRS) and the Medicine Hat Formation respectively. For the development of the site, the shallow target was selected as the initial primary target and the deeper one as a secondary target. Since the work shown in this thesis is mainly focused on the primary target, this section will describe the target interval and seal characteristics corresponding to the primary target.

The Upper Cretaceous Belly River Group is predominant in the Southern Alberta Plains, and it is comprised of the Foremost, Oldman and Dinosaur Park formations. The Dinosaur Park Formation is the uppermost formation of the Belly River Group, and the Foremost Formation is the primary target of CO_2 injection at the FRS (ERCB and AGS, 2010).

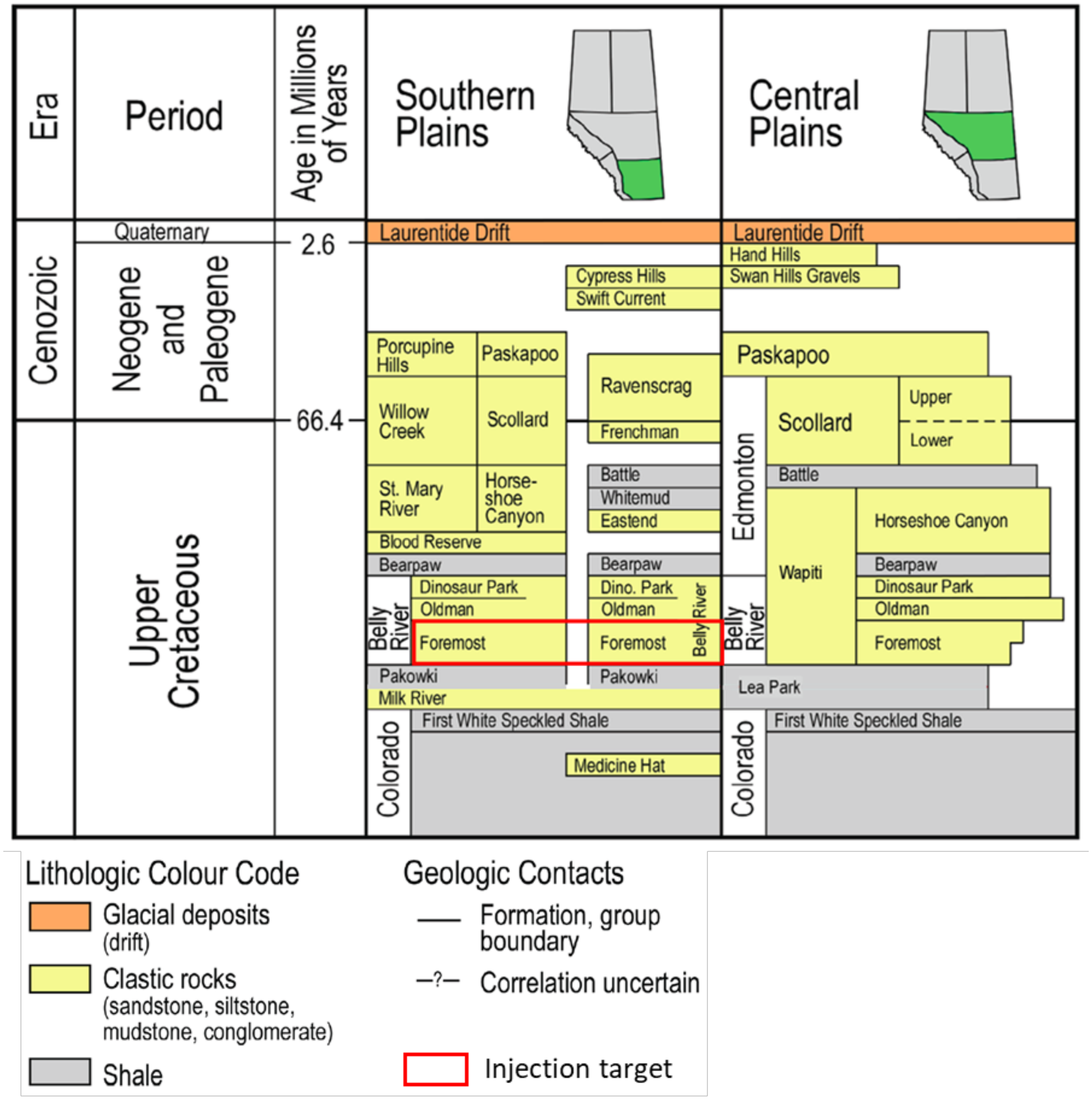

Figure 2.6 Southern Alberta Plains stratigraphic column, injection target highlighted with the red box (Modified from AER and AGS 2013).

In Southeastern Alberta, the lowermost section of the Foremost Formation was deposited in a coastal to shallow-marine environment. The Basal Belly River Sandstone in the Foremost Formation is the result of several coarsening-upward cycles, generally incised by fluvial channels. The BBRS is considered a substantial hydrocarbon reservoir in Alberta (Dawson et al., 1994). According to Hamblin and Abrahamson (1996), the Basal Belly River Sandstone consists of seven stacked composite regressive cycles dominated by shoreline sandstones oriented north-south. The

BBRS is described as fine to medium-grained sandstone with poorly to well-sorted grains with low sphericity, and the grains are generally loosely packed with calcite cement pore-fill (Hamblin and Abrahamson, 1996). At the FRS, the BBRS is present in the injection well between 295.65 m and 301.65 m deep. It is directly overlain by mudstones, coals and fine sandstones of the McKay Coal Zone, which constitutes the seal for the BBRS injection zone, the top of which occurs on top of the last cored coal at 264.16 m (Osadetz et al., 2017).

The Foremost Formation is comprised of interbedded successions that in addition to the basal sandstone at the base, it is also composed of interbedded sandstone, siltstone, carbonaceous shales and coal seams (Dawson et al., 1994; Glass, 1990; Hamblin & Abrahamson, 1996). The two more prominent coal zones are the Taber coal zone located at the top of the formation and the McKay coal zone overlain the BBRS which is commonly used as a marker to identify the BBRS (Dawson et al., 1994; Glass, 1990). In the injection well, the contact between the BBRS and the McKay Coal Zone can be identified easily, while the McKay Coal Zone acts as a seal of the BBRS (Dongas, 2016; Osadetz et al., 2017).

Figure 2.7 displays the wireline logs from the injection well and the two observation wells. The gamma-ray log and the sonic P-wave velocity logs are shown in red and blue respectively. The zone of interest is highlighted with red rectangles, note the scale difference per well.

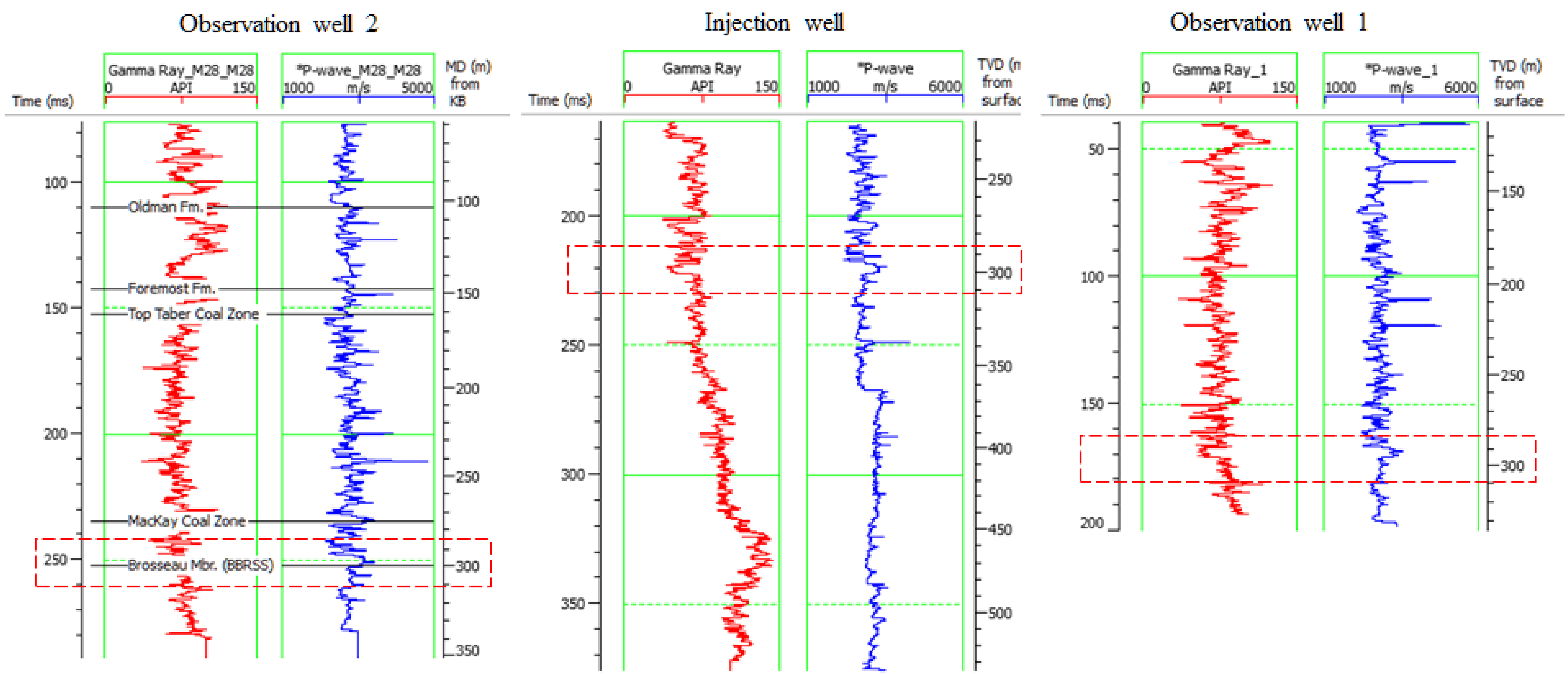

Figure 2.7 Wireline logs of Injection Well and Observation Wells at the Field Research Station. The gamma-ray log is shown in red, and P-wave velocity is shown in blue. Formation Tops of Observation Well 2 are shown in black and the zone of interest is marked with red rectangles.

2.2 Datasets

Since the establishment of the Field Research Station, surface seismic and vertical seismic profiles (VSP) surveys have been acquired. Among these surveys, a 3D surface seismic survey was acquired in 2014 as a baseline. Figure 2.8 displays an example of the PP and PS seismic volumes processed by Dr. Helen Isaac (Lawton et al. 2017).

VSP surveys have been recorded at the FRS between May 2015 and September 2018. In this study, three datasets were used. One recorded in May 2015 and the other two acquired in May and July 2017. The survey geometry and acquisition parameters of each dataset are described in the following sections. Note that the work shown in this thesis is mainly focused on the VSP data acquired at the injection well and geophysical observation well.

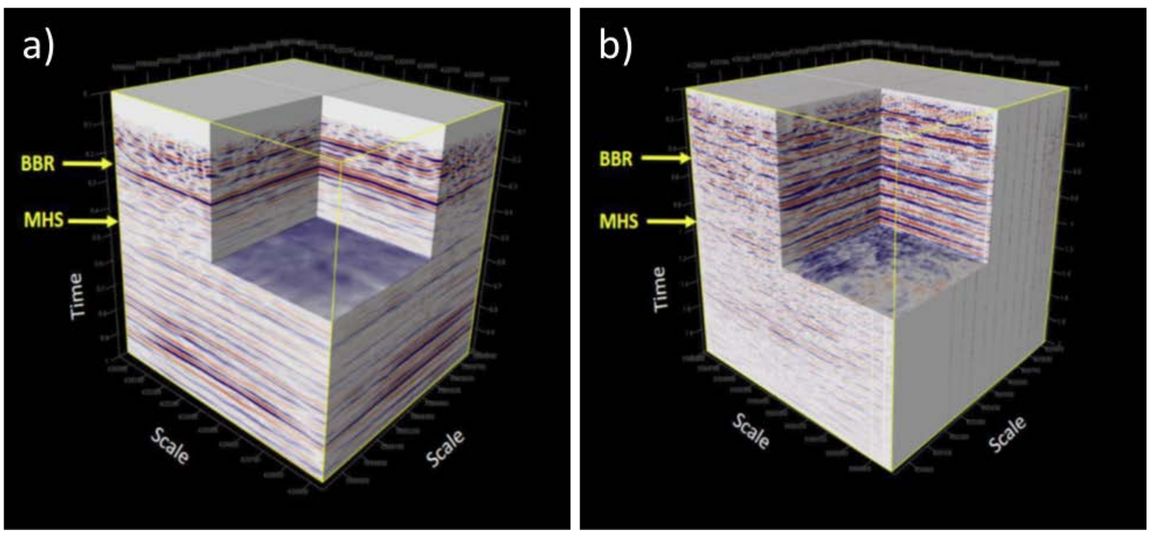

Figure 2.8 FRS baseline seismic volumes acquired in 2014. a) PP waves, b) PS waves.

2.2.1 Dataset 1: Walk around VSP

In May 2015 two 2D surface seismic lines and a three-component (3C) walk-away and half walk-around VSP survey were recorded at the FRS with the collaboration of the Microseismic Industry Consortium from the University of Calgary. The geometry for the VSP surveys is illustrated in Figure 2.8. The source was an IVI EnviroVibe, sweeping from 10 to 200 Hz linearly over 16 seconds with four additional seconds of listening time. The recording system was a three-component ESG SuperCable; it was deployed at three different levels to cover depths ranging from

106 to 496 meters with 15 m spacing between receivers. The two VSP source lines were acquired three times, once for each tool placement in the well. The walk away source line (NE-SW orientation) had 10 m spacing between Vibe Points (VP). The half walk around, or semi-circular source line had a 400 m radius from the well and VP every five degrees (Hall et al., 2015). Due to difficulties with the dataset, only the half walkaround data was used in this thesis mainly for azimuthal anisotropy analysis. This analysis is discussed in more detail in Chapter three of this thesis.

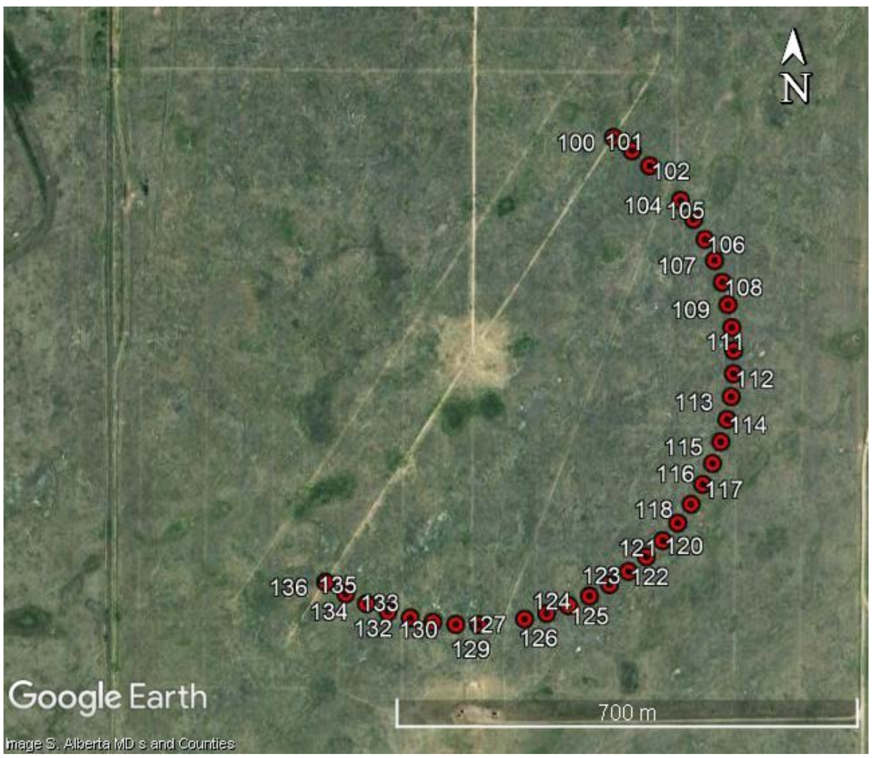

Figure 2.9 Acquisition geometry of VSP survey acquired in May 2015. Walk around source points are marked in red (Google Earth, 2019).

2.2.2 Dataset 2 and 3: Zero offset and walk away VSP

In May and July 2017, multiple VSP surveys were acquired at the FRS. The geometry design of the VSP surveys included various walk-away VSP centred in the geophysical well with the following orientations: NE-SW, NW-SE for May survey, and N-S and E-W for July survey (Figure 2.9). The datasets were recorded using the 24-level 3C geophone array and integrated fibre optic cables in the geophysical observation well for DAS acquisition. Table 2.1 lists some of the DAS acquisition parameters of datasets 2 and 3. The source was the same IVI EnviroVibe used for the first dataset, but in this case, it swept from 10 to 150 Hz linearly over 16 seconds with an additional 3 seconds listening time. For DAS datasets, the interrogator unit used was a first-generation Silixa iDAS with a gauge length of 10 m and an output trace spacing of 0.25 m. These datasets were utilized for two separate analysis; a zero offset VSP processing and a walk away VSP processing; these are discussed in Chapters four and five respectively.

Table 2.1 DAS acquisition parameters

Interrogator unit	1st generation Silixa iDAS
Gauge length	10 m
Output trace spacing	0.25 m
Total depth of fibre optic cables	334.43 m

2.3 Software

For this thesis VISTA Desktop Seismic Data Processing Software provided by Schlumberger was used for processing the data. MATLAB by MathWorks (including CREWES toolbox) was also used in different parts of this research. CGG Hampson-Russell software was utilized for synthetic seismogram generation. Further information regarding the MATLAB codes generated in this thesis can be found in the appendix A.

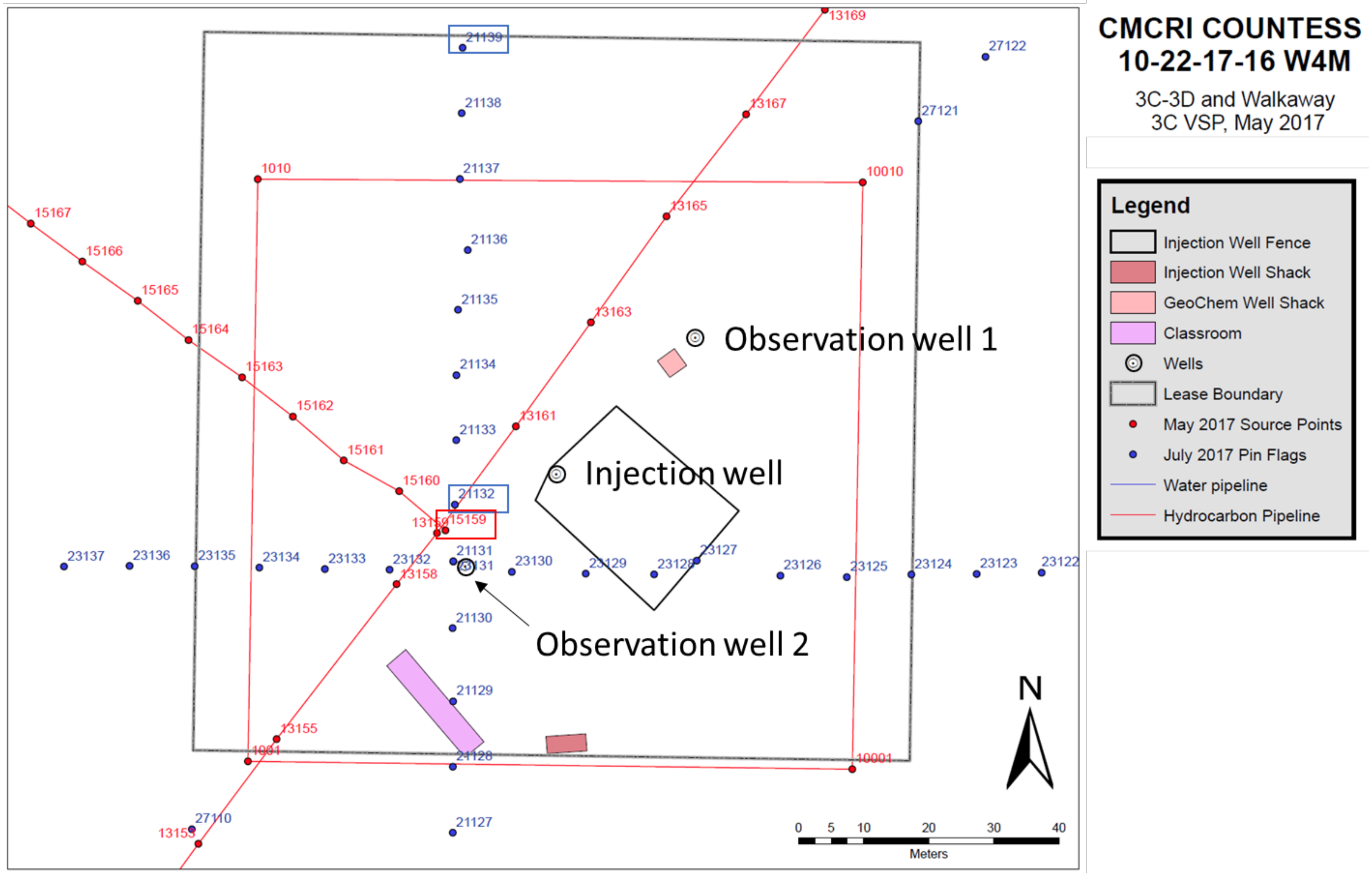

Figure 2.10 VSP survey geometry from May in red and July in blue. The source points used for the zero offset VSP processing are highlighted with a red and blue rectangle for May and July surveys, respectively.

Chapter Three: **VSP azimuthal traveltime analysis**

In this chapter, the results of a Vertical Seismic Profile (VSP) azimuthal traveltime analysis are discussed. The study was performed by processing and analyzing a half walk-around VSP survey, acquired in May 2015, with the purpose of identifying possible azimuthal anisotropy present at the Field Research Station (FRS) and contribute with the characterization of the CO_2 injection study area. In order to achieve this, first break traveltime analysis from the VSP survey was undertaken. The identification of a sinusoidal trend in the traveltimes versus azimuth within the data would identify the fast and slow velocity directions and establish a relation between the FRS area and the Western Canada stress orientation (NE-SW). In addition to the azimuthal traveltime analysis, an estimation of the incidence angle was calculated from the VSP data rotation and then compared to the incidence angle obtained from a ray tracing method.

3.1 Acquisition parameters and procedure of the VSP azimuthal traveltime analysis

The acquisition parameters of the walk around VSP survey are shown in Table 3.1. The receiver was ESG SuperCable®, an innovative tool for wireline monitoring with a multi-use recording system that consists of an analog sensor instrumentation usually used in permanent reservoir monitoring applications (ESG Solutions, 2018). The multicomponent tool was deployed in the injection well at three different levels covering depths from 106 m to 496 m. Each tool sensor had a spacing of 15 m. The seismic source was the University of Calgary IVI Enviro Vibe. Vibroseis trucks are a commonly used seismic source where a vibrator is used to generate seismic waves at a particular bandwidth and length (Sheriff, 2002). The frequency of the sweep for the walk around VSP survey was 10 to 200 Hz over 16 seconds. The offset or radius was of 400 m, a reasonable distance given the depth of the CO_2 injection target at 350 m, the azimuthal increment was of 5 degrees for broad coverage. The workflow performed for the azimuthal traveltime analysis is listed in Figure 3.1. Each step of the procedure will be explained in the following sections.

Table 3.1 acquisition parameters for the half walk around VSP.

Acquisition parameters	**Walk around VSP**
Receiver type	3C SuperCable® (3 levels)
Receiver range	106 – 496 m
Receiver spacing	15 m
Source type	Enviro Vibe
Vibroseis frequency and sweep	10 – 200 Hz, 16 s
Walk around source interval	5°
Walk around offset (radius)	400 m

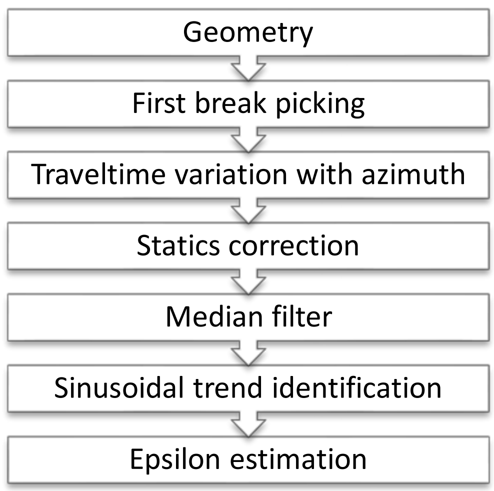

Figure 3.1 Azimuthal traveltime analysis workflow.

3.1.1 Geometry and first break picks

Setting up the acquisition geometry of the dataset was the first step of the workflow, Figure 3.2 shows the geometry of the survey. The receivers are shown in green and the source points or vibe points (VP) are shown in black.

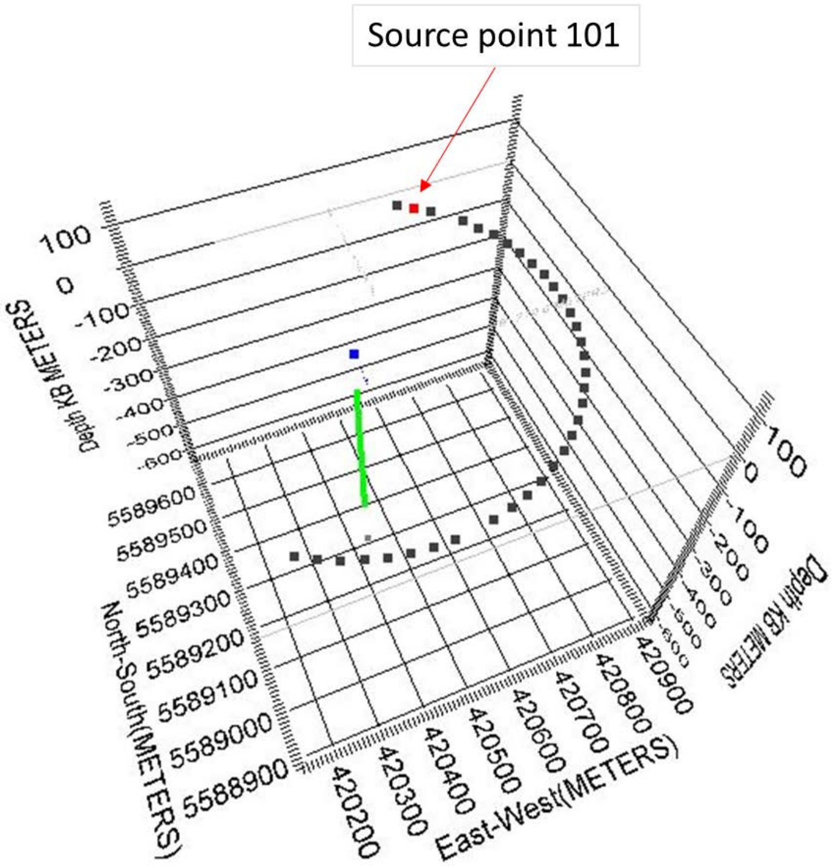

Figure 3.2 Walk-around VSP geometry (Line 204). VPs in black, receivers in green and wellhead in blue. Highlighting source point 101 in red.

Once the headers of the dataset were appropriately sorted, the first breaks from the geophone array for each VP in the walk-around VSP (Line 204) were picked for the vertical and horizontal components. Figures 3.3 – 3.6 show an example of the first break picks of source point 101 of each component respectively displayed with Automatic Gain Control (AGC) of a window length of 250 ms. AGC is a method to adjust the amplitudes of the traces for visualization purposes based on statistical observations of the amplitude decay of the input traces. The root-mean-square of the amplitudes is calculated over a given window, in this case of 250 ms, to create an amplitude model. The AGC output is obtained by dividing the input traces by the amplitude model (Margrave, 2014). Notice that 6 of the 27 traces were identified as bad traces and had to be nulled. Figure 3.3 shows raw the vertical component and Figure 3.4 shows the raw vertical component after the bad traces were nulled, similarly with Figures 3.5 and 3.6. Additionally, the second trace of the vertical component seems to start recording before the rest of the receivers; one possible reason could be an irregularity between the time on the receiver and the Global Positioning System (GPS) measurement used during the recording. The data recorded with that geophone were not taken into consideration for the rest of the analysis.

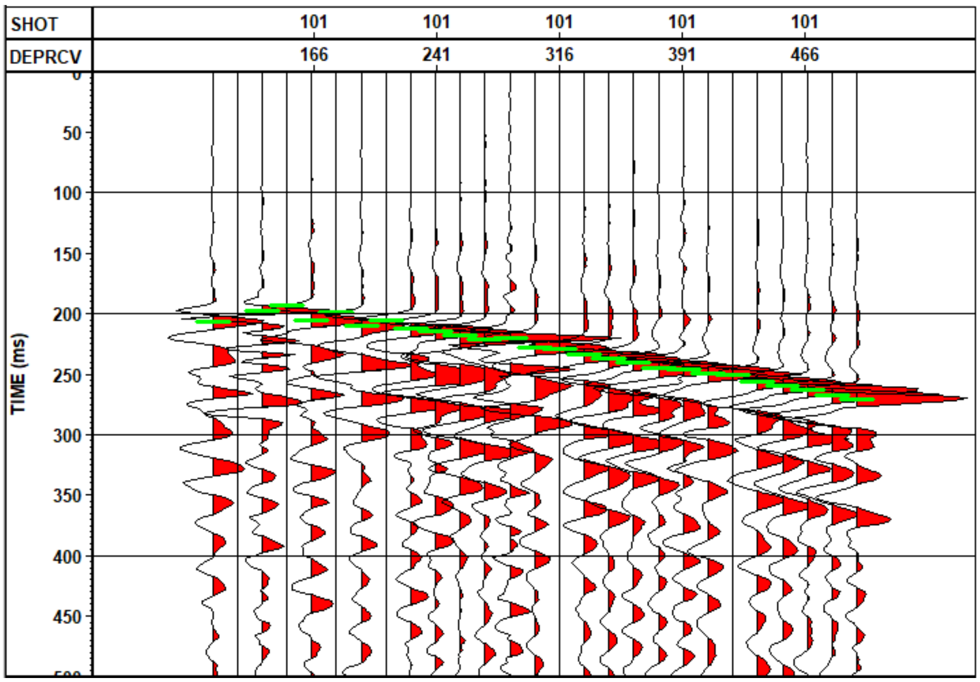

Figure 3.3 Raw vertical component of VP 101 with first breaks in green and AGC.

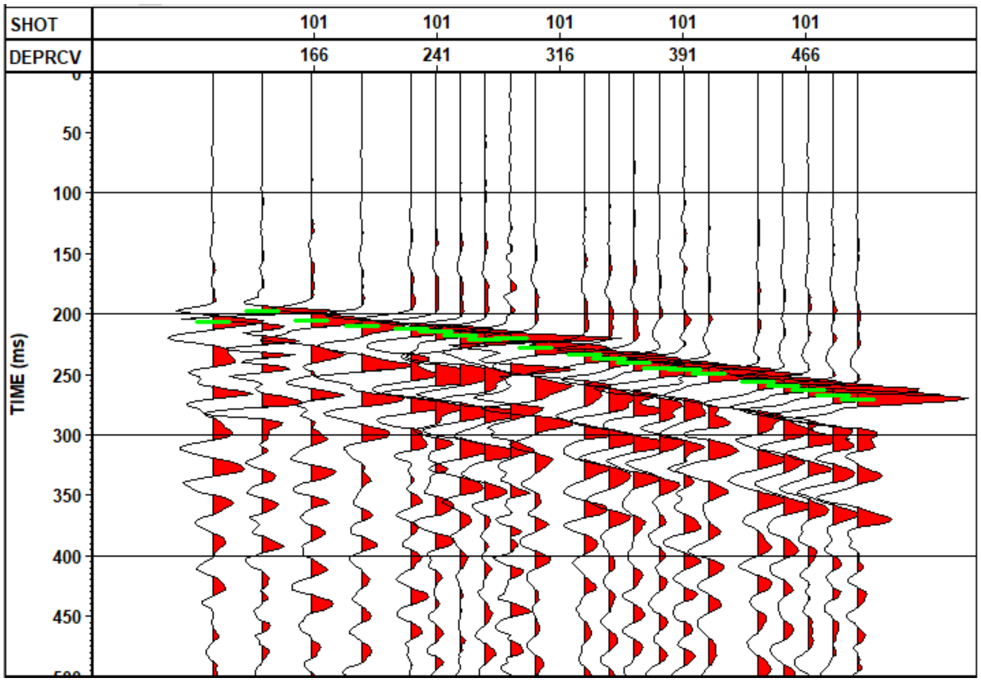

Figure 3.4 Raw vertical component of VP 101 with first breaks in green and AGC after nulling bad traces.

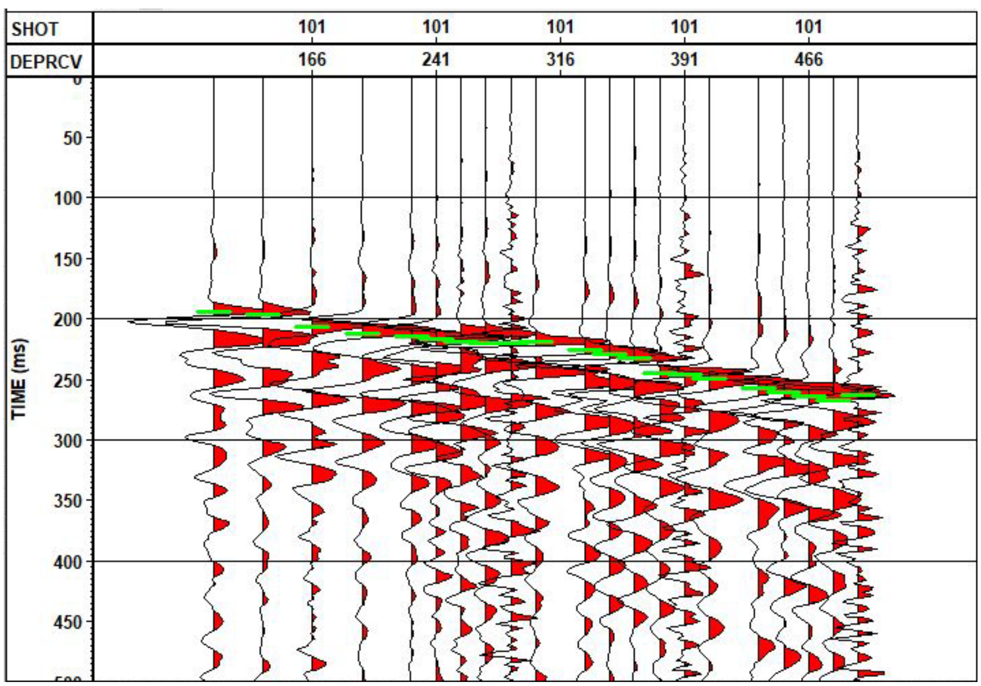

Figure 3.5 Raw horizontal component 1 of VP 101 with first breaks in green and AGC after nulling bad traces.

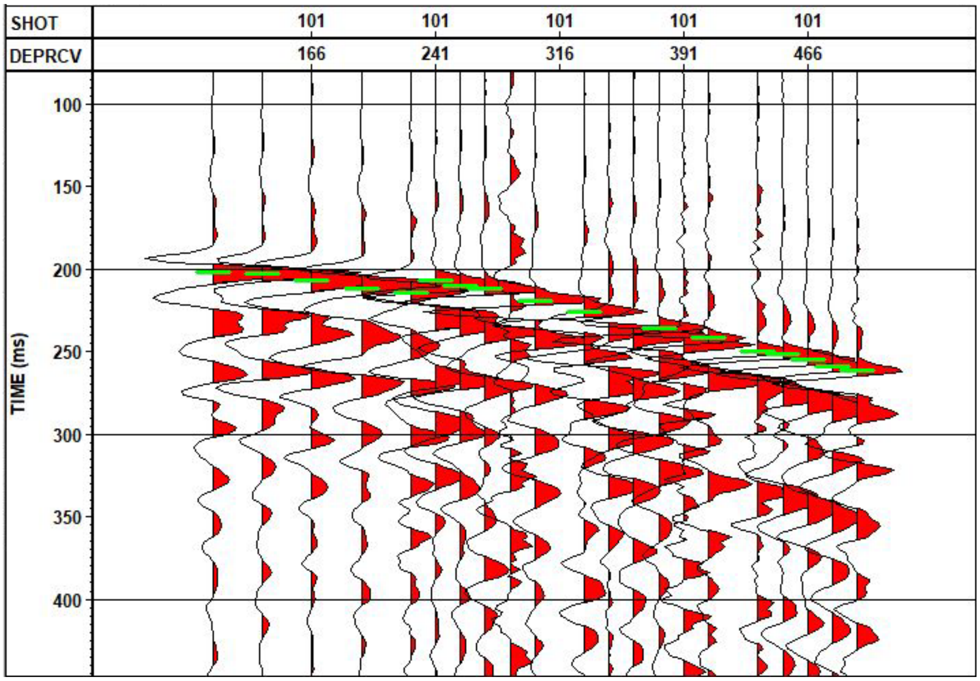

Figure 3.6 Raw horizontal component 2 of VP 101 with first breaks in green and AGC after nulling bad traces.

3.1.2 Traveltime variation with azimuth

The first break traveltimes of the vertical component of each receiver in the walk around VSP (Line 204) were plotted as a function of azimuth. When sorting seismic data into azimuthal gathers, the presence of a sinusoidal variation in traveltime could be an indication of azimuthal anisotropy (HTI) (Liu et al., 2012). These traveltime variations can be caused by vertical fractures, and given the regional stress field of the FRS, the possibility of oriented fractures is possible. Since the acquisition design of the walk around VSP was a semi-circle, we would expect to identify one period of a sinusoidal traveltime variation. Figure 3.7 represents an example of the plot generated using MATLAB software after the first break picks were exported from VISTA. The location of the MATLAB script can be found in the appendix A.1. The X-axis indicates the azimuth, Y-axis the traveltime in seconds and each coloured line corresponds to the traveltime of each receiver depth as a function of azimuth. Notice that each point in the plot seems to follow the general trend, indicating good precision of the picks. Nevertheless, source statics corrections were applied with the intention of reducing possible noise present in the data, caused by variable shot statics.

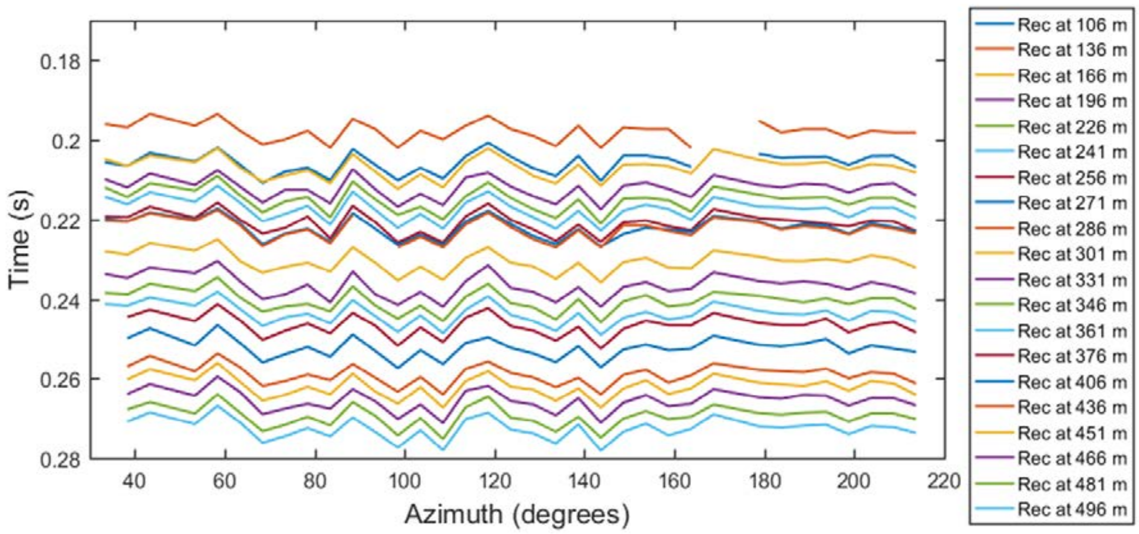

Figure 3.7 First break picks as a function of azimuth coloured by receiver depth.

3.1.3 Statics correction

The purpose of applying statics corrections is to compensate for the variations generated by changes in elevation, weathering layer or the reference datum (Sheriff, 2002). The shot statics from a 3D seismic survey acquired at the FRS in 2014 (Isaac and Lawton, 2014) were utilized to correct the statics present in the walk around VSP dataset. Since the FRS is located in southern Alberta, a region that is known to be generally flat; we would expect that any possible variations may be related to the near-surface layer and not to topography. The shot statics in the study area were interpolated to generate a contour map of the shot statics. Then, the VP of the walk around VSP were superimposed over the contour map and a static value for each VP of the walk around survey was interpolated from the 3D grid.

The contour map was smoothed to decrease the sharpness present in the contour lines due to the interpolation (Figure 3.8). Nevertheless, the original values were used for the statics correction. After applying the correction, the traveltime variation plot as a function of azimuth was updated, and several missing points were also interpolated (Figure 3.9). Even though the noisy trend is still present because the static correction itself was small, there are some slight variations noticeable, for example, a time shift in the curves that seems to be constant. And there is a steadier trend in time as the azimuth increases.

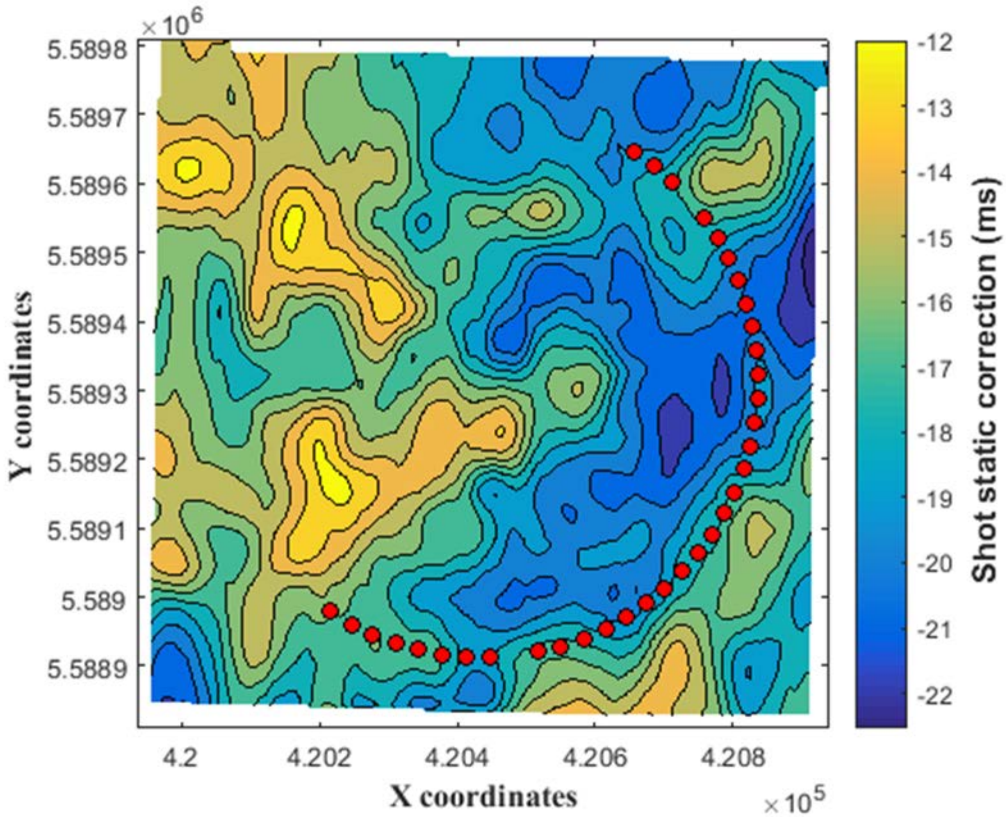

Figure 3.8 Shot statics contour map of a 3D surface seismic with the source points shown in red.

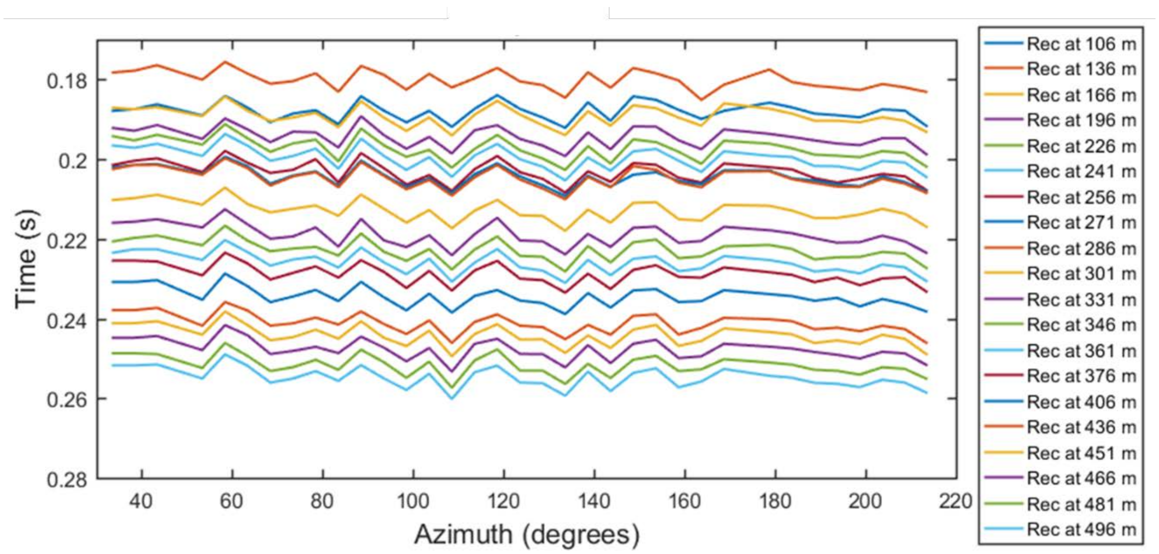

Figure 3.9 First break picks as a function of azimuth coloured by receiver depth after source static corrections have been applied.

3.1.4 Median filter and sinusoidal trend identification

As an attempt to identify a sinusoidal trend within the data, a gentle median filter was applied to smooth the data. Different samples were tested and a median filter of 7 samples was selected, with the filtered data shown in Figure 3.10. A smaller number of samples maintained the noisy trend but a larger number of samples oversmoothed the dataset. After applying the median filter, the noisy trend was attenuated, and a flatter trend was obtained. A possible indicator of a sinusoidal trend is the subtle change in time between 90 and 150 degrees of azimuth and more importantly, it affects each receiver level. Moreover, after increasing the time scale, a slight sinusoidal trend is noticeable (Figure 3.11) from where the fast direction can be identified at approximately 40 degrees azimuth, which coincides with Western Canada (NE-SW) stress orientation (Heidbach et al., 2016). An interesting remark is the general change in the first arrivals from left to right. There seems to be a delay in the first arrivals of the higher azimuths when we would expect a similar response between each edge of the semi-circle or first and last source point. One possible reason for this behaviour could be that the injection well is deviated as the geological dip in the area varies slightly to the northwest (Osadetz et al., 2017).

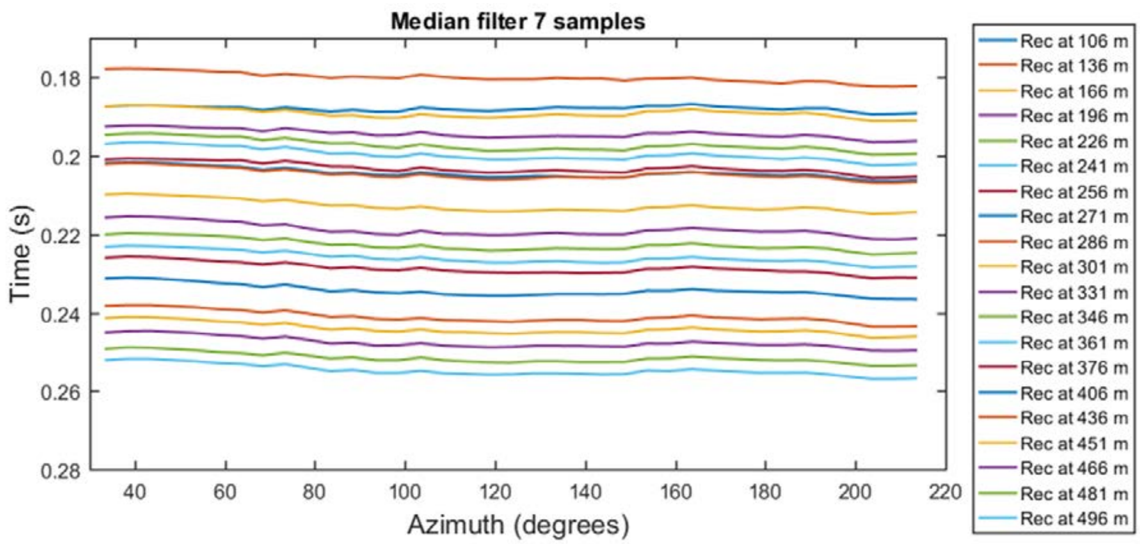

Figure 3.10 First break picks as a function of azimuth coloured by receiver depth after source static corrections and a median filter of 7 samples were applied.

.

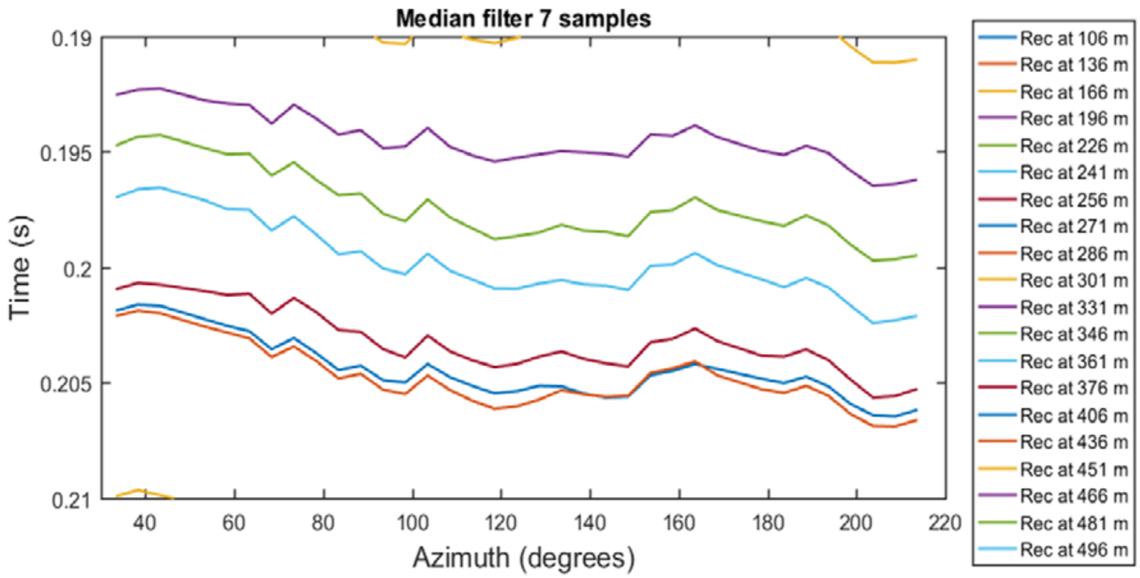

Figure 3.11 First break picks as a function of azimuth coloured by receiver depth after source static corrections and median filter of 7 samples at a larger scale.

3.1.5 Estimation of the anisotropy parameter epsilon (ε)

Following the identification of the fast direction within the FRS, we continue with the analysis by estimating the anisotropy parameter Epsilon defined by Thomsen (1986) as the fractional difference between vertical and horizontal P-wave velocities (Equation 3.1)

$$\varepsilon = \frac{v_p\left(\frac{\pi}{2}\right) - \alpha_0}{\alpha_0} \tag{3.1}$$

where α_0 is the vertical P-wave velocity and $v_p\left(\frac{\pi}{2}\right)$ is the horizontal P-wave velocity (Liu and Martinez, 2012). Taking in consideration that the focus of his work was VTI media, and for that case the fast direction is horizontal, and the slow direction is vertical, Equation 1 can be described as the fractional difference between the fast and slow velocities (Equation 3.2),

$$\varepsilon = \frac{v_{fast} - v_{slow}}{v_{slow}} \tag{3.2}$$

To calculate a value for epsilon, we first completed a residual estimation. This was done by fitting polynomial equations of different orders to the data in a least-squares sense. This estimation was done for 1st order (straight line) and 3rd order polynomials at three receiver locations (shallow, middle and deep). Figures 3.12 – 3.17 display the residual calculation in time and velocity. Plot (a) shows the fitting lines overlaying the data, and the residuals obtained from each fitting line is shown in the plot (b). As we can see, the 3rd order fits data better, and the residual values range from -2 to 2 milliseconds and -20 to 20 m/s, respectively. From the velocity variations, we were able to estimate the anisotropy parameter epsilon by using Equation 2. This calculation was done for the same three receiver locations. The average result obtained was 0.02 and this small value of epsilon is indicative of weak anisotropy.

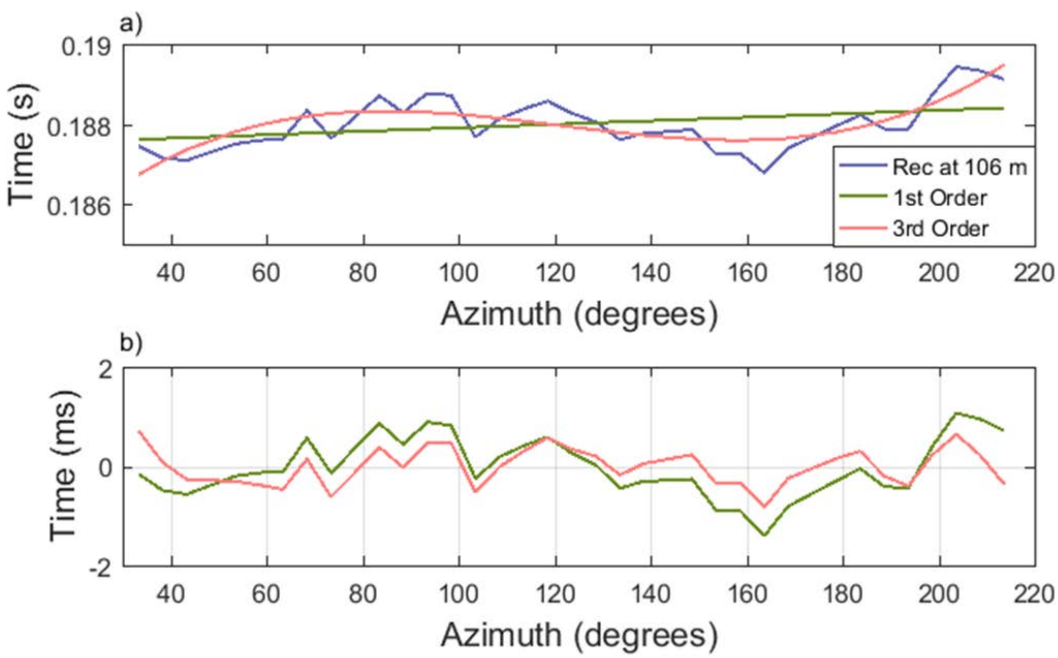

Figure 3.12 a) Traveltime residual estimation of the receiver at 106 m depth. b) Residuals obtained by fitting lines of 1st and 3rd order polynomial (in green and pink respectively) to the data.

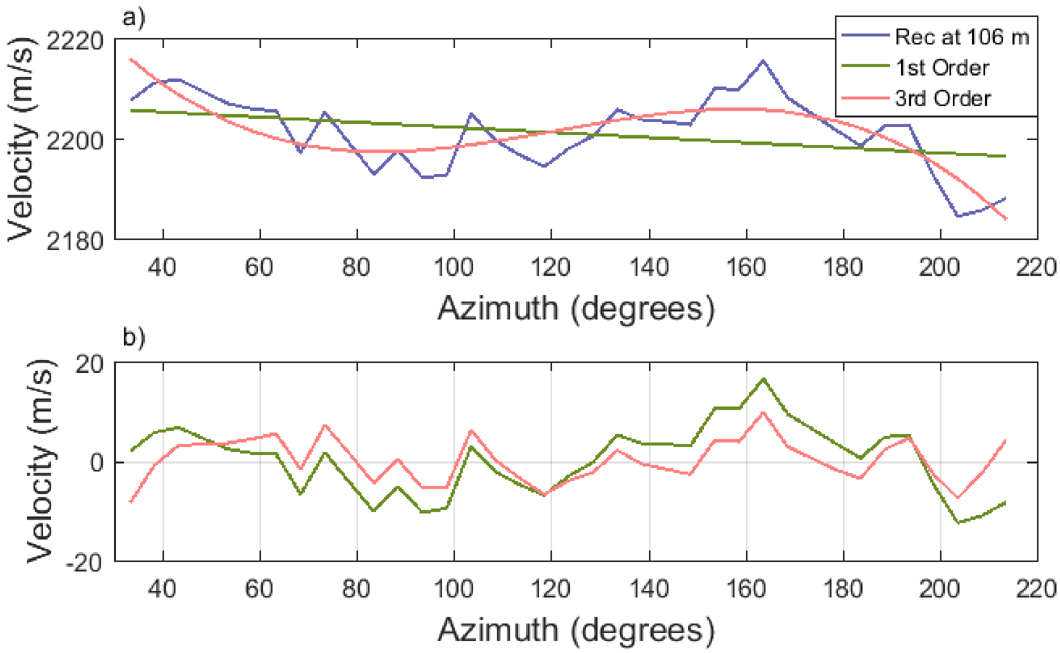

Figure 3.13 a) Velocity residual estimation of the receiver at 106 m depth. b) Residuals obtained by fitting lines of 1st and 3rd order polynomial (in green and pink respectively) to the data.

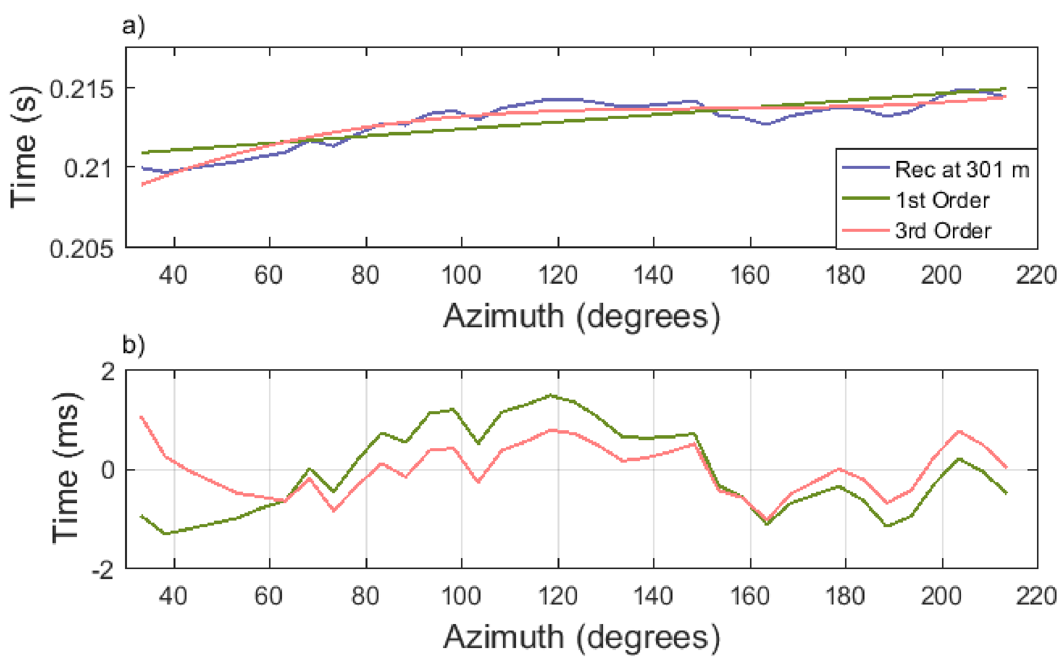

Figure 3.14 a) Traveltime residual estimation of the receiver at 301 m depth. b) Residuals obtained by fitting lines of 1st and 3rd order polynomial (in green and pink respectively) to the data.

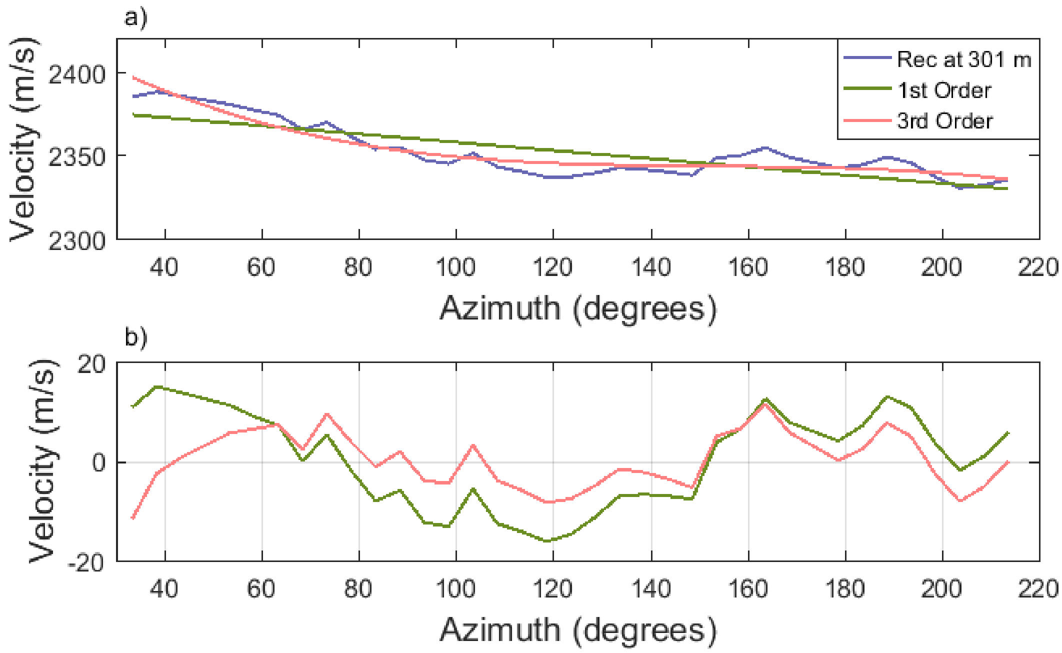

Figure 3.15 a) Velocity residual estimation of the receiver at 301 m depth. b) Residuals obtained by fitting lines of 1st and 3rd order polynomial (in green and pink respectively) to the data.

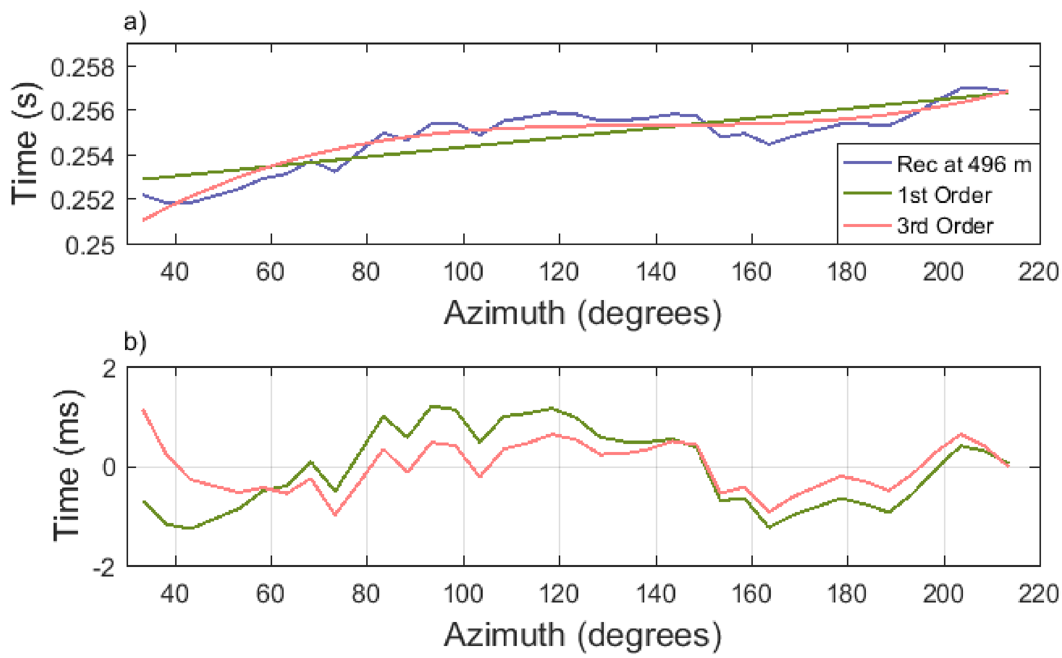

Figure 3.16 a) Traveltime residual estimation of the receiver at 496 m depth. b) Residuals obtained by fitting lines of 1st and 3rd order polynomial (in green and pink respectively) to the data.

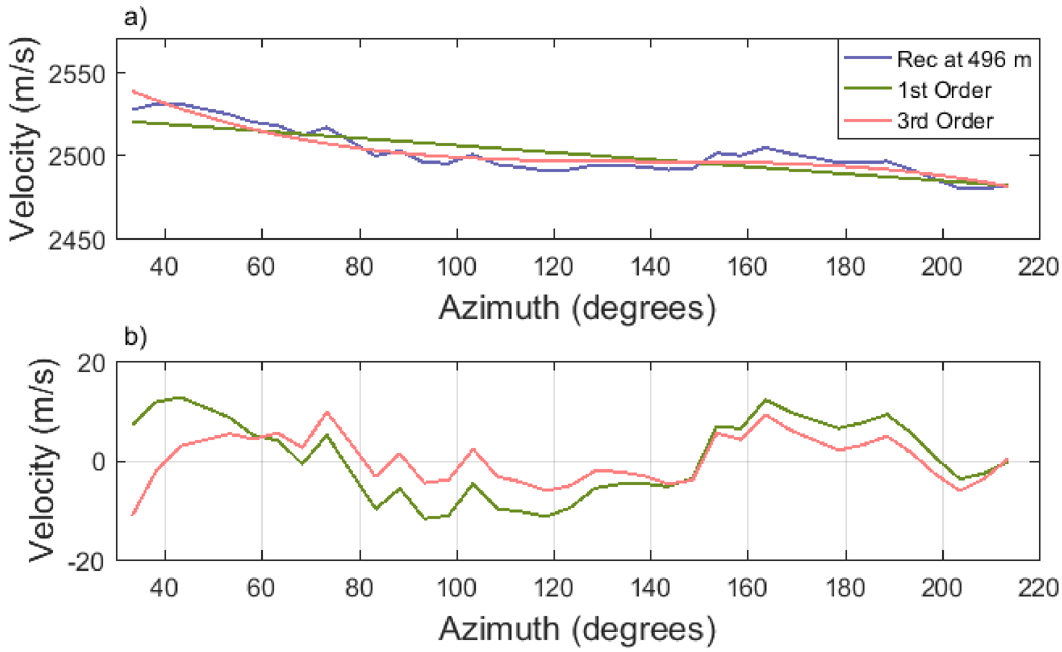

Figure 3.17 a) Velocity residual estimation of the receiver at 496 m depth. b) Residuals obtained by fitting lines of 1st and 3rd order polynomial (in green and pink respectively) to the data.

3.2 VSP data rotation

The following part of this analysis was to rotate the half walk-around VSP dataset to better understand the trajectory and incidence angles of the seismic waves travelling from the source point to the receiver array as the source to well azimuth changes. The horizontal components H1 and H2 were rotated in the Hmax and Hmin direction to align the energy in the source-receiver direction. Then, the vertical component Z and Hmax were rotated in the Hmax' and Z' direction, in order to have the data oriented in the radial and transverse components. The results of the second rotation were compared with the incidence angle calculated with a ray-tracing computation of a velocity model created from a sonic log of the injection well. Figure 3.17 represents a schematic of the workflow followed in this section. Each step will be explained in detail below.

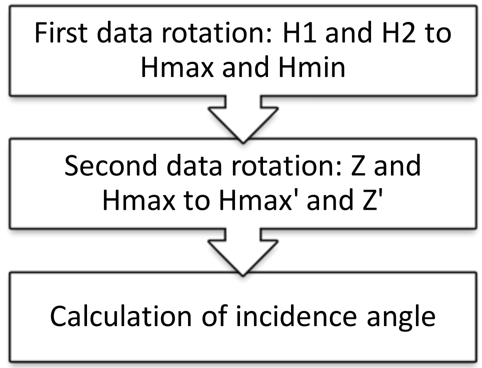

Figure 3.18 VSP data rotation workflow

3.2.1 Hodogram analysis

In a three component (3C) VSP survey, we record data from three different channels at any given tool location. These channels represent the vertical (Z) and horizontal components (H1 and H2) of each geophone (Hinds et al., 1996). The orientation of the horizontal components in the wellbore is usually unknown as the tool rotates as it is moved up and down the well (Pereira et al., 2010). Therefore, the processing workflow of the 3C walk-around VSP data generally includes the orientation of the components using a hodogram analysis. Once the orientation is estimated, the data is rotated into the radial and transverse components (Hinds et al., 1996; Horne et al., 2000).

A hodogram is the display of the motion or path of a particle as a function in time. As mentioned previously, it is used to determine the orientation of the receivers in a borehole (Sheriff, 2002). Furthermore, a hodogram analysis consists of plotting on an orthogonal axis the recorded data of two components (e.g. H1 and H2) at a fixed window of time, generally around the first break picks. In this case, several window lengths were tested varying from 50 to 200 ms. The selected window was of 100 ms as it effectively contained the first arrivals. During this process, the use of a colour-coded display of the data can be useful when identifying parts in the plot and its correlation to the data in the time window. From this plot, we obtain a rotation angle chosen with a regression line going through the hodogram display. This angle is used to polarize the input data onto two principal axes that are normal (Hmin) and tangential (Hmax) to the source-receiver plane (Hardage, 1983; Hinds et al., 1996). An example of a hodogram is shown in Figure 3.19. This example corresponds to VP 100 and a receiver at 166 m depth. The hodogram plot and the selected rotation angle is shown in (a) where the X and Y axis corresponds to the amplitudes of the input traces H1 and H2, respectively. The time window used for the analysis is shown on top of the input traces H1 and H2 with a shaded area (b), and the output traces after the rotation are shown in (c). Notice how the majority of the energy is now in the first output trace (Hmax) and the remaining energy on the second output (Hmin). In this case, the rotation angle was of 81.8 degrees as marked with the black arrow in the plot and measured from the X-axis in a counter clock direction.

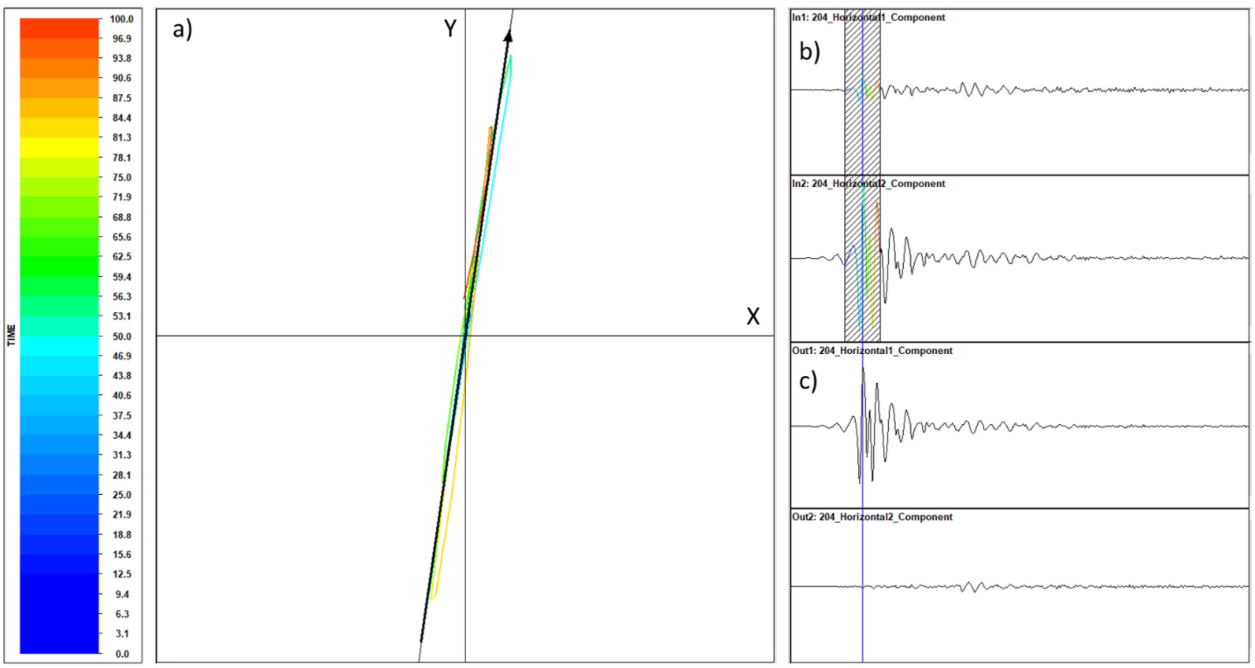

Figure 3.19 Example of a hodogram analysis of VP 100 and a geophone at 166 m depth. a) hodogram plot, b) input traces: H1 and H2 components, c) output traces Hmax and Hmin.

3.2.2 First data rotation

The first data rotation polarizes the energy from the horizontal components H1 and H2 to the source-receiver plane in the Hmax and Hmin direction, as we mentioned earlier. Figure 3.20 displays a plan view schematic of the first rotation for a given VP. Where the H1 and H2 components direction are shown in purple, the azimuth (theta) of the VP is shown in red. The resulting component rotation to Hmax and Hmin and the rotation angle (phi) is shown in orange. The difference between the azimuth and the rotation angle (Theta') is shown in green. The first rotation was performed using VISTA and MATLAB to quality control the results and obtain a better understanding of the process. A crossplot comparing the results of three VPs is shown in Figure 3.21. The script of the data rotation can be found in the appendix A.2.

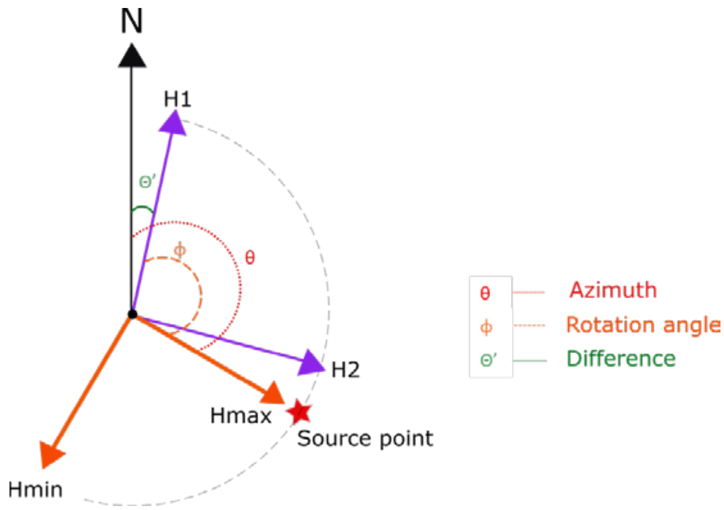

Figure 3.20 Schematic plan view of a source point in red. The semi-circle line represents the survey geometry and the wellbore head is represented in black.

The VPs 101, 120 and 131 were selected for this comparison to have a broad range of different azimuth across the survey. The X-axis corresponds to the rotation angle obtained in VISTA and Y-axis the rotation angle from MATLAB. Good comparisons between the results from VISTA and MATLAB were obtained. Nevertheless, there are several outliers in Figure 3.21 that could be associated with the difficulty of identifying the first arrivals in the horizontal components.

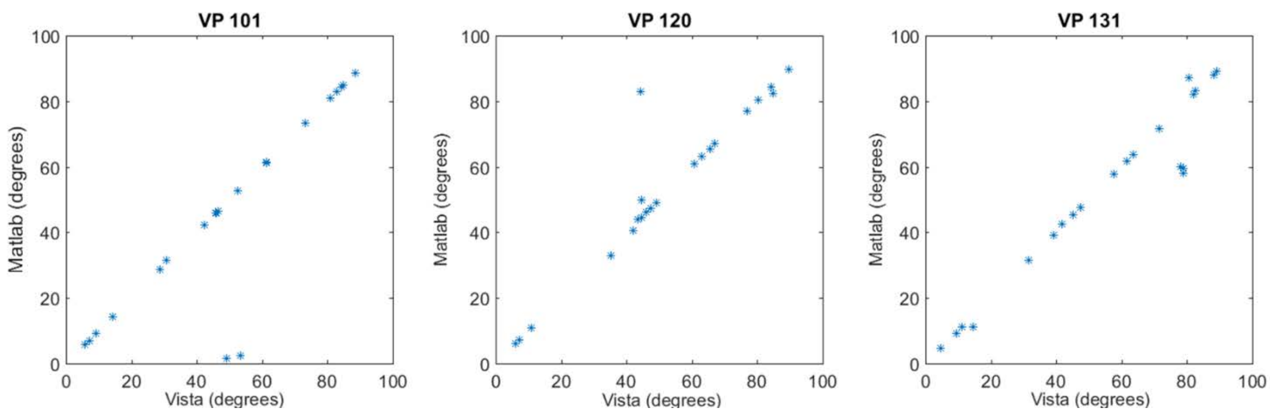

Figure 3.21 Crossplot of rotation angles obtained in VISTA and MATLAB for VPs 101, 120, 131.

As mentioned before, since ESG SuperCable® was deployed in the well at three different levels, the difference between the azimuth of the source point and the rotation angle of the horizontal components for each level should have a similar value. Knowing the azimuth (theta in Figure 3.20) of each VP and using it to calculate the difference between the azimuth and the obtained rotation angle (phi), it is possible to estimate the orientation of the geophone's horizontal components as the SuperCable® was moved inside the borehole. Table 3.2 list the values obtained with VISTA and MATLAB for the VPs selected previously. Similarly, Figures 3.22 and 3.23 show the calculated azimuth (Theta') of the receivers as a function of depth for the same VPs 101, 120 and 131 using the results from VISTA and MATLAB, respectively. The X-axis shows the calculated azimuth of the geophones and the Y-axis displays the depth of the receivers. Each dotted curve represents the azimuth variation of the geophones (star symbol) per VP. As expected, the receivers have a similar orientation across the survey. Nonetheless, there are small variations that suggest the possible rotation of the receivers in the tool after being deployed in the well at three different levels. Notice the similarity in the results obtained for both VISTA and MATLAB. As an example, Figures 3.24 and 3.25 show the data after the first rotation for VP 101 displayed with AGC (window length of 250 ms). Where Figure 3.24 represents the Hmax component and Figure 3.25 represents the Hmin component. Notice how the amplitude of the first arrivals is stronger in Hmax compared to Hmin, which is expected, after transferring the energy from the H1 and H2 components to Hmax and Hmin components.

Table 3.2 Estimation of geophones orientation for VPs 101, 120 and 131 using the rotation angles obtained from the first rotation with VISTA and MATLAB.

Receiver depth (m)	**VP 101**		**VP 120**		**VP 131**	
	VISTA	**MATLAB**	**VISTA**	**MATLAB**	**VISTA**	**MATLAB**
106	73.27	73.28	76.86	76.86	71.67	71.67
136	88.5	88.44	89.79	89.80	89.13	89.14
166	45.92	45.91	44.65	44.62	57.67	57.64
196	5.72	5.84	7.2	7.21	4.66	4.66
226	28.73	28.76	67.07	67.08	39.14	39.16
241	61.45	61.50	65.57	65.52	61.74	61.70
256	45.75	45.85	49.1	49.11	45.31	45.25
271	9.26	9.16	46.14	46.30	14.63	11.24
286	52.5	52.58	44.37	82.99	78.8	58.08
301	14.18	14.16	10.97	10.98	11.07	11.12
331	7.12	6.98	6.04	6.03	9.37	9.30
346	61.39	61.21	60.74	60.74	63.72	63.75
361	82.74	82.78	84.39	84.42	82	82.07
376	84.84	84.88	63	63.01	88.11	88.11
391	53.34	2.40	43.36	44.00	78.76	59.55
406	46.61	46.61	47.31	47.31	47.54	47.57
436	42.22	42.19	42.05	40.63	41.78	42.60
451	80.91	81.05	80.2	80.45	82.46	83.16
466	84.2	84.30	84.97	82.25	80.57	87.26
481	30.79	31.61	35.33	32.80	31.58	31.60
496	49.01	1.56	44.5	49.96	78.08	59.97

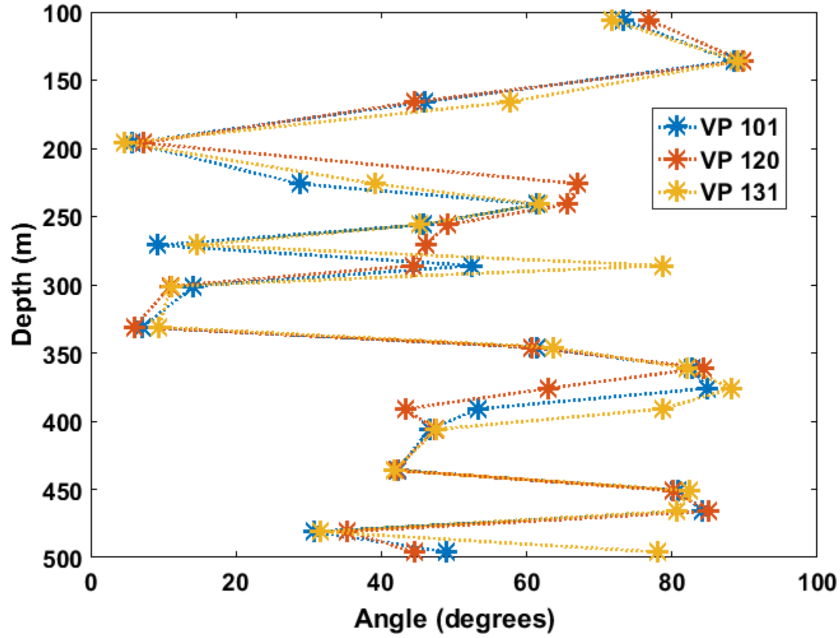

Figure 3.22 Estimated receivers azimuth for VPs 101, 120 and 131. Results obtained from VISTA.

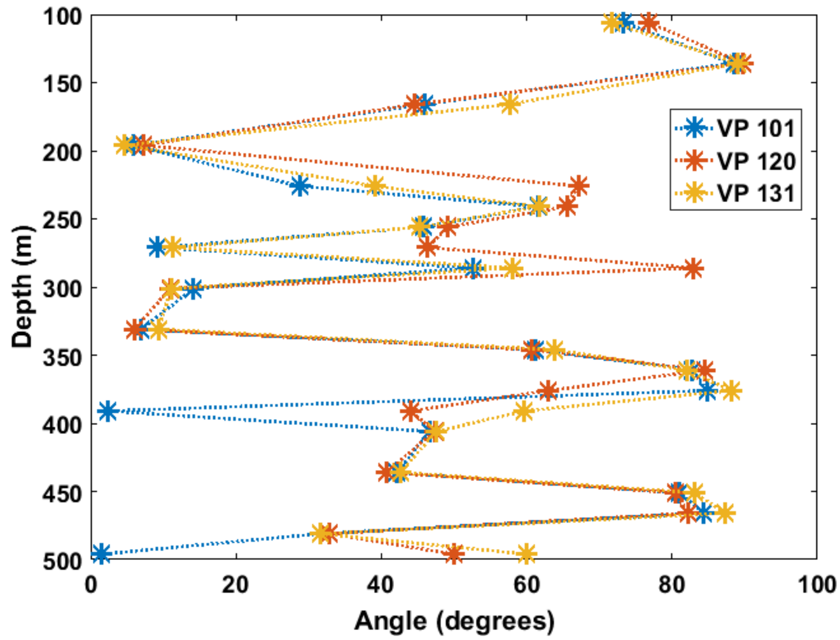

Figure 3.23 Estimated receivers azimuth for VPs 101, 120 and 131. Results obtained from MATLAB.

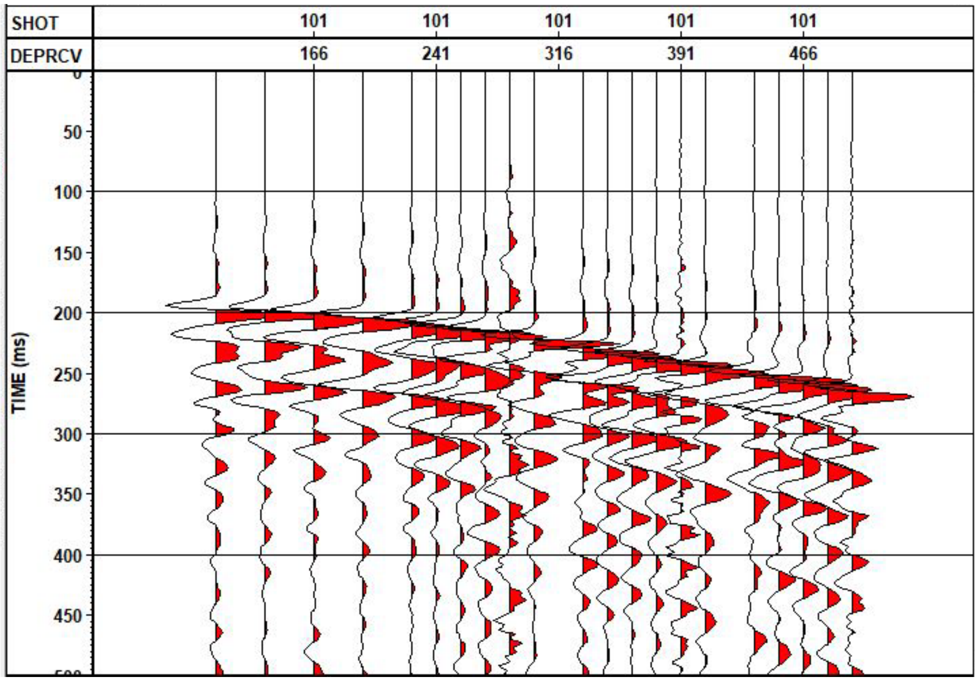

Figure 3.24 Example of the Hmax component after the first rotation, line 204, VP 101 with AGC.

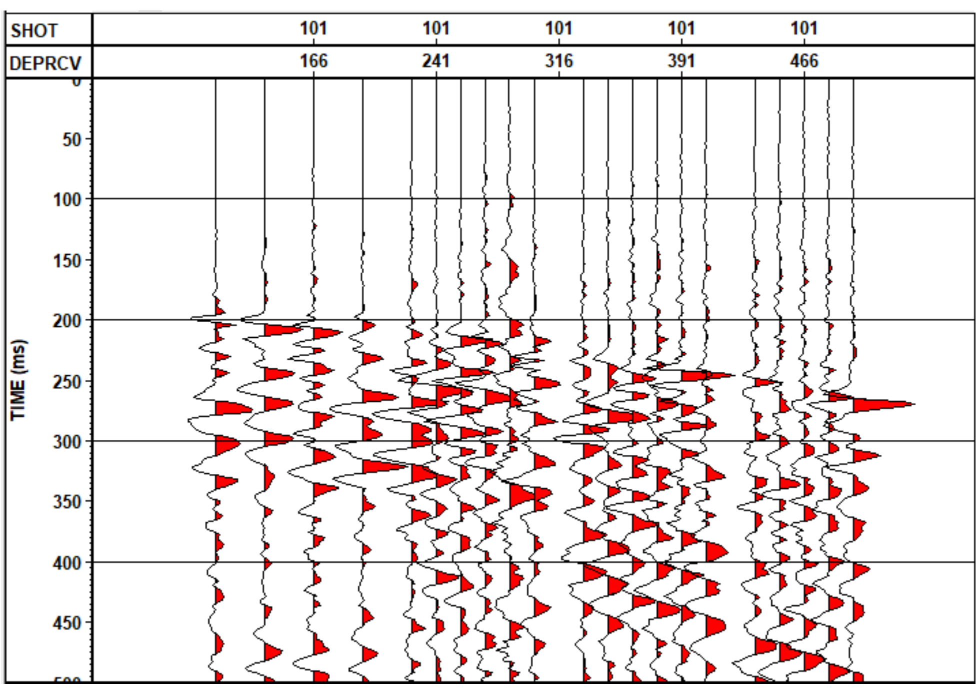

Figure 3.25 Example of the Hmin component after the first rotation, line 204, VP 101 with AGC.

3.2.3 Second data rotation

The second rotation consists of the same hodogram analysis procedure with different input data, in this case, we want to polarize the vertical component Z and Hmax obtained from the first rotation. This rotation yields Z' and Hmax' components where Hmax' is oriented in the direction of the wavefront propagating from the source, also known as radial component and contains downgoing events and upgoing SV events whereas the transversal component (Z') contains upgoing events product of the reflected waves. Figure 3.26 shows a diagram of the rotation. Where, the source point is marked with a red star, the inputs Z and Hmax are shown in orange, and the orientation after the rotation, Hmax' and Z' are shown in green as well as the rotation angle (theta).

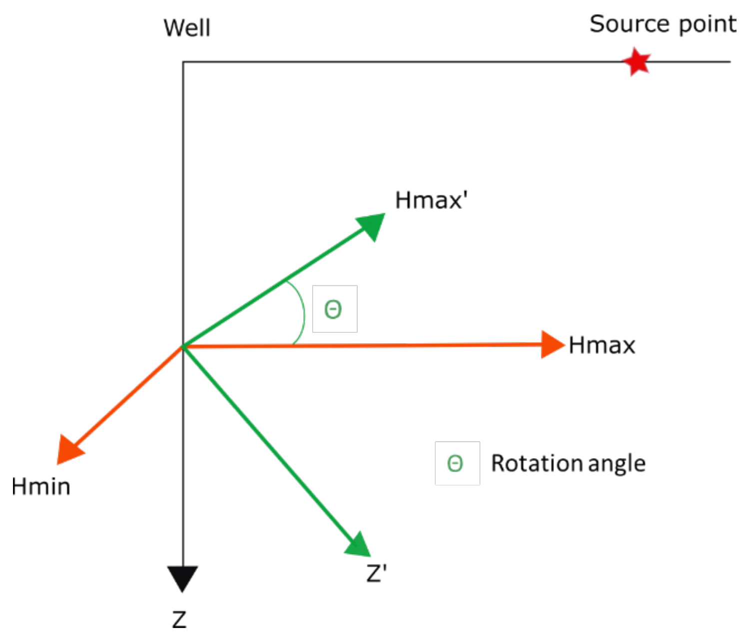

Figure 3.26 Schematic view of the second rotation. The source point is in red. The input, Z and Hmax are shown in orange and the output, Hmax' and Z' are shown in green.

The rotation angles obtained from the second hodogram analysis, for the VP 101, 120 and 131, were compared with the incidence angle calculated with a ray tracing model created in MATLAB. In this case, we define the incident angle as the angle of a ray-path with respect to the horizontal, as we are interested in a vertical interface since we are analyzing VSP data (Figure 3.27). A velocity model was computed using the sonic log from the injection well 100/10-22-017-

16W4/00. Figure 3.28 shows the sonic log used for the velocity model (a) and the calculated P-wave in a block display (b). Notice that the first measurement of the sonic log was at approximately 222 m depth; therefore, a constant velocity layer was placed between the surface and that depth. The velocity used for the constant layer was the replacement velocity used for the shot statics (2600 m/s). With the P-wave velocity profile, a velocity model was created by duplicating the profile across an offset of 400 m. Figure 3.29 displays the velocity model, a source point is located at zero offset marked with a red star and the receivers are located at 400 m from the source and are shown with blue triangles.

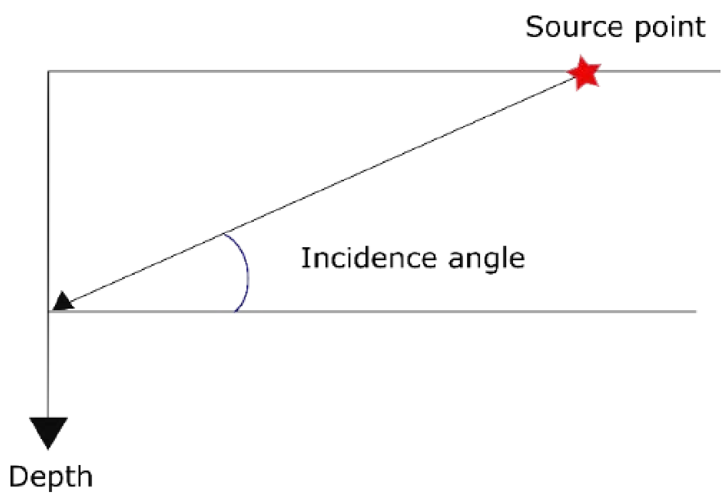

Figure 3.27 Schematic of the incidence angle definition used for the analysis.

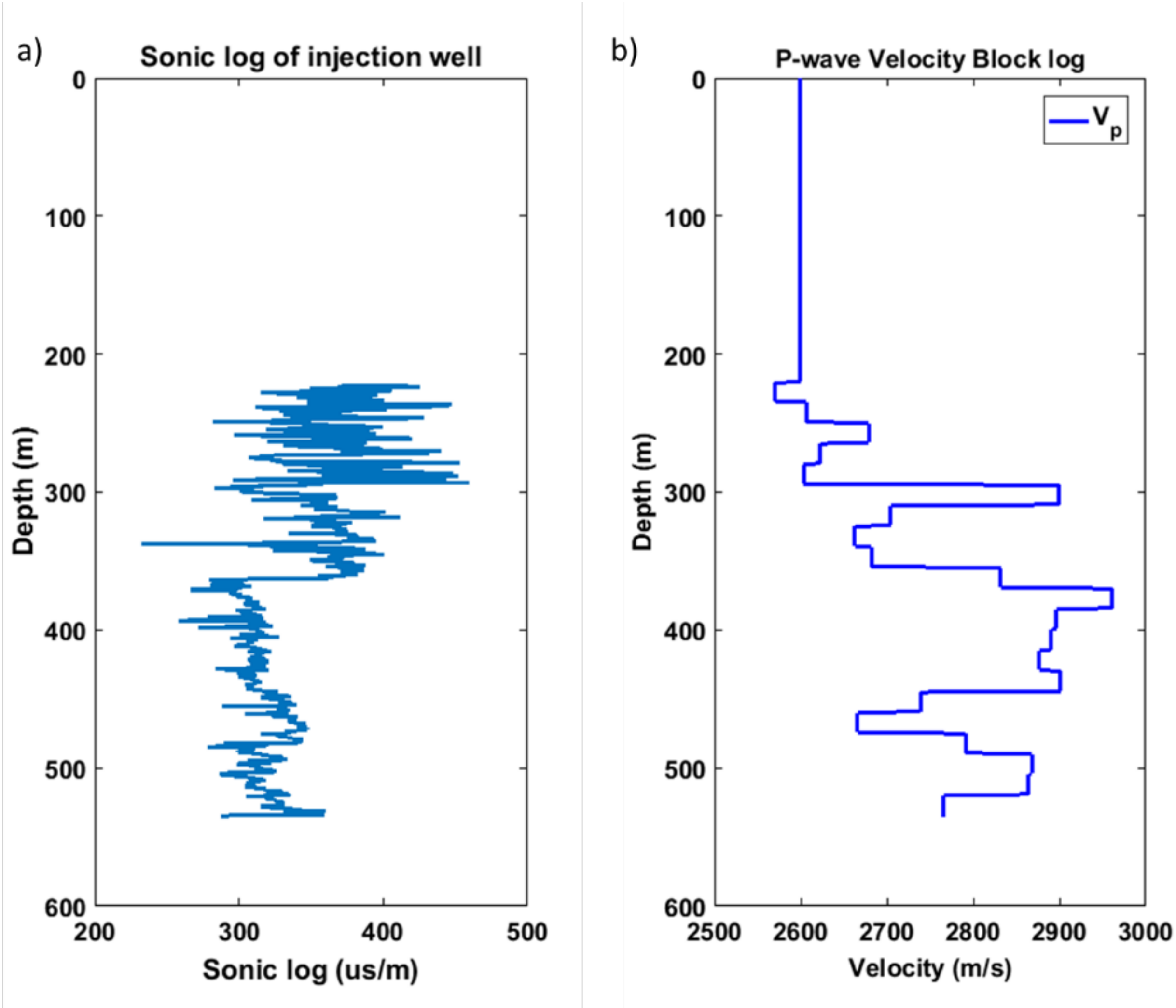

Figure 3.28 Well logs of the injection well. a) sonic log, b) P-wave velocity obtained from the sonic log.

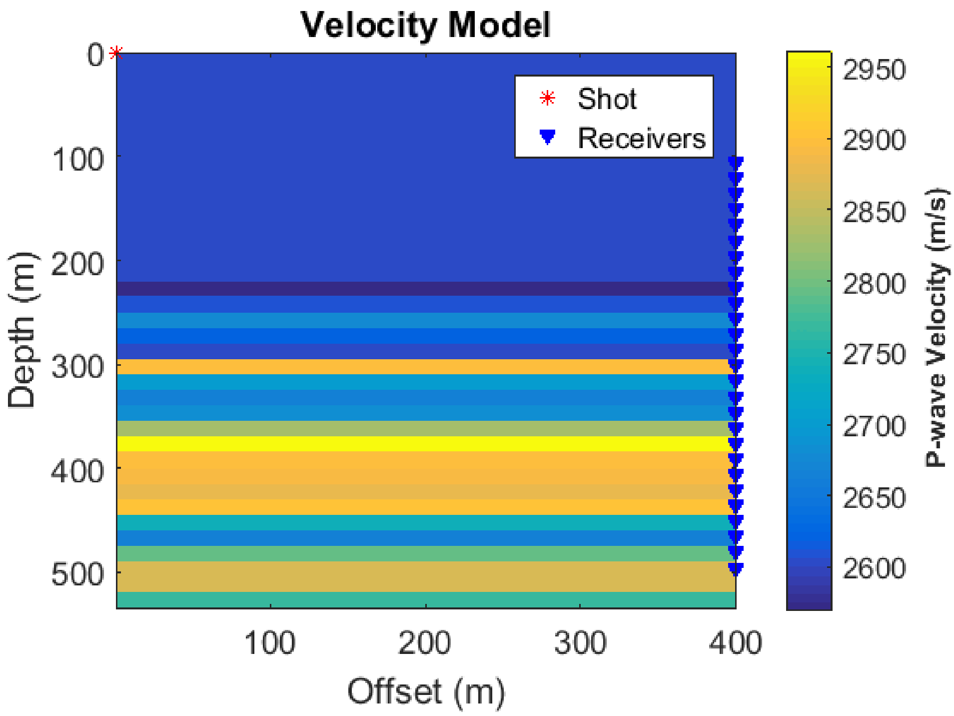

Figure 3.29 Velocity model generated from the sonic log. Source point in red, receivers in depth shown with blue triangles.

Once the velocity model was created, a raytracing function was used to compute the rays of the direct waves from a source point on the surface with an offset of 400 m to all the receivers in the borehole. The ray path parameter p was obtained as an output of the raytracing function, and it was used to calculate the incident angle. The ray path parameter p, for horizontal velocity layers is defined as follows (Sheriff, 2002):

$$p = \frac{dt}{dx} = \frac{\sin(\alpha)}{V} \tag{3.3}$$

where dt/dx is the reciprocal of apparent velocity, V is instantaneous velocity and α is the angle a ray path makes with the vertical. The velocity model and the rays traced from the source point of 400 m offset is shown in Figure 3.30, where the direct wave rays are shown in red.

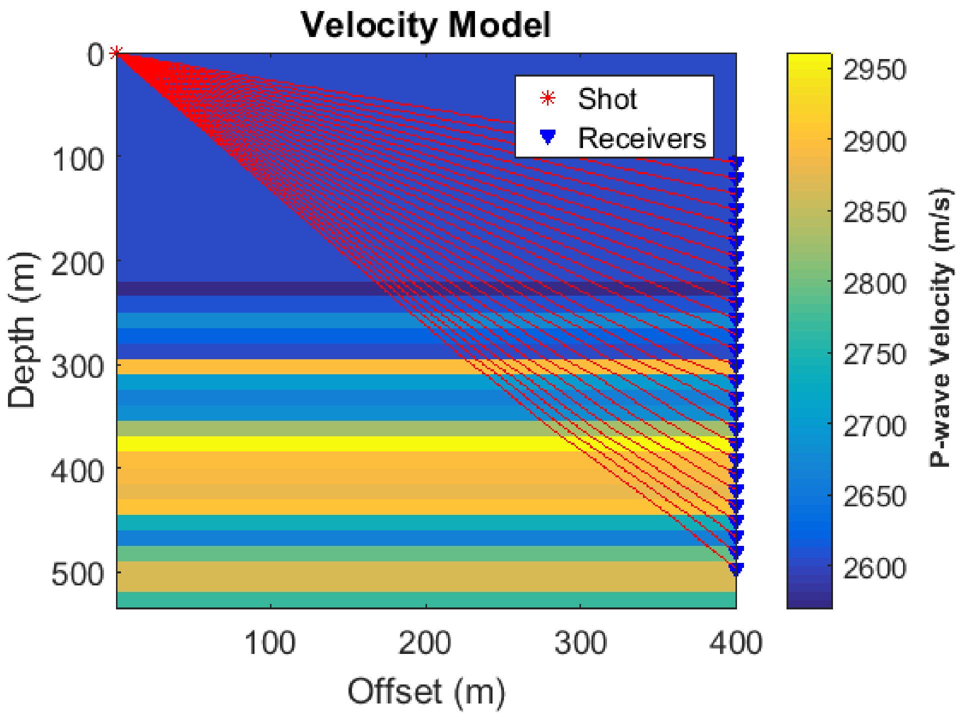

Figure 3.30 Ray-traced velocity model for a source point of 400 m offset.

The calculated incidence angle from the ray-traced velocity model was compared to the angle obtained from the second rotation with the hodogram analysis. The comparison is shown in Figure 3.31 for the same VPs 101, 120 and 131. The X-axis displays the angle in degrees, and the Y-axis corresponds to the depth, each curve represents a VP and the incidence angle from the velocity model is shown with purple triangles. There is a good correlation between the incident angle obtained from the ray-tracing velocity map and the rotation angles obtained from the second hodogram analysis for VP 101, 120 and 131. Nevertheless, there are some outliers in the rotation angles that are associated with the receivers at 286 m, 391 m and 496 m depth. Note that the outliers present in Figure 3.21 are also associated with these receivers. The traces corresponding to the outliers are shown in Figures 3.32 and 3.33 that display an example of the data after the second rotation for VP 101. The affected traces show a noisy trend that seems to be present along each step of the process and it is evident in the raw components H1 and H2 (Figures 3.5 and 3.6). Even though, the raw vertical component does not show those traces as bad or dead, from this point forward those traces should be classified as bad traces and thorough quality control should be applied at the beginning of the process to avoid this issue.

Table 3.3 Rotation angle from the second hodogram analysis for VPs 101, 120 and 131 compared to the angle of incidence obtained with a ray-traced model in MATLAB.

Receiver depth (m)	**VP 101 Vista**	**VP 120 Vista**	**VP 131 Vista**	**Incident angle MATLAB**
106	3.33	17.14	21.33	14.84
136	1.88	4.31	4.96	18.78
166	10.24	29.89	18.82	22.54
196	15.56	15.08	22.53	26.11
226	30.17	29.25	37.53	29.47
241	20.84	26.28	21.62	31.10
256	28.56	35.42	34.13	32.80
271	51.67	47.04	67.93	34.45
286	3.36	6.07	3.47	35.94
301	22.43	31.77	25.53	37.61
331	36.07	45.32	34.2	40.64
346	32.95	41.33	30.85	41.90
361	39.64	41.63	38.86	43.20
376	39.27	38.58	30.03	44.59
391	87.79	2.07	24.96	45.95
406	27.81	33.36	31.65	47.17
436	44.1	44.12	52.93	49.40
451	37.08	39.54	52.06	50.40
466	38.23	38.25	51.32	51.27
481	44.43	49.39	44.27	52.12
496	81.91	55.1	89.99	53.00

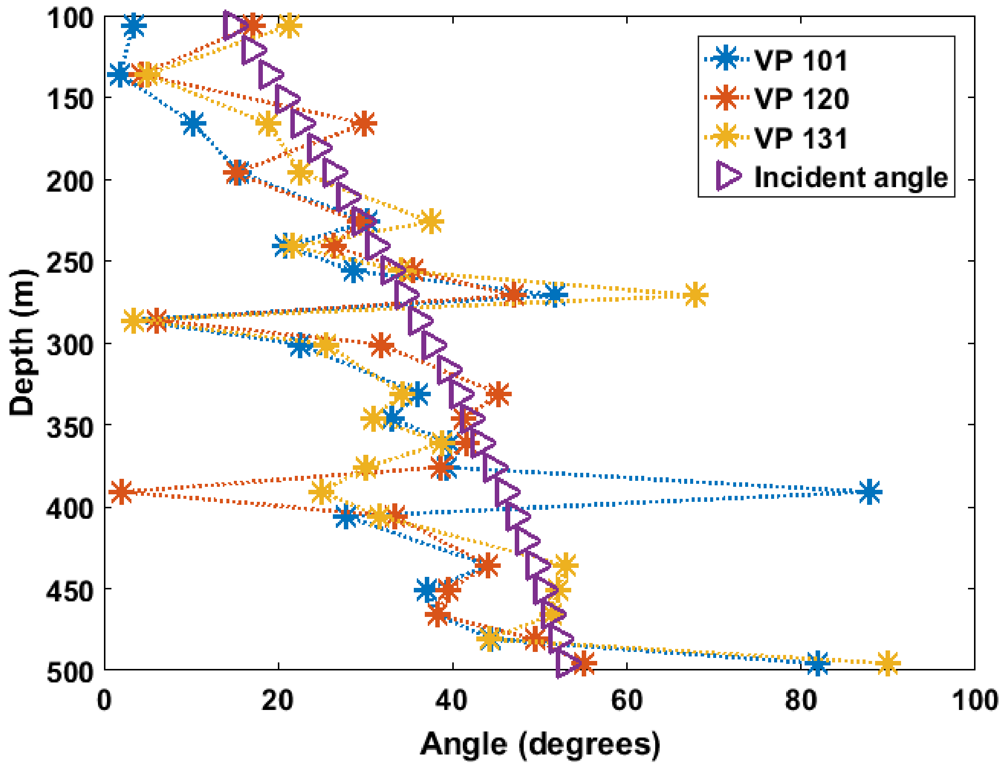

Figure 3.31 Incident angle obtained from the ray-tracing velocity model (purple triangles) and second rotation angles obtained for VP 101, 120 and 131 using hodogram analysis.

Figure 3.32 represents the Hmax' component and Figure 3.33 represents the Z' component. From the results of the two rotations, we obtained the radial (Hmax') and transverse (Z') components that can be used for the isolation of downgoing and upgoing P-waves and S-waves. In our case, we were able to estimate the direction of the receivers in the well during the deployment of the tool at different levels while obtaining significant results on their orientation.

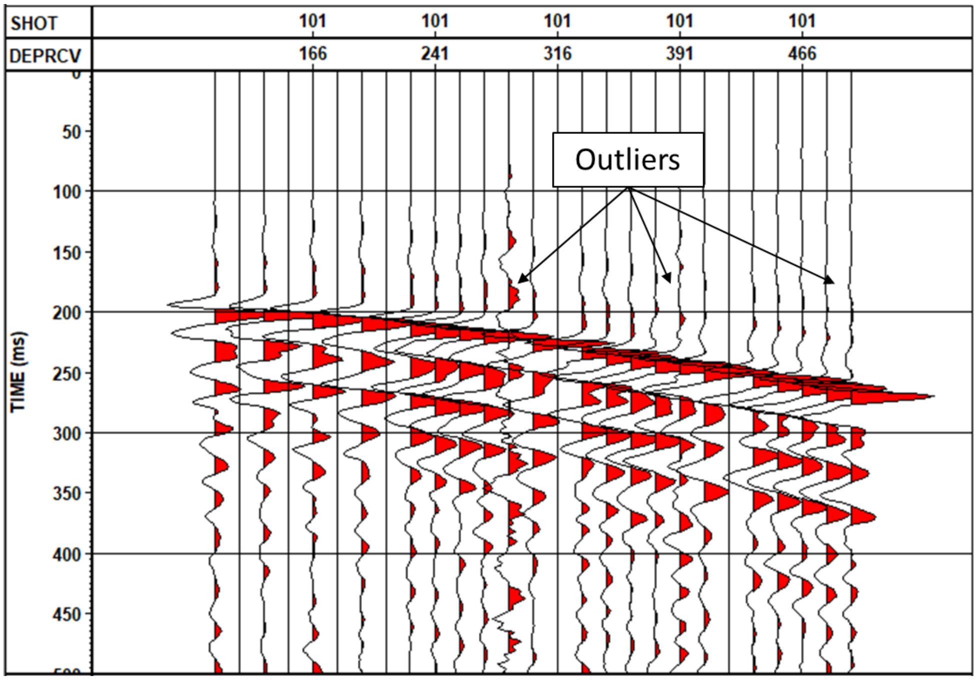

Figure 3.32 Example of the Hmax' component after the second rotation, line 204, VP 101 with AGC.

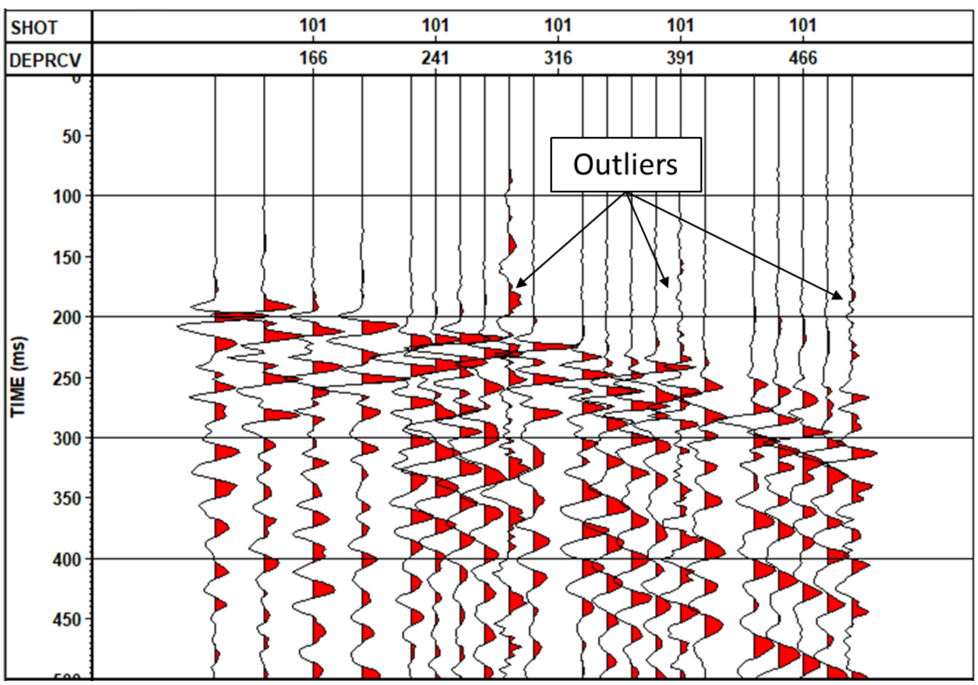

Figure 3.33 Example of the Z' component after the second rotation, line 204, shot 101 with AGC.

3.3 Conclusions

VSP azimuthal analysis was performed by studying the first arrival traveltimes and deduced velocity variations with source-well azimuths. This was performed utilizing the first break traveltime variations with respect to the azimuth of every receiver. After a static correction and a median filter were applied, a smooth trend was observed. A slight sinusoidal trend is noticeable for the traveltime variation, which is indicative of weak azimuthal anisotropy (HTI). The fast direction identified is to the northeast. From the traveltime and velocity residual calculation we were able to estimate an approximate value for epsilon equal to 0.02, indicative of weak anisotropy. As part of the initial steps of the processing flow, the rotation of the horizontal components H1 and H2 to Hmax and Hmin showed similar results obtained with VISTA and MATLAB. After obtaining the rotation angle and comparing it for three different source points, the receivers showed a similar orientation with some variations. For the second data rotation, the incidence angle was calculated with two methods; the hodogram analysis and a ray-tracing velocity model. Both methods yield similar results, although three traces were classified as bad traces because the estimated incidence angle did not correlate with the other traces and after analyzing the raw data, we noticed that those traces showed a repetitive noisy behaviour along the process. This highlights the importance of quality control the data throughout each step in the analysis.

Chapter Four: **Processing of DAS and geophone zero offset VSP data at the CaMI Field Research Station**

As discussed previously, one of the main objectives of the Field Research Station (FRS) is the implementation of new technologies for a better understanding and development of a monitoring program for the CO_2 injection site. In this chapter we discuss the processing flow of three zero offset VSP surveys acquired with two different recording systems; Distributed Acoustic Sensing (DAS) and a borehole geophone array. The three source points (VPs) selected for processing (Figure 2.5) were acquired at different offsets and with a different number of sweeps. The first VP was acquired in May 2017, at 6 m offset from Observation Well 2, the number of stacked sweeps or vertical fold was three. The second and third VPs were acquired in July 2017 at 9 m and 80 m from Observation Well 2 with 16 and 10 stacked sweeps respectively. For the DAS dataset, both fibre optic configurations available at the FRS (straight fibre and the helical wound cable (HWC)) were included during the processing of the zero offset VSP. The DAS dataset was acquired using Silixa interrogator unit; table 4.1 lists some of the parameters of this system.

Table 4.1 DAS acquisition parameters

DAS parameters	Zero offset VSP
Interrogator unit	1st generation Silixa iDAS
Gauge length	10 m
Output trace spacing	0.25 m
Source type	Enviro Vibe
Vibroseis frequency and sweep	10 – 150 Hz, 16 s
Offset of VPs 132, 159 and 139	6 m, 9 m and 80 m

Prior to the processing, a calibration of the fibre optic data was necessary to determine the depth of the DAS channels. If the channel spacing and the total length of the fibre are known, estimating the depth of the DAS channels should not be difficult especially for short and vertical wellbores (e.g. Wu et al., 2015). In our case, there is uncertainty about trace locations in the well as the cable loops back to the surface. For this reason, we are interested in first determining an accurate depth registration of DAS channels. In the following sections, I explain in detail the procedure of the depth registration as well as the processing flow utilized for both DAS and geophone datasets.

4.1 DAS depth calibration

Since the fibre deployed in the observation wells loops down and up the wellbore, a quality control step of the data from each segment of the fibre loop was completed by cross-correlating both segments. The process consisted of first separating each segment of the fibre, then truncate them at the desired length, in this case, our area of interest is located at approximately 250 ms; therefore, we selected a truncation time of 500 ms. To normalize the inputs, an amplitude mean scaling function was applied to both segments by calculating a scale for each trace sample within the defined scale window and multiplying it by the entire trace (VISTA help, Schlumberger 2015). Then the cross-correlation was applied for a window length of 500 ms where the zero-lag was chosen to be in the centre of the window at 250 ms. Figure 4.1 displays an example of the cross-correlation of the straight fibre cable, where (a) and (b) are the inputs, the down loop segment and the up loop segment respectively; and (c) is the result of the cross-correlation. As expected, the result shows that the event of maximum amplitude coincides with the zero-lag time (250 ms), meaning there is a good correlation between both sides of the fibre optic cable. From this point, we continued our analysis focusing on one segment of the fibre optic cable, namely the down loop section. Another possible approach to have in mind for future processing flows could be the stacking of the mirror figure of the other segment to improve the fold of the dataset and take advantage of both upgoing and downgoing sections of the fibre.

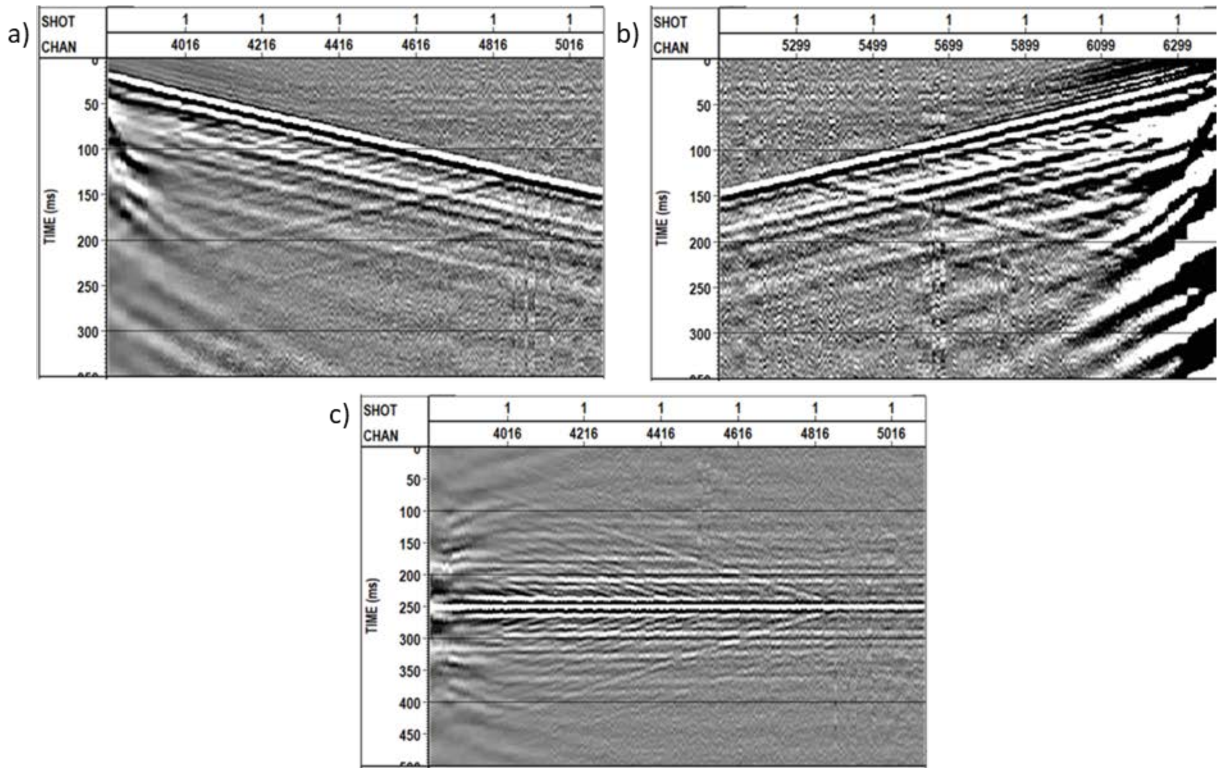

Figure 4.1 Cross-correlation of straight fibre segments of VP 132, line 21. a) down loop segment, b) Up loop segment, c) cross-correlation result.

After obtaining a good correlation between both segments of the fibre, we proceeded with the depth calibration. This calibration consisted of a cross-correlation of the DAS data with the first and last trace of the geophone array. Both datasets should be the same length in time. Therefore, the geophone traces were truncated to match the DAS trace length of 1001 ms. Then, the traces of the shallowest and deepest receiver of the geophone array at 191.24 m and 306.24 m respectively, were duplicated for the number of DAS channels per source gather. In the straight fibre case, the geophone traces were duplicated 1301 times, whereas, for the HWC, the geophone traces were duplicated 1531 times. Then, each DAS and geophone dataset were cross-correlated, the parameters of the cross-correlation had a window length of 1000 ms and the zero lag time in the middle of the window at 500 ms. The corresponding channel of the maximum amplitude event at the zero-lag time (500 ms) will be the DAS channel that shares the depth of the first or last trace of the geophone array. Figure 4.2 displays an example of the calibration. The straight fibre DAS gather corresponding to line 21, VP 132 is shown at the top left (a) and the duplicated geophone trace at 191.24 m depth at the top right (b), and the result of the cross-correlation from the two gathers is shown at the bottom of the figure (c). The red line highlights the crossing point of the maximum amplitude event and the zero-lag time, identifying the channel number that matches the depth of the first geophone at 191.24 m depth.

The same procedure was repeated for the deepest geophone (306.24 m) and the process was repeated for the HWC fibre data. The results of VP 132 are shown in Table 4.2, where the identified traces are listed for straight and HWC fibre. Notice that the last row of the table displays the depth aperture. The true depth aperture or the difference between the first and last geophone is 115 m, for the straight DAS it was calculated by subtracting the identified traces and then dividing it by the output trace spacing of the fibre. Knowing the channel spacing of the straight fibre (0.25 m), we would expect a total of 460 traces over that depth range. In this case, the number of traces obtained from the calibration was 456. A difference of 4 traces, which is equivalent to a 1 m depth difference is an acceptable number giving the small spacing between traces. For the HWC case, there is an uncertainty on the output trace spacing since there are two fibre helixes that are wrapped around a mandrel causing a decrease in the original output trace spacing of the fibre (0.25 m). We estimated the HWC output trace spacing using the total depth of the helical fibre in the Observation Well 2 and the number of traces of a zero offset VSP. According to the completion diagram of the Observation Well 2 (shown in Chapter 2), the bottom of the HWC is at 334.43 m from Kelly Bushing (KB) and an HWC zero offset VSP has 1430 traces per gather. Thus, the estimated output trace spacing for HWC fibre is the ratio between the length of the fibre and the number of traces, yielding 0.23 m. From the depth registration, we obtained 481 traces, equivalent to a difference of 4.37 m in the depth aperture between the first and last geophone utilizing the estimated output trace spacing of 0.23 m.

Table 4.2 Depth registration result of line 21, VP 132.

	Depth (m)	Straight DAS trace	HWC DAS trace
First geophone trace	191.24	800	895
Last geophone trace	306.24	1256	1376
Depth aperture	**115**	**114**	**110.63**

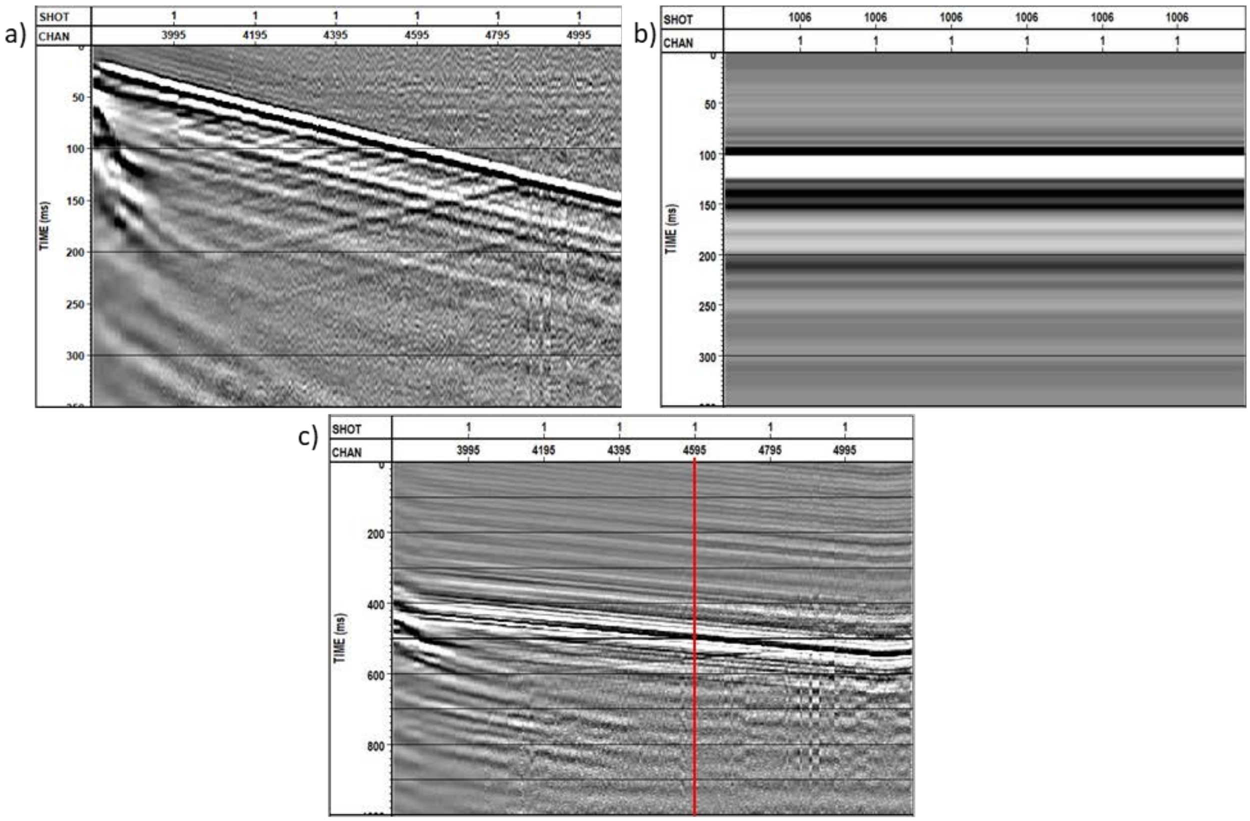

Figure 4.2 Depth registration result of straight fibre, VP 132. a) DAS gather, b) duplicated geophone channel at 191.24 m. c) cross-correlation output, red line marks DAS channel corresponding at that depth (channel # 4595, trace # 800).

Figure 4.3 shows an example of the geophone traces at 191.24 m and 306.24 m (a) and the corresponding straight (b) and HWC (C) DAS channels after the depth calibration. There is an evident difference in frequency, and a phase shift is also noticeable between DAS and geophone traces. These differences could be associated with the measurements recorded by each system. As mentioned previously, DAS measures the strain rate of the fibre and the geophones record the velocity of the particle. The traces shown in Figure 4.3 highlight the importance of converting DAS data to a geophone like response to properly compare both datasets. In addition to these remarks, there is a good match between the geophone traces and DAS traces. The depth registration was performed for the remaining VPs (VP 159, VP 139), Table 4.3 lists the results obtained. A difference between the first and last geophone depth of 0 to 3.25 meters (0 to 13 traces) was obtained for the straight fibre. Whereas for the HWC, the resulting difference ranged from 2.3 m to 4.37 m (21 to 50 traces). The most substantial difference obtained for the straight fibre corresponded to VP 139, meanwhile for the HWC the highest difference was for VP 132.

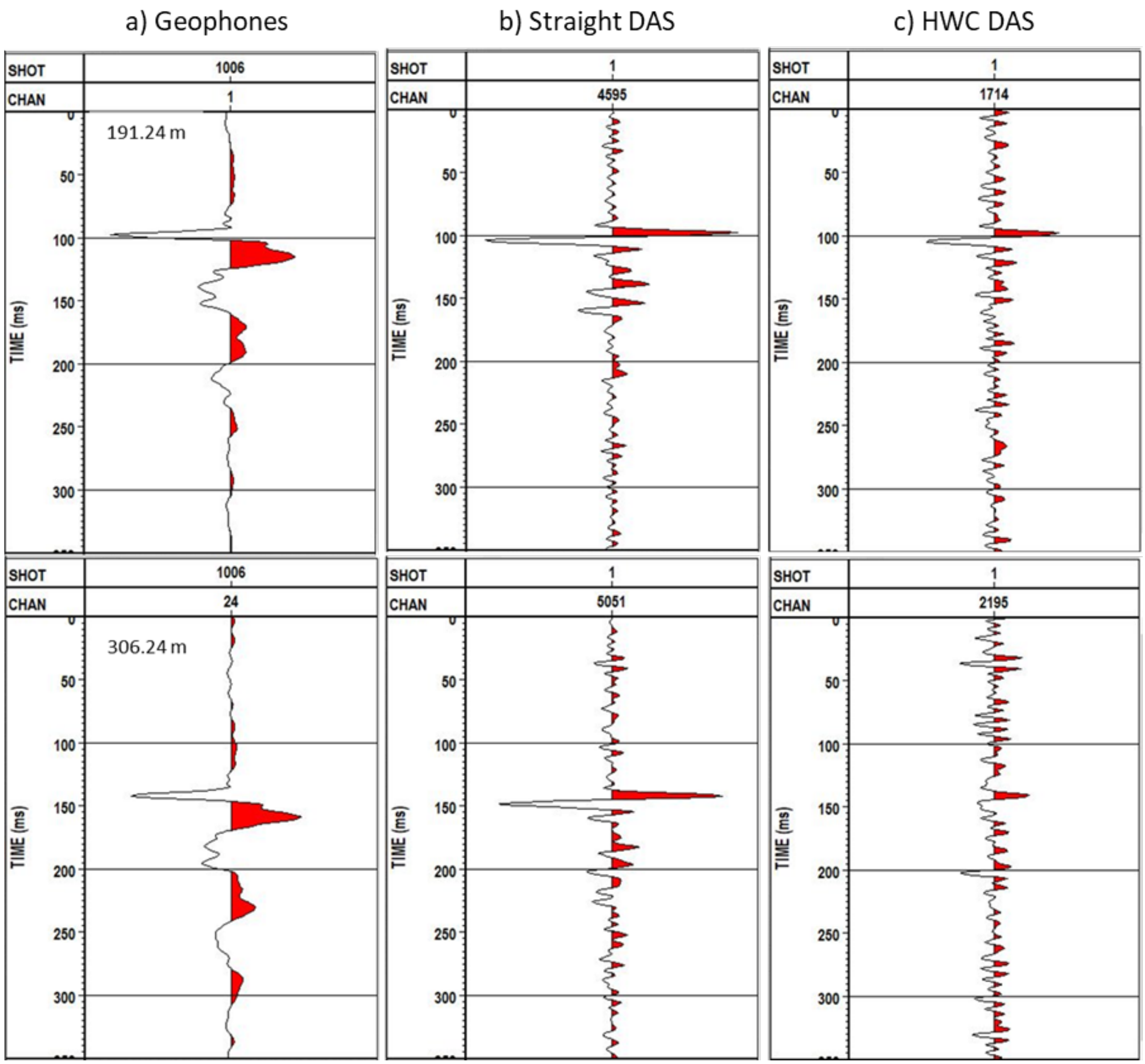

Figure 4.3 Straight and HWC traces after depth correlation. a) Geophone trace at 191.24 m (top) and Geophone trace at 306.24 m (bottom). b) Straight fibre traces, c) HWC fibre traces.

Table 4.3 Depth registration result of line 21, VPs 159 and 139.

	Depth (m)	Straight DAS		HWC DAS	
		VP 159	**VP 139**	**VP 159**	**VP 139**
First geophone trace	191.24	835	756	914	831
Last geophone trace	306.24	1295	1203	1396	1341
Depth aperture	**115**	**115**	**111.75**	**110.86**	**117.3**

As mentioned previously in Chapter 1, an approach to convert DAS signal from strain rate to strain by integrating DAS data with respect to time was tested (Daley et al., 2016). With the intention of obtaining a geophone like response to compare the data from both recording systems accurately. This DAS conversion is also included in Chapter 5 for the processing flow of the walk away VSP. After integrating DAS data with respect to time, the depth registration step was also applied to the integrated DAS datasets (straight fibre and HWC). Figure 4.4 displays an example of the cross-correlation of the integrated DAS data and the duplicated geophone traces at 306.24 m for VP 132. The integrated straight DAS gather corresponding to line 21, VP 132 is shown at the top left (a), and the duplicated geophone trace at 306.24 m depth at the top right (b), and the result of the cross-correlation from the two gathers is shown at the bottom of the figure (c). The red line highlights the crossing point of the maximum amplitude event and the zero-lag time, identifying the channel number that matches the depth of the last geophone of the array. Similarly, Figure 4.5 shows the geophone traces used for the calibration and the obtained integrated traces for straight fibre and HWC. Notice how the phase shift of Figure 4.3 is not present and there is a good correlation between DAS and geophone traces in terms of frequency and phase. Finally, Tables 4.4 and 4.5 lists the traces obtained with the calibration of the integrated DAS data and the corresponding difference in the depth aperture for VP 132 and VPS 159 and 139 respectively.

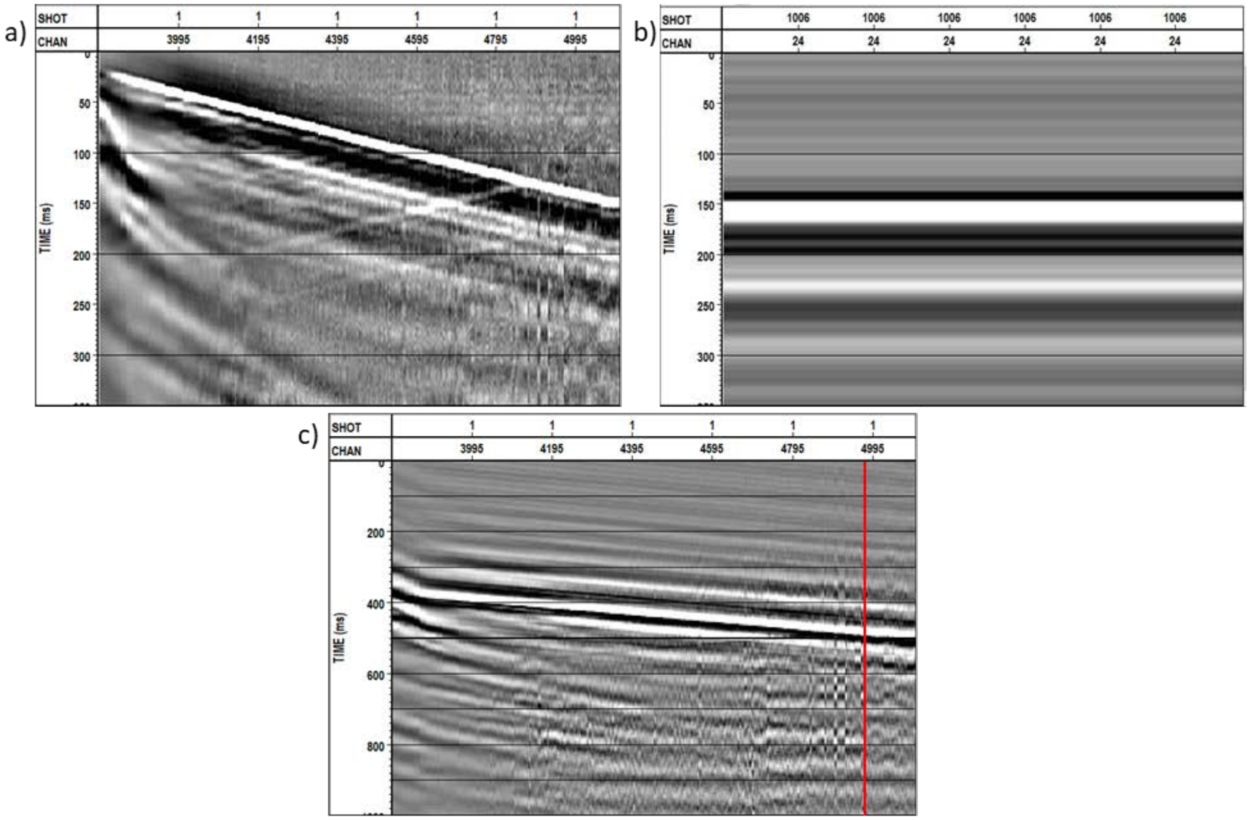

Figure 4.4 Depth registration result of integrated straight fibre, VP 132. a) integrated DAS gather, b) duplicated geophone channel at 306.24 m. c) cross-correlation output, red line marks DAS channel corresponding at that depth (channel # 4984, trace # 1189).

Table 4.4 Depth registration of integrated DAS, line 21, VP 132.

	Depth (m)	Integrated straight DAS trace	Integrated HWC DAS trace
First geophone trace	191.24	748	1714
Last geophone trace	306.24	1189	2195
Depth aperture	**115**	**114**	**110.63**

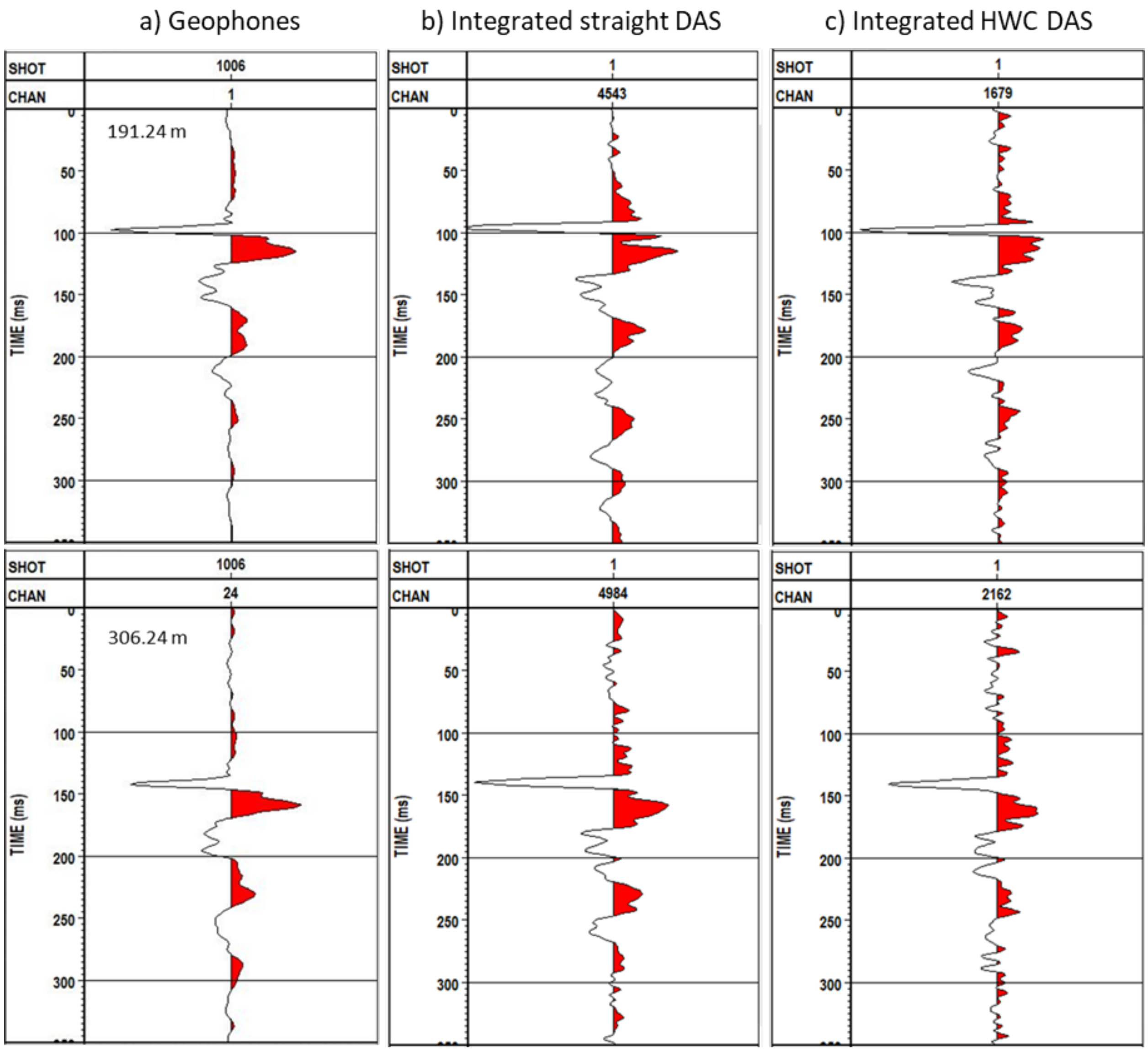

Figure 4.5 Integrated straight and HWC traces after depth correlation. a) Geophone trace at 191.24 m (top) and Geophone trace at 306.24 m (bottom). b) Straight fibre, c) HWC fibre traces.

Table 4.5 Depth registration results of integrated DAS, line 21, VPs 159 and 139.

	Depth (m)	Integrated straight DAS trace		Integrated HWC DAS trace	
		VP 159	**VP 139**	**VP 159**	**VP 139**
First geophone trace	191.24	797	805	891	888
Last geophone trace	306.24	1256	1248	1378	1373
Depth aperture	**115**	**114.75**	**110.75**	**112.01**	**111.55**

An additional approach for the depth calibration was designed, consisting of a time difference analysis of the DAS and geophone data by plotting the time difference of the first arrivals as a function of depth. The geophone first break picks were interpolated every 0.125 m within the coverage of the geophone array (191.24 to 306.24 m) to provide first break picks for each DAS trace. Further information regarding the script used for this analysis can be found in the appendix A.3. Figure 4.6 shows an example of this approach for straight fibre and HWC for VP 132. The X-axis corresponds to the depth and the Y-axis to the number of DAS traces, and the colour bar indicates the difference between the first break picks of the geophones and DAS which ranges from -60 to 60 ms. The zero-time difference is shown in white and the overlaying black line highlights the minimum value of the time difference per sample. The variations of the black line correspond to the changes in DAS first break picks due to the large number of channels per source gather. A depth aperture of 113.75 m was obtained for the straight fibre and 114.77 m for HWC. Tables 4.6 and 4.7 lists the results obtained with this analysis of raw DAS for VP 132 and VPs 159 and 139.

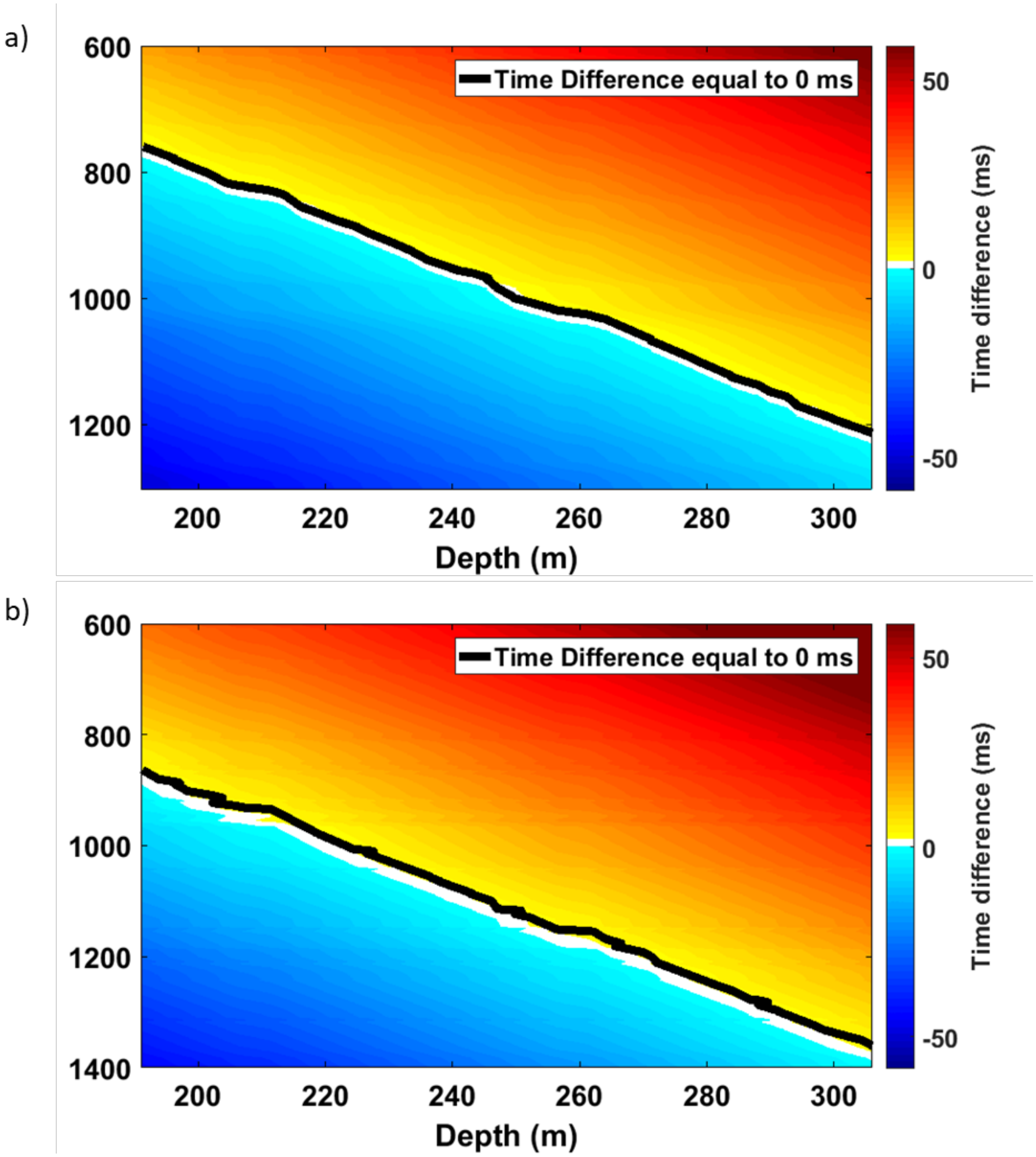

Figure 4.6 Time difference analysis for DAS depth registration. a) straight fibre, b) HWC.

Table 4.6 Time difference analysis result of raw DAS, line 21, VP 132.

	Depth (m)	Straight DAS trace	HWC DAS trace
First geophone trace	191.24	778	896
Last geophone trace	306.24	1233	1395
Depth aperture	**115**	**113.75**	**114.77**

Table 4.7 Time difference analysis result of raw DAS, line 21, VPs 159 and 139.

	Depth (m)	Straight DAS trace		HWC DAS trace	
		VP 159	**VP 139**	**VP 159**	**VP 139**
First geophone trace	191.24	881	835	958	964
Last geophone trace	306.24	1341	1286	1456	1467
Depth aperture	**115**	**115**	**112.75**	**114.54**	**115.69**

Similarly, Figure 4.7 shows the results for the integrated straight and HWC DAS of VP 132. From which a depth aperture of 113.75 m was obtained for the integrated straight DAS and for the integrated HWC we obtained 112.01 m. Table 4.8 shows the results for VP 132 and Table 4.9 list the results obtained for the integrated DAS of VPs 159 and 139. Note that the time difference approach was used as a contribution to the cross-correlation method to quality control the results and generate a graphic correlation to identify the corresponding DAS trace at a given depth easily. After a good depth registration was obtained from both methods, the receiver depth was updated and the procedure of the zero offset VSP processing was continued.

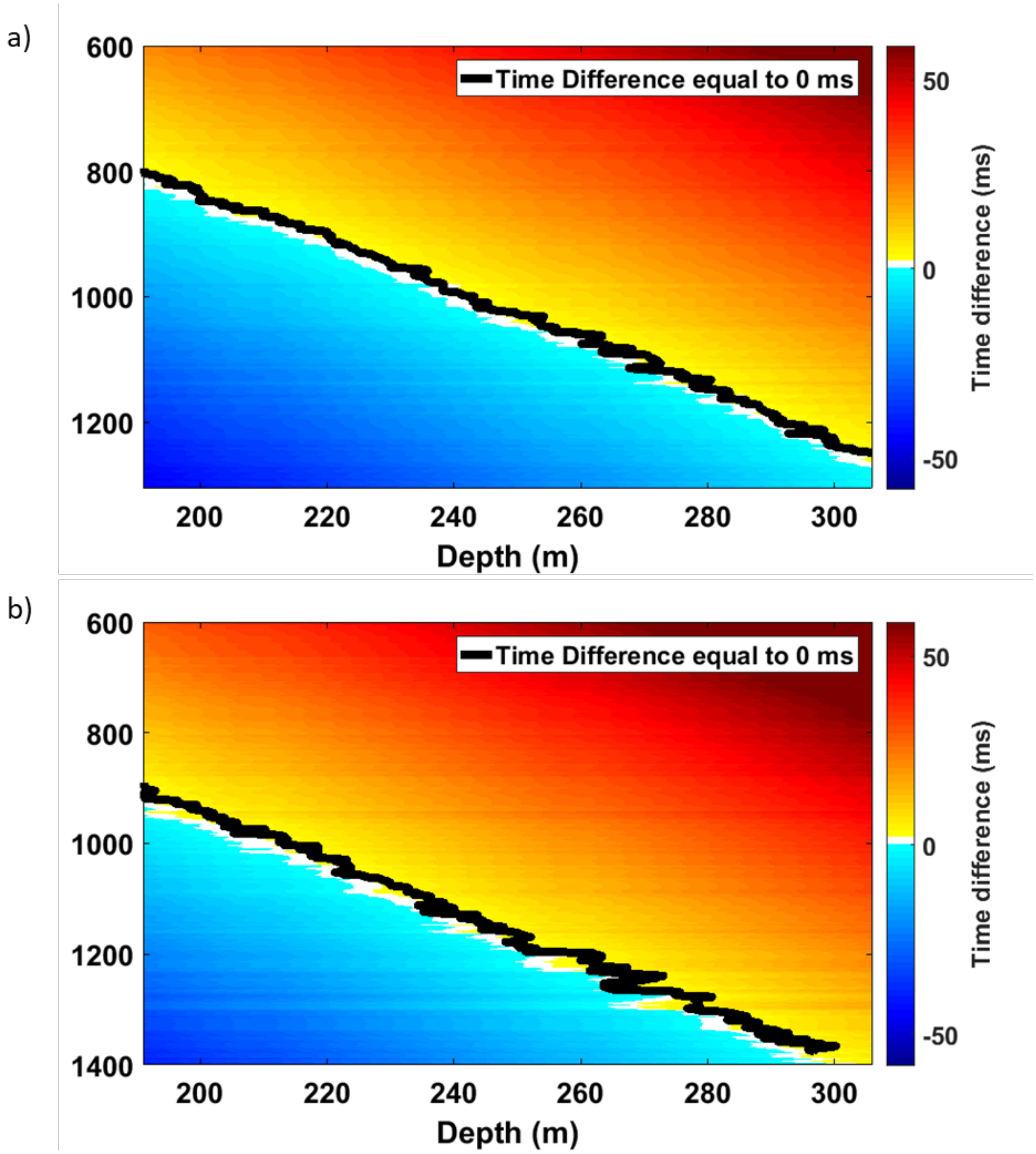

Figure 4.7 Time difference analysis for depth registration of integrated DAS. a) straight fibre, b) HWC.

Table 4.8 Time difference analysis result of integrated DAS, line 21, VP 132.

	Depth (m)	Integrated straight DAS trace	Integrated HWC DAS trace
First geophone trace	191.24	821	935
Last geophone trace	306.24	1276	1422
Depth aperture	**115**	**113.75**	**112.01**

Table 4.9 Time difference analysis result of integrated DAS, line 21, VPs 159 and 139.

	Depth (m)	Integrated straight DAS trace		stain HWC DAS trace	
		VP 159	**VP 139**	**VP 159**	**VP 139**
First geophone trace	191.24	924	875	992	1012
Last geophone trace	306.24	1375	1331	1483	1452
Depth aperture	**115**	**112.75**	**114**	**112.93**	**101.20**

4.2 Zero offset VSP processing

A standard zero offset processing flow was used for both DAS and geophone datasets as the processing of DAS VSP data is similar to regular VSP processing sequence (Wu et al., 2015) with slight variations in the parameters related to the fibre optic cable configurations. Figure 4.8 displays the flow that was applied to both datasets for the three VPs previously mentioned, taken and modified from Bubshait (2010).

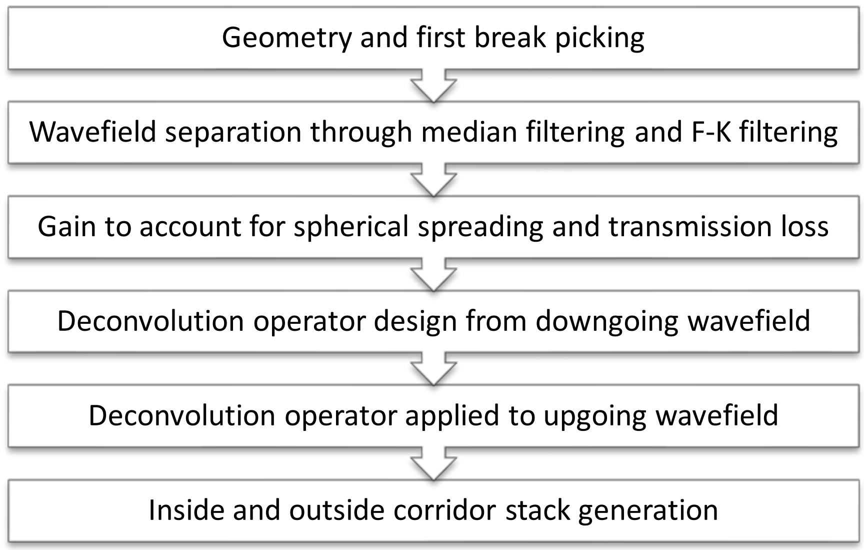

Figure 4.8 Generalized zero offset VSP processing flow (modified from Bubshait, 2010).

The following sections will explain the procedure while showing an example of both datasets from VP 132. However, only the final product of the processing flow corresponding to the outside corridor stacks will be shown for the other two source points.

4.2.1 Geometry and first break picking

When processing seismic data, it is essential to set up the geometry of the survey correctly, especially if the data is acquired with two different recording systems. In this case, the three VPs selected for processing should have similar header information for DAS and geophones datasets, except for the difference in the receiver depth range as discussed in the previous section. From the multicomponent geophone array, only the vertical component was used for the zero offset VSP processing because most of the energy recorded at a near offset VP will contain P-waves predominantly and the contribution of the horizontal components of the 3C geophone array would be minimal.

Once the geometry was uploaded into VISTA software, picking of the first breaks was completed for both datasets per VP. As an example, Figure 4.9 shows the straight DAS and geophone source gather with Automatic Gain Control (AGC) of 250 ms window length applied and the labels identifying several events that will be of reference in the following sections.

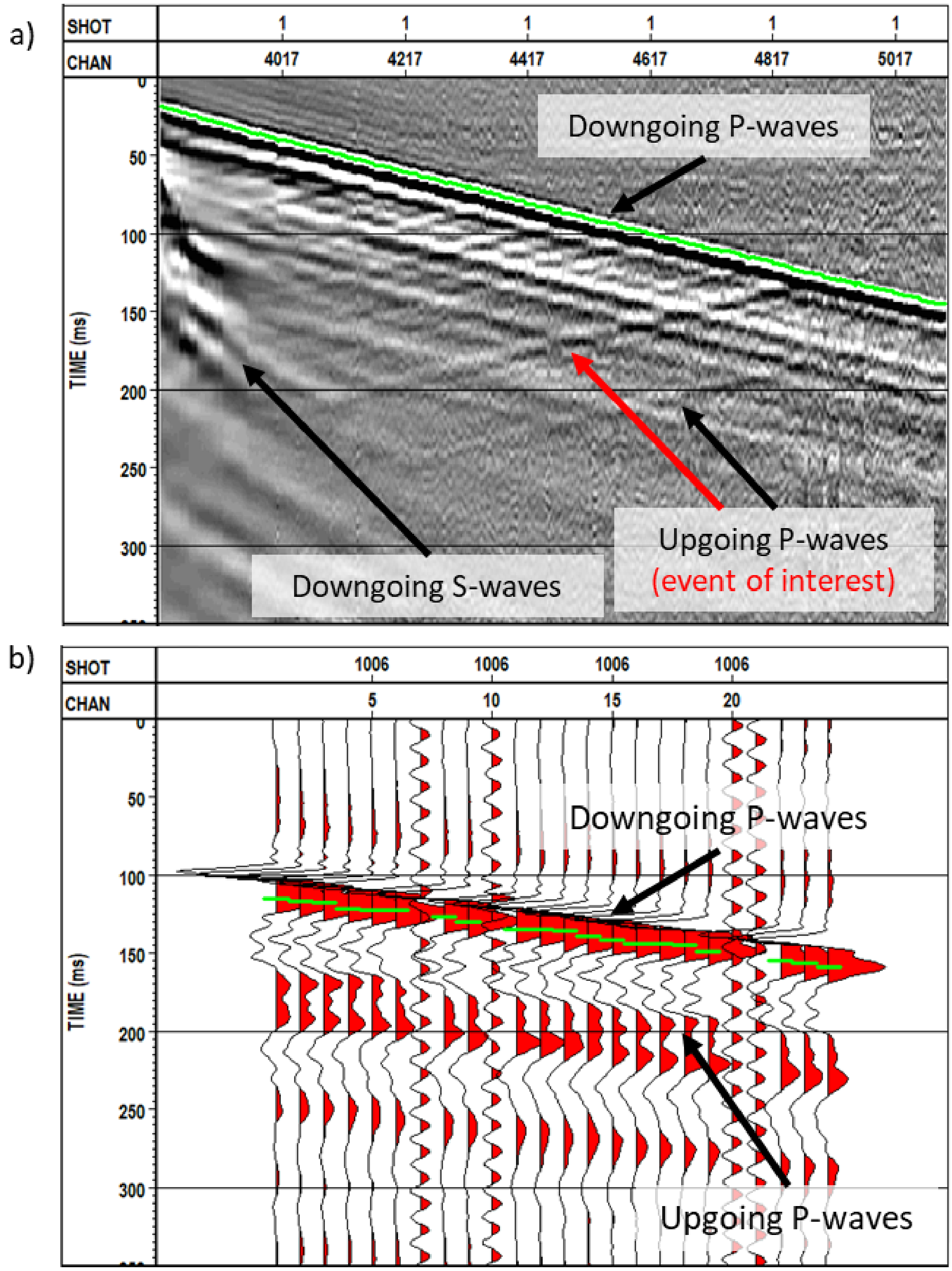

Figure 4.9 Raw source gathers of VP 132. a) straight DAS and b) geophone array. Labels of P-waves and S-waves downgoing and upgoing events are shown in black. The CO_2 injection target the Basal Belly River Sandstone (BBRS) is shown with the red arrow.

Figure 4.10 shows VP 132 source gathers of both fibres and geophones with AGC of 250 ms window length. The first break picks are shown in green. Notice that DAS datasets are displayed with variable density due to the large number of traces per gather, whereas the geophone data is shown in wiggle trace mode. The geophone array had four dead traces that were removed and interpolated with a 2D trace interpolation function available in VISTA that follows the Anti-Leakage Fourier Transform (ALFT) approach (Xu et al., 2005). The trace interpolation is performed in the frequency - wave number domain (F-K) and consisted of two steps, the initial approximation where a deconvolution operator is created with dead and live traces and then is used to deconvolve the input. This is followed by an iterative process that consists on the estimation of the spectrum distortion or "leakage" from where spectrum components larger than the threshold are selected and stored in each iteration until the minimum energy spectrum component is reached. Then all the selected components are subtracted from the input data and the reconstructed traces from the spectrum components should fit the original measurements (Xu et al. 2005; VISTA Help, Schlumberger 2015). The result of the geophone data after the interpolation is shown in Figure 4.10(d), note that the interpolation outcome was the dataset utilized for the rest of the processing flow. As Figure 4.9, downgoing and upgoing P-wave events are visible in Figure 4.10. Downgoing S-waves are also noticeable in DAS datasets and the CO_2 injection target is easily identified in both DAS and geophone datasets as the strong upgoing reflector, also labelled in Figure 4.9 with a red arrow. Table 4.10 lists the first break picks of both DAS and geophone datasets. For reference, the straight and HWC DAS first breaks are shown with a sample interval similar to the geophones spacing (5 m).

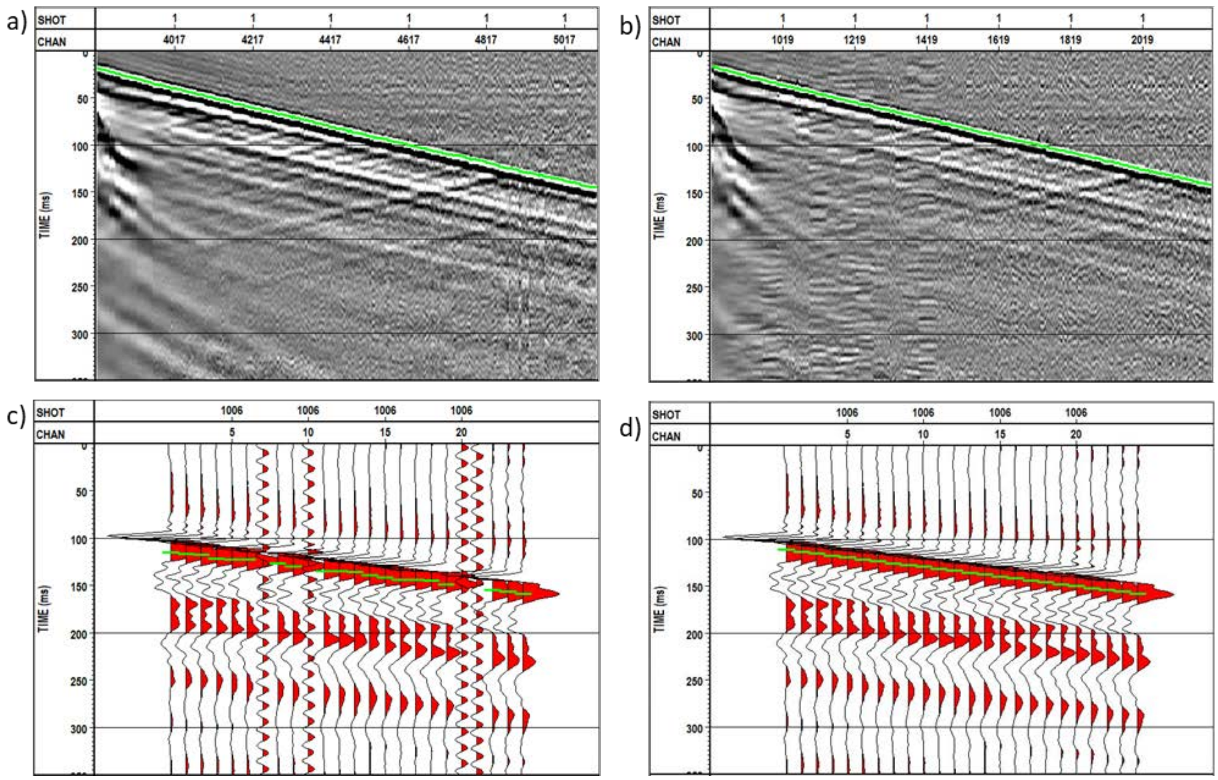

Figure 4.10 First break picks of VP 132 in green. a) Straight DAS, b) HWC DAS, c) Geophone vertical component with dead traces and d) Geophone vertical component after interpolation of the dead traces.

Table 4.10 First break traveltimes of VP 132 of geophones and DAS with a 5 m interval spacing.

Receiver depth (m)	Geophones first break traveltime (ms)	Straight DAS first break traveltime (ms)	HWC DAS first break traveltime (ms)
191.24	111.31	99.62	85.08
196.24	113.34	102	86.68
201.24	115.37	103.75	88.97
206.24	117.4	105.28	91.13
211.24	119.43	107.65	92.3
216.24	121.46	109.83	94.51
221.24	123.49	111.53	96.74
226.24	125.52	113.57	98.24
231.24	127.54	115.28	100.97
236.24	129.57	116.97	102.51
241.24	131.6	119.32	104.17
246.24	133.63	121.27	106
251.24	135.66	124.08	107.86
256.24	137.69	126.08	110.18
261.24	139.72	127.62	111.8

266.24	141.75	129.68	113.24
271.24	143.77	131.29	116.07
276.24	145.8	133.6	117.18
281.24	147.83	135.21	119.53
286.24	149.86	136.96	121.26
291.24	151.89	138.46	124.63
296.24	153.92	141.26	125.71
301.24	155.95	141.93	127.83
306.24	157.97	144.47	129.92

Then the first break picks of the zero offset gathers interval velocities were calculated. In seismic data, the interval velocity is defined as an average velocity for a particular interval expressed as follows:

$$V_{int} = \frac{\Delta z}{\Delta t} \tag{4.4}$$

where, $\Delta z = z_2 - z_1$ and $\Delta t = t_2 - t_1$ are the thickness of the interval and the traveltime across the interval, respectively. This equation generates a velocity profile or a 1D velocity model that will be used for the walk away VSP processing discussed in Chapter 5. Similarly, the root-mean-square velocity (V_{rms}) is defined by the following expression (Sheriff, 2002):

$$V_{rms} = \sqrt{\frac{\sum_i V_k^2 t_i}{\sum_i t_i}} \tag{4.5}$$

where V_k and t_i are the velocity and time at a given interval. The use of this expression includes the assumption of horizontal layers and straight ray-paths.

Figures 4.11 display the velocity profiles obtained for straight DAS is shown in blue and HWC DAS is shown in green. Similarly, the obtained geophone velocity profile is shown in Figure 4.12. The first break picks as a function of depth are displayed on the left side of each figure whereas the interval velocity and the RMS velocity are shown on the right side of the figures. The high density of traces on DAS datasets and the small channel spacing cause unexpected changes in the interval velocity profile resulting in a non-blocky and noisy trend. To account for this, we resampled the number of traces used for the velocity profile calculation. An arithmetic mean function was applied to DAS datasets every 60 and 65 traces for the straight and HWC DAS respectively. The number of traces selected for the arithmetic mean was based on the output trace spacing (0.25 m and 0.23 m) to obtain a new trace spacing equivalent to 15 m and 14.95 m for straight and HWC DAS respectively. Additional information regarding the script used for this step can be found in the appendix A.4. After resampling the DAS datasets (Figure 4.11), we observe a good correlation between the straight DAS and HWC DAS, where both, the first break times and the velocity profiles show an overlap between the two fibre configurations. In addition, the interval velocity profiles present a blocky appearance as we would expect. When comparing the geophone interval velocity profile with DAS velocity profiles, we also observe a good correlation in the deepest section where the geophone array has coverage (191.24 m to 306.24 m). Note the change in the depth scale in Figure 4.12.

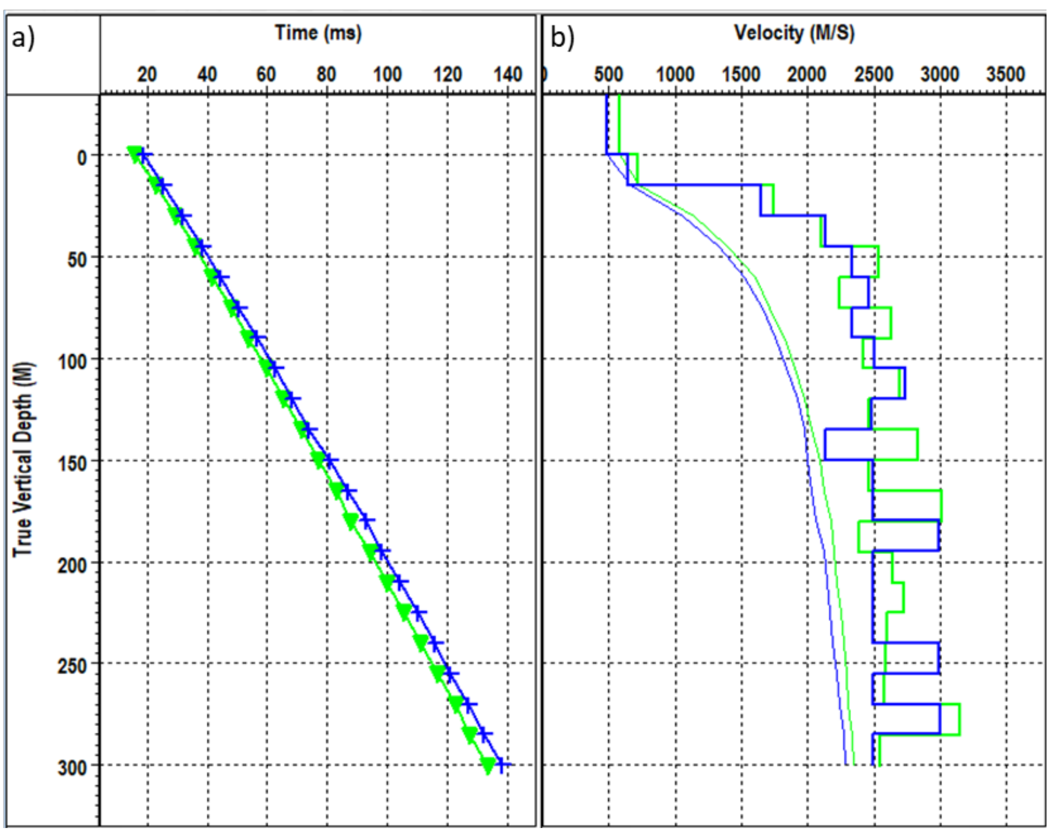

Figure 4.11 Straight fibre (blue) and HWC (green) velocity profile. a) first break times versus depth. b) interval velocity (thick curve) and RMS velocity (thin curve).

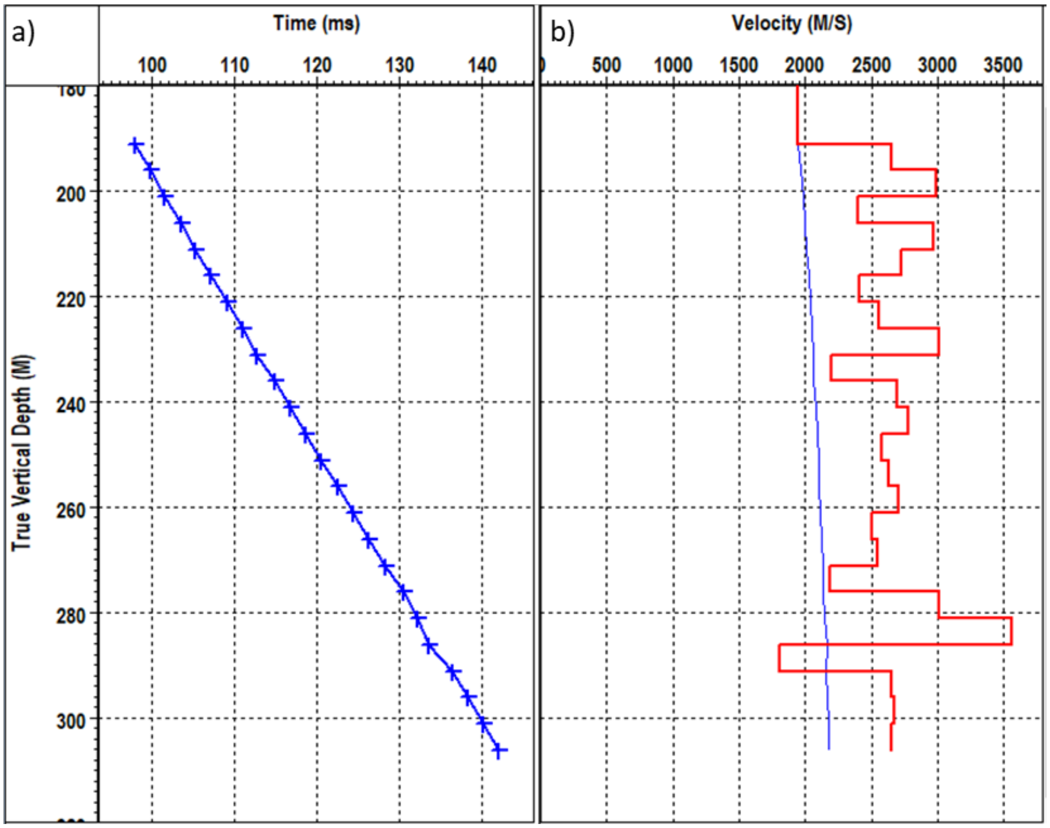

Figure 4.12 Geophone velocity profile. a) first break times versus depth in blue. b) interval velocity (red) and RMS velocity (blue).

4.2.2 Wavefield separation

To isolate the downgoing events from the upgoing events, a median filter was applied to each VP. This type of filter is defined as a non-linear filter that yields a median value from a running window (Hardage, 1983; Sheriff, 2002). The input is a window of a selected length; generally, an odd number of points is chosen. The traces within the window are sorted in an amplitude ascending mode. And the median value corresponds to the trace in the (N + 1)/2 position, where N is the number of traces or points. The process is repeated across the entire dataset as the window slides down a point at a time (Hardage, 1983; Hinds et al., 1996).

Several tests were conducted to find the right length of the filter for each dataset. For both the straight and HWC optic data, a median filter of 91 points corresponding to 22.75 m and 20.93 m length was utilized respectively. Even though the straight and HWC DAS have different output trace spacing and number of traces per gather, a higher or lower number of samples in the median filter for the HWC fibre did not seem to have a significant impact in the wavefield separation, therefore we decided to use the same number of samples for both fibres. Meanwhile, for the geophone data, a median filter of 5 points, corresponding to a 25 m length was selected. Note that these values vary significantly due to the difference in the number of traces and trace spacing of the datasets.

The first step of the wavefield separation process is to flatten the input data at a datum with respect to the first break times. Figure 4.13 represents the data after a flattening function was applied at 100 ms. Then, a mean scaling function was applied by calculating a scale for each trace sample within the defined scale window and multiplying it by the entire trace (VISTA help, Schlumberger 2015). The chosen scale window ranges from 90 to 110 ms to ensure an amplitude enhancement of the first arrivals. Followed by the median filter, the upgoing events were removed from the input data by subtracting the downgoing wavefield from the input data, resulting in the upgoing wavefield.

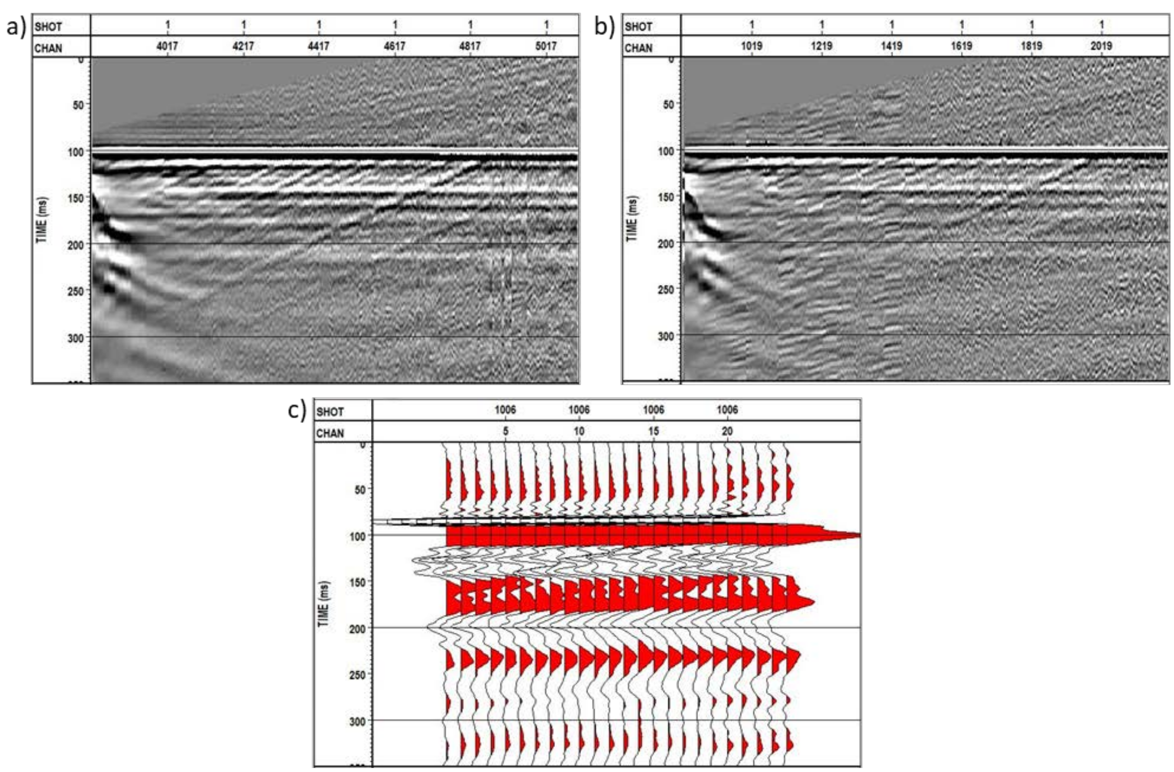

Figure 4.13 VP 132 after flattening function with AGC applied: a) straight DAS, b) HWC DAS, c) geophone vertical component after dead trace interpolation.

Figures 4.14 and 4.15 display the downgoing and upgoing wavefield after the median filter and a reverse flattening function was applied to visualize the data at field record time (FRT). A good separation of the downgoing wavefield was obtained for both datasets, as shown in Figure 4.14. Nevertheless, the DAS upgoing wavefield in Figure 4.15(a) and (b) still include P and S-wave downgoing events. These lower frequency events were isolated from the upgoing wavefield with a frequency-wavenumber (F-K) filter, as described in detail in the following section.

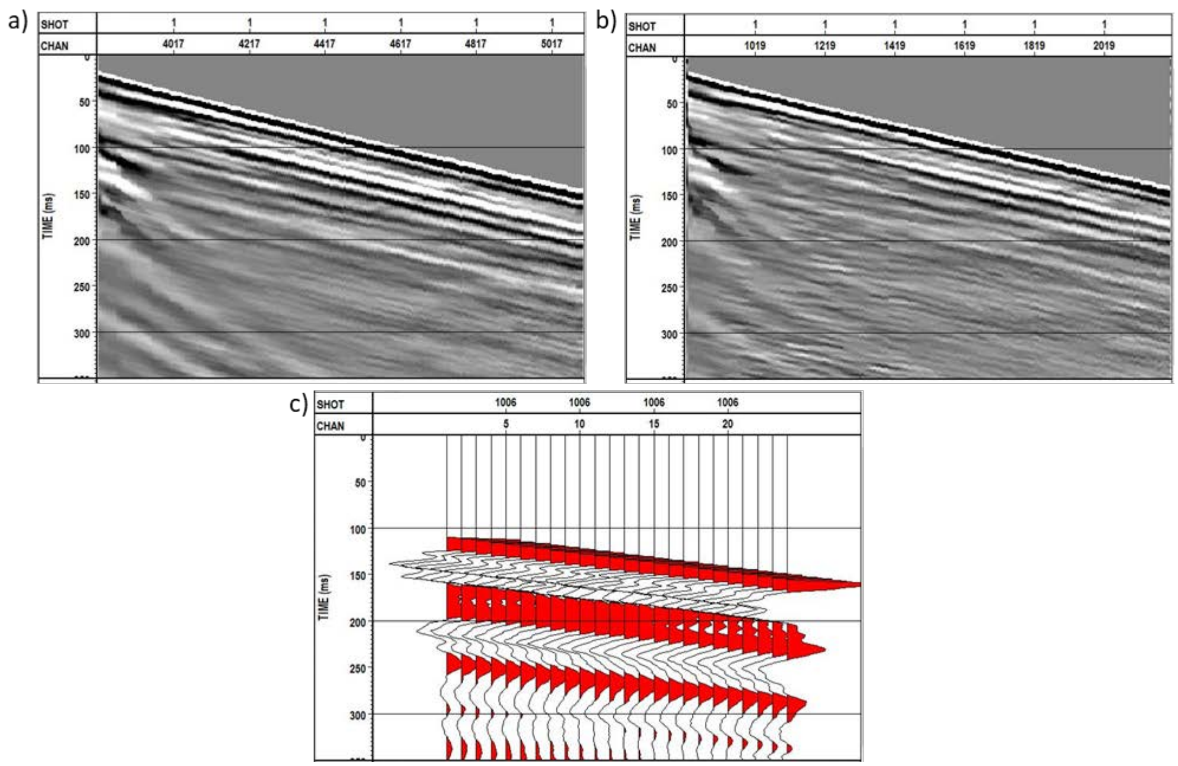

Figure 4.14 Downgoing wavefield of VP 132 after application of a median filter to remove upgoing wavefield with AGC applied: a) straight DAS, b) HWC DAS, c) geophone vertical component after dead trace interpolation.

The frequency-wavenumber (F-K) filtering consists of removing energy from seismic data in the F-K domain. This is achieved by transforming the input data in the time-depth domain to F-K domain through a 2D Fourier transform. As described by Hardage (1983), when the data is transformed to the F-K domain, the downgoing and upgoing events are located in different sections of the wavenumber plane. This is due to the difference in the direction of the wave propagation and the magnitude of the velocities. Generally, downgoing energy is defined with a positive propagation velocity whereas the upgoing energy is arbitrarily defined with negative velocity. As a result, the downgoing energy is mapped in the positive wavenumber quadrant and the upgoing energy in the negative quadrant. Then, rejection zones are designed to filter the undesired events (Hardage, 1983; Hinds et al.,1996; Sheriff, 2002). Therefore, a rejection rectangle covering the positive K quadrant will isolate the upgoing wavefield. Figure 4.16 shows the F-K filter design and Figure 4.17 displays the resulting DAS upgoing wavefield after the F-K filter. Note that the F-K filter was only applied to DAS datasets since the median filter applied to the geophone dataset yield a good separation of the wavefield.

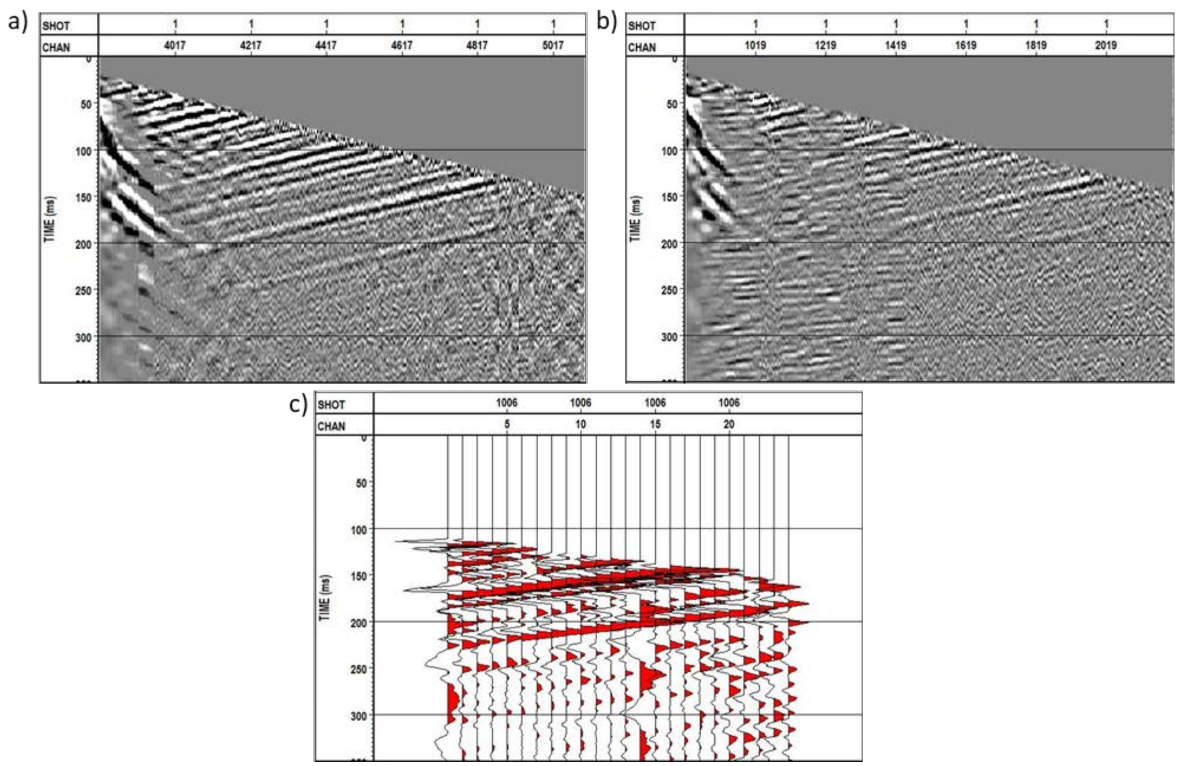

Figure 4.15 Upgoing wavefield of VP 132 after the median filter with AGC applied: a) straight DAS, b) HWC DAS, c) geophone vertical component after dead trace interpolation.

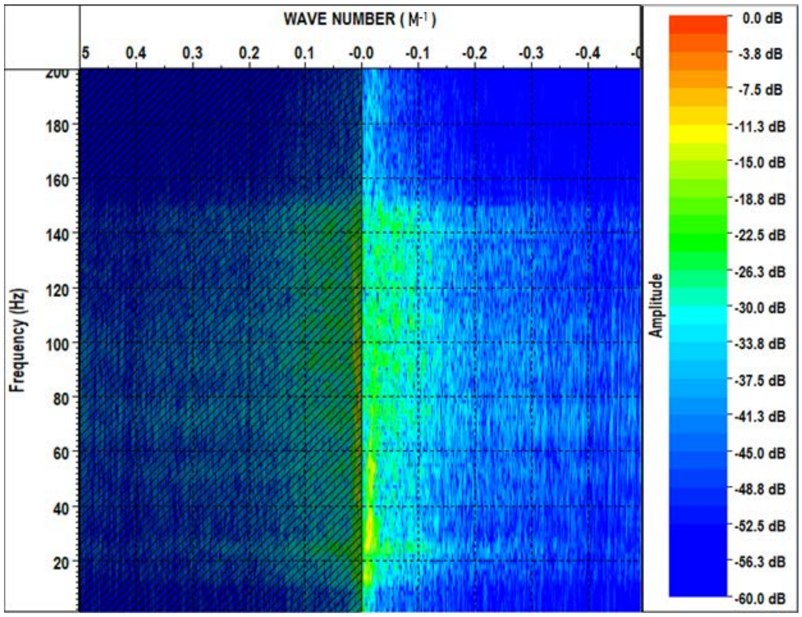

Figure 4.16 F-K filter design for wavefield separation.

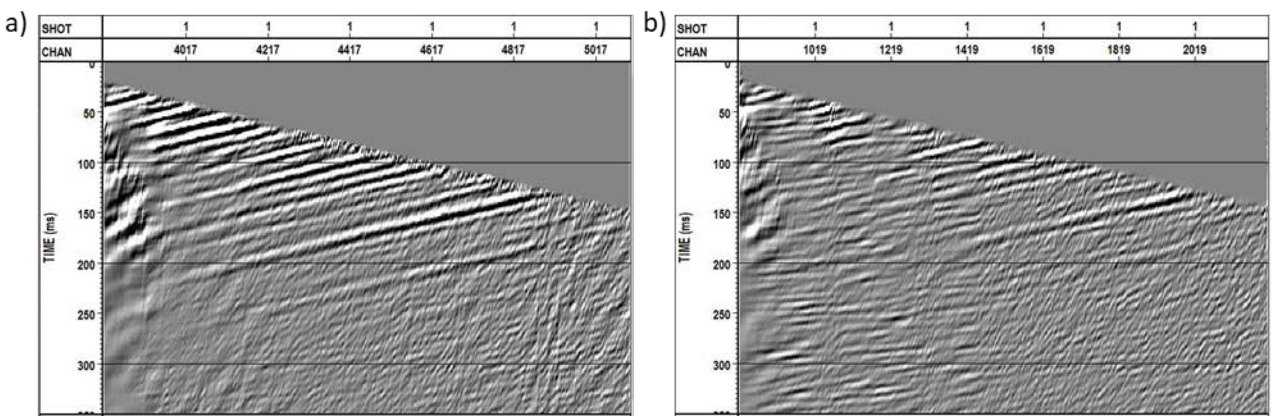

Figure 4.17 Upgoing wavefield of VP 132 after F-K filter with AGC applied: a) straight DAS, b) HWC DAS.

4.2.3 Deconvolution

The next step was to create a deconvolution operator and apply it to the upgoing wavefield to attenuate multiples present in the data. The process consists of flattening the downgoing wavefield, deconvolving the wavefield at a given time window to obtain the deconvolved downgoing wavefield. These steps are then applied to the upgoing wavefield to obtain a deconvolved wavefield with the same deconvolution operator. The deconvolution window selected starts at 80 ms to 380 ms which contains most of the energy and multiples present in the data after being flattened at 100 ms. A post-deconvolution bandpass filter was applied to remove part of the noise generated with the deconvolution process. We tested different frequency bands and the one with the best result was selected; it consisted of: a low truncation frequency of 5 Hz, a low-cut frequency of 10 Hz, a high-cut frequency of 115 Hz and a high truncation frequency of 140 Hz. Figure 4.18 shows the downgoing wavefield after deconvolution and the bandpass filter was applied for the straight DAS, HWC DAS and the geophone datasets respectively.

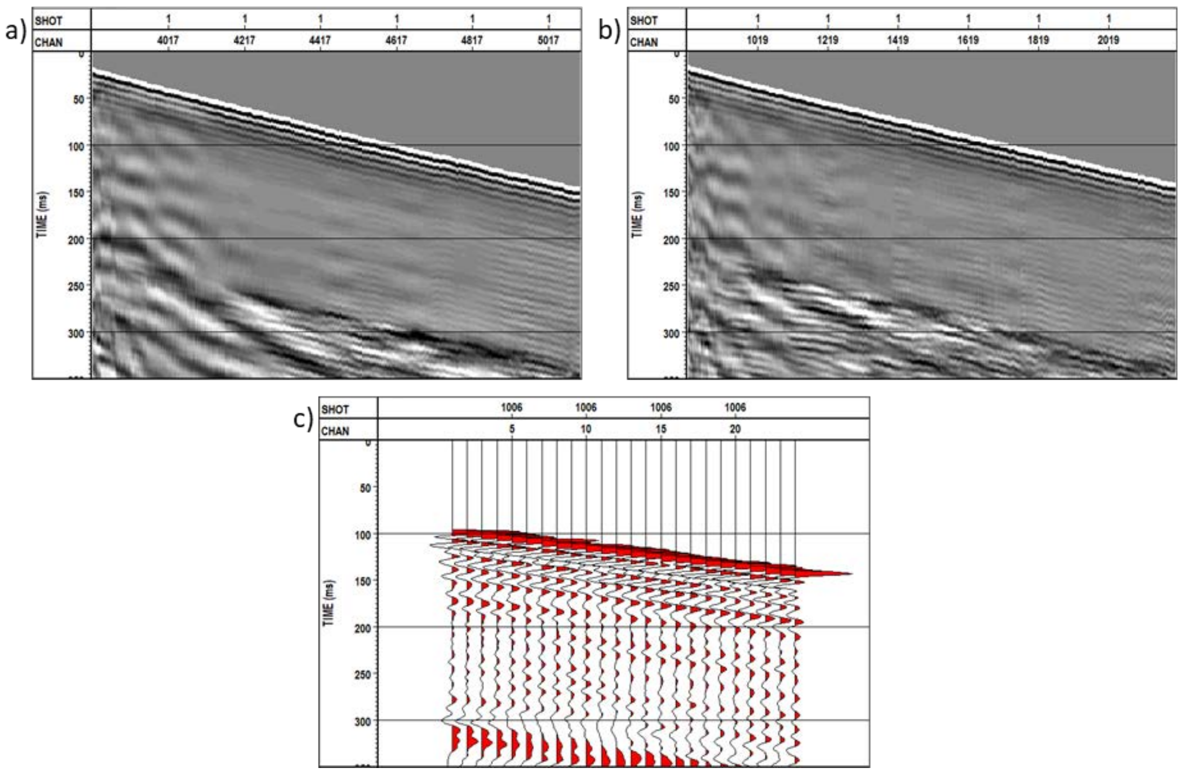

Figure 4.18 Downgoing wavefield of VP 132 after deconvolution, with AGC applied: a) straight DAS, b) HWC DAS, c) geophone vertical component after dead trace interpolation.

Similarly, Figure 4.19 displays the upgoing wavefield after deconvolution and the bandpass filter for the straight DAS, HWC DAS and the geophone datasets, respectively. Overall, the deconvolution seems to have generated a good result as the upgoing and downgoing events appear sharper and better defined. In addition, there is an evident attenuation of multiples after the deconvolution process.

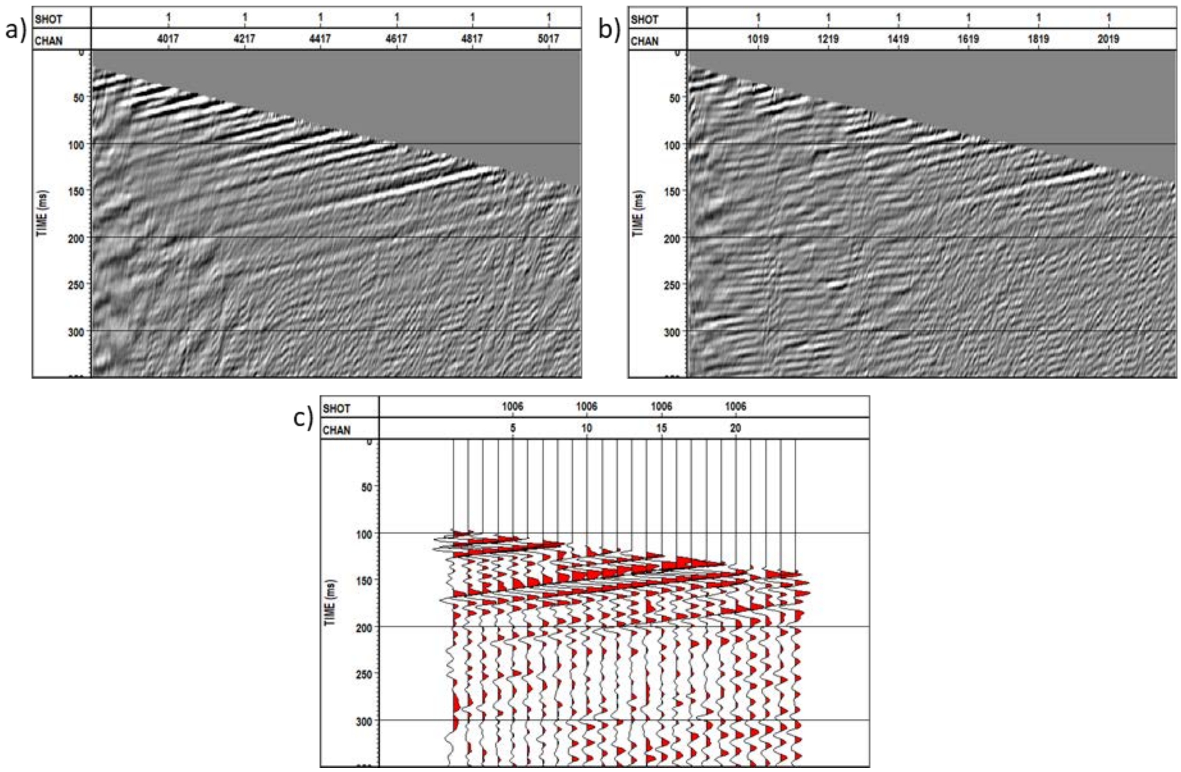

Figure 4.19 Upgoing wavefield of VP 132 after deconvolution, with AGC applied: a) Straight DAS, b) HWC DAS, c) Geophone vertical component after dead traces interpolation.

To further analyze the outcome of the deconvolution, a comparison of the amplitude spectra was performed. The amplitude spectra of the upgoing wavefield of each dataset before and after deconvolution are displayed in Figures 4.20 and 4.21. Each figure shows the amplitude spectrum of an arbitrary trace in black and the average amplitude spectrum of the entire wavefield in blue. DAS datasets before deconvolution seem to display a good frequency range, similar to the vibroseis sweep with a maximum frequency of 150 Hz where the amplitudes appear to be relatively constant as the frequency increases. The geophone dataset has a weaker frequency range, but the amplitude is higher compared to DAS. Note that the geophone array only covers the zone of interest between 191.24 – 306.24 m depth, compared to the fibre optic cables that have full coverage in the wellbore. This could be one of the reasons for the difference between the amplitude spectra and it is recommended to compare the amplitude spectrums using the same depth window for future analysis.

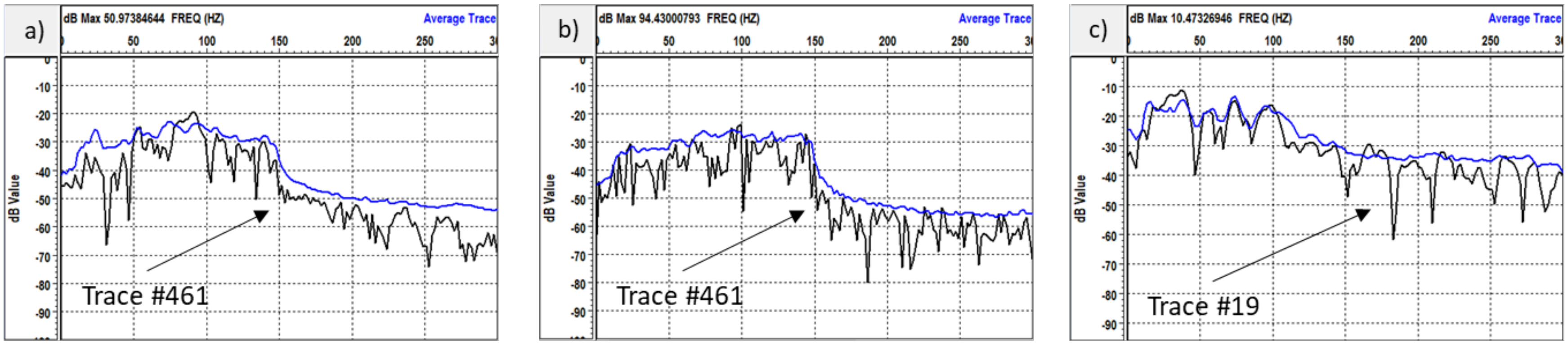

Figure 4.20 Amplitude spectra of VP 132 upgoing wavefield. a) straight DAS, b) HWC DAS, c) geophone vertical component after dead trace interpolation. Arbitrary trace spectrum is shown in black and the average amplitude spectrum of the entire wavefield in blue.

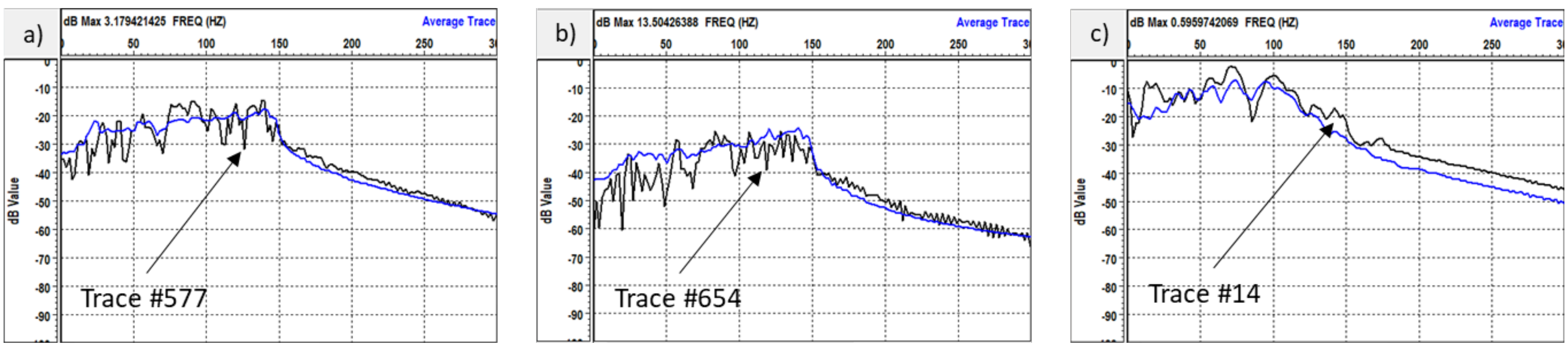

Figure 4.21 Amplitude spectra of VP 132 upgoing wavefield after deconvolution. a) straight DAS, b) HWC DAS, c) geophone vertical component after dead trace interpolation. Arbitrary trace spectrum is shown in black and the average amplitude spectrum of the entire wavefield in blue.

After deconvolution, both datasets show an increase in the amplitudes. DAS amplitude spectra display an interesting behaviour where the amplitudes at higher frequencies seem higher than the amplitudes at lower frequencies. This generates a slight slope in the average amplitude curve between 50-150 Hz that do not necessarily resembles white reflectivity as expected after a deconvolution process. This effect needs further analysis as is not present in the geophone dataset and could be a particular aspect of the fibre that has not been studied yet.

4.2.4 Corridor stack

The final step in the workflow is to generate the inside and outside corridor stacks, generally considered as the final product of a zero offset VSP processing. The outside corridor stack is defined as the summation of the processed upgoing traces that have been shifted to two-way time (TWT) and are stacked over a window or corridor along the first break traveltime. The result is a narrow seismic section that contains primary reflections without multiples. A portion of the remaining section of the VSP after the outside corridor stack is generated can also be stacked and is referred to as the inside corridor stack. The inside corridor stack contains both primaries and multiple reflected upgoing waves. The comparison of the inside and outside corridor stacks provides an indication of multiple contamination in the data (Hinds et al., 1996; Hinds, Kuzmiski, Botha, & Anderson, 1984). The workflow consists of flattening the input data; in this case, the deconvolved upgoing wavefield to 100 ms. Then, an exponential gain function is applied to account for spherical spreading and transmission losses. This is followed by a reverse flattening to return the data to field record time (FRT) and then apply a Normal Moveout (NMO) correction. This correction is generally used to account for the time delay of traces as a function of offset where the velocity profiles calculated previously are utilized. The corrected data is converted to TWT by multiplying the first break times by two. Then a bandpass filter and a median filter are applied to improve the signal to noise ratio. The median filter consisted of 15 points for DAS datasets and 5 points for the geophone dataset. This is then followed by an additional bandpass filter to clean the data. Finally, the inside and outside corridor mute of 50 ms width are applied to a depth of 310 m for DAS and 290 m for geophones. The muted data are stacked, and the resulting trace is duplicated 10 times to obtain the inside and outside corridor stacks.

Figures 4.22, 4.24 and 4.26 display some of the outputs of the workflow, including the upgoing wavefield after NMO correction, bandpass and median filter (a), the inside corridor mute (b) and the outside corridor mute (c) for the straight DAS, HWC DAS and the geophone datasets in TWT with AGC applied. For reference, the CO_2 injection target, the Basal Belly River Sandstone (BBRS) is noticeable at approximately 250 ms, marked with a red arrow in the following figures. Likewise, Figures 4.23, 4.25 and 4.27 show the inside and outside corridor stack of ten traces in TWT with AGC applied.

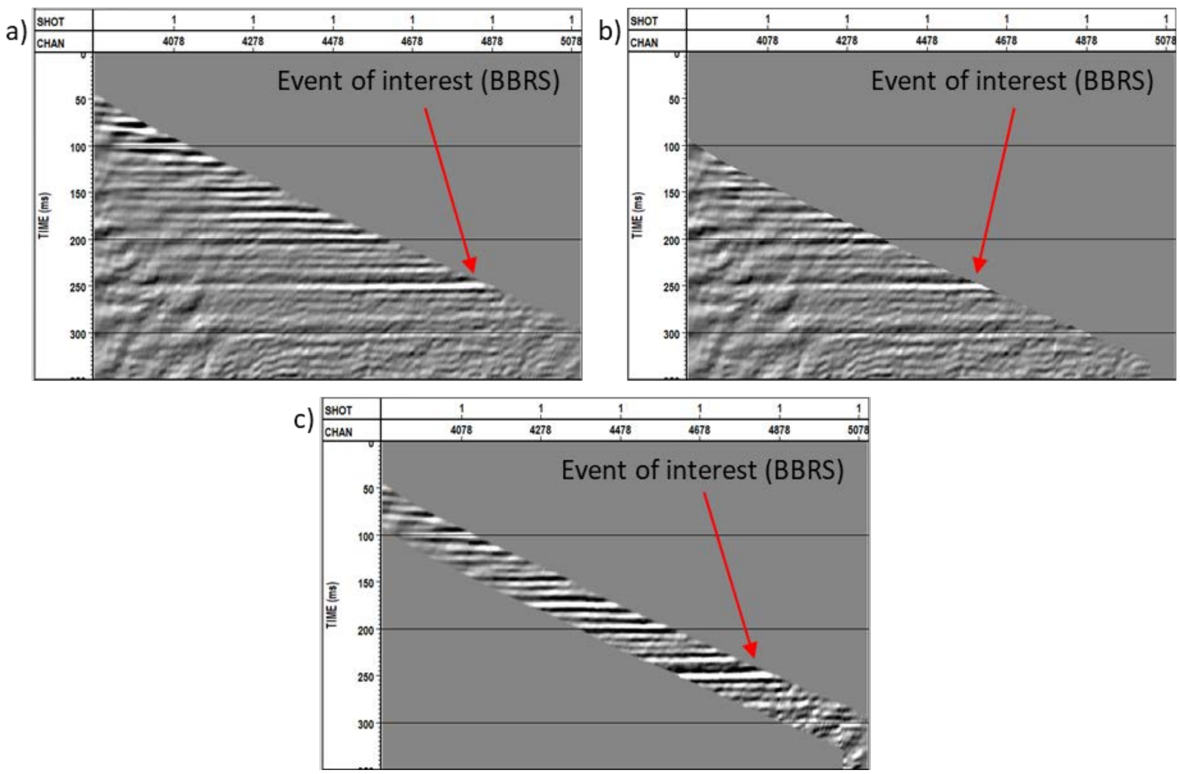

Figure 4.22 Straight DAS upgoing wavefield of VP 132 in two-way time and AGC applied: a) upgoing wavefield, b) 50 ms inside corridor mute, c) 50 ms outside corridor mute. The CO_2 injection target the Basal Belly River Sandstone (BBRS) is shown with the red arrow.

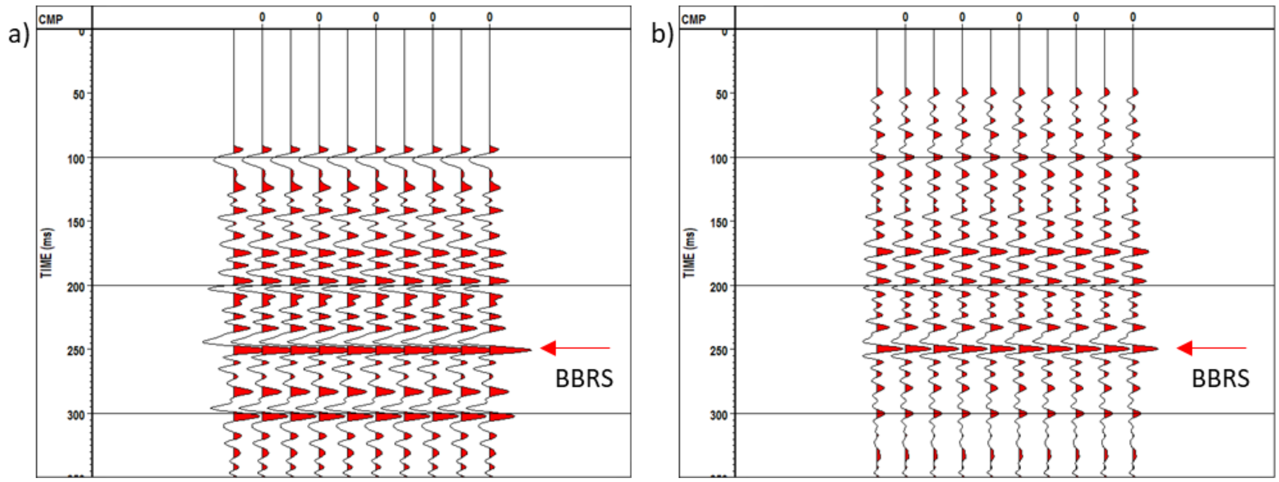

Figure 4.23 Straight DAS corridor stacks of VP 132 with AGC applied: a) inside corridor stack, b) outside corridor stack. The CO_2 injection target the Basal Belly River Sandstone (BBRS) is shown with the red arrow.

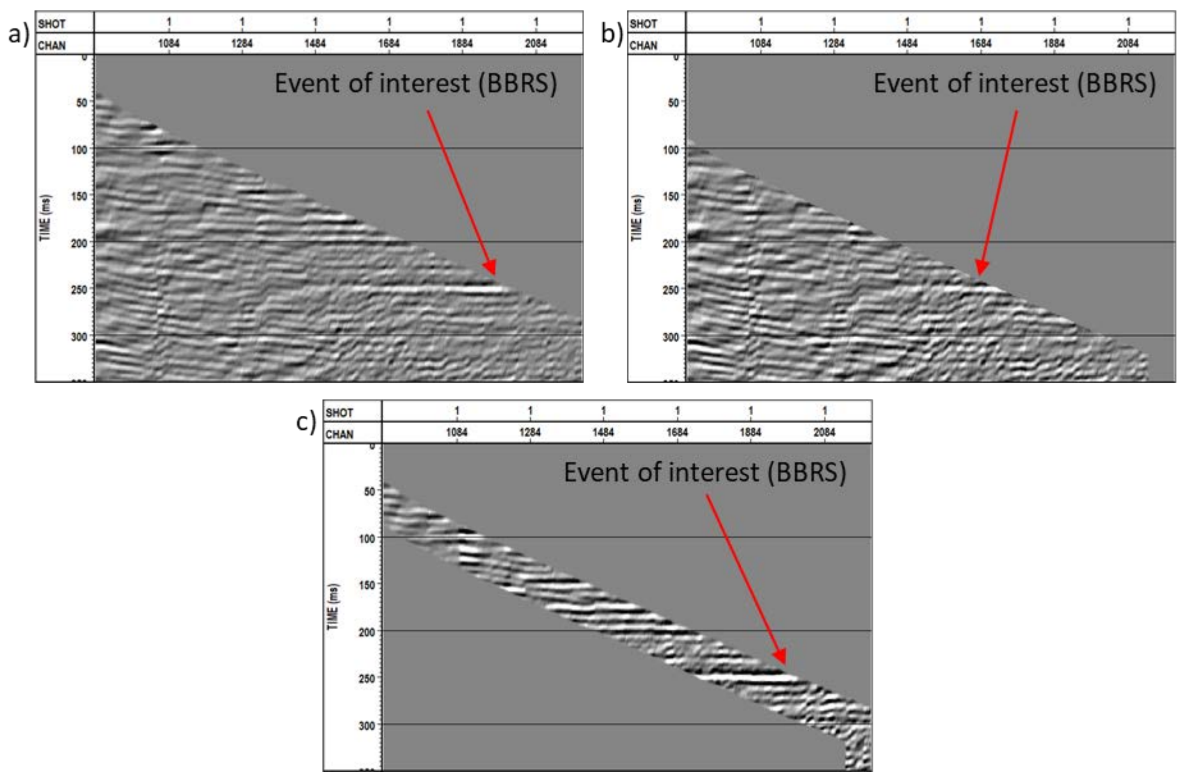

Figure 4.24 HWC DAS upgoing wavefield of VP 132 in two-way time and AGC applied: a) upgoing wavefield, b) 50 ms inside corridor mute, c) 50 ms outside corridor mute. The CO_2 injection target the Basal Belly River Sandstone (BBRS) is shown with the red arrow.

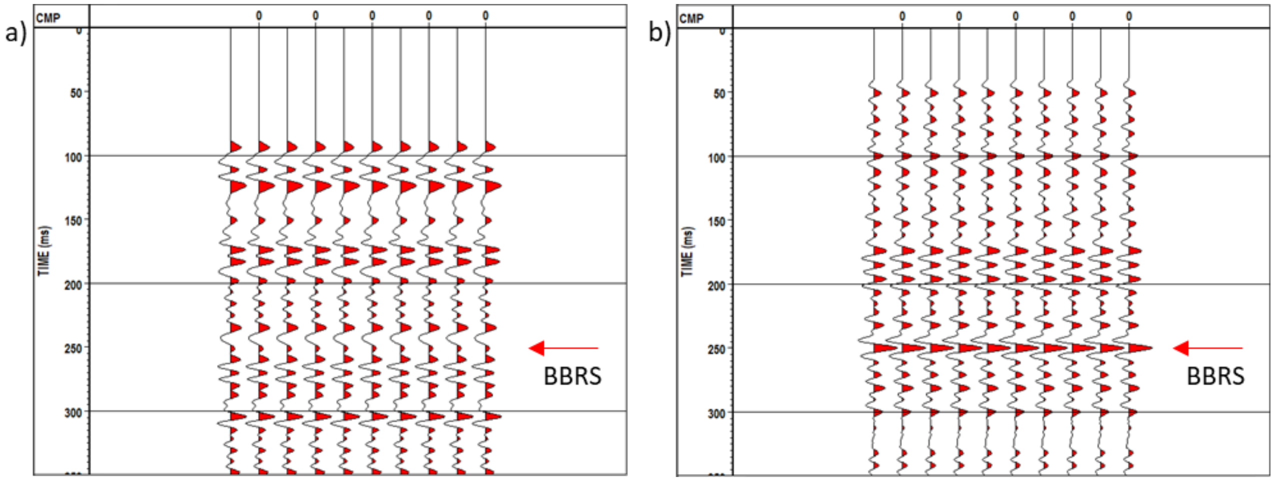

Figure 4.25 HWC DAS corridor stacks of VP 132 with AGC applied: a) inside corridor stack, b) outside corridor stack. The CO_2 injection target the Basal Belly River Sandstone (BBRS) is shown with the red arrow.

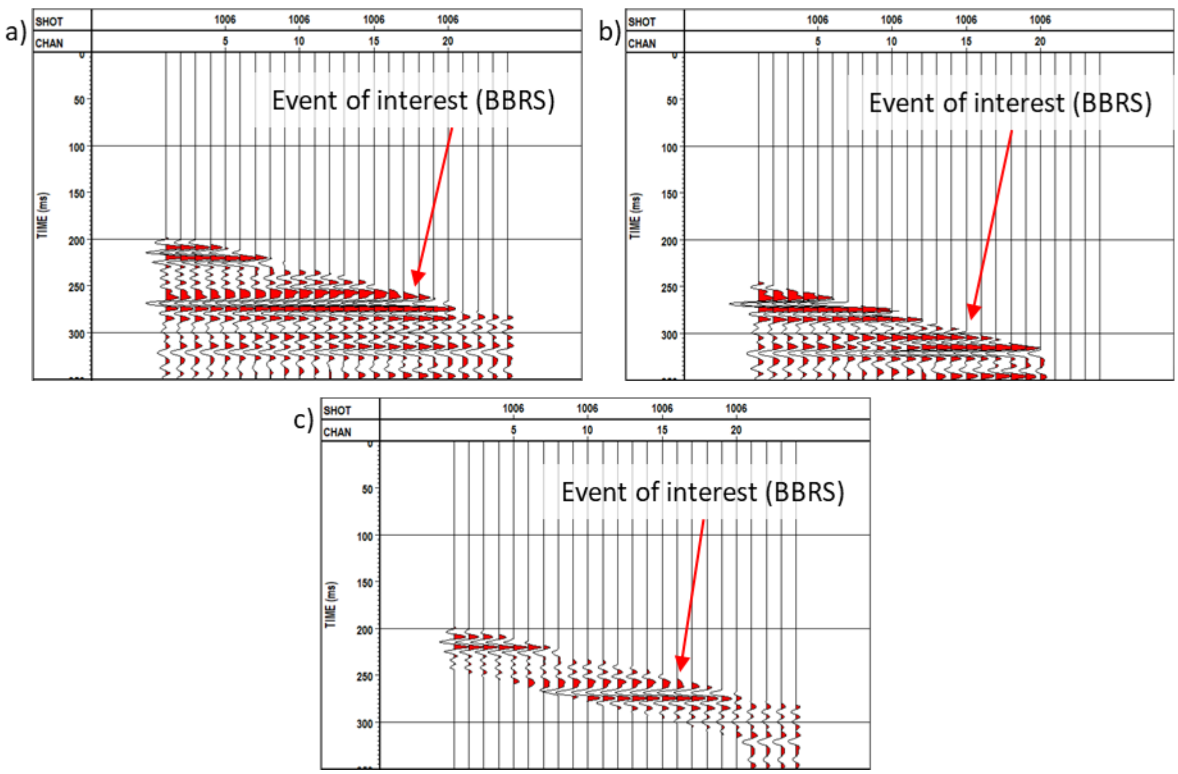

Figure 4.26 Geophone vertical component upgoing wavefield VP 132 in two-way time and AGC applied: a) upgoing wavefield, b) 50 ms inside corridor mute, c) 50 ms outside corridor mute. The CO_2 injection target the Basal Belly River Sandstone (BBRS) is shown with the red arrow.

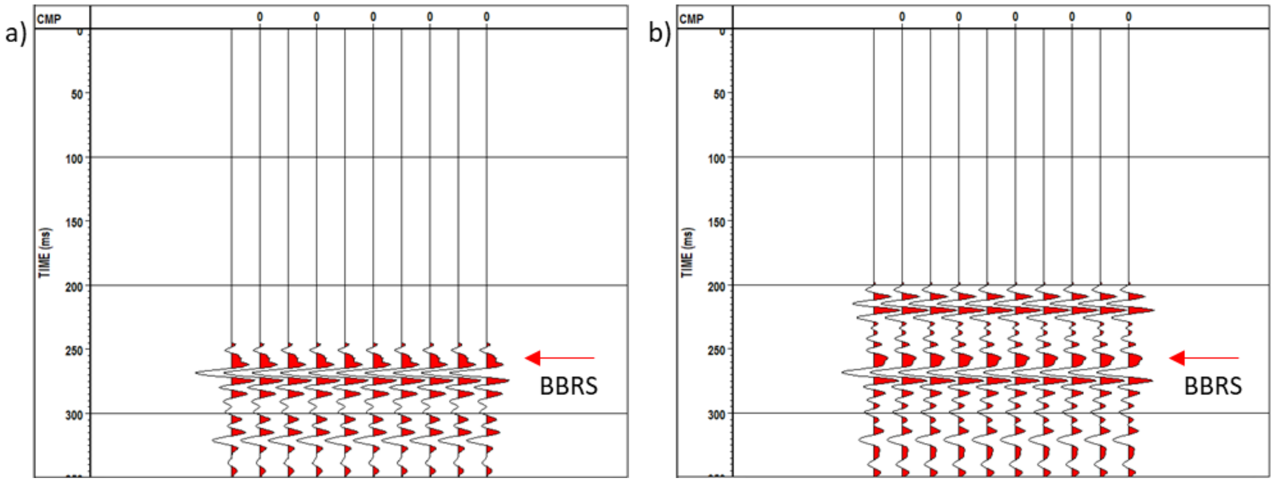

Figure 4.27 Geophone vertical component corridor stacks of VP 132 with AGC applied: a) inside corridor stack, b) outside corridor stack. The CO_2 injection target the Basal Belly River Sandstone (BBRS) is shown with the red arrow.

In general, there is a good correlation between the inside and outside corridor stacks of each dataset, straight DAS, HWC DAS and geophones. However, there are some differences in the amplitude and seismic character of some of the events. These differences are more evident in DAS datasets and one possible explanation could be the noise present in these datasets rather than the presence of multiples in the data. Furthermore, when comparing the inside and outside corridor stacks of the HWC DAS, it is difficult to identify the event of interest (BBRS) in the inside corridor stack, even though it is visible in the inside corridor mute. When stacking the inside corridor mute, the positive amplitude of the BBRS could have been attenuated by other amplitudes that could be associated with the noise present in the data. This observation can be indicative of the effect of the noise in DAS data. As mentioned before, the HWC DAS dataset has a lower signal to noise ratio than straight DAS visible on every step of the processing flow. When comparing DAS and geophone corridor stacks, DAS corridor stacks beside being noisier, present a better illumination in the shallow section due to the full fibre coverage in the well. A time shift is also noticeable between DAS corridor stacks and geophone corridor stack. The time shift is noticeable when comparing the event of interest, in DAS datasets it is at approximately 250 ms and for the geophones is at 257 ms. The possible reasons for the time delay present in the geophone array are discussed in the following section with the rest of the processing results.

4.3 Results and discussion

In this section, the processing results of the remaining source points (VP 159 and VP 139) are displayed. The results shown below comprise the outside corridor mute and outside corridor stack for each dataset. The inside corridor mute and inside corridor stack were not included in the results because the differences observed between the inside corridor stack and outside corridor stack of VP 132 seem to be related to noise rather than the presence of significant multiples in the data. The results of VP 159 and VP 139 are shown below followed by a comparison of the results per source point with a synthetic seismogram generated using the wireline logs of the Observation Well 2 and a wavelet extracted from the downgoing wavefield.

4.3.1 Vibe point 159

The obtained outside corridor mute and the outside corridor stack of VP 159 are shown in Figures 4.28, 4.29 and 4.30, corresponding to the straight DAS, HWC DAS and geophone datasets respectively. Where (a) consist of the outside corridor mute and (b) the outside corridor stack. Each display has either AGC or a specific amplitude gain applied as described in the figure caption. Additionally, the event of interest (BBRS) is marked with a red arrow.

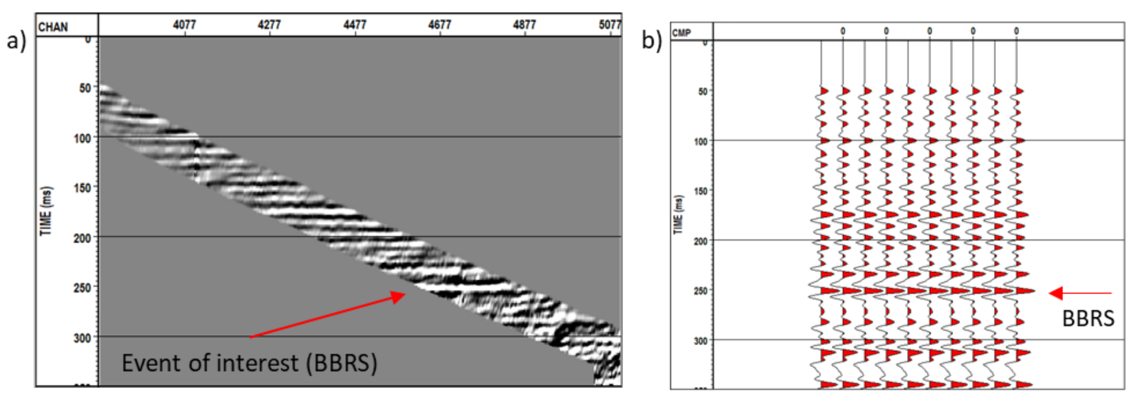

Figure 4.28 Straight DAS outside corridor mute and stack of VP 159: a) outside corridor mute, b) outside corridor stack with +6db of amplitude gain. The CO_2 injection target the Basal Belly River Sandstone (BBRS) is shown with the red arrow.

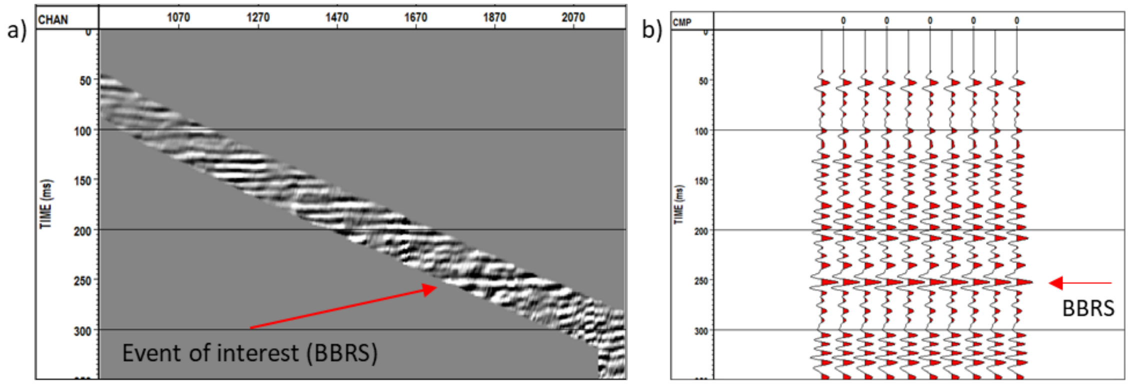

Figure 4.29 HWC DAS outside corridor mute and stack of VP 159: a) outside corridor mute, b) outside corridor stack with +6db of amplitude gain. The CO_2 injection target the Basal Belly River Sandstone (BBRS) is shown with the red arrow.

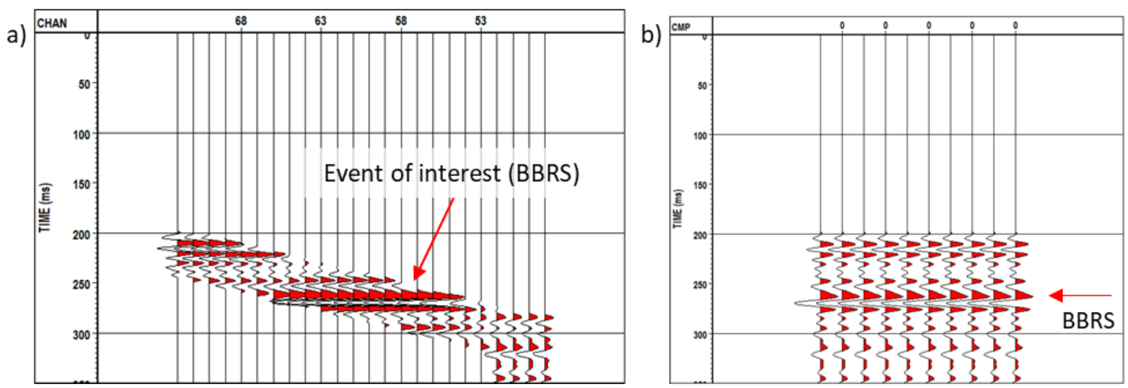

Figure 4.30 Geophone outside corridor mute and stack of VP 159: a) outside corridor mute with +6db of amplitude gain, b) outside corridor stack. The CO_2 injection target the Basal Belly River Sandstone (BBRS) is shown with the red arrow.

4.3.2 Vibe point 139

Similarly, the outside corridor mute and outside corridor stack obtained for VP 139 are shown in Figures 4.31 – 4.33 corresponding to each dataset; straight DAS, HWC DAS and geophones displayed with AGC or other specified amplitude gains. The CO_2 injection target (BBRS) is also highlighted with a red arrow.

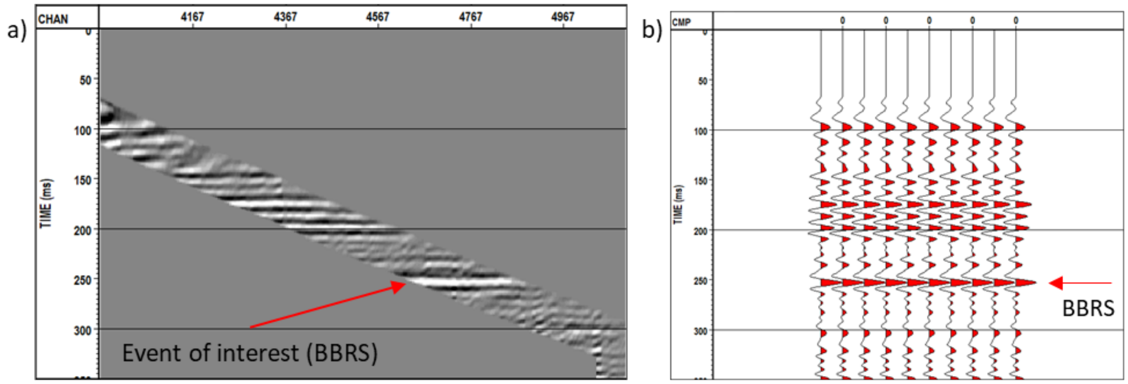

Figure 4.31 Straight DAS outside corridor mute and stack of VP 139: a) outside corridor mute with +6db of amplitude gain, b) outside corridor stack. The CO_2 injection target the Basal Belly River Sandstone (BBRS) is shown with the red arrow.

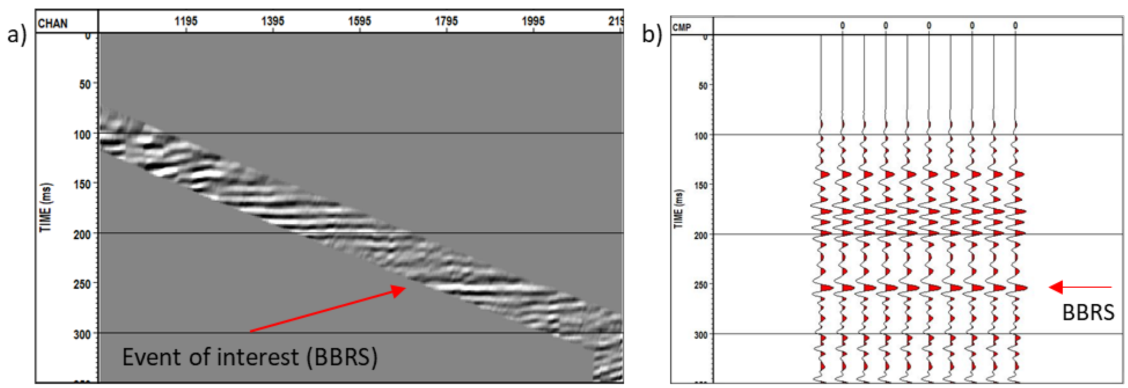

Figure 4.32 HWC DAS outside corridor mute and stack of VP 139 with +3db of amplitude gain: a) outside corridor mute, b) outside corridor stack. The CO_2 injection target the Basal Belly River Sandstone (BBRS) is shown with the red arrow.

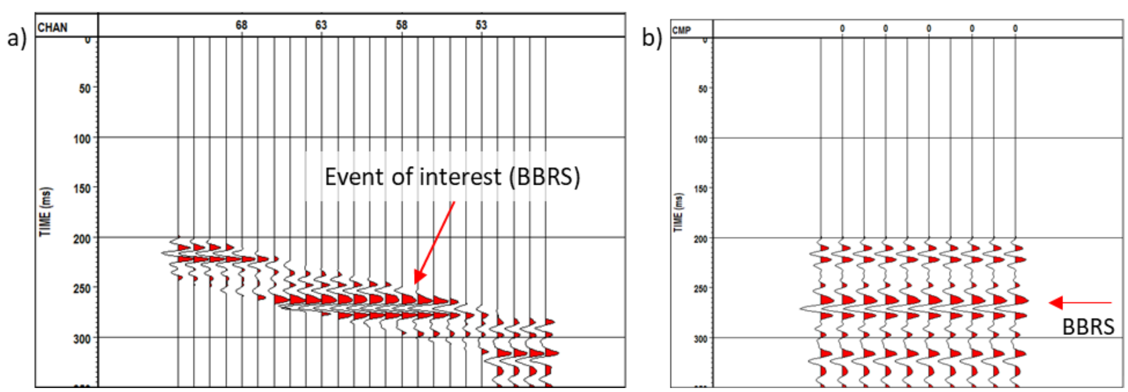

Figure 4.33 Geophone outside corridor mute and stack of VP 139 with AGC: a) outside corridor mute with +9db of amplitude gain, b) outside corridor stack. The CO_2 injection target the Basal Belly River Sandstone (BBRS) is shown with the red arrow.

Consistently with VP 132, the results obtained for VP 159 and VP 139 show a good correlation with the results of VP 132. The injection target is noticeable in both source points and with each dataset. However, the time shift in the geophone dataset was also identified in VPs 159 and 139. The time shift is more evident when comparing the datasets per VP as shown in Figures 4.34, 4.35 and 4.36. Taking the injection target as a reference, it is visible at approximately 250 ms in DAS datasets whereas, for the geophones, is between 255 ms - 265 ms. This time difference might be caused by a delay between recording systems during the acquisition, or it could also be related to the different measurements recorded by each system. As mentioned previously, geophones record the velocity of the particle; meanwhile, DAS records the strain rate of the fibre. In Chapter 5, we include the processing results of integrated DAS datasets similar to the ones used for the depth calibration at the beginning of this chapter as an attempt to compare them with the geophone dataset during the processing workflow of a walk-away VSP line.

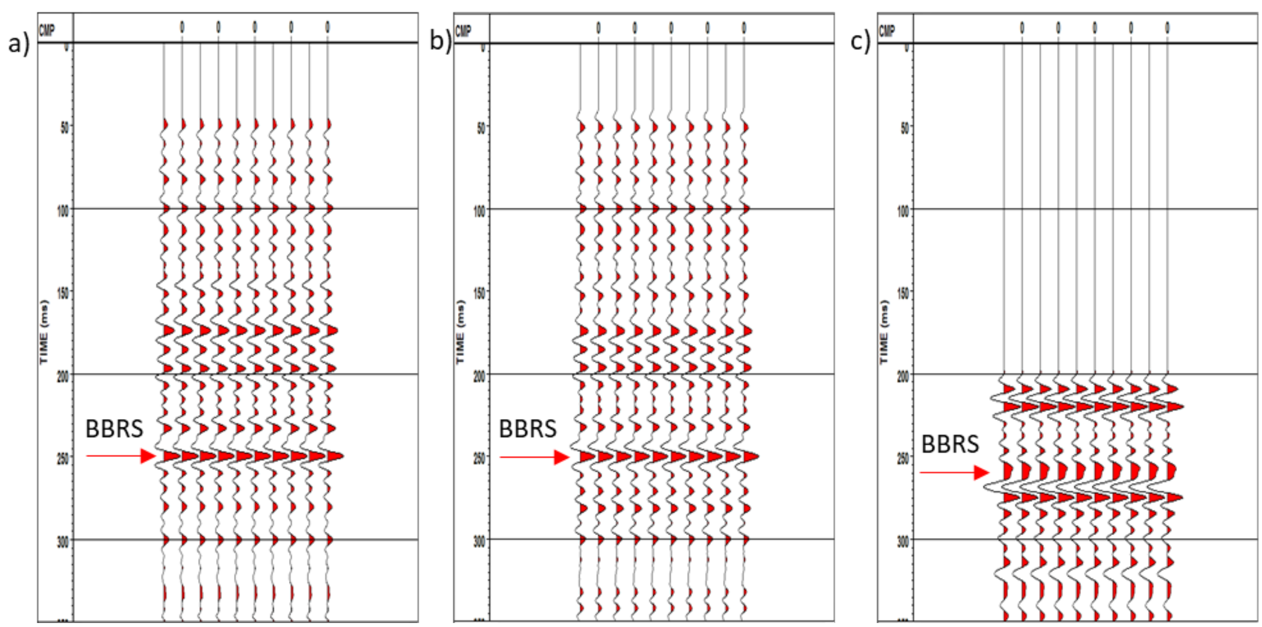

Figure 4.34 Outside corridor stack of VP 132 with AGC applied: a) Straight DAS, b) HWC DAS, c) geophone vertical component. The CO_2 injection target the Basal Belly River Sandstone (BBRS) is shown with the red arrow.

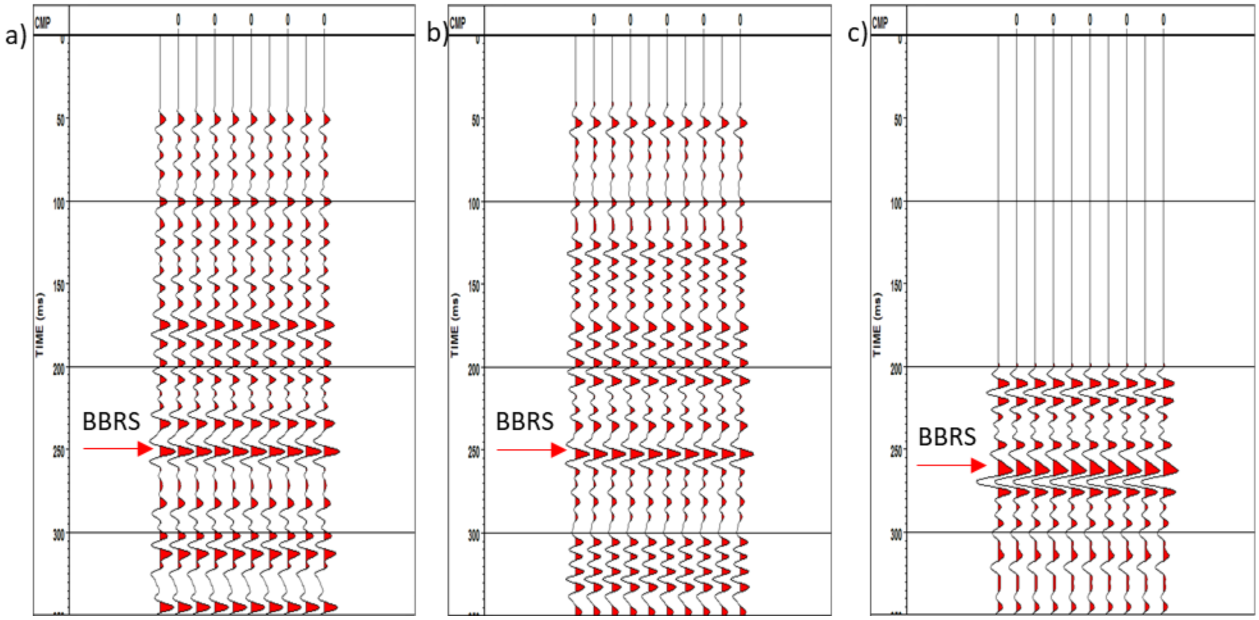

Figure 4.35 Outside corridor stack of VP 159: a) Straight DAS with +6db of amplitude gain, b) HWC DAS with +6db of amplitude gain, c) geophone vertical component. The CO_2 injection target the Basal Belly River Sandstone (BBRS) is shown with the red arrow.

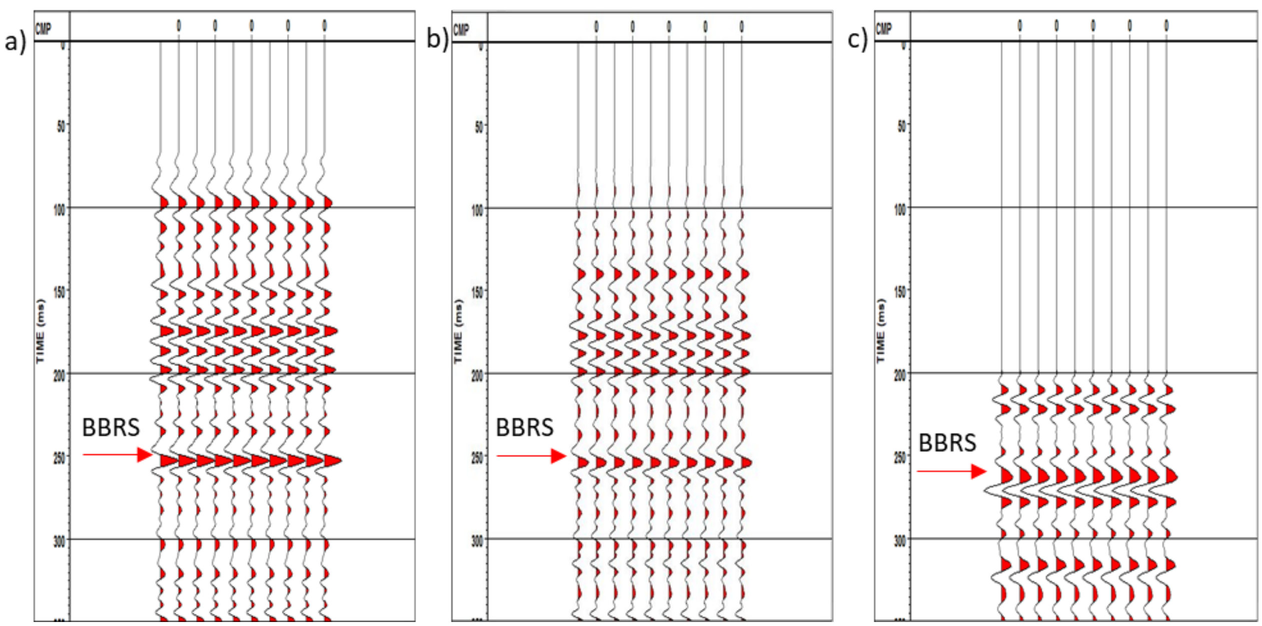

Figure 4.36 Outside corridor stack of VP 139 with AGC. a) Straight DAS, b) HWC DAS, c) geophones. The CO_2 injection target the Basal Belly River Sandstone (BBRS) is shown with the red arrow.

To complete the assessment of the zero offset VSP processing, the wireline logs of the Observation Well 2 were utilized to generate a synthetic seismogram in Hampson & Russell software. First, a statistical wavelet was extracted from the downgoing wavefield of a straight DAS zero offset VSP (Figure 4.37). The available wireline logs consisted of gamma-ray log and P-wave velocity that were logged from the surface to the bottom of the well at 350 m depth. These well logs were edited prior to their use by removing noisy points in the shallower section; in addition, a density log was computed using Gardner's equation. The extracted statistical wavelet and the edited P-wave velocity log and the computed density log were the inputs for the synthetic seismogram generation. Figure 4.38 displays the Observation Well 2 wireline logs: the gamma-ray log is shown in red, the P-wave velocity is shown in blue and the computed density log is shown in green and the formation tops are shown with black lines across the well log section. The obtained synthetic seismogram is also shown in Figure 4.38 next to the wireline logs.

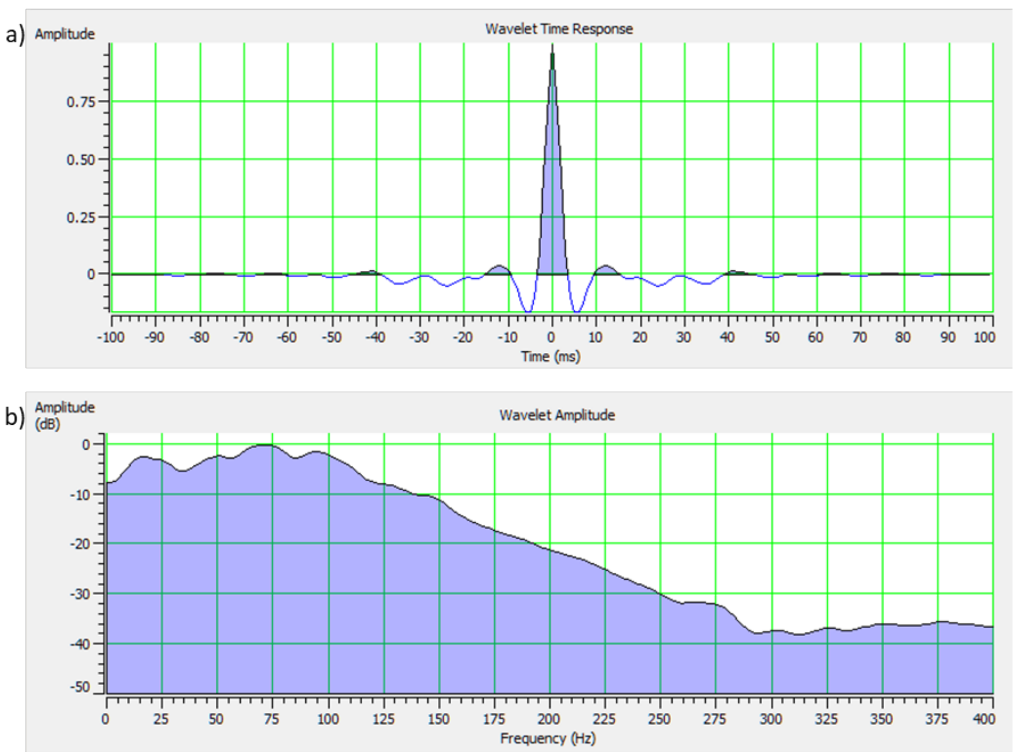

Figure 4.37 Statistical wavelet (a) and the amplitude spectrum (b) extracted from downgoing wavefield of straight DAS, VP132.

The synthetic seismogram was then compared to the obtained corridor stacks and Figure 4.39 displays the tie between the corridor stacks of VP 132 and the synthetic seismogram shown in blue. A good match is noticeable between the straight DAS and HWC DAS corridor stacks with the synthetic seismogram. Most of the events in the seismogram correlate with the events in the corridor stacks. However, there are some small differences in amplitude and slight time shifts. On the other hand, when comparing the geophone corridor stack with the synthetic seismogram, the time shift previously mentioned is also noticeable. A recommendation for future analysis is to generate synthetic seismograms with the wireline logs of the Injection well as the well logs range is from 200 m to 500 m depth.

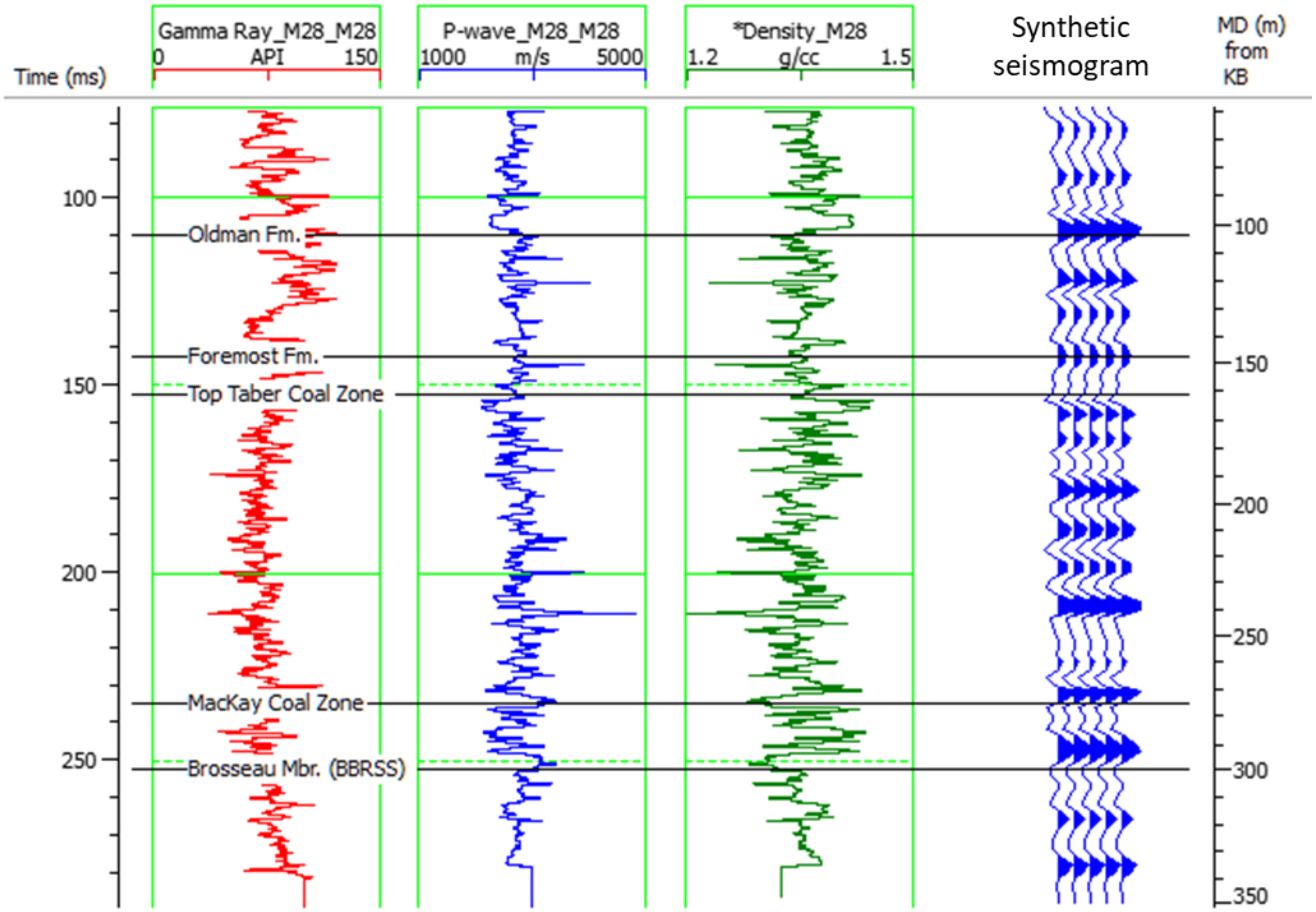

Figure 4.38 Wireline logs of the Observation Well 2 and synthetic seismogram. From left to right: gamma-ray log (red), P-wave velocity (blue), computed density log (green), tops are shown with black lines and the synthetic seismogram is shown in blue.

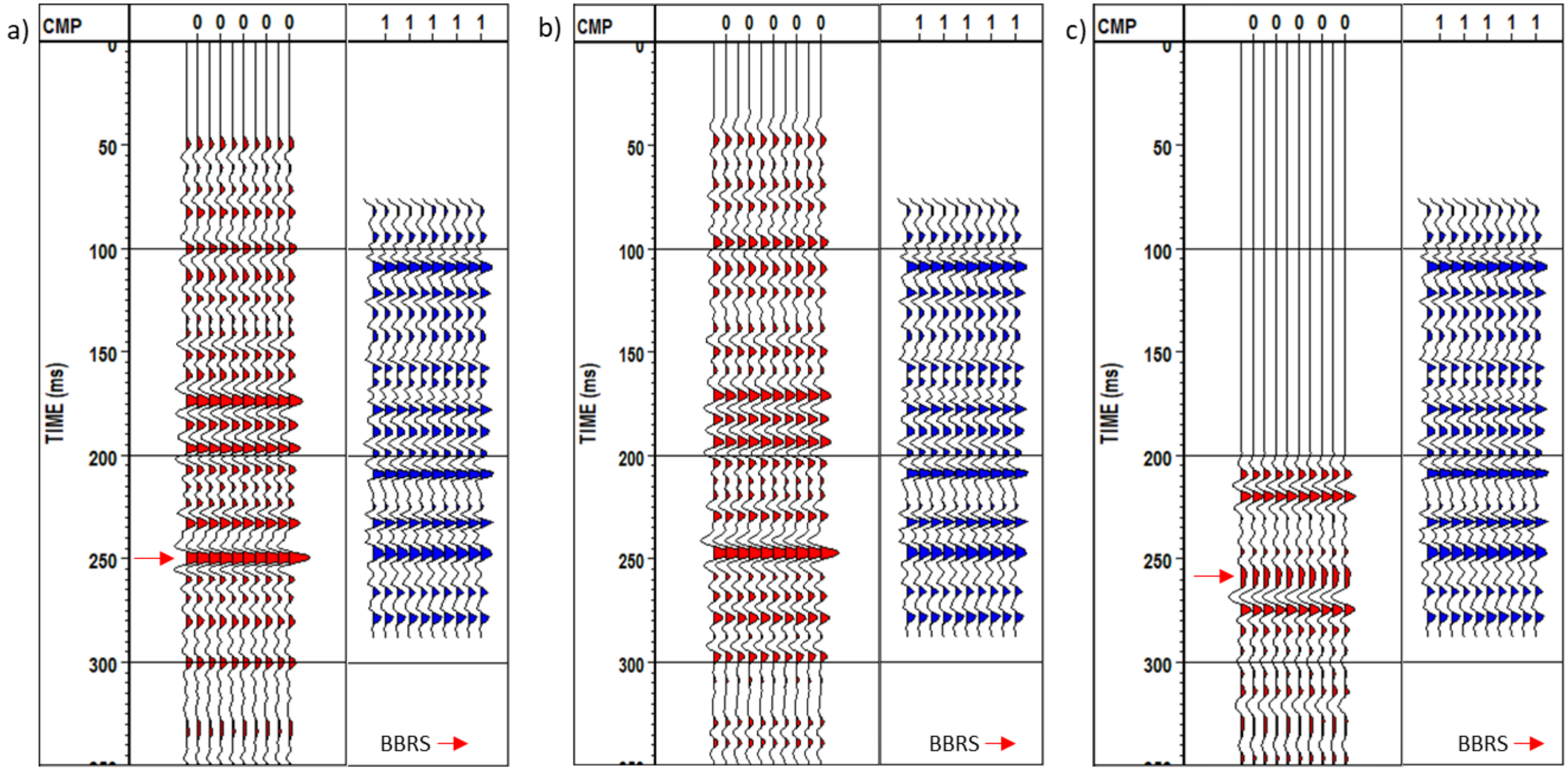

Figure 4.39 Outside corridor stacks of VP 132 with AGC applied and the synthetic seismogram shown in blue: a) Straight DAS, b) HWC DAS with +3dB, c) Geophone array. The CO_2 injection target the Basal Belly River Sandstone (BBRS) is shown with the red arrow.

4.4 Conclusions

Three zero offset VSP source points selected from the May and July 2017 VSP acquisition campaign at the FRS were processed. These surveys were acquired with two recording systems; a borehole geophone array and DAS, both deployed in the Observation Well 2. DAS datasets were calibrated with the geophone array to identify the corresponding depth of each DAS channel. There was an accurate result between the cross-correlation of the first and last geophone trace, a maximum difference of 4.75 m was calculated from two different calibration methods for VP 132. Whereas for VP 159 and VP 139, a maximum difference of 4.14 m and 13.8 m was obtained. After following a standard processing workflow, a good correlation was obtained between the corridor stack of the straight DAS, HWC DAS and geophone datasets for each VP. The CO_2 injection target is noticeable in every corridor stack obtained. Nevertheless, a time difference of approximately 10 ms is noticeable between DAS and geophone corridor stacks. The cause of the time shift is still under investigation and some possible causes are the difference in the measurements recorded by the geophones and DAS or a time delay during the acquisition of the survey. Some attempts to convert DAS signal into a geophone response were tested by integrating DAS data with respect to time. The depth registration step was applied to the integrated DAS and the results were similar to the raw DAS results. Chapter 5 includes the processing results of the integrated DAS walk away VSP.

Chapter Five: **Walk away VSP processing of DAS and geophone data**

In this chapter, we describe the processing of walk away Vertical Seismic Profile data (VSP) acquired with Distributed Acoustic Sensing (DAS) and borehole geophones in the geophysics Observation Well. The survey was acquired in July 2017 using two recording systems; straight and helical wound fibre (HWC) for DAS and a 3C 24-level geophone array. Each step of the workflow is described in the following sections including a comparison between the straight and helical fibre optic cables and the geophone array. Additionally, the processing of integrated DAS datasets was undertaken with the attempt to resemble the geophone response. Lastly, the results of the processed VSP data were compared to seismic sections of the 3D surface seismic survey that was acquired at the FRS in 2014.

5.1 Data set and processing flow

A north-south profile line was selected for processing among the different walk away VSP surveys acquired in 2017 since it has a consistent number of vibroseis sweeps per source point (6 in this case), which we will refer to as vertical fold. Figure 5.1 shows the geometry of the line, where source points (VPs) are marked with red dots and the wells are marked with black dots. The source points numbering increases from south to north, and the spacing between points varies from 10 m to 30 m, note that these offset variations or gaps in the line are associated with infrastructure present in the field. The blue circles represent the seventeen source points selected for processing. This selection was based on the quality of the raw source gathers, where the farthest offsets had a weaker response, especially for DAS datasets. In addition, the selected VPs are distributed in an equivalent number of points from each side of the well for consistency. Observation well 2 is highlighted in orange and the offset range of the selected VPs goes from 9 m to 220 m approximately increasing from the wellhead towards the sides of the walk away line.

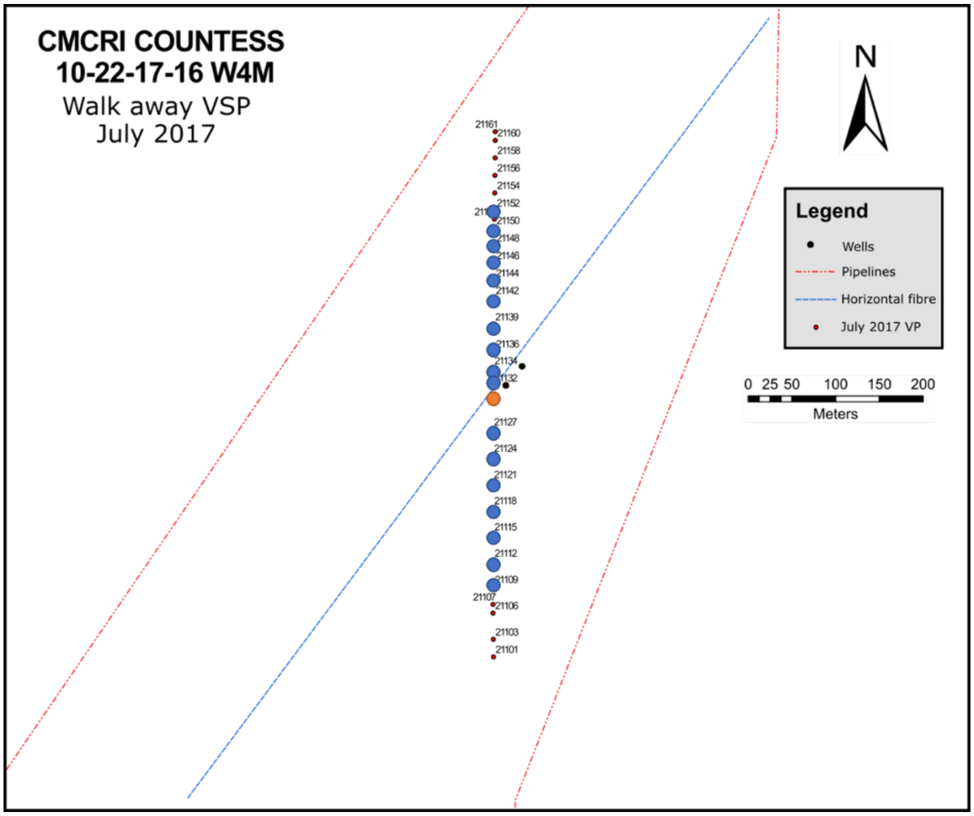

Figure 5.1 Geometry survey of walk away VSP. Source points in red and wells marked with black. Red dashed lines indicate pipelines and the blue line indicate the horizontal trench with fibre optic cables. The source points selected for discussion are marked in blue circles and Observation Well 2 is shown in orange.

The seismic source used for the acquisition was an IVI EnviroVibe with a linear sweep from 10 to 150 Hz over 16 s with 3 s of listening time. The recording systems comprised optical fibres with a nominal gauge length of 10 m and output trace spacing of 0.25 m, and a 24-level 3-component (3C) geophone array covering at depths from 191.24 to 306.24 m with a 5 m spacing. Figure 5.2 displays a schematic of the optical fibre loop deployed at the FRS and highlighting Observation Well 2 equipment.

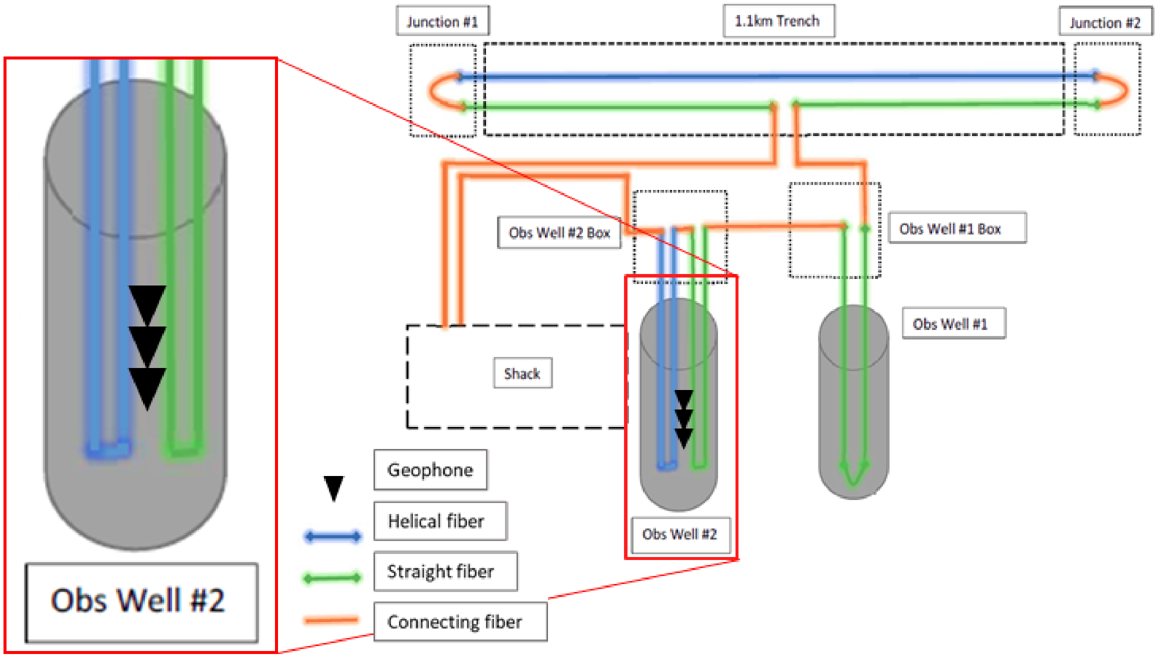

Figure 5.2. Schematic of the fibre optic cables installed at the FRS. Our focus is on Observation Well 2 highlighted with a red rectangle (modified from Lawton et al. 2017).

A standard processing flow that was applied to the datasets is displayed in Figure 5.3; it consisted of geometry and first break picking, depth registration of DAS traces relative to the geophones, wavefield separation through median filters and F-K filters for DAS datasets. A deconvolution operator was designed from the downgoing wavefield and applied to the upgoing wavefield, followed by VSP-CDP transform and stacking.

For the multicomponent geophone dataset, additional steps were performed prior to the wavefield separation. The horizontal components (H1 and H2) were rotated to obtain the radial and transverse components. During the rotation of the horizontal components, the estimation of the direction of H1 and H2 was completed following a similar approach described in Chapter 3 with the walk around VSP. In this chapter, we show the processing results for both the vertical component and the rotated data.

In the following sections, we discuss and compare the straight and HWC DAS datasets with the geophone dataset on each step of the processing flow. The same procedure was performed to the integrated DAS datasets with the attempt to obtain a more consistent comparison. As mentioned in previous chapters, the output measurement of the interrogator used in this survey is strain rate. Therefore, we applied Daley et al. (2016) approach to convert strain rate to strain by integrating DAS data with respect to time.

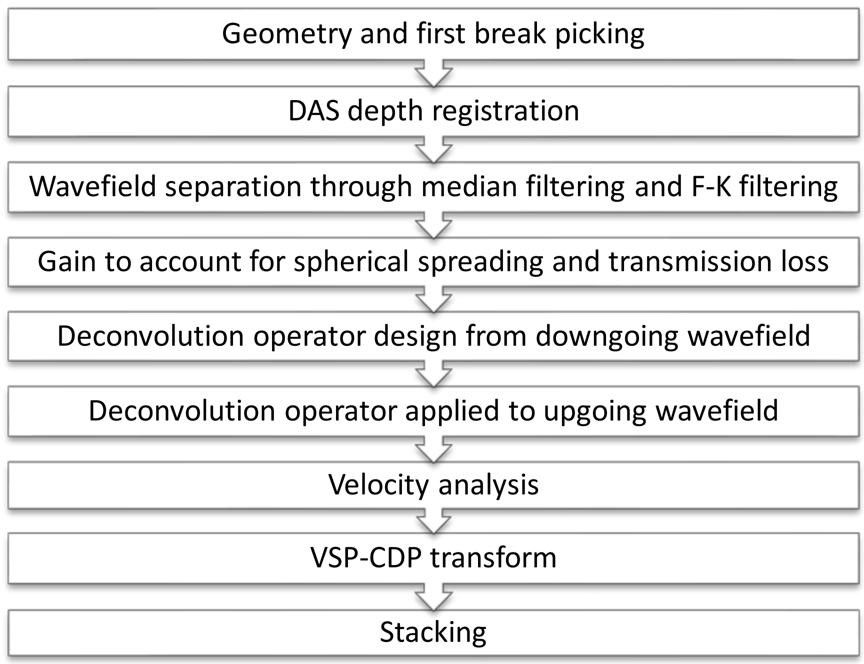

Figure 5.3 Generalized walk away VSP processing flow.

The results of the processing steps per dataset are presented in the following order: raw DAS, integrated DAS, vertical component geophone and rotated geophone data.

As an example, Figure 5.4 shows raw DAS datasets, straight fibre (a) and HWC (b) with respect to the geophone vertical component (c), with Automatic Gain Control (AGC) applied (250 ms window). In general, there is a good identification of downgoing and upgoing waves in each dataset. As the offset increases, the time difference of the first arrivals as well as the arrival of head or turning waves is noticeable in DAS datasets thanks to the full coverage of the fibre in the well. Additionally, the HWC data seems to have a lower signal to noise ratio (S/N) than the straight DAS.

Signal to noise ratio is a commonly used approach to measure the level of desired energy or signal versus undesired (noise) or total energy. It is mathematically defined as the division of the energy of the signal over remaining energy (noise) or S/N. It is also defined as the signal divided by the total energy such as S/(S+N) (Schlumberger, 2019a; Sheriff, 2002). Accurate quantification of the ratio is known to be challenging to obtain because of the difficulty in separating the signal from the noise. In this case, since we are dealing with two different types of measurements, for DAS and geophones, it is important to perform a proper estimation for each dataset.

For DAS datasets, a signal and noise window were selected for each raw source gather. The noise window selected consisted of the section before the first arrival whereas the window for the signal consisted of a rectangle starting at the first arrivals increasing in time. In order to obtain a rectangular shape for each window, the gathers were firstly flattened and then separated. Figure 5.5(a) and 5.5(b) show as an example the windows selected for source point 121. Then, the signal to noise ratio per VP was obtained by dividing the root mean square (RMS) of the signal by the RMS of the noise. Figure 5.5(c) shows the S/N obtained for straight DAS and HWC DAS as a function of offset, highlighting the difference between both datasets. Notice how the S/N is generally higher for source points closer to the well between VPs 127-134 in both cases. Another remark is the decrease of the S/N as the offset increases and even more interesting is the lack of symmetry in the decay from each side of the well. The S/N ratio seems to decrease at a higher rate on the northern section of the line (VPs 132-151) for both the straight and HWC datasets. For the geophones, a similar approach was performed, in this case also comparing the vertical component with a horizontal component. Figure 5.6 displays source gather of VP 121 (a), the flattened gather with the signal and noise windows selected (b) and the S/N obtained for both components in blue and green respectively (c). In this case, the S/N variations observed in both components seem to follow a similar trend along the northern part of the line, whereas the southern section shows more fluctuations in the horizontal component.

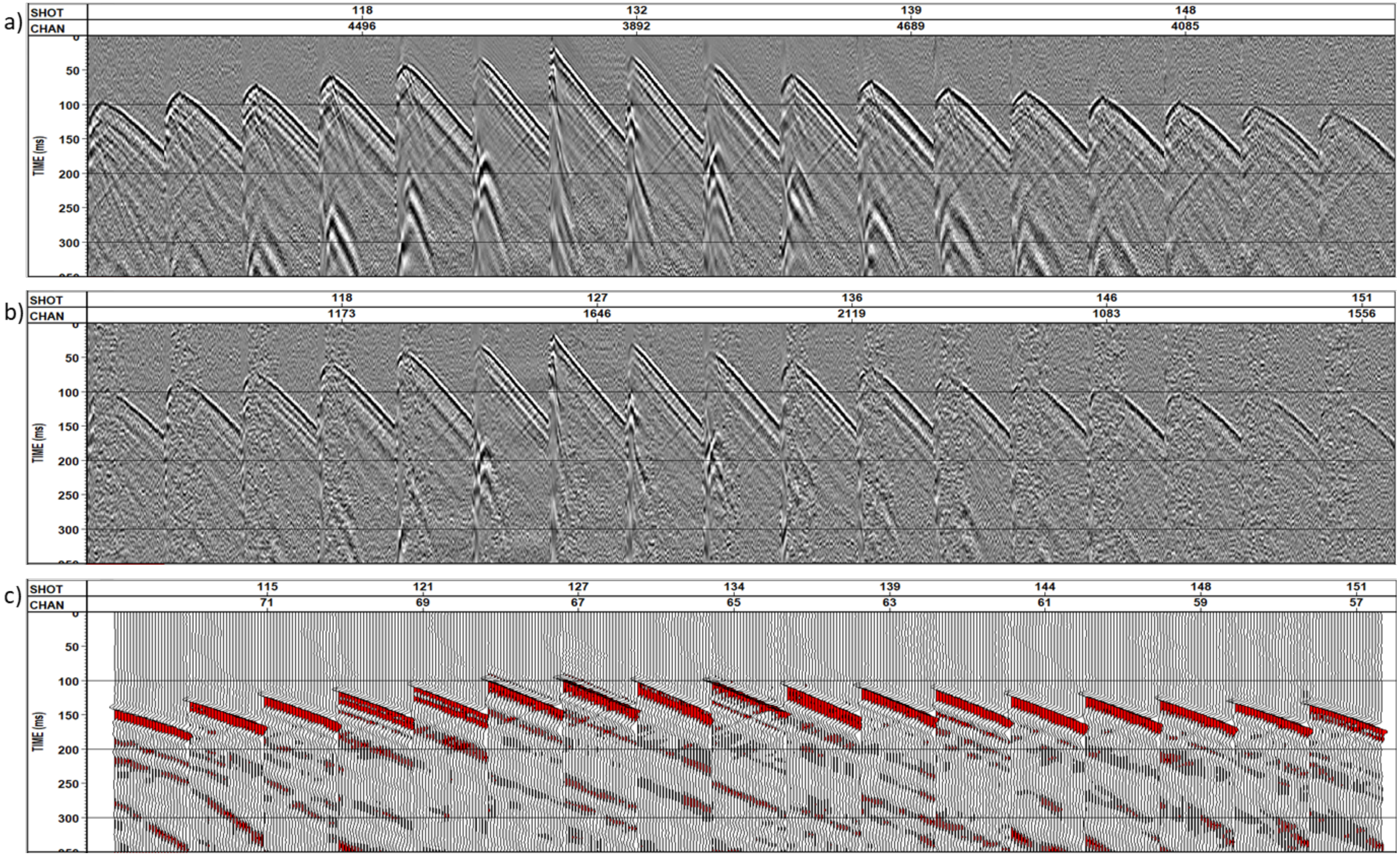

Figure 5.4 Raw DAS and geophone source gathers of walk away VSP, with AGC applied: a) straight DAS, b) HWC and c) geophone vertical component.

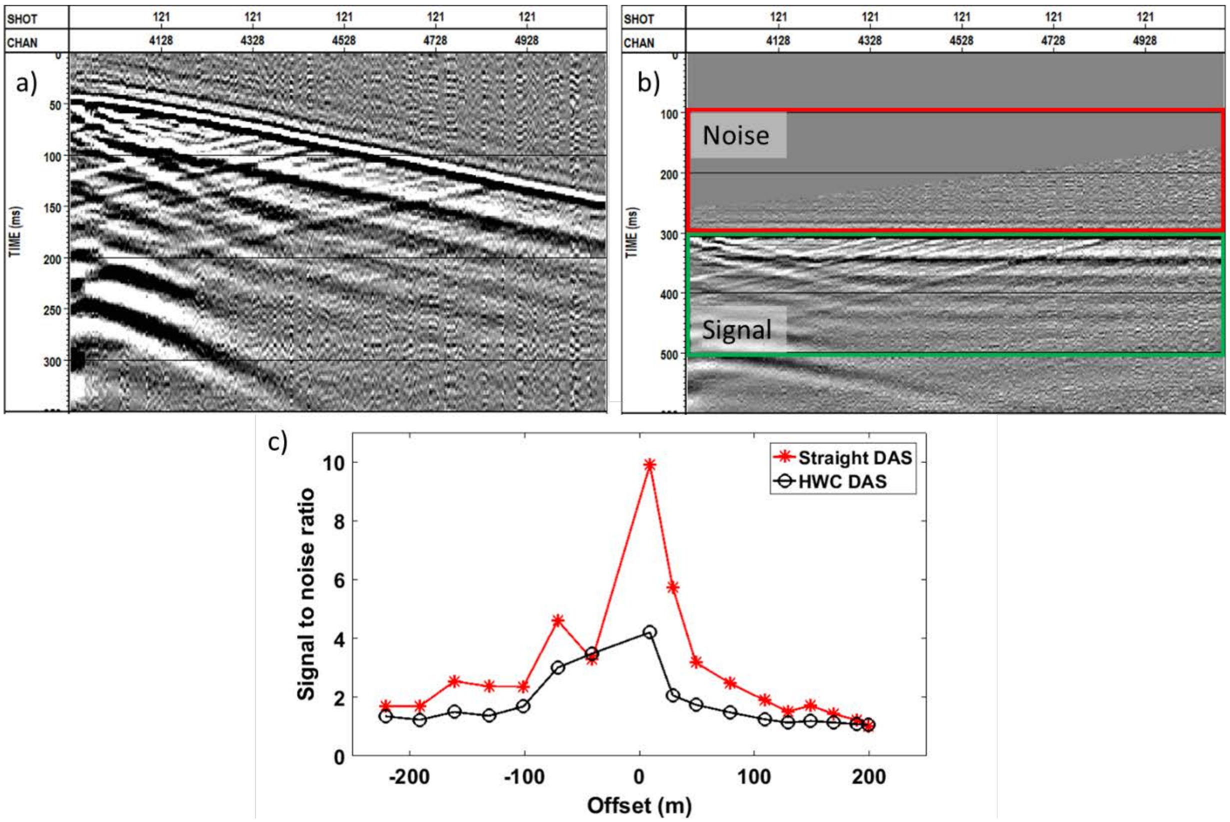

Figure 5.5 Signal to noise estimation of DAS datasets: a) straight DAS source gather with AGC applied, b) flattened source gather with AGC applied; the signal window is shown in green and noise window shown in red, c) S/N of straight DAS in red and HWC DAS in black.

Although, to properly compare the S/N of DAS and geophones, the depth interval and the number of traces per window should be similar. Figure 5.7 shows the S/N obtained after resampling DAS datasets every 5 m and selecting a window with the same depth interval (191.24 -306.24 m). Now we observe a correlation between DAS and geophone S/N. HWC DAS seems to have the lowest S/N while straight DAS shows a higher ratio for source points closer to the well. The geophones show a consistent behaviour per source point although the horizontal component shows a higher S/N in the southern part of the line. Note that for the S/N estimation, the raw components were used, and this variation could be related to traces with reversed polarity prior to the rotation of the components.

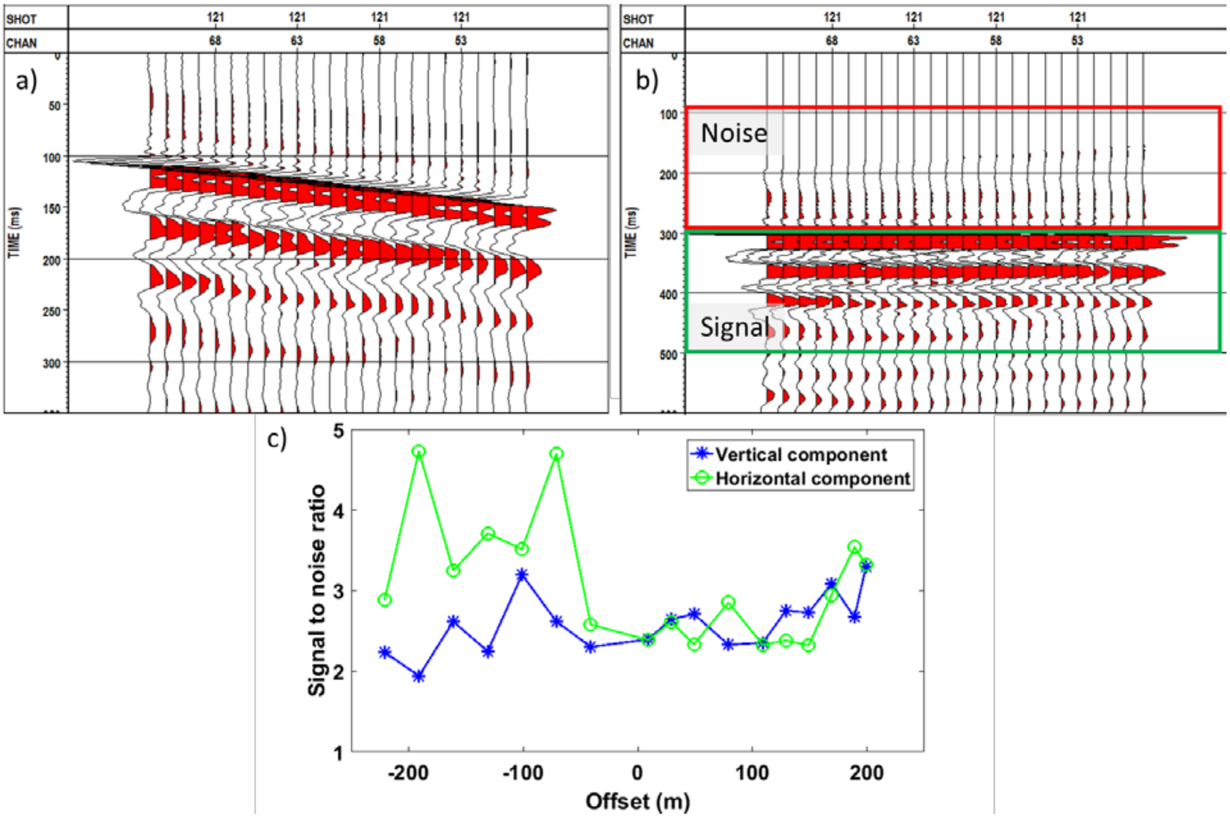

Figure 5.6 Signal to noise estimation of geophone dataset: a) vertical component source gather with AGC, b) flattened source gather with AGC; the signal window is shown in green and noise window shown in red, c) S/N of vertical component in red and a horizontal component in black.

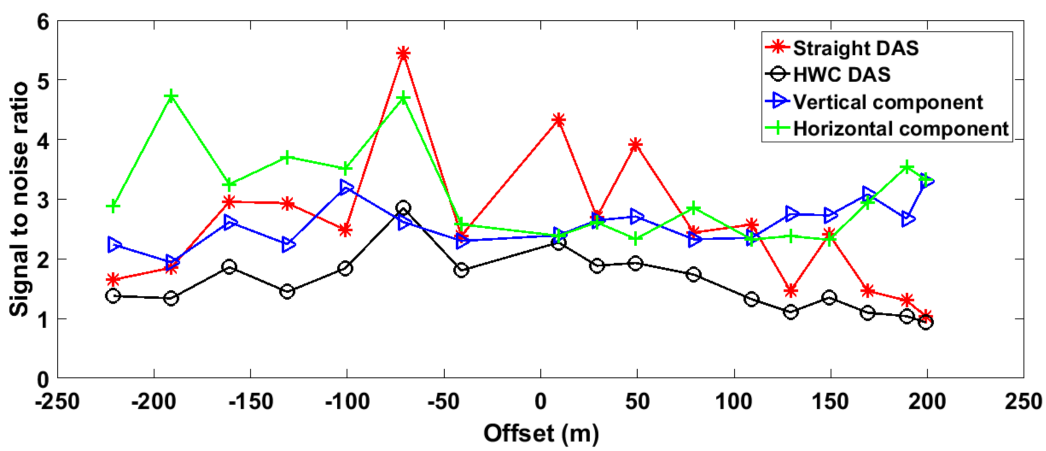

Figure 5.7 Signal to noise ratio estimation of DAS and geophone datasets at the same depth interval with a similar number of traces per window.

5.1.1 Geometry and first break picks

The first step of the processing flow was to upload the geometry of the survey, after which picking of the first arrivals was completed for each dataset. Figure 5.8 shows the first break picks in green (displayed with AGC). As described in Chapter 4, the calculation of the interval velocities of a zero offset VP was performed by applying a mean function to DAS datasets every 60 and 65 traces for the straight and HWC DAS respectively (Figure 4.11). The obtained interval velocity profiles are used for the VSP-CDP transform.

Knowing that one of the limitations of DAS is the uncertainty of the exact location in depth of each trace (Mateeva et al., 2014), we performed a depth registration analysis similar to the one described in the previous chapter. For the straight fibre optic cable, the output trace spacing is 0.25 m and for a total depth of 330 m in the well, we would expect approximately 1320 traces per source gather. For the HWC, there is a higher uncertainty due to the fibre being helically wound on a mandrel. In this case, the trace with the latest first arrival time was identified at a zero offset gather and for a total depth of 330 m, and a trace spacing of 0.23m is obtained. Then, the corresponding depth of the DAS traces was updated before continuing with the workflow.

The geophone array has four dead traces that were removed and interpolated following the same method described in Chapter 4. Figure 5.8c shows the vertical component of the geophone dataset set after the interpolation. Figure 5.9 shows the first break picks of the integrated DAS. An interesting observation is the change of the first break picks after integration of the DAS data shifting from a peak to zero crossing. This variation occurs when a wavelet is integrated, a phase shift of 90° is observed. The first break picks of the integrated DAS were re-picked as a peak to maintain the consistency throughout the process.

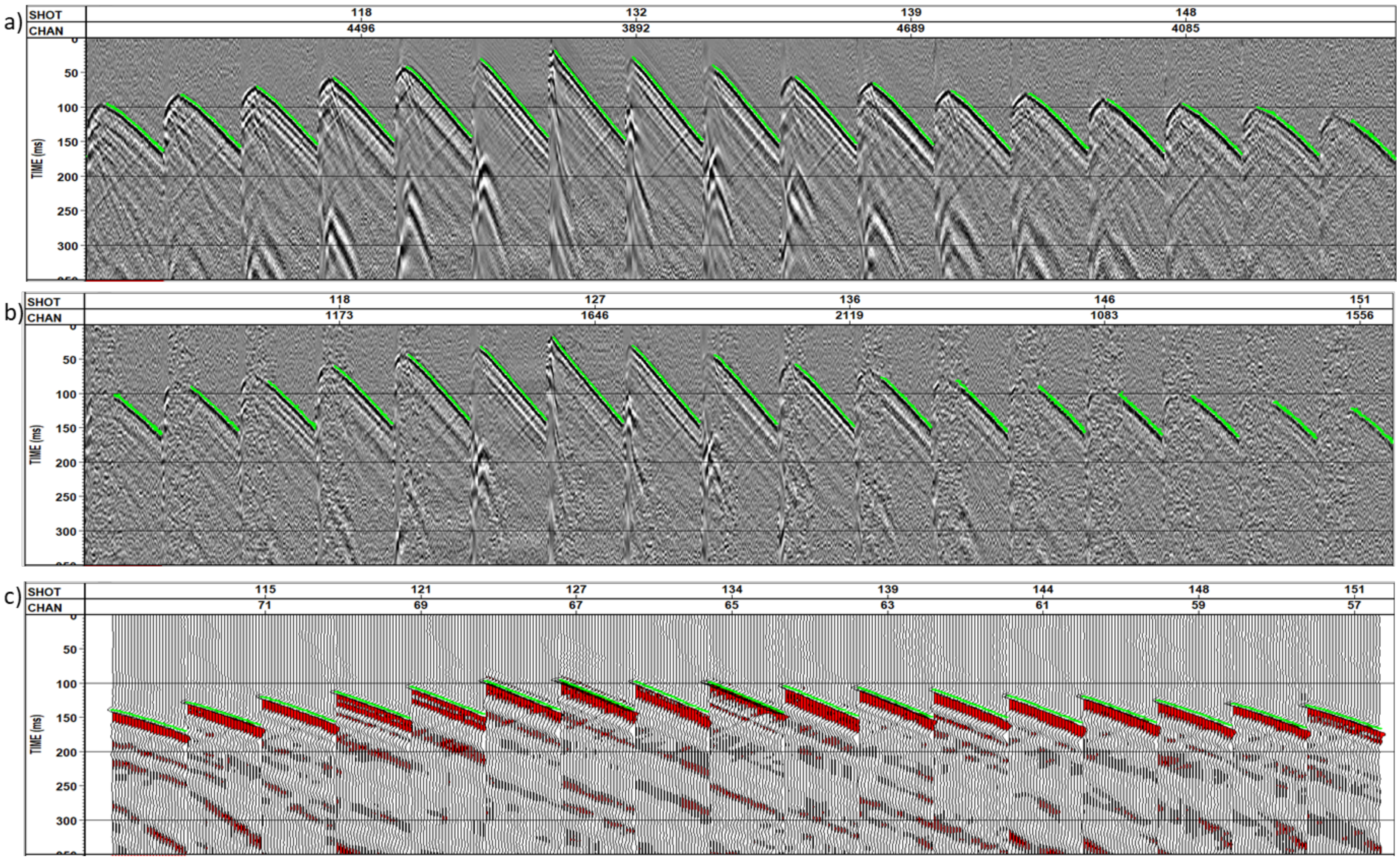

Figure 5.8. First break times shown in green with AGC applied: a) straight DAS, b) HWC DAS and c) geophone vertical component.

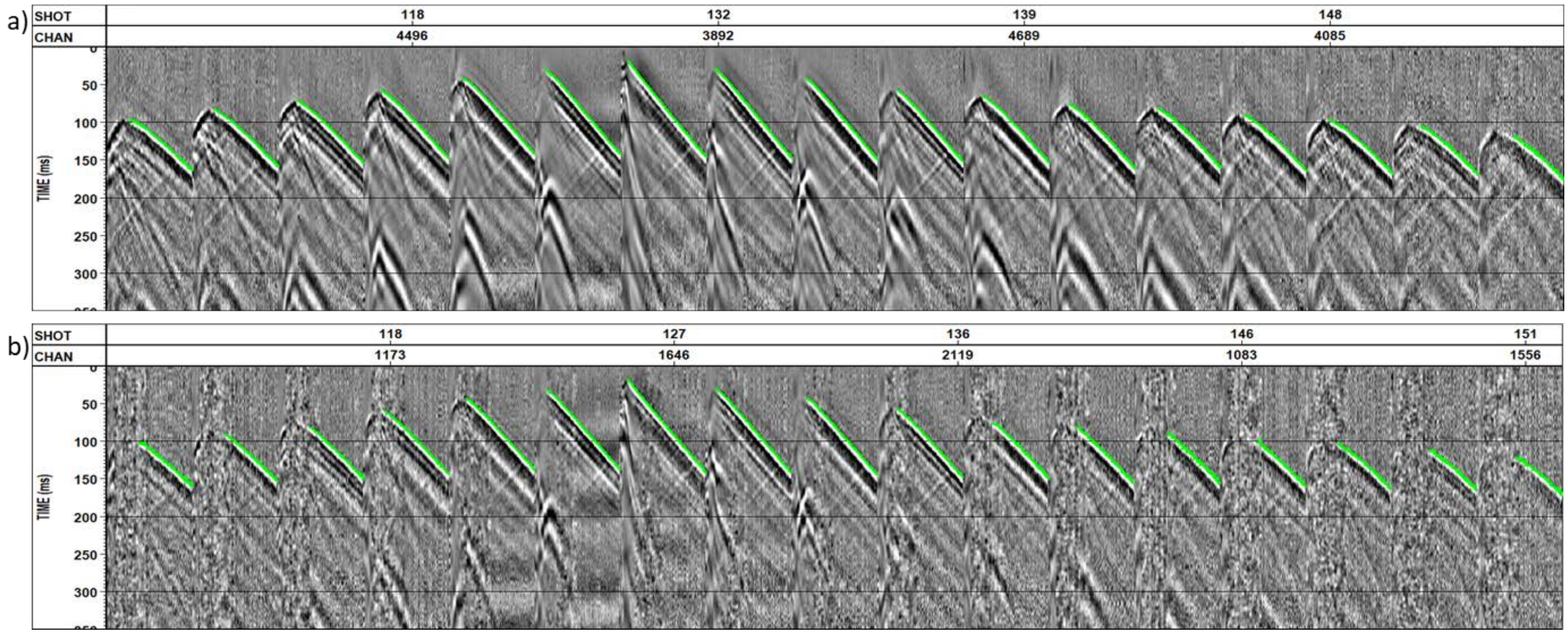

Figure 5.9. First break times of integrated DAS shown in green with AGC applied: a) straight DAS, b) HWC DAS.

5.1.2 Wavefield separation

A median filter was used to separate the downgoing and upgoing wavefields. Several tests were performed to identify the right length of the median filter for each dataset. For both the straight DAS and HWC DAS, a median filter of 91 points corresponding to 22.75 m and 20.93 m length was selected. Even though the straight and HWC DAS have different output trace spacing and number of traces per gather, a median filter with a higher or lower number of samples did not seem to have a significant impact in the wavefield separation of the HWC DAS, therefore we decided to use the same number of samples for both DAS datasets. For the geophone dataset, a median filter of 5 points, equivalent to 25 m length was selected. Note that these values vary significantly due to the difference in the number of traces and trace spacing of each dataset. In both cases, a good separation of the downgoing and upgoing waves was achieved. Nevertheless, the DAS data still had some downgoing events remaining in the upgoing wavefield. Therefore, an F-K filter was also applied. Figures 5.11 to 5.16 show the downgoing and upgoing wavefield of the straight DAS, HWC DAS and geophone vertical component and rotated data, respectively.

Prior to the wavefield separation of the multicomponent geophone data, several steps were completed. The first step consisted of two data rotations through a hodogram analysis. The horizontal components (H1 and H2) were rotated to Hmax and Hmin where the Hmax is oriented in the well-source plane and Hmin is perpendicular (Hinds et al., 1996). The second rotation was applied to the vertical component (Z) and Hmax. The output Hmax' is oriented in the direction of the wavefront thus, is also known as radial component and contains downgoing events and upgoing SV events. The second output of the rotation, the transverse component (Z') contains upgoing events produced by the reflected waves. Following the geophone data rotation, a time-variant polarization was also performed since the hodogram analysis assumes a constant angle of incidence. With this polarization, we assume the rotation angle changes with time. We used a ray-tracing model and a velocity model from a zero offset VSP. After this last rotation, we obtained a more accurate wavefield separation from where upgoing P-waves and S-waves can be separated afterwards. In addition, we also estimated the orientation of H1 and H2 per geophone following a similar approach discussed in Chapter 3. The estimated azimuth of the components is equivalent to Theta', the difference angle between the azimuth of the VP and the rotation angle (Figure 3.20).

Note that the dead traces present in the geophone array were not taken into consideration for this estimation. Figure 5.10 shows an example of the Theta' angle obtained for 4 different vibe points (VP 146, VP 151, VP 115 and VP 109). There is a good correlation between each geophone level per VP, although, some of the geophone levels present some variations that could be associated with errors in the rotation angle during the hodogram analysis.

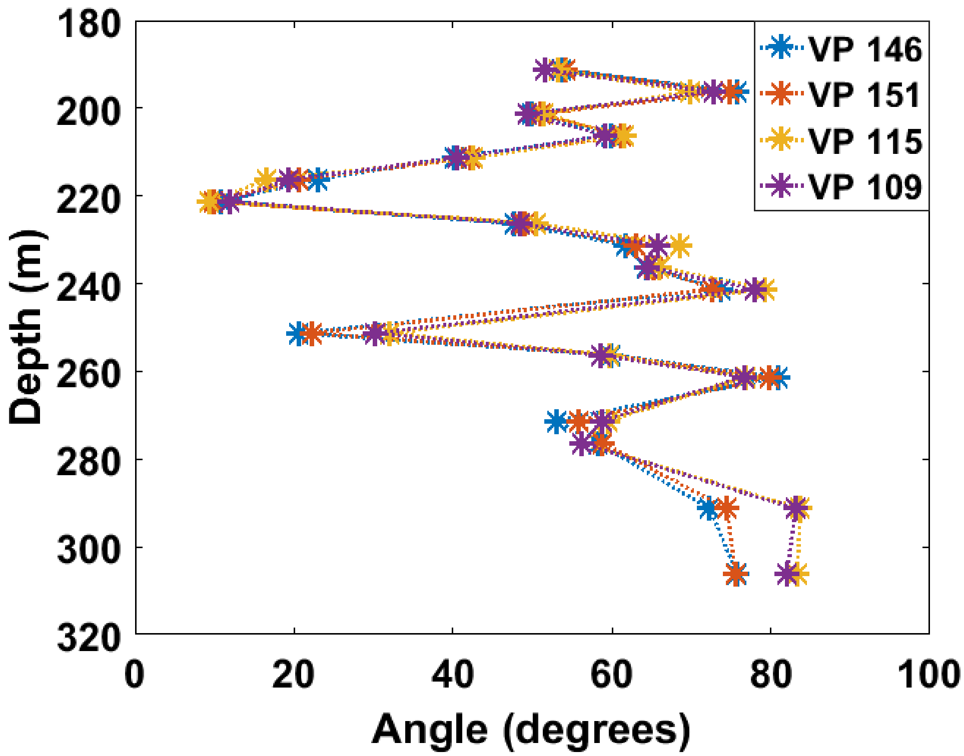

Figure 5.10 Estimated orientation of horizontal components for VPs 146,151,115 and 109.

After completing these steps of the processing, a good wavefield separation was obtained for each dataset. However, there are some upgoing events remaining in the DAS downgoing wavefields, especially for the farthest offsets of approximately 200 m from the well (Figures 5.11(a), 5.12(a), 5.13(a), 5.14(a)). Additionally, several downgoing S-wave events are also noticeable in both the straight and HWC that also seem to be more predominant as the offset increases. Overall, the upgoing wavefield has a good representation of the injection target, the Basal Belly River Sandstone (BBRS) with an approximate depth of 300 m (bright event in Figures 5.11(b), 5.12(b), 5.13(b), 5.14(b), 5.15(b) and 5.16(b)).

Raw DAS:

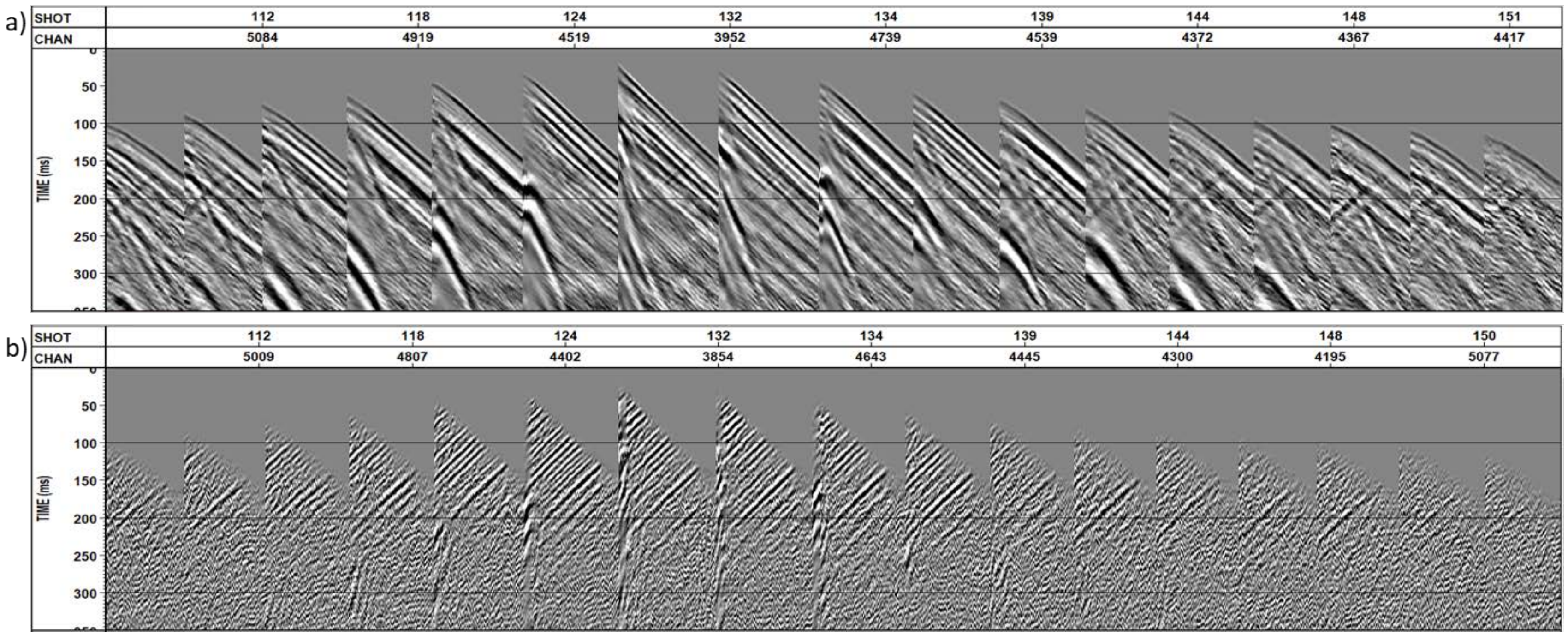

Figure 5.11. Wavefield separation of straight DAS with AGC applied: a) downgoing wavefield displayed with +3 dB, b) upgoing wavefield displayed with +6 dB.

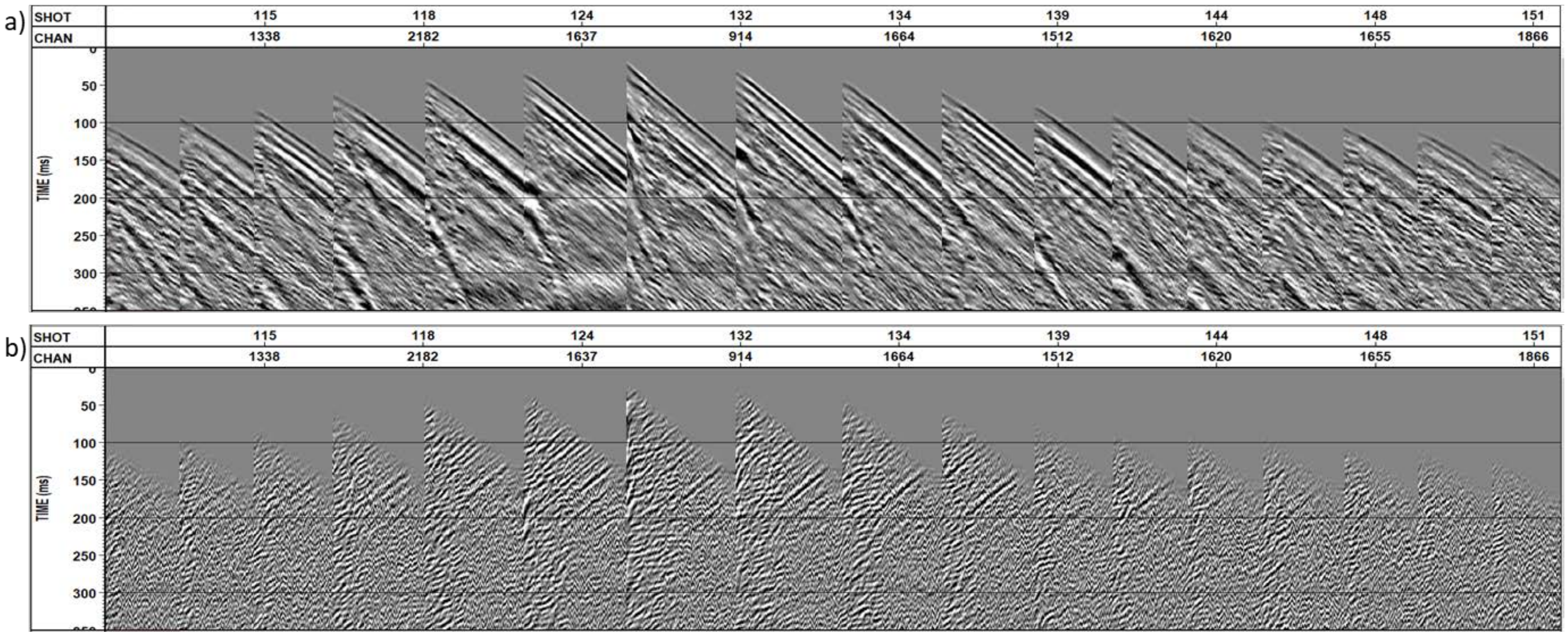

Figure 5.12. Wavefield separation of HWC DAS with AGC applied: a) downgoing wavefield displayed with +3 dB, b) upgoing wavefield displayed with +6 dB.

Integrated DAS:

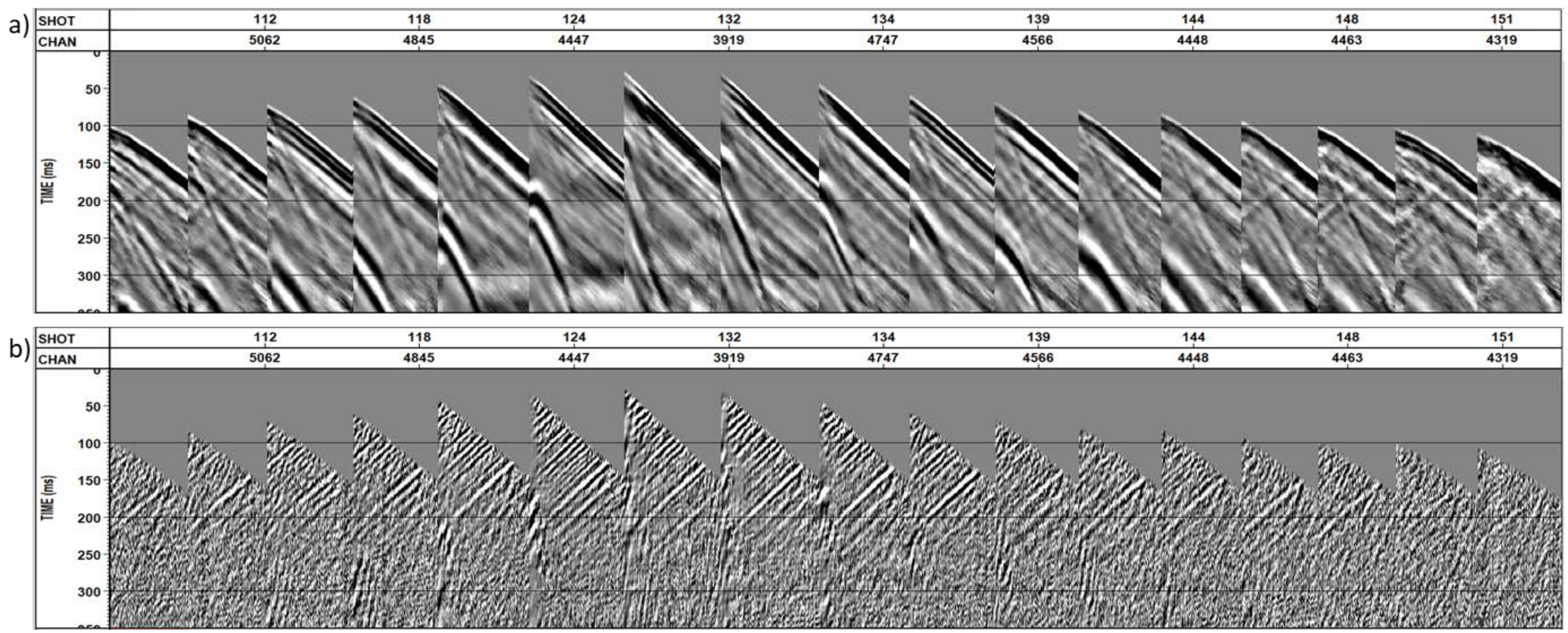

Figure 5.13. Wavefield separation of integrated straight DAS with AGC applied: a) downgoing wavefield displayed with +3 dB and b) upgoing wavefield displayed with +6 dB.

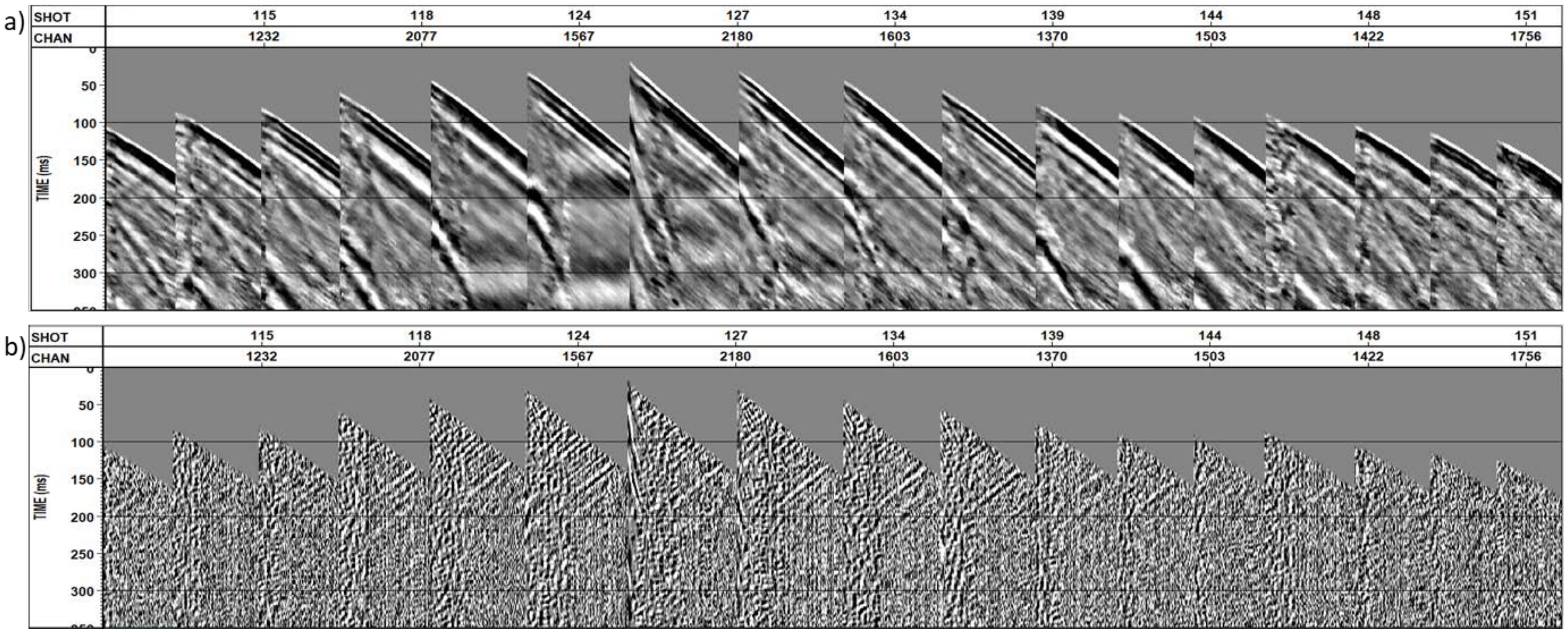

Figure 5.14. Wavefield separation of integrated HWC DAS with AGC applied: a) downgoing wavefield displayed with +3 dB and b) upgoing wavefield displayed with +9 dB.

Geophones:

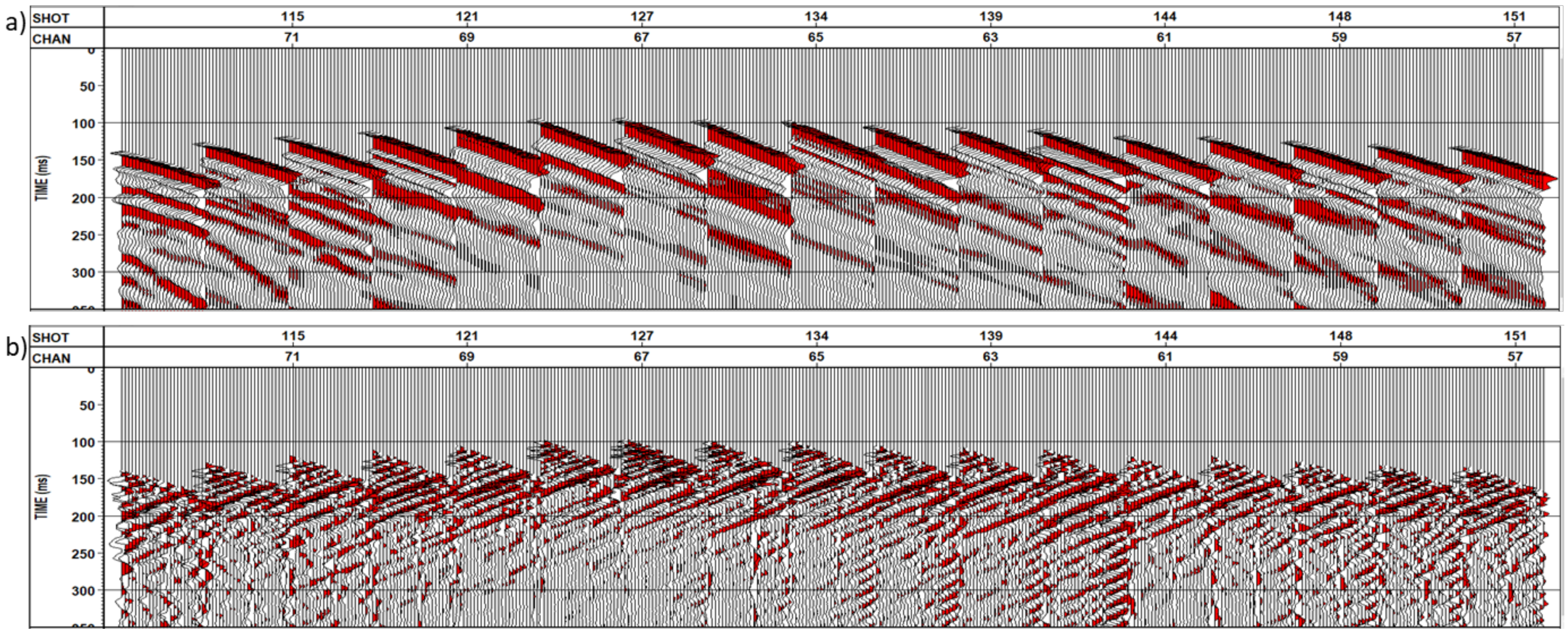

Figure 5.15. Wavefield separation of geophones (vertical component). a) downgoing wavefield displayed with -6 dB and b) upgoing wavefield displayed with -9dB.

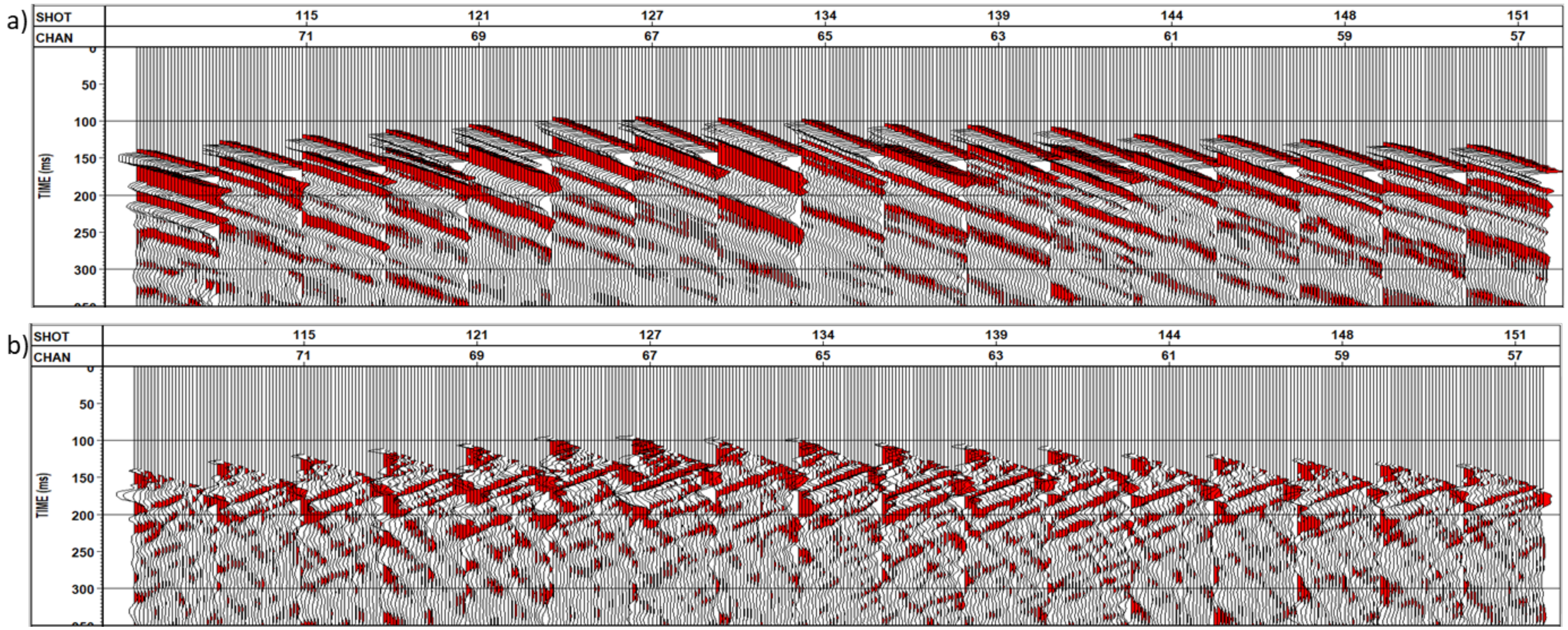

Figure 5.16. Wavefield separation of geophones (multicomponent data) with AGC applied: a) downgoing wavefield and b) upgoing wavefield.

5.1.3 Deconvolution

With the downgoing wavefield, a deconvolution operator was generated and then applied to the upgoing wavefield of each dataset with the attempt of attenuating any possible multiples present in the data as well as obtaining a better definition of the events. The process consists of flattening the downgoing wavefield, deconvolving the wavefield at a selected time window, then the same steps are applied to the upgoing wavefield. After several tests, the deconvolution window selected starts at 80 ms with a length of 300 ms. These parameters were selected since the data was flattened at 100 ms and the deconvolution window contains most of the energy and multiples present in the data. Additionally, a post-deconvolution bandpass filter was applied to remove part of the noise generated with the deconvolution process. Different frequency bands were tested and the filter with the best result consisted of: a low truncation frequency of 5 Hz, a low-cut frequency of 10 Hz, a high-cut frequency of 115 Hz and a high truncation frequency of 140 Hz. Figures 5.17-5.22, display the downgoing and upgoing wavefields after the deconvolution operator and the bandpass filter was applied, showing an improvement in the image in every dataset. The events seem sharper and continuous; however, the HWC DAS shows a weaker response compared to the straight DAS; this could be associated with the S/N difference of straight and HWC DAS.

Raw DAS:

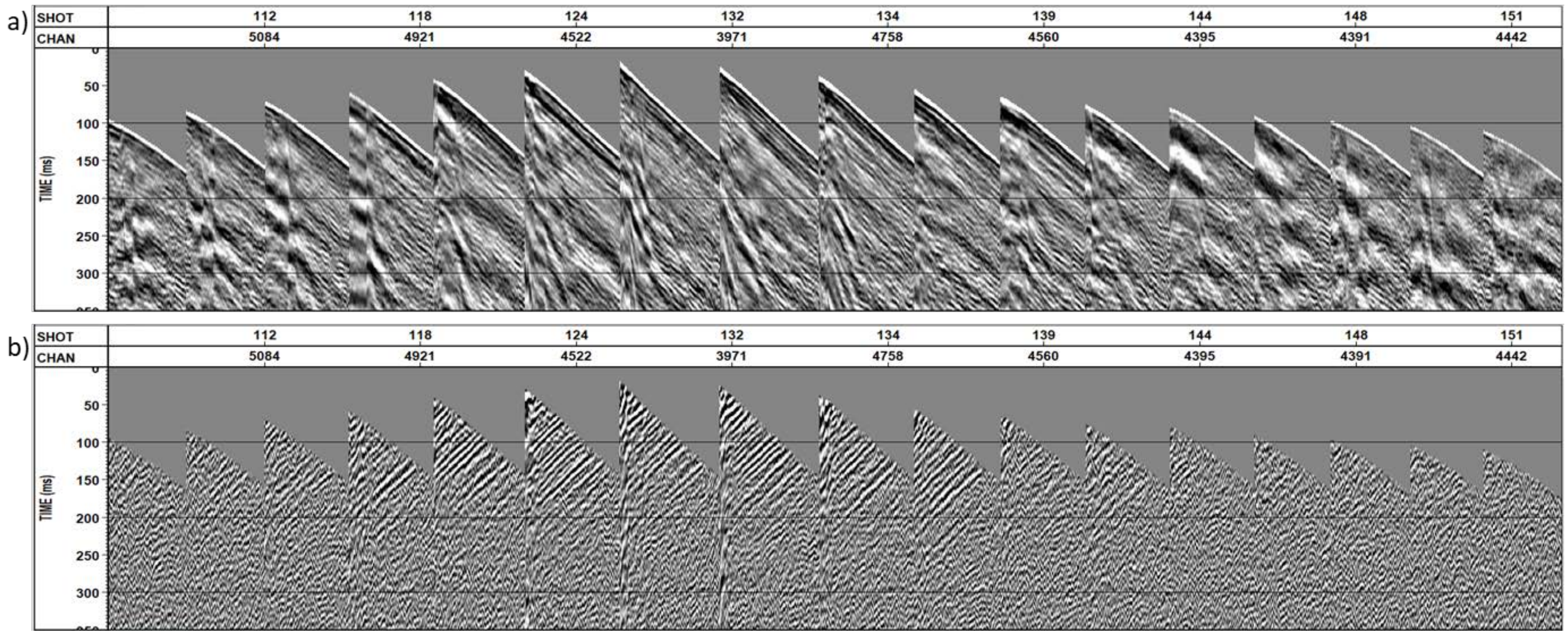

Figure 5.17. Raw straight DAS wavefields after deconvolution with AGC applied: a) downgoing wavefield with +3 dB and b) upgoing wavefield with +6 dB.

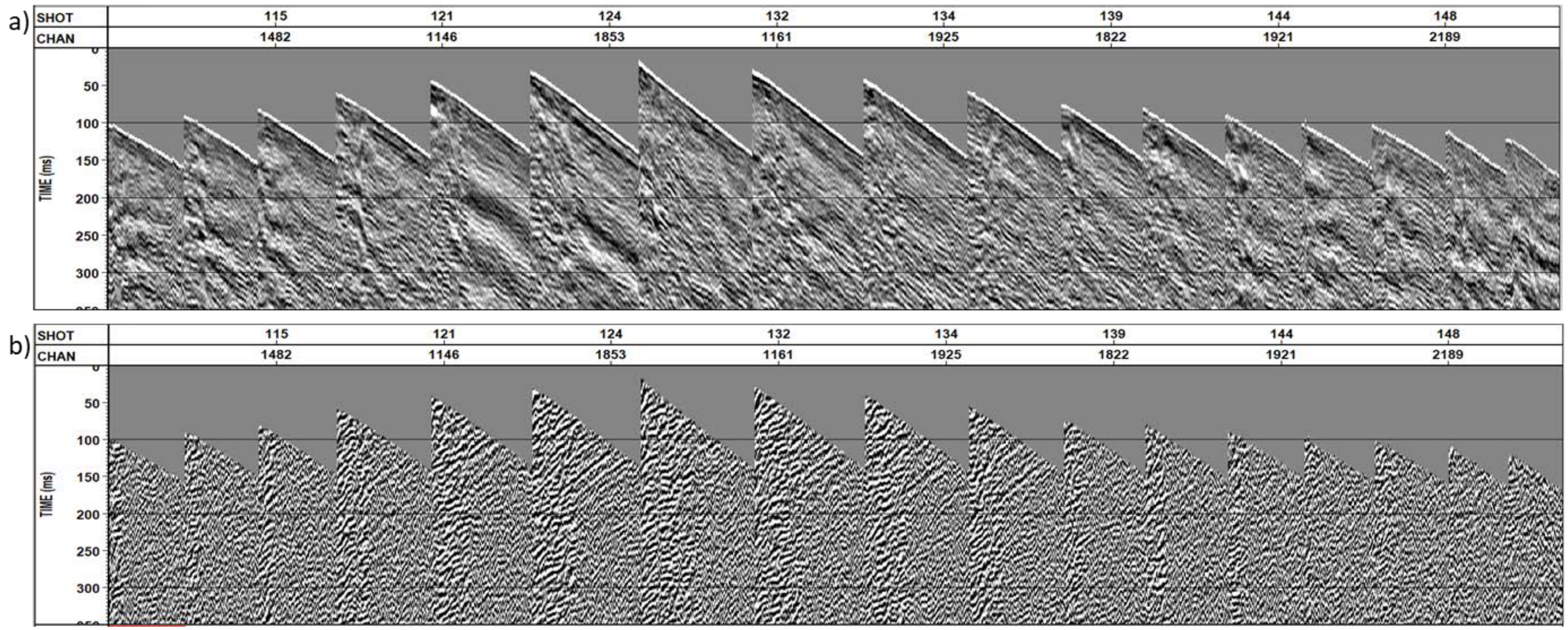

Figure 5.18. Raw HWC DAS wavefields after deconvolution with AGC applied: a) downgoing wavefield +3 dB and b) upgoing wavefield with +12 dB.

Integrated DAS:

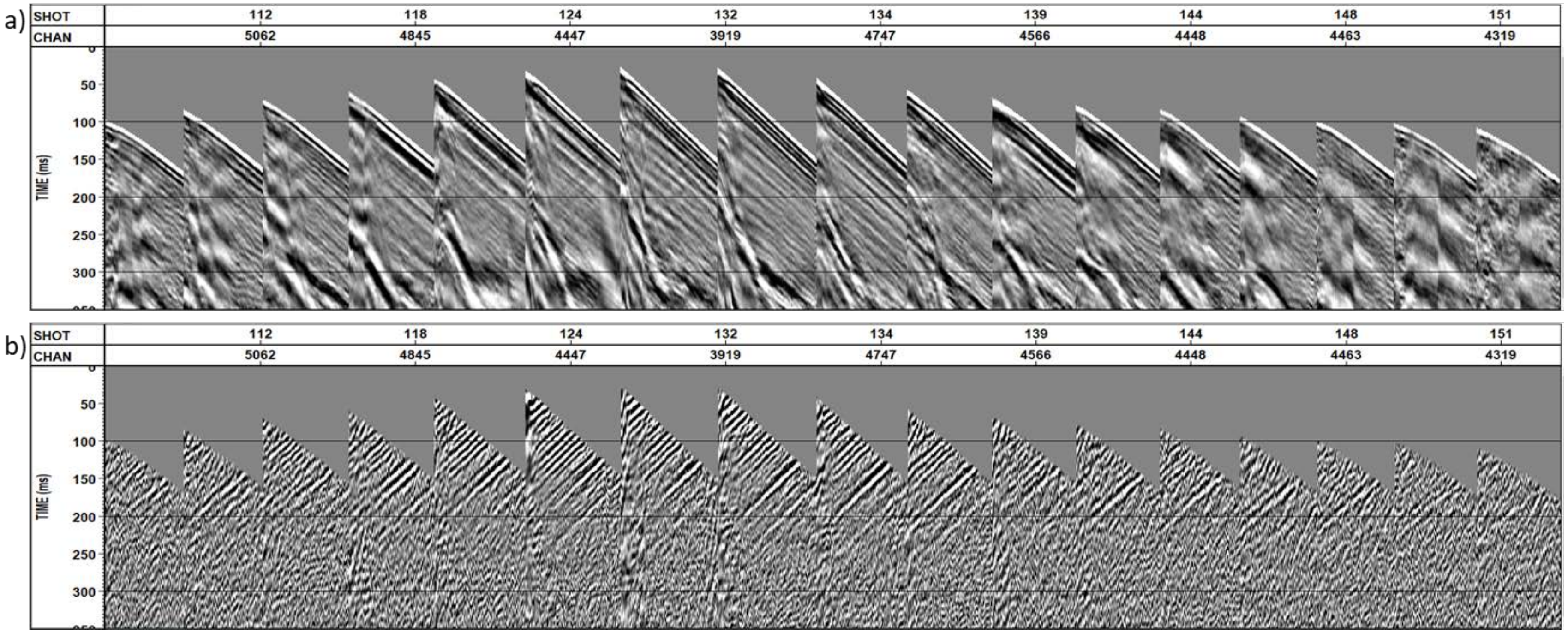

Figure 5.19. Integrated straight DAS wavefields after deconvolution with AGC applied: a) downgoing wavefield with +3 dB and b) upgoing wavefield with +6 dB.

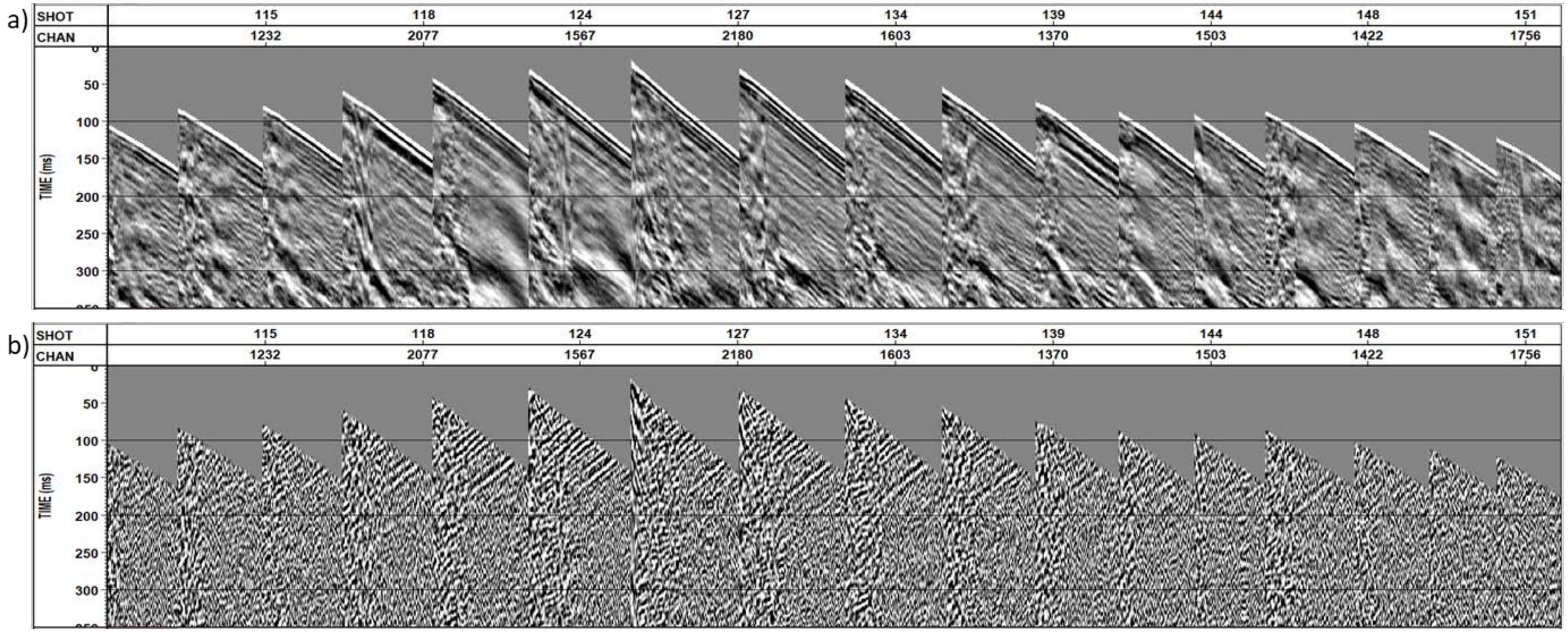

Figure 5.20. Integrated HWC DAS wavefields after deconvolution with AGC applied: a) downgoing wavefield with +3 dB and b) upgoing wavefield with +12 dB

Geophones:

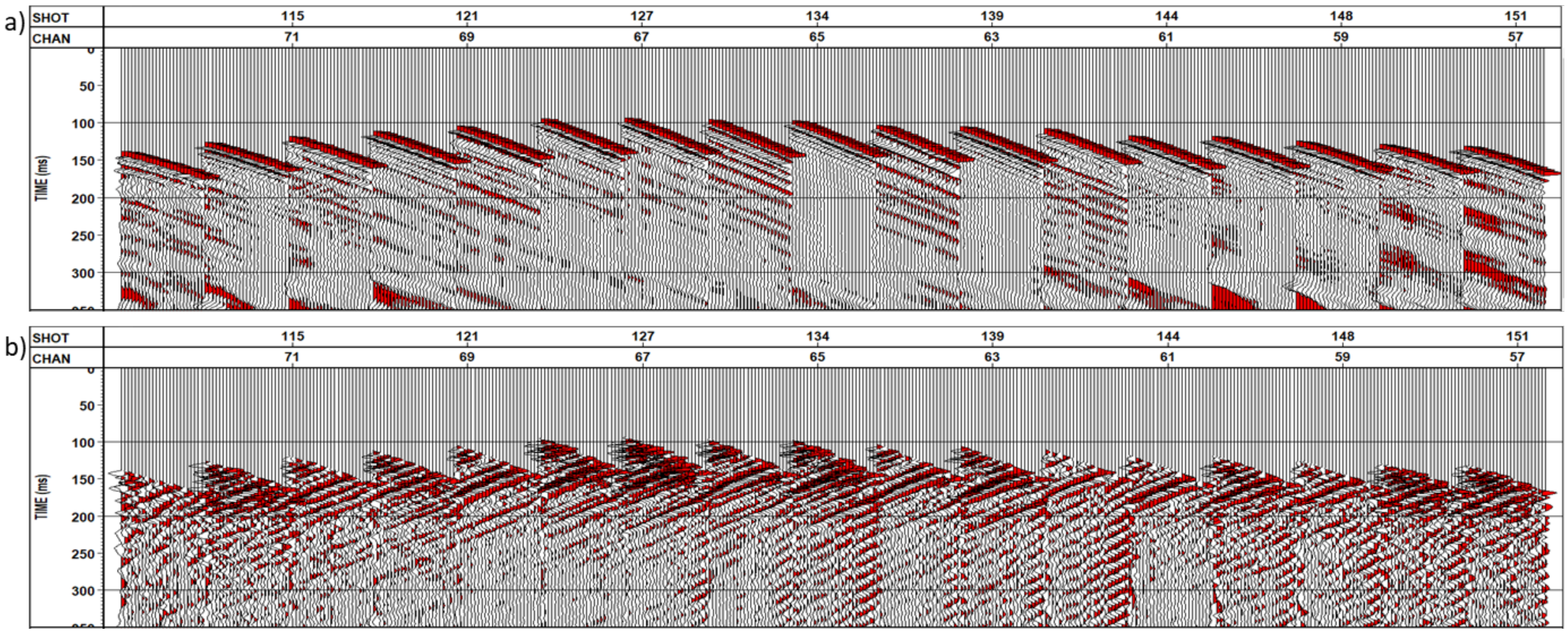

Figure 5.21. Geophone wavefields (vertical component) after deconvolution: a) downgoing wavefield with -6 dB and b) upgoing wavefield with -9 dB.

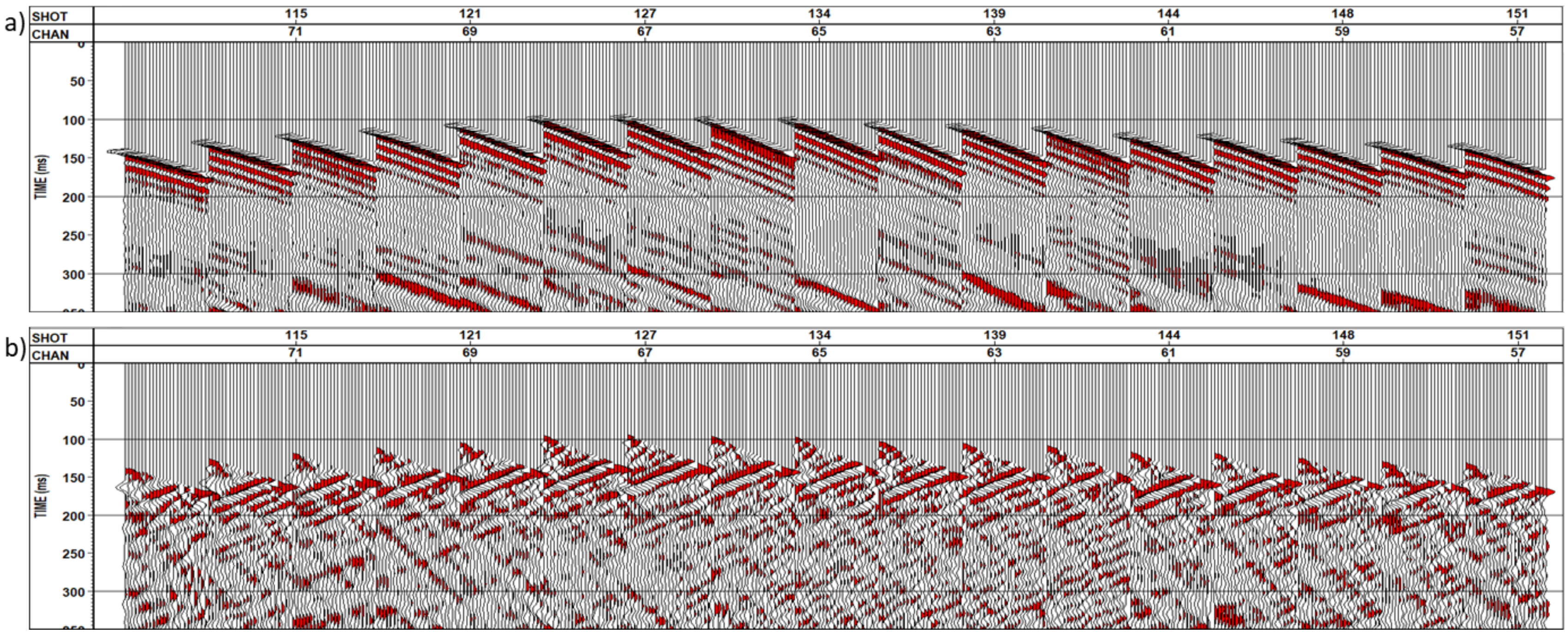

Figure 5.22. Geophone wavefields (multicomponent data) after deconvolution: a) downgoing wavefield with -6 dB and b) upgoing wavefield with -3 dB.

To further analyze the outcome of the deconvolution, a comparison of the amplitude spectra was performed. As an example, the source point 121 was selected for the comparison because it has an offset of 100 m from the well. The amplitude spectra of the upgoing wavefield of each dataset before and after deconvolution are shown in Figures 5.23- 5.28. Each figure shows the amplitude spectrum of an arbitrary trace in black and the average amplitude spectrum of the entire source gather wavefield in blue.

DAS datasets before deconvolution display a good frequency range, similar to the vibroseis sweep with a maximum frequency of 150 Hz. The amplitude of the raw DAS spectrums seems to increase with the frequency, whereas the amplitudes of the integrated DAS spectrums seem to decay with higher frequencies. The geophone datasets show a weaker frequency range, although the amplitudes are higher compared to DAS. Knowing that the geophone array is deployed in the zone of interest between 191.24 m to 306.24 m depth, while the fibre optic cables have full coverage in the wellbore. We also looked at the amplitude spectrums of DAS datasets at a similar depth window than the geophones and there are no evident changes compared to the entire amplitude spectrum per source gather.

Raw DAS:

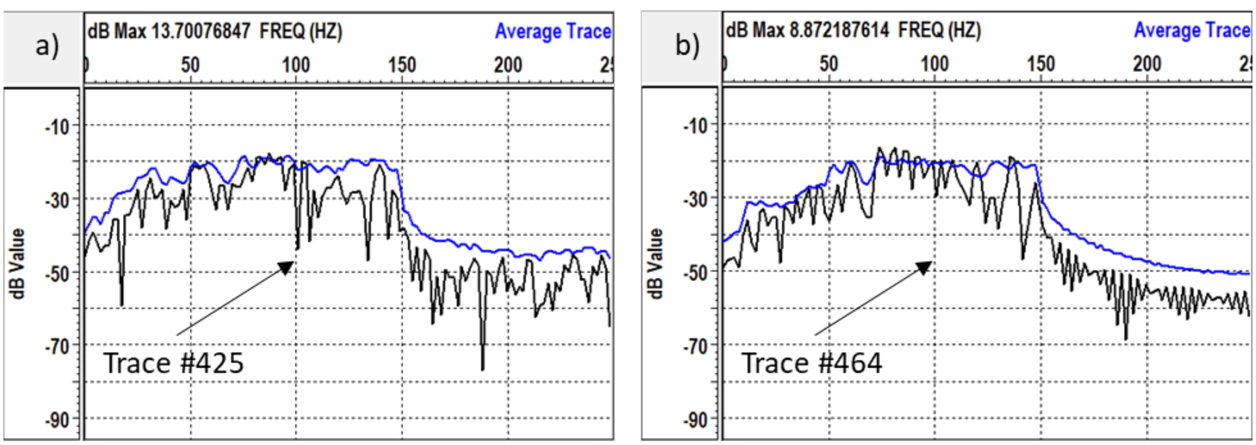

Figure 5.23 Raw straight DAS amplitude spectrum of VP 121. a) upgoing wavefield, b) upgoing wavefield after deconvolution. Arbitrary trace spectrum is shown in black and the average amplitude spectrum of the entire wavefield in blue.

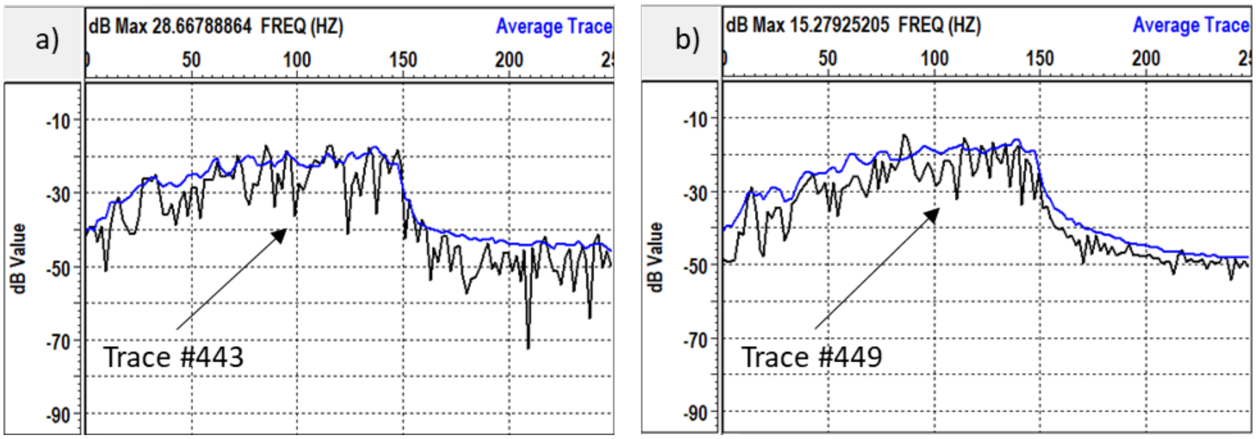

Figure 5.24 Raw HWC DAS amplitude spectrum of VP 121. a) upgoing wavefield, b) upgoing wavefield after deconvolution. Arbitrary trace spectrum is shown in black and the average amplitude spectrum of the entire wavefield in blue.

Integrated DAS:

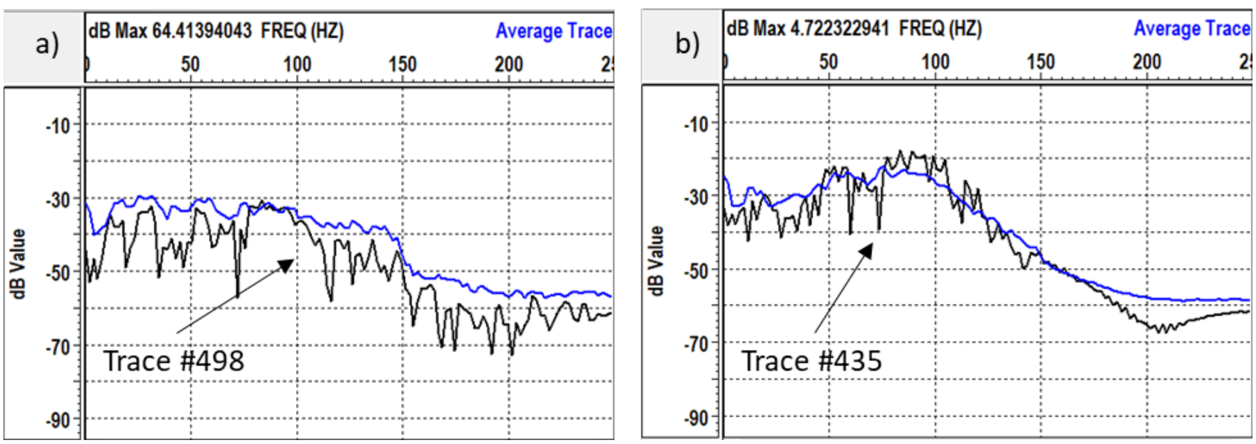

Figure 5.25 Integrated straight DAS amplitude spectrum of VP 121. a) upgoing wavefield, b) upgoing wavefield after deconvolution. Arbitrary trace spectrum is shown in black and the average amplitude spectrum of the entire wavefield in blue.

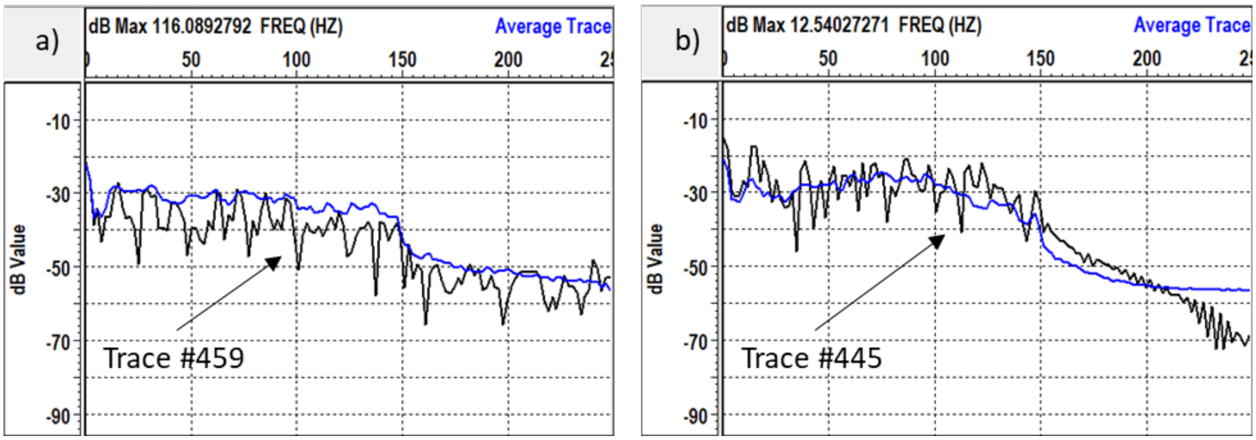

Figure 5.26 Integrated HWC DAS amplitude spectrum of VP 121. a) upgoing wavefield, b) upgoing wavefield after deconvolution. Arbitrary trace spectrum is shown in black and the average amplitude spectrum of the entire wavefield in blue.

Geophones:

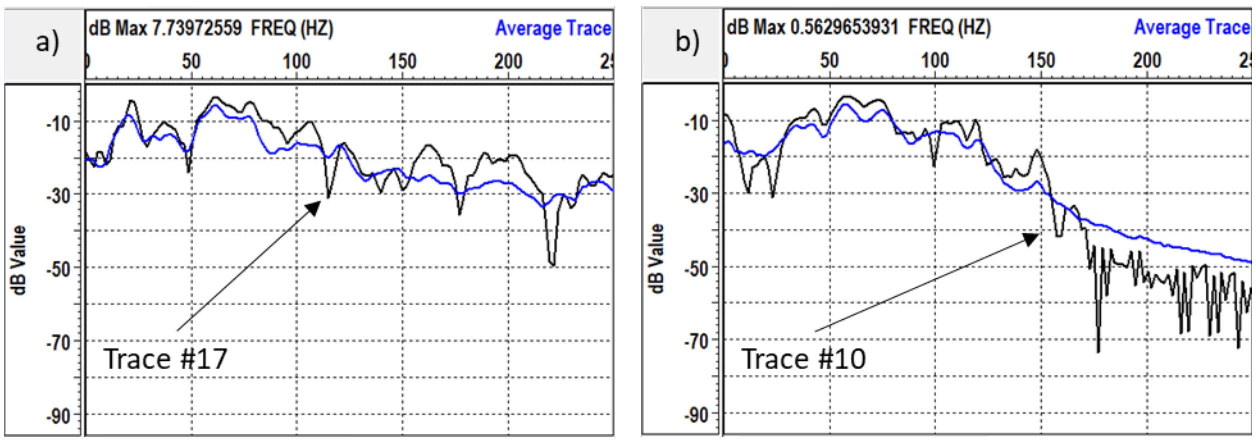

Figure 5.27 Geophone (vertical component) amplitude spectrum of VP 121. a) upgoing wavefield, b) upgoing wavefield after deconvolution. Arbitrary trace spectrum is shown in black and the average amplitude spectrum of the entire wavefield in blue.

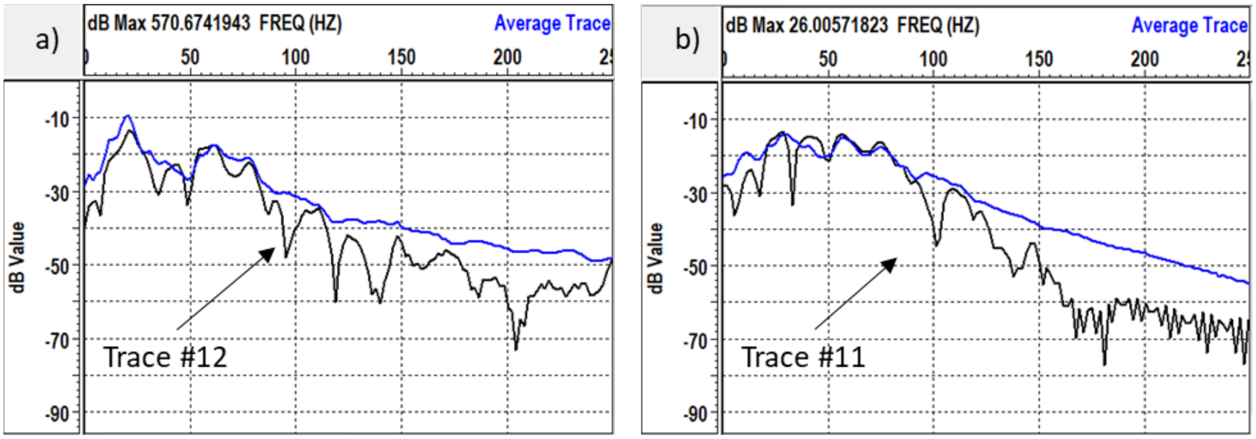

Figure 5.28 Geophone (multicomponent data) amplitude spectrum of VP 121. a) upgoing wavefield, b) upgoing wavefield after deconvolution. Arbitrary trace spectrum is shown in black and the average amplitude spectrum of the entire wavefield in blue.

After deconvolution, each dataset shows a slight increase in amplitudes. Moreover, the integrated DAS datasets seem to have the highest increase in the amplitudes, especially for higher frequencies. The geophone datasets show a significant increase in the amplitudes corresponding to the higher frequencies. Several DAS amplitude spectra display an interesting behaviour where the amplitudes at higher frequencies seem higher than the amplitudes at lower frequencies (Figures 5.24, 5.25). This generates a small slope in the average amplitude curve (blue) between 10-150 Hz that do not necessarily resembles an average white reflectivity as expected after a deconvolution process. This effect needs further analysis as is not evident in the geophone datasets and could be a characteristic of DAS that has not been studied yet.

5.1.4 VSP-CDP transform

The VSP-CDP transform is a mapping procedure that moves offset VSP reflections to their corresponding reflection point assuming a zero dip (Sheriff, 2002). The mapping displays coverage from the wellhead to the farthest reflection given by the velocity model available and the VSP geometry (Hinds et al., 1996). Among the parameters used for the VSP-CDP transform, for DAS datasets, a mean function was applied to every 16 and 17 traces for straight DAS and HWC DAS (appendix A.5). This was performed to resample the input data to a channel spacing of 4m and 3.91 m for straight and HWC DAS respectively. The trace spacing output selected was 2 m, approximately half of the channel spacing after the DAS data selection. The velocity models used for the transform are the same profiles obtained in Chapter 4 shown below (Figures 5.29 and 5.30) that were obtained from the first break arrivals of a zero offset VSP. Figure 5.29(a) shows the first break picks as a function of depth of straight DAS in blue and HWC DAS in green, and Figure 5.29(b) shows the interval velocity and RMS velocity of the straight DAS in blue and HWC DAS in green. Similarly, Figure 5.30 (a) shows the first break picks of the geophones vertical component in blue and (b) corresponds to the interval velocity in red and the RMS velocity in blue.

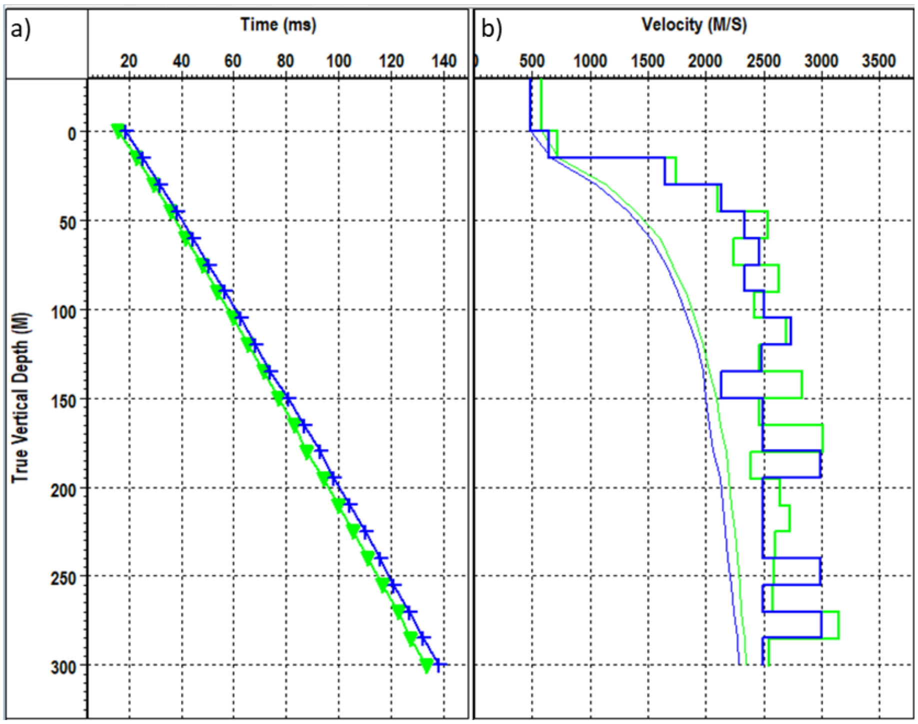

Figure 5.29 Straight fibre (blue) and HWC (green) velocity profile. a) first break times versus depth. b) interval velocity (thick curve) and RMS velocity (thin curve).

The VSP-CDP transform was applied to each source point and the obtained mapped result of six different VPs for each dataset are shown in Figures 5.31-5.36. These VPs were selected as they have similar offsets from the well on each section of the walk away VSP. Moreover, (a), (b) and (c) correspond to the southern part of the line whereas (d), (e) and (f) correspond to the northern part of the line from the well. The VPs number and their corresponding offset from the well are: (a) VP 112, 191 m offset; (b) VP 118, 131 m offset; (c) VP 127, 41 m offset; (d) VP 136, 49 m offset; (e) VP 144, 129 m offset; (f) VP 150, 189 m offset. Each subfigure is displayed with AGC and additional amplitude gain as labelled in the figure's caption. The approximate position of the Observation Well 2 is marked with a blue circle and offset from the well increases to the right.

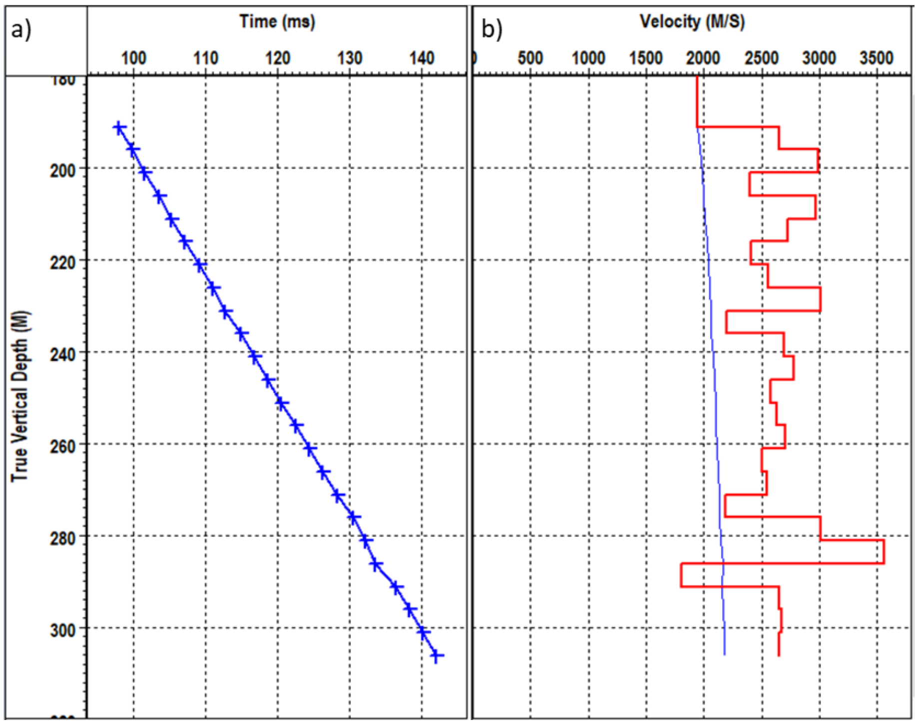

Figure 5.30 Geophone velocity profile. a) first break times versus depth in blue. b) interval velocity (red) and RMS velocity (blue).

A good imaging result was obtained and there is an excellent identification of events along the increasing offsets. The CO_2 injection target (BBRS) located at approximately 250 ms (marked with a red arrow) is noticeable in each dataset and for every offset. HWC data shows a weaker amplitude response compared with the straight DAS mapped results. The integrated DAS datasets mapped results seem to be clearer and the events are more continuous across the section than the raw DAS imaging results. The geophone mapped results also show a good representation and continuity of the events along the section, although the differences in amplitude and frequency are visible when compared to DAS sections. In addition, DAS datasets yield a better illumination in the shallow section due to the full coverage of the fibre in the well compared to the geophone coverage that is restricted to the zone of interest between 191.24 m and 306.24 m.

Raw DAS:

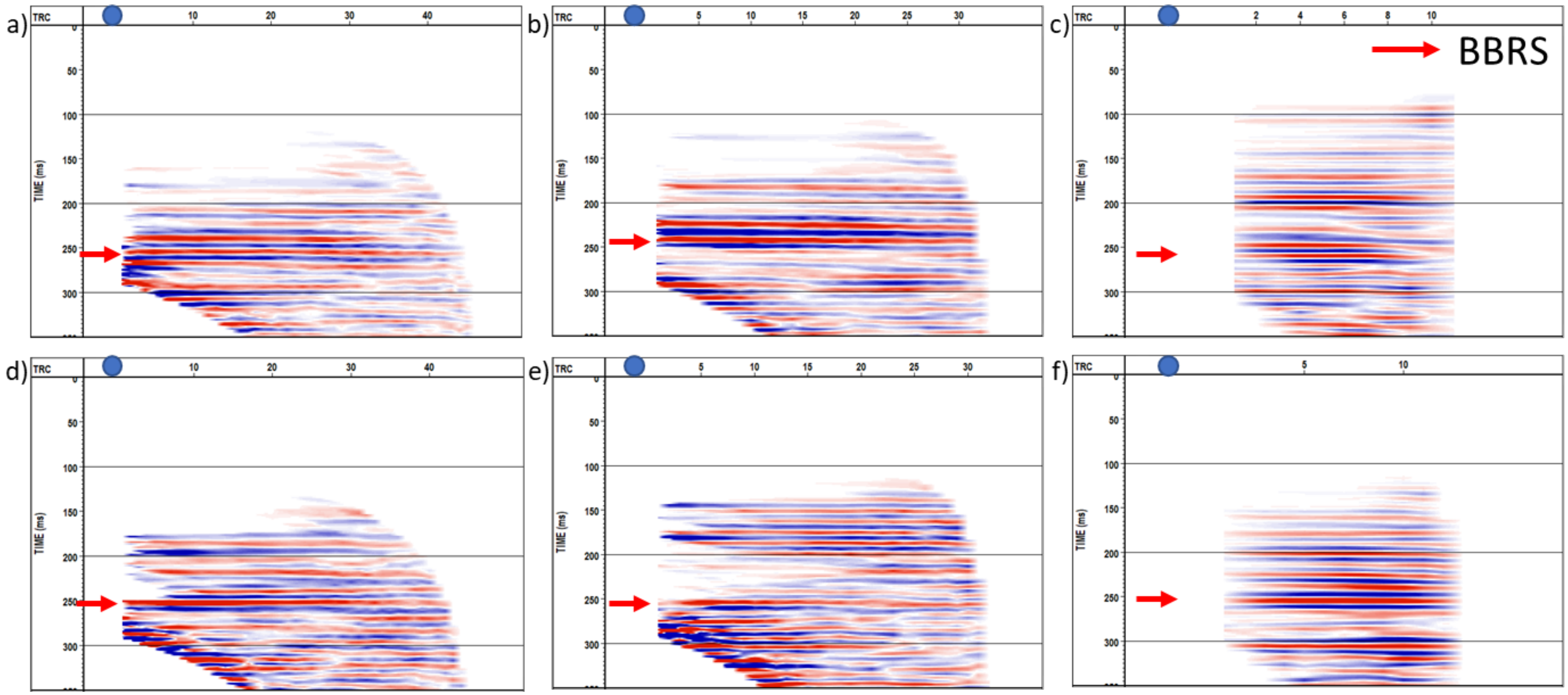

Figure 5.31 VSP-CDP transforms of raw straight fibre at different offsets from the well; a) VP 112 at 191 m offset with AGC and +3 dB; b) VP 118 at 131 m offset with AGC and +3 dB; c) VP 127 at 41 m offset with +3 dB; d) VP 136 at 49 m offset with +3 dB; e) VP 144 at 129 m offset with AGC and +6 dB; f) VP 150 at 189 m offset with AGC and +6 dB.

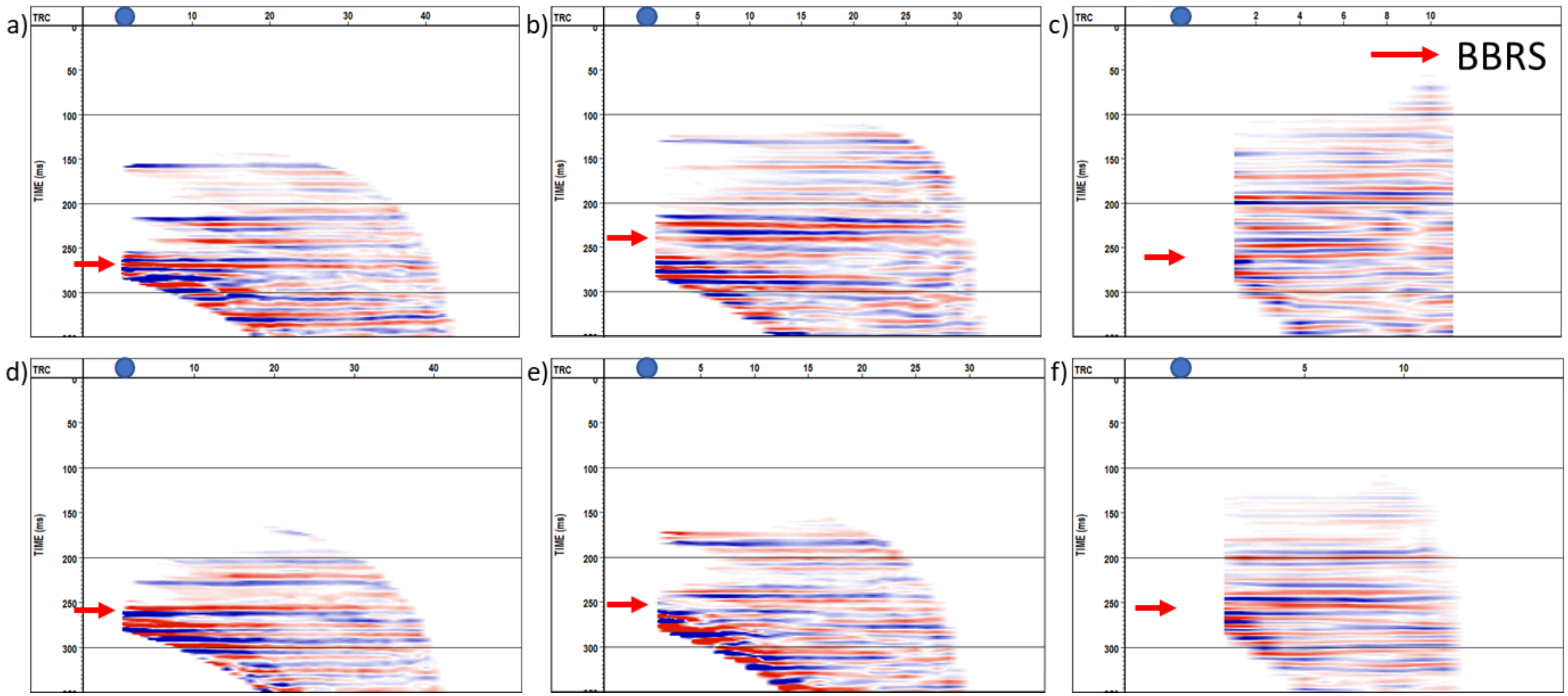

Figure 5.32. VSP-CDP transforms of raw HWC at different offsets from the well: a) VP 112 at 191 m offset with AGC and +6 dB; b) VP 118 at 131 m offset with AGC and +3 dB; c) VP 127 at 41 m offset with AGC; d) VP 136 at 49 m offset with AGC; e) VP 144 at 129 m offset with AGC and +6 dB; f) VP 150 at 189 m offset with AGC and +6 dB.

Integrated DAS:

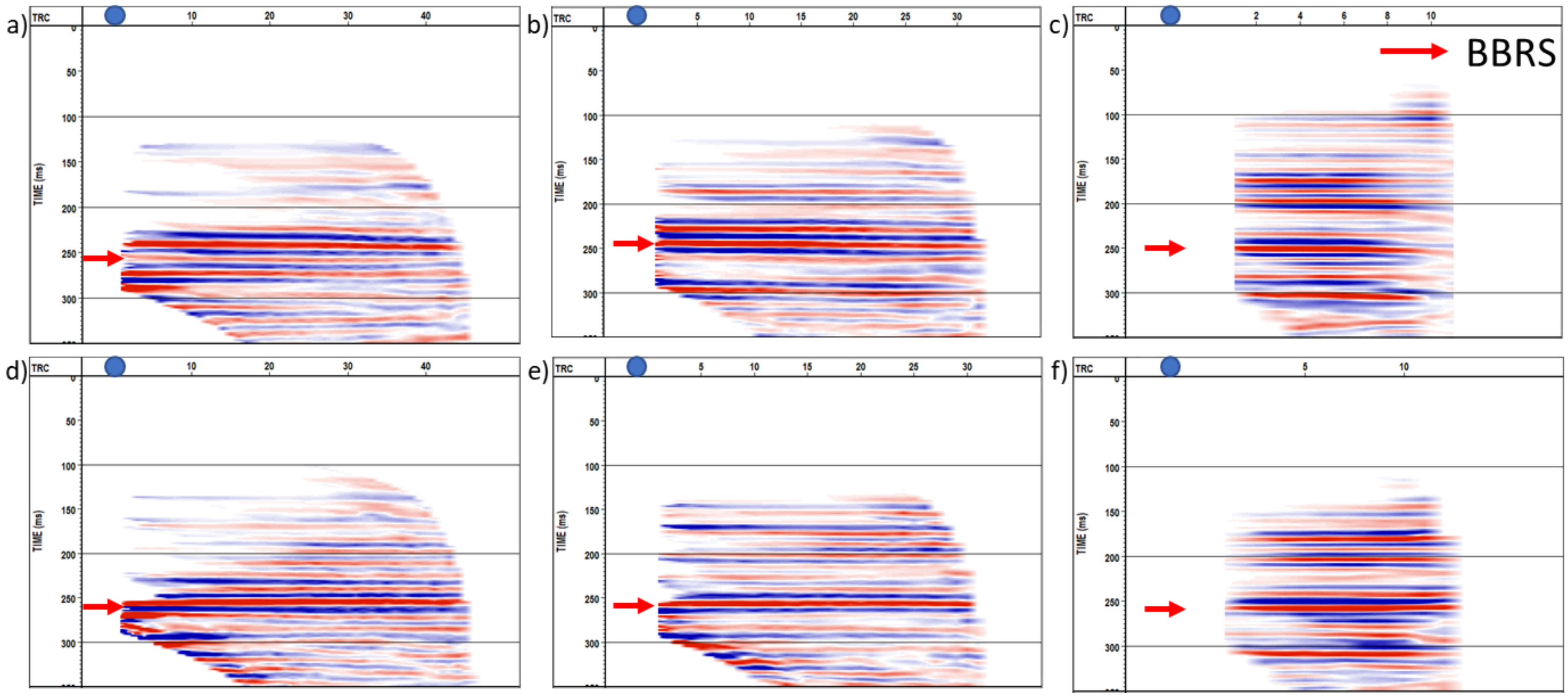

Figure 5.33. VSP-CDP transforms of integrated straight fibre at different offsets from the well: a) VP 112 at 191 m offset with +3 dB; b) VP 118 at 131 m offset with AGC and +3 dB; c) VP 127 at 41 m offset with +3 dB; d) VP 136 at 49 m offset with +3 dB; e) VP 144 at 129 m offset with AGC and +3 dB; f) VP 150 at 189 m offset with AGC and +6 dB.

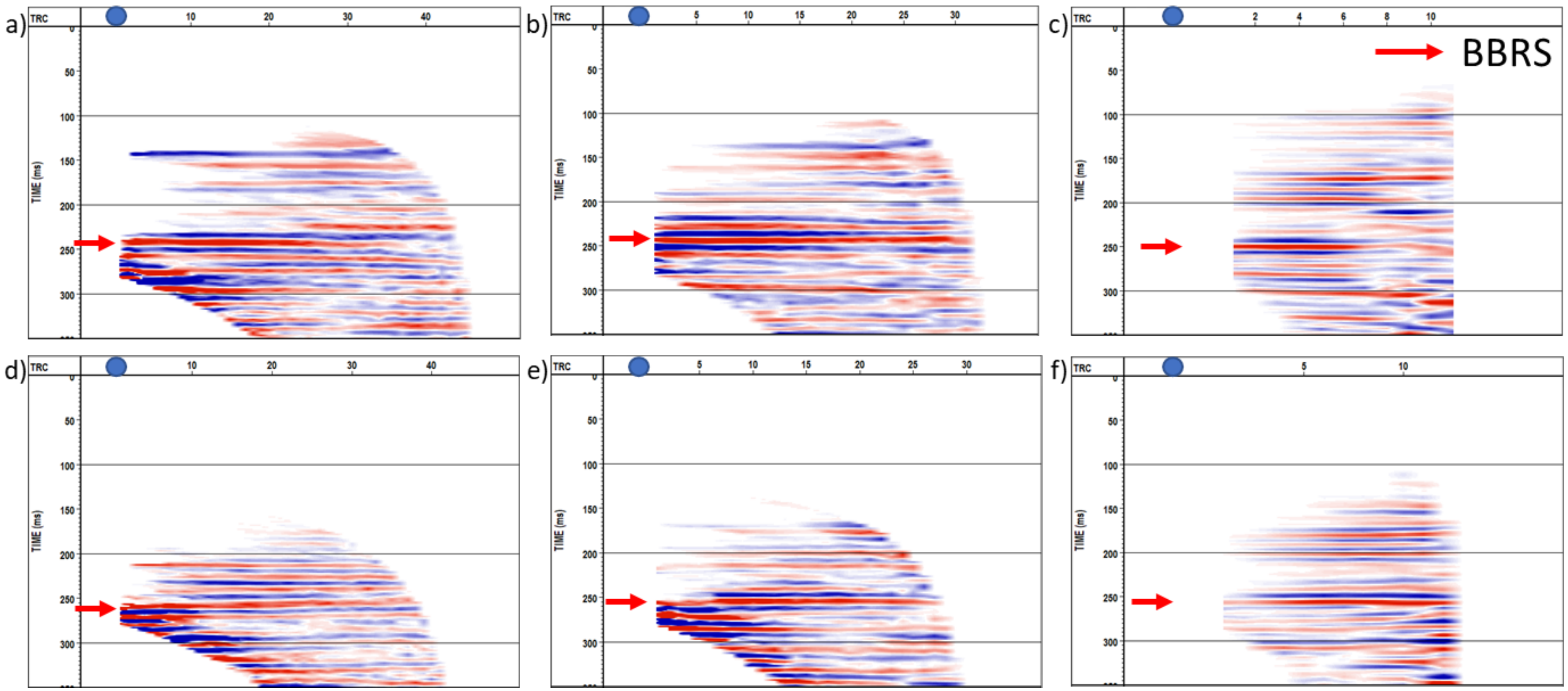

Figure 5.34. VSP-CDP transforms of integrated HWC at different offsets from the well: a) VP 112 at 191 m offset with AGC and +6 dB; b) VP 118 at 131 m offset with AGC and +3 dB; c) VP 127 at 41 m offset with +3 dB; d) VP 136 at 49 m offset with +3 dB; e) VP 144 at 129 m offset with AGC and +6 dB; f) VP 150 at 189 m offset with AGC and +6 dB.

Geophones:

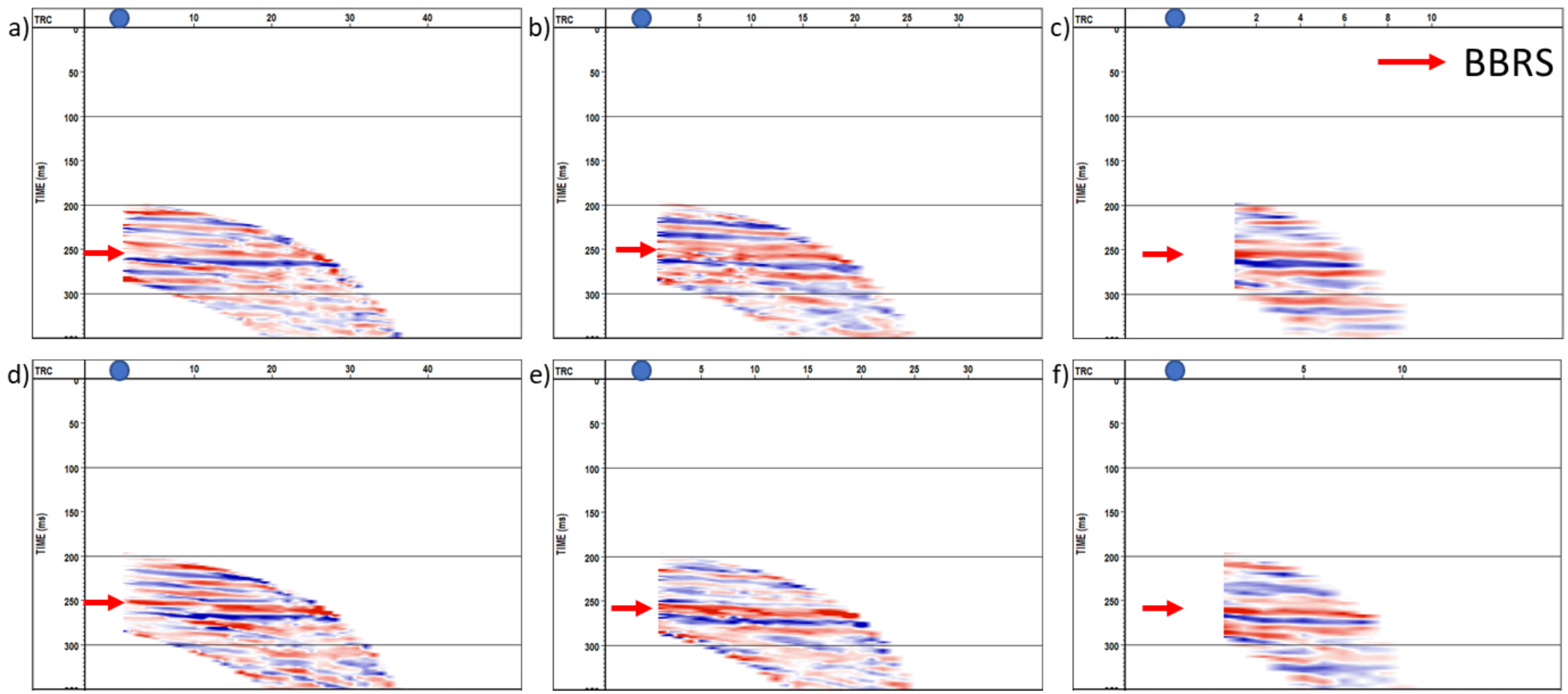

Figure 5.35. VSP-CDP transforms of geophone array (vertical component) at different offsets from the well: a) VP 112 at 191 m offset with AGC; b) VP 118 at 131 m offset with AGC; c) VP 127 at 41 m offset with AGC; d) VP 136 at 49 m offset with AGC; e) VP 144 at 129 m offset with AGC; f) VP 150 at 189 m offset with +6 dB.

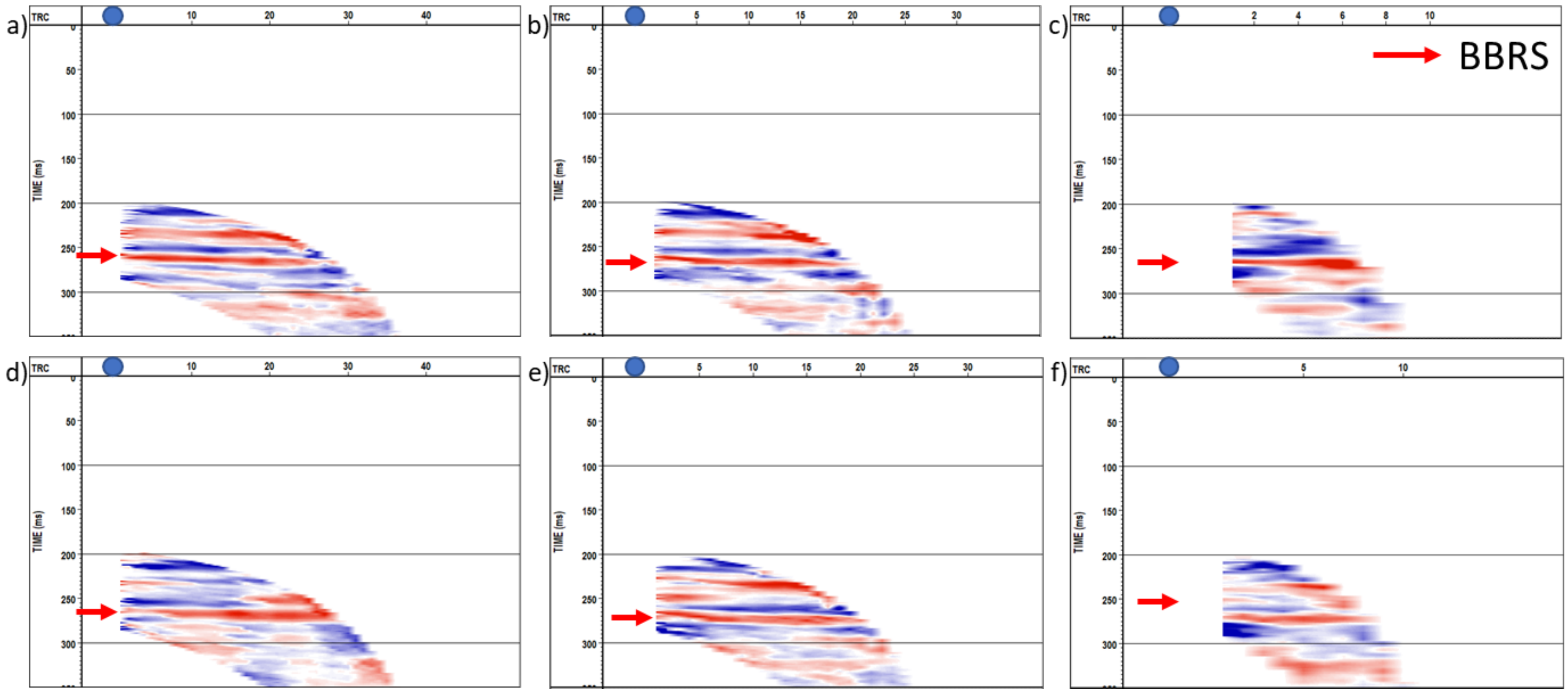

Figure 5.36. VSP-CDP transforms of geophone array (after rotation) at different offsets from the well: a) VP 112 at 191 m offset with AGC; b) VP 118 at 131 m offset with AGC; c) VP 127 at 41 m offset with AGC; d) VP 136 at 49 m offset with AGC; e) VP 144 at 129 m offset with AGC; f) VP 150 at 189 m offset with AGC.

5.1.5 Stacking

The mapped seismic section obtained from the VSP-CDP transform of each source point was then stacked to yield a final imaging result. Prior stacking, a source statics correction was applied to each VSP-CDP mapped section. This was performed applying a similar approach to the one described in Chapter 3. Figure 5.37 displays the source statics contour map with the walk away source points shown in red. After the statics correction and the stacked sections were obtained, a mean scaling function was applied. Figures 5.38 to 5.43 show the imaging results obtained for each dataset. The approximate position of the Observation Well 2 is marked with a blue circle and offset from the well increases to the right. The final stacked sections show a significant improvement after the statics correction was applied. The events are clearer and more continuous across the section. For every dataset, the event of interest, the Basal Belly River Sandstone (BBRS) at approximately 250 ms (marked with red arrow) is noticeable and continuous along the section. However, the mapped results of the HWC datasets have an inferior result compared to the straight DAS. The events show a weaker amplitude response compared to straight DAS and the events show some discontinuity in the stacked sections. This applies for both the raw DAS and integrated DAS datasets, although the imaging seems to improve in the integrated case slightly.

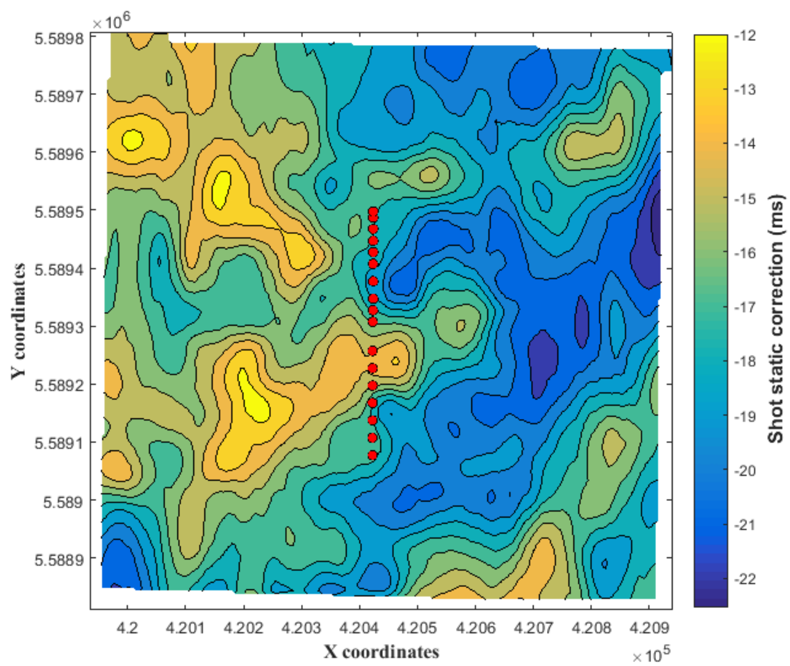

Figure 5.37 Source statics contour map. Walk away source points are marked with red points.

Raw DAS:

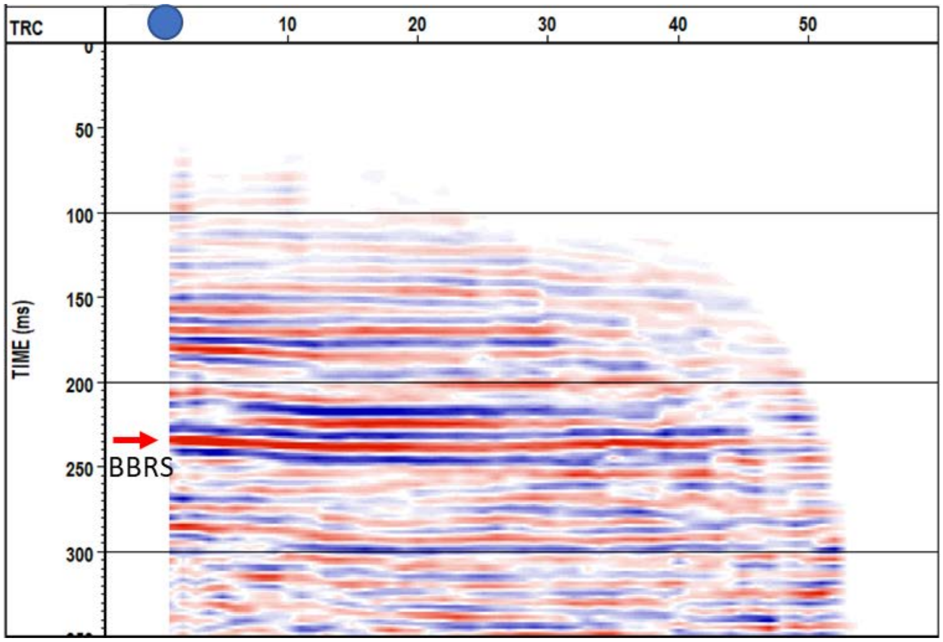

Figure 5.38. VSP-CDP stack of raw straight DAS displayed with AGC. The CO_2 injection target the Basal Belly River Sandstone (BBRS) is shown with the red arrow.

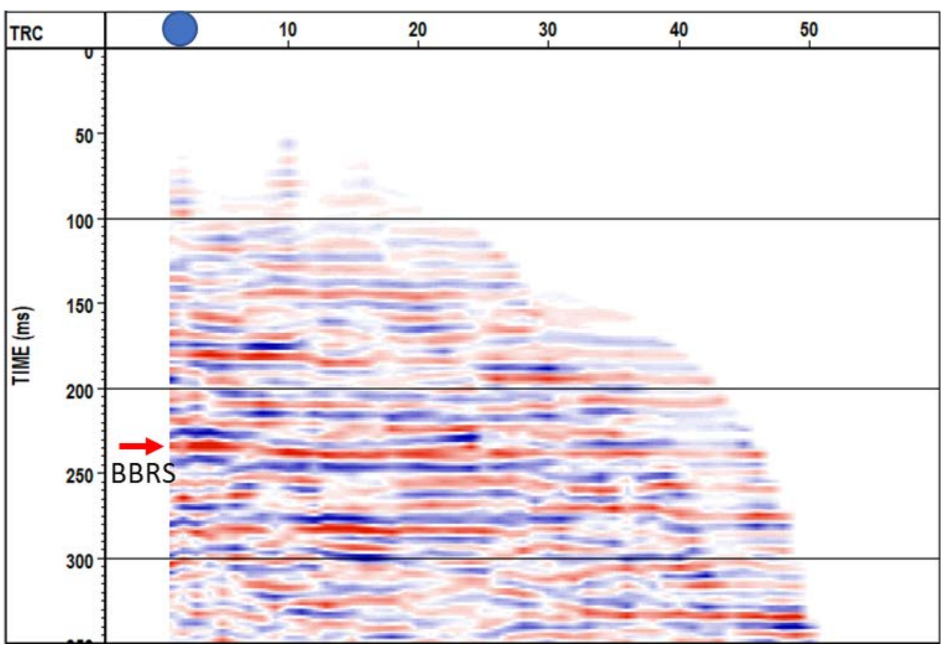

Figure 5.39 VSP-CDP stack of raw HWC DAS displayed with AGC. The CO_2 injection target the Basal Belly River Sandstone (BBRS) is shown with the red arrow.

Integrated DAS:

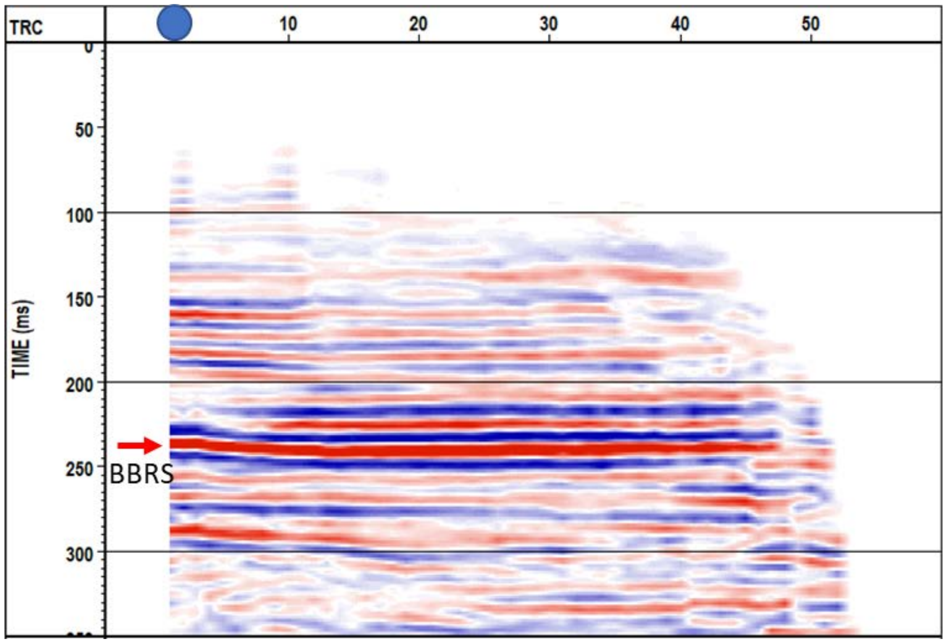

Figure 5.40. VSP-CDP stack of integrated straight DAS displayed with AGC. The CO_2 injection target the Basal Belly River Sandstone (BBRS) is shown with the red arrow.

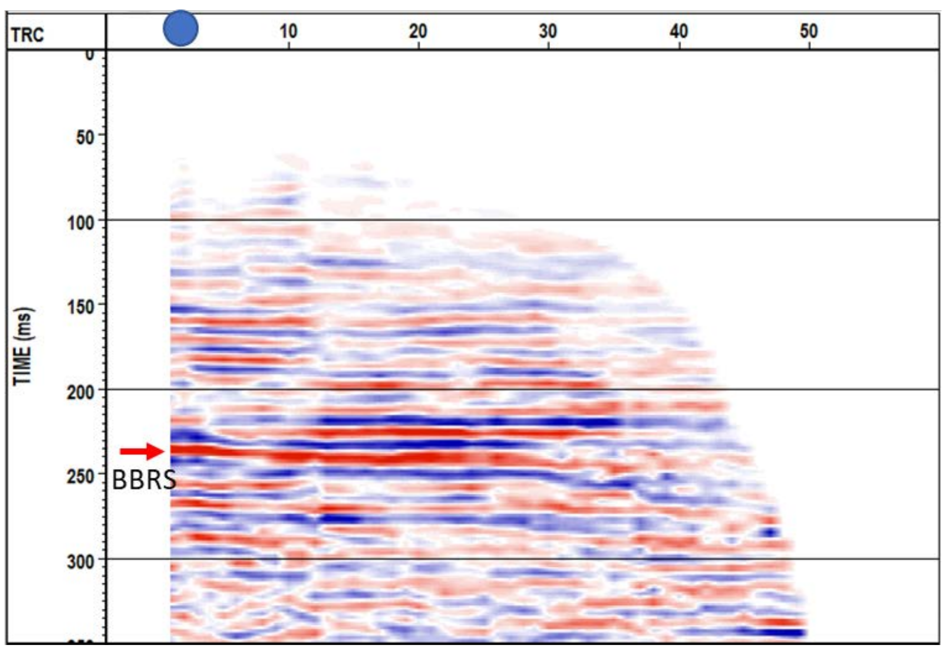

Figure 5.41 VSP-CDP stack of integrated HWC DAS displayed with AGC. The CO_2 injection target the Basal Belly River Sandstone (BBRS) is shown with the red arrow.

Geophones:

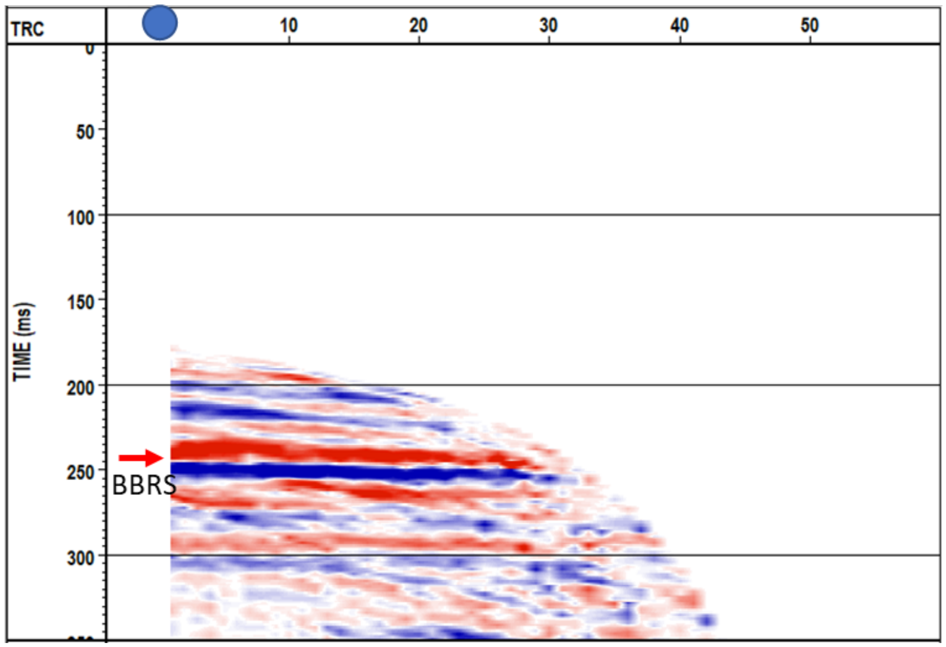

Figure 5.42. VSP-CDP stack of geophone vertical component displayed with AGC. The CO_2 injection target the Basal Belly River Sandstone (BBRS) is shown with the red arrow.

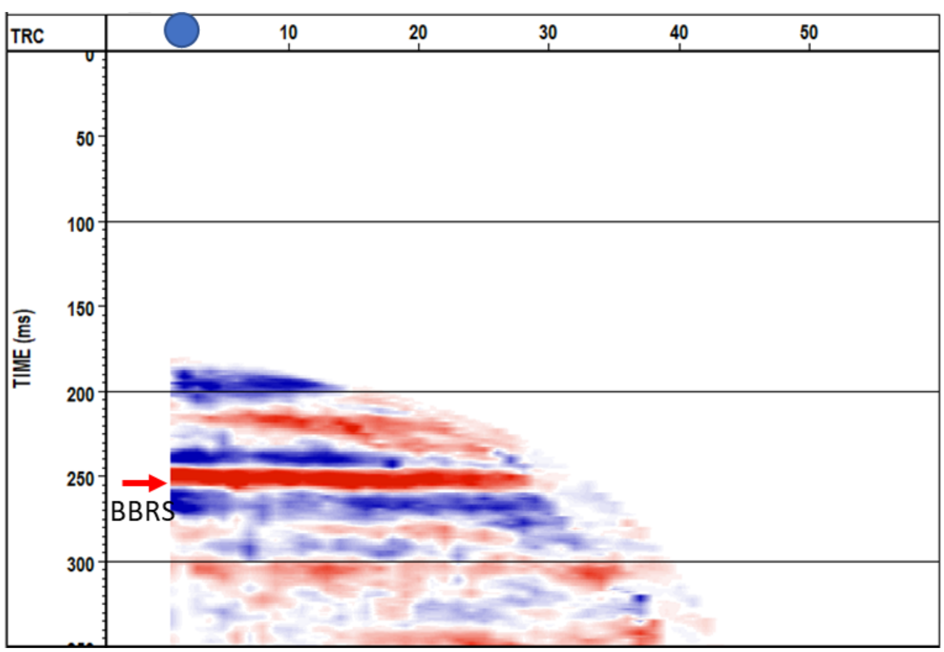

Figure 5.43 VSP-CDP stack of geophone rotated data displayed with AGC. The CO_2 injection target the Basal Belly River Sandstone (BBRS) is shown with the red arrow.

5.2 Discussion

After reviewing the results of each step in the processing flow, we have noticed several important differences between the datasets. For example, the raw straight DAS data has a higher S/N than the HWC DAS. The integrated DAS has better imaging of the seismic events compared to the raw DAS. The DAS data yields a broader illumination in the shallow section with respect to the geophones that were deployed across the injection zone.

In the wavefield separation, we noticed the identification of head waves in DAS datasets again related to the full coverage of fibre in the well. As the offset increases, more S-wave events are also present in the data which is expected due to the difference in the angle of incidence of the rays as they travel from the source to the receivers in the well. There is a good correlation between the upgoing events identified in both DAS and geophone datasets. After deconvolution, the events seem better defined and continuous, in particular for the HWC DAS that showed weaker events as the offset increased. The amplitude spectra before and after deconvolution showed a slight increase of the amplitudes for each dataset, although, for DAS datasets, the amplitudes seemed to increase at higher frequencies. From the VSP-CDP transforms, there is a good imaging result of the events for each dataset, the event of interest (BBRS) is identified at every offset. The integrated DAS seems to have a more continuous correlation of the events and the geophone dataset has a subtler appearance with respect to DAS, which proves one of the advantages of this method, higher resolution data. Similarly, with the stacked sections, the injection target is visible and seems better defined in the integrated DAS.

The obtained stacked sections were also compared with a 3D seismic survey acquired at the FRS in 2014 as part of the baseline. The inline (99) selected for the comparison crosses the Observation Well 2. Figures 5.44, 5.45 and 5.46 display the comparison of the stacked sections obtained from the processing with the surface seismic inline. Each figure corresponds to the comparison of raw DAS, integrated DAS and geophone datasets, respectively. The CO_2 injection target (BBRS) is marked with red arrows.

As mentioned before, straight DAS stacked sections seems to have a better display of the CO_2 injection target compared to the HWC fibre. This applies for both the raw and integrated sections (Figures 5.44(c) and 5.45(c)), even though the integrated section shows a better continuity of the events, the reflectors seem to vary across the section generating a non-flat appearance that disagrees with the known flat stratigraphy of the area.

In general, DAS results shown a good correlation with the surface seismic inline. Nevertheless, there is an evident time shift of approximately 15 ms to 20 ms between the DAS stacked section and the seismic inline. A possible explanation for this time shift could be a difference in the datum between the seismic data and the elevation of the Observation Well 2 wellhead. On the other hand, the geophone results show a good correlation with the surface seismic inline. The vertical component stacked section displays a similar response as DAS results, where the time difference is also noticeable. The section of the multicomponent data has a good identification of the BBRS, but it lacks continuity in other events that are better defined in the vertical component section. Another interesting observation is an apparent time shift between the geophone vertical component and the multicomponent geophone stacked sections. These observations can also be associated with remaining SV waves after the rotation and time-variant polarization. Further analysis of the multicomponent geophone data is highly recommended in future procedures as it could help explain the differences seen in the results shown here as well as the other time shift observed in the zero offset corridor stacks discussed in Chapter 4.

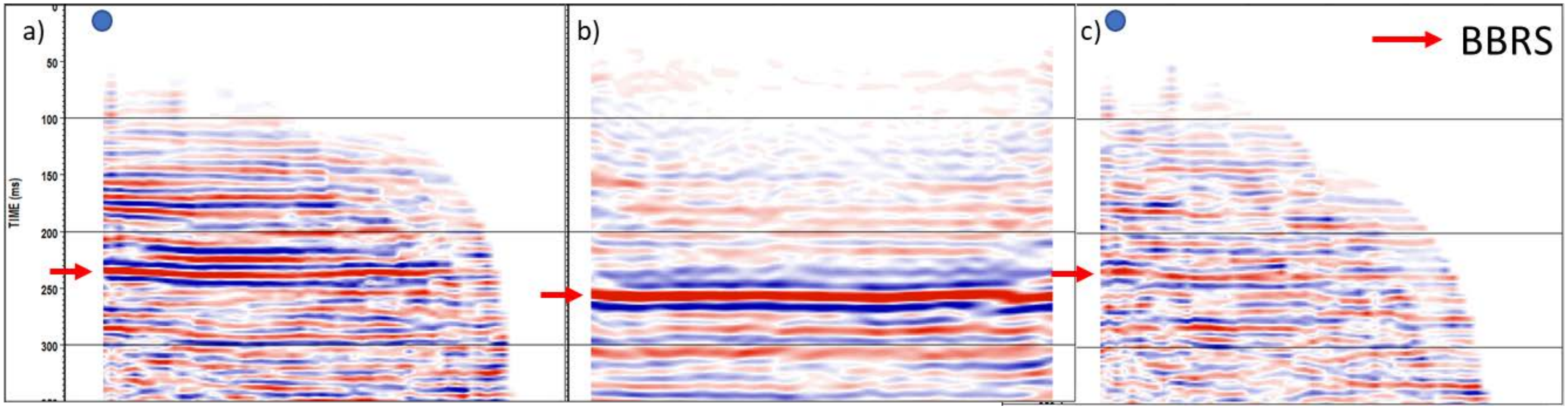

Figure 5.44. Raw DAS stacked sections comparison displayed with AGC: a) straight DAS, b) surface seismic inline, c) HWC DAS. The CO_2 injection target the Basal Belly River Sandstone (BBRS) is shown with the red arrow.

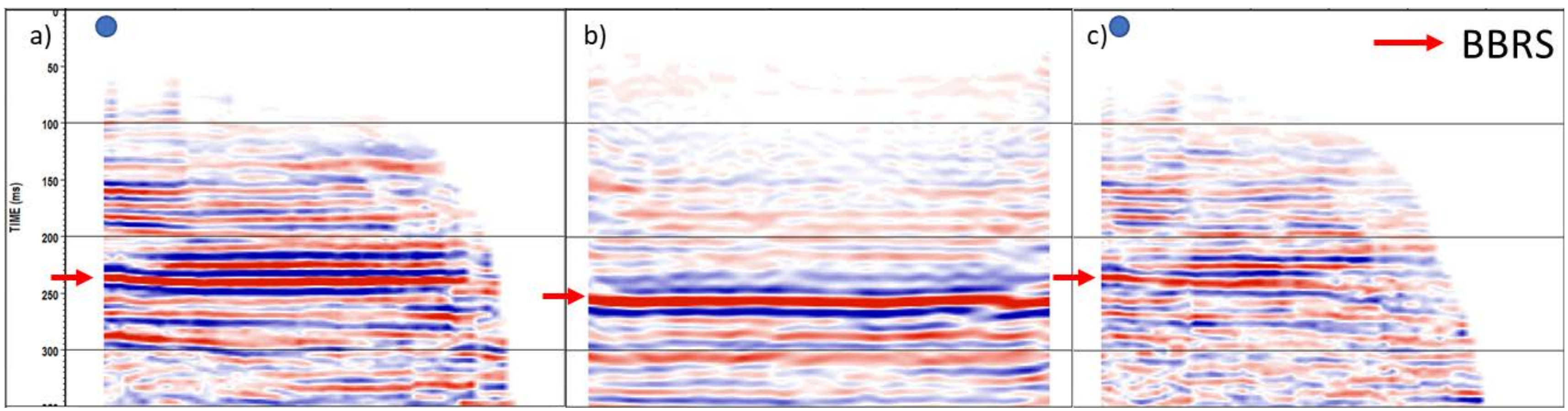

Figure 5.45. Integrated DAS stacked sections comparison displayed with AGC: a) straight DAS, b) surface seismic inline, c) HWC DAS. The CO_2 injection target the Basal Belly River Sandstone (BBRS) is shown with the red arrow.

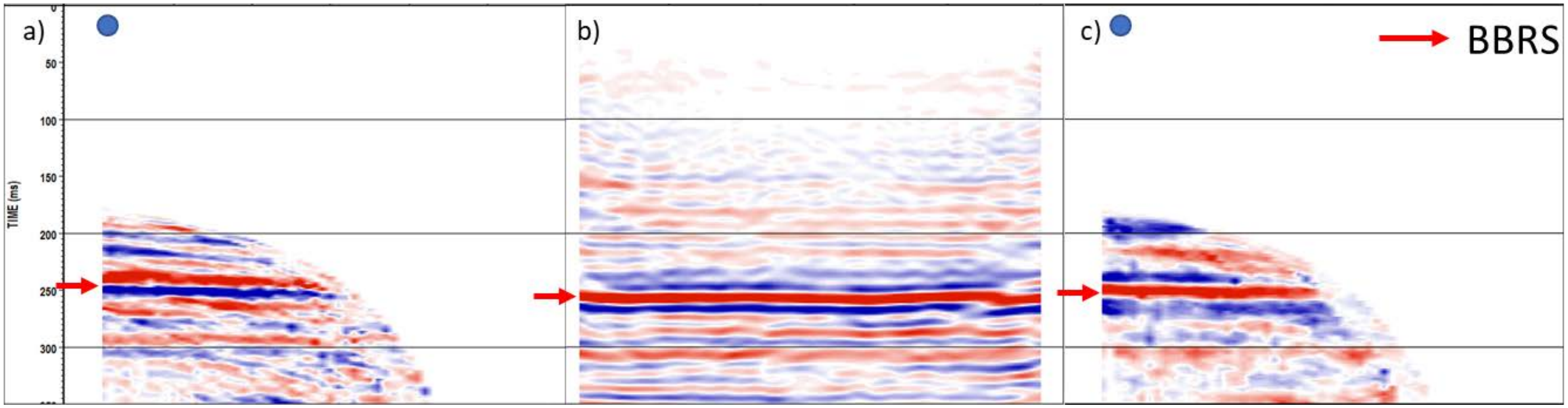

Figure 5.46. Geophone stacked sections comparison displayed with AGC: a) geophones vertical component, b) surface seismic inline, c) multicomponent geophone. The CO_2 injection target the Basal Belly River Sandstone (BBRS) is shown with the red arrow.

5.3 Conclusions

A walk away VSP line acquired at the Field Research Station in July 2017 was processed while performing a thorough comparison between DAS and geophone datasets. The analysis included the assessment of the straight and HWC DAS as well as the geophone's vertical component and multicomponent data. Additionally, the same procedure was applied to the integrated DAS datasets.

A good correlation between the DAS datasets and the geophone data is visible. Having a full coverage of the fibre optic cables in the well yields better imaging results in the shallow section. Clear identification of the CO_2 injection target was obtained for the raw and integrated straight fibre. Although, the HWC DAS results showed a weaker and less continuous result across the mapped section.

Each processed dataset (straight DAS, HWC DAS and geophone) yielded an excellent imaging result that can be correlated to surface seismic data. DAS datasets present better illumination in the shallow section due to the fibre cable full coverage in the well. The CO_2 injection target was identified in each dataset while showing a good match with the surface seismic baseline. Nevertheless, there is an evident time difference between the stacked sections and the surface seismic that is presumed to be caused by a difference in the datum of the surface seismic and elevation of the wellhead of the Observation Well 2.

Chapter Six: **Conclusions and recommendations**

6.1 Conclusions

The success of risk assessments and monitoring protocols in Carbon Capture and Storage (CCS) projects is associated with the variety of multidisciplinary surveys developed throughout the lifetime of the project. Among these, borehole seismic surveys play a crucial point in the monitoring of CO_2 injection, particularly in the vicinity of the CO_2 injection well. The primary objectives of this thesis were the processing, interpretation and analysis of three Vertical Seismic Profile (VSP) surveys. This included testing and comparing the recently developed Distributed Acoustic Sensing (DAS) technology with cemented geophones. The following sections highlight the conclusions and observations obtained from the workflows applied to the three datasets acquired at the Field Research Station (FRS) in Newell County, Alberta.

6.1.1 Dataset 1: Walk around VSP

- A VSP azimuthal analysis was performed by studying the first arrival traveltimes to estimate velocity variations with source-well azimuth; this was achieved through the analysis of first break traveltime variations as a function of the azimuth.
- A slight sinusoidal trend was observed for the traveltime variation, indicative of weak azimuthal anisotropy (HTI). The fast direction was identified as southwest to northeast. From the residual calculation of traveltime and velocity, we estimated an approximate value for epsilon equal to 0.02, indicative of weak anisotropy.
- The rotation of the horizontal components through hodogram analysis helped build a procedure to estimate the original orientation of the H1 and H2 elements in the wellbore. This methodology was later applied to the geophones permanently installed in Observation Well 2. Additionally, the estimation of the incidence angle with a ray-traced velocity model served as a threshold to corroborate the rotation angles obtained from the hodogram analysis.

6.1.2 Dataset 2: Zero offset VSP

- Three DAS and geophone zero offset VSP source points (VP) recorded in May and July 2017 were processed following a VSP standard workflow.
- A depth registration step was applied to DAS dataset to identify the corresponding depth of each DAS channel. Two approaches were completed; a cross-correlation between DAS and geophone traces; and a time difference analysis. An accurate result was obtained from both methods. The cross-correlation approach yield a maximum difference of 4.75 m whereas the time difference analysis showed a higher difference of 13.8 m associated with the VP at an 80 m offset from the observation well. We noticed how the accuracy of the depth registration seems to be dependent on the number of sweeps and offsets of the VPs.
- Conversion of the DAS signal into a geophone response was tested to compare both datasets accurately. The depth registration of the integrated DAS yields more accurate results than the raw DAS data. Also, an evident similarity in frequency and phase was obtained from the integrated DAS with respect to the geophone dataset.
- The final product of a zero offset VSP processing, namely a corridor stack, was obtained for the straight, HWC and geophone datasets for each VP. A time difference of approximately 10 ms is noticeable between DAS and geophone corridor stacks. The cause of the time shift is still under analysis, although some conjectures indicate it might be caused by the difference in the trigger time recorded by the geophones and DAS recording system during the acquisition of the surveys.

6.1.3 Dataset 3: Walk away VSP

- The processing of a DAS and geophone walk away VSP dataset acquired at the FRS in July 2017 was completed. It included the assessment of the raw and integrated straight and HWC DAS as well as the geophone's vertical component and multicomponent data.
- The estimation of the signal to noise ratio (S/N) was performed per VP for the DAS and geophone datasets. The results showed that the HWC has the lowest S/N whereas the straight DAS shows the higher S/N when in the proximity to the Observation Well 2. The vertical component of the geophones has a constant S/N per VP, but the horizontal

component shows some variations in S/N at the southern section of the line. In general, the vertical component of the geophones shows a higher S/N compared to DAS.

- A good correlation was obtained between the DAS datasets and the geophone data after processing. Having a full coverage of the fibre optic cables in the well yields better imaging result in the shallow section. Clear identification of the injection target was achieved for the raw and integrated straight fibre, although the results obtained for the HWC fibre seemed less continuous in the zone of interest.
- An excellent imaging result was obtained from the processed datasets (straight DAS, HWC DAS and geophone) that were correlated to surface seismic data. The CO_2 injection target was identified in each stacked section and showed a good match with the surface seismic baseline. Although a time difference is observed, it is most likely associated with a difference in the datum that can be corrected when the geometry parameters are confirmed. DAS datasets also display seismic events in the shallow section that can be helpful for further studies of the overburden section. Overall, the results obtained provide a positive impact on DAS applications for subsurface imaging while carrying on the study of this technology and encouraging our understanding of DAS.

As previously mentioned, one of the major contributions of this work was the development of a workflow to process DAS datasets. As seen throughout chapters 4 and 5 and in the concluding remarks shown above, in order to follow a standard VSP processing flow, DAS datasets had to be accommodated to obtain reliable results along the process. The following highlight some of the most crucial points:

- The depth registration step is a key aspect of DAS processing as mentioned in Chapter 4. Without it, the uncertainty on the exact location of DAS channels persists and it can lead to geometry issues that can alter the confidence in the results. The use of geophone data in this stage was essential as the depth and spacing of the geophones in the wellbore were known, and this information was necessary to tie DAS channels to their corresponding depths accurately.
- Another critical aspect of DAS processing for borehole imaging is the calculation of interval velocities using the first break traveltimes. When DAS output trace spacing is

considerable small (e.g. 25 cm), it is necessary to resample the data to a larger trace spacing to mitigate the variations in the traveltimes caused by the high density of DAS traces. The approach applied to account for this was described in Chapter 4.

- Similarly, when applying the VSP-CDP transforms to DAS datasets, the large number of traces per source gather and their small trace spacing, can cause difficulties in the procedure that can result in inaccurate mapping results. This can be resolved by resampling the data to a larger trace spacing that is suitable given the bin size selected for the VSP-CDP transform.

6.2 Recommendations for future work

A series of recommendations are listed below based on the observations of this thesis to enhance the workflow efficiency as well as maximize the utility of the datasets available:

- Analyze the available well logs and if possible merge upper and lower sections of the well logs to generate a complete coverage of the injection and observation wells.
- Perform a thorough anisotropy analysis with the walk around data available. Compare the results with the newly acquired surveys with multi-azimuth geometry.
- Process the walk away VSP survey acquired with the walk around VSP and compare its results with the ones shown in Chapter 5 to test the time lapse monitoring procedures.
- Prior processing, invert and stack DAS gathers from each loop of the fibre optic cable in the wells, to increase the fold of the data and potentially remove some of the noise.
- Repeat the cross-correlation approach for the depth registration for every geophone trace and merge the results to generate a more accurate estimation of DAS channel depth registration.
- Fully convert DAS signal to geophone response by integrating raw DAS data with respect to time and factorizing the propagation speed along the fibre to obtain the particle velocity of the fibre as described by Daley et al., (2016).
- Generate additional synthetic seismograms with wavelets extracted from surface seismic and the sonic logs from each well and compare them to the one shown in Chapter 4.
- Test different filters for HWC DAS data to better understand the fibre configuration and to obtain an improved imaging result.

- Migrate the VSP-CDP transforms prior stacking and compare with the non-migrated results shown in Chapter 5. Create a composite plot including the VSP-CDP mapping results.
- Process additional walk away VSP surveys and merge the sections in a 3D display to interpret the results and perhaps establish a VSP baseline with the different VSP lines available.
- Continue the analysis of the multicomponent geophone data to help explain the differences seen in Chapters 4 and 5 with respect to DAS imaging results and the surface seismic data.

References

AER, & AGS. (2013). Subsurface Stratigraphic Picks for the Milk River 'Shoulder,' Alberta Plains: Including Tops for the Milk River Formation and Alderson Member of the Lea Park Formation.

Bubshait, S. (2010). *VSP processing for coal reflections*. University. of Calgary.

CaMI. (2013). Containment and Monitoring Institute (CaMI) Carbon Management Canada & University of Calgary Introduce a new Field Research Station (FRS).

Cassell, B. (1984). Vertical seismic profiles - an introduction. *First Break*, *1*(November), 9–19.

Daley, T. M., Miller, D. E., Dodds, K., Cook, P., & Freifeld, B. M. (2016). Field testing of modular borehole monitoring with simultaneous distributed acoustic sensing and geophone vertical seismic profiles at Citronelle, Alabama. *Geophysical Prospecting*, *64*(5), 1318–1334.

Dawson, F. M., Evans, C. G., Marsh, R., & Richardson, R. (1994). Chapter 24 Uppermost Cretaceous and Tertiary Strata of the Western Canada Sedimentary Basin. In *Geological Atlas of the Western Canada Sedimentary Basin* (pp. 387–406).

Dean, T., Hartog, A., & Frignet, B. (2015). Seismic without sensors – distributed vibration sensing. *ASEG Extended Abstracts*, (2), 1–4.

Dongas, J. M. (2016). *Development and Characterization of a Geostatic Model for Monitoring Shallow CO2 Injection*. University of Calgary.

Eaid, M., Li, J., & Innanen, K. (2017). A coupled DAS shaped-fibre and 3D elastic finite difference wave model. *CREWES Research Report*, *29*, 12.1-12.19.

EPA. (2017). *Inventory of U.S. Greenhouse Gas Emissions and Sinks*.

ERCB, & AGS. (2010). *Top of the Belly River Group in the Alberta Plains: Subsurface Stratigraphic Picks and Modelled Surface*.

ESG Solutions. (2018). *Microseismic Hydraulic Fracture Monitoring*. *https://www.esgsolutions.com/oil-and-gas/hydraulic-fracture-mapping-and-monitoring*.

Glass, D. (1990). *Lexicon of Canadian Stratigraphy Volume 4, Western Canada , Including Eastern British Columbia, Alberta, Saskatchewan and Southern Manitoba*. (D. J. Glass, Ed.), *CSPG Lexicon of Canadian stratigraphy* (Vol. 4). Calgary: Canadian Society of Petroleum Geologists.

Hall, K. W., Isaac, J. H., Wong, J., Bertram, K. L., Bertram, M. B., Lawton, D. C., … Eaton, D. W. (2015). Initial 3C-2D surface seismic and walkaway VSP results from the 2015 Brooks SuperCable experiment. *CREWES Research Report*, *27*, 23.1--23.22.

Hamblin, A. P., & Abrahamson, B. W. (1996). Stratigraphic architecture of “Basal Belly River” cycles, Foremost Formation, Belly River Group, subsurface of southern Alberta and southwestern Saskatchewan. *Bulletin of Canadian Petroleum Geology*, *44*(4), 654–673.

Hardage, B. A. (1983). *Vertical Seismic Profiling: Principles*. Geophysical Press.

Hartog, A. (2017). *An introduction to distributed optical fibre sensors*. (A. Mendez, Ed.), *Series in fiber optic sensors*. CRC Press. Taylor & Francis Group.

Hartog, A., Frignet, B., Mackie, D., & Clark, M. (2014). Vertical seismic optical profiling on wireline logging cable. *Geophysical Prospecting*, *62*(4), 693–701.

Heidbach, O., Rajabi, M., Reiter, K., & Ziegler, M. (2016). World Stress Map 2016, GFZ Data Service.

Hinds, R., Anderson, N., & Kuzmiski, R. (1996). *VSP Interpretive Processing*. Society of Exploration Geophysicists.

Hinds, R., Kuzmiski, R., Botha, W., & Anderson, N. L. (1984). Chapter 12 - Vertical and Lateral Seismic profiles.

Horne, S. A., Slater, C. P., Hill, A., & Wijnands, F. (2000). Walkaround VSPs for fractured reservoir characterization. *SEG Technical Program Expanded Abstracts 2000*, 1401–1404.

Hornman, K., Kuvshinov, B., Zwartjes, P., & Franzen, a. (2013). Field Trial of a Broadside-sensitive Distributed Acoustic Sensing Cable for Surface Seismic. *75th EAGE Conference & Exhibition, London*, (June 2013), 10–13.

Innanen, K. (2016). A geometrical model of DAS fibre response. *CREWES Research Report*, *28*, 1–24.

Innanen, K. (2017). Determination of seismic-tensor strain from Helical Wound Cable-Distributed Acoustic Sensing cable with arbitrary and nested-helix winds. In *SEG Technical Program Expanded Abstracts* (Vol. 1, pp. 926–930).

IPCC. (2014). *Summary for Policymakers*. *Climate Change 2014: Synthesis Report. Contribution of Working Groups I, II and III to the Fifth Assessment Report of the Intergovernmental Panel on Climate Change*.

Isaac, J. H., & Lawton, D. C. (2014). *Preparing for experimental CO2 injection: Seismic data analysis*. *CREWES Research Report* (Vol. 26).

Kuvshinov, B. N. (2016). Interaction of helically wound fibre-optic cables with plane seismic waves. *Geophysical Prospecting*, *64*(3), 671–688.

Lawton, D. C., Bertram, M., Bertram, K., Hall, K. W., & Isaac, H. (2014). A 3C-3D seismic survey at a new field research station near Brooks, Alberta. *CREWES Research Report*, *26*(Mmv), 48.1--48.18.

Lawton, D. C., Osadetz, K. G., & Saeedfar, A. (2017). Monitoring technology innovation at the CaMI Field Research Station, Brooks, Alberta. *GeoConvention*, (Mmv), 1–4.

Lawton, D. C., Osadetz, K. G., Saeedfar, A., & Macquet, M. (2017). Monitoring technology innovation at the CaMI Field Research Station, Brooks, Alberta. *Geoconvention Slides 2017*.

Lecomte, F., Broutin, P., & Lebas, E. (2010). *CO2 Capture Technologies to Reduce Greenhouse Gas Emissions*.

Lecomte, F., Broutin, P., Lebas, E., & Jones, T. (2010). *CO2 Capture: Technologies to Reduce Greenhouse Gas Emissions*. Editions Technip.

Liu, E., & Martinez, A. (2012). *Seismic Fracture Characterization*. https://doi.org/https://doi.org/

Lumens, P., Franzen, A., Hornman, K., Grandi Karam, S., Hemink, G., Kuvshinov, B., … Zwartjes, P. (2013). Cable development for distributed geophysical sensing with a field trial in surface seismic, *879435*(May 2013), 879435.

Margrave, G. F. (2014). *Methods of Seismic Data Processing (CREWES)*. (CREWES, Ed.) (Geophysics). Calgary: The Department of Geology and Geophysics.

Mateeva, A., Lopez, J., Potters, H., Mestayer, J., Cox, B., Kiyashchenko, D., … Detomo, R. (2014). Distributed acoustic sensing for reservoir monitoring with vertical seismic profiling. *Geophysical Prospecting*, *62*(4), 679–692.

Mondanos, M., Parker, T., Milne, C. H., Yeo, J., Coleman, T., & Farhadiroushan, M. (2015). Distributed temperature and distributed acoustic sensing for remote and harsh environments. *SPIE Sensing Technology + Applications*, (May 2015), 94910F.

Osadetz, K., Lawton, D., Amin, S., & Luc, R. (2017). CMC Research Inc. Field Research Station and Shell Quest - Field Trip. Calgary.

Parker, T., Shatalin, S., & Farhadiroushan, M. (2014). Distributed Acoustic Sensing - A new tool for seismic applications. *First Break*, *32*(2), 61–69.

Pereira, A. M., & Jones, M. (2010). *Fundamentals of Borehole Seismic Technology*. Schlumberger.

Rubin, E., Meyer, L., & de Coninck, H. (2005). IPCC Special Report on Carbon Dioxide Capture and Storage: Technical Summary. *Rite.or.Jp*.

Schlumberger. (2019a). Schlumberger Oilfield Glossary.

Schlumberger. (2019b). VISTA Help.

Sheriff, R. (2002). *Encyclopedic Dictionary of Applied Geophysics* (Fourth). Society of Exploration Geophysicists.

Thomsen, L. (1986). Weak elastic anisotropy. *GEOPHYSICS*, *51*(10), 1954–1966.

Willis, M. E., Ellmauthaler, A., & Wu, X. (2016). Calibration of Distributed Acoustic Sensing (DAS) VSP Data. *EAGE*, (June).

Wu, H., Wong, W.-F., Yang, Z., Wills, P. B., Lopez, J. L., Li, Y., … Mateeva, A. (2015). Dual-well 3D vertical seismic profile enabled by distributed acoustic sensing in deepwater Gulf of Mexico. *Interpretation*, *3*(3), SW11-SW25.

Xu, S., Zhang, Y., Pham, D., & Lambar, G. (2005). Antileakage Fourier transform for seismic data regularization. *Geophysics*, *70*(4), 87–95.

APPENDIX A: MATLAB CODES

A list of the MATLAB codes generated during this research is shown below. The files are classified according to the process and referenced within the thesis. The files can be found in the supplementary data with their corresponding name.

A.1. Traveltime variation of walk around VSP (Chapter 3)

File name: File name: "ucalgary_2019_gordonferrebus_adriana_a1-traveltime-variation.m"

A.2. Multicomponent geophone array, data rotation (Chapter 3)

File name: File name: "ucalgary_2019_gordonferrebus_adriana _a2-data-rotation.m"

A.3. DAS depth registration, time difference analysis (Chapter 4)

File name: "ucalgary_2019_gordonferrebus_adriana _a3-time-difference-analysis.m."

A.4. Velocity profile calculation, zero offset trace averaging (Chapter 4)

File name: "ucalgary_2019_gordonferrebus_adriana _a4-velocity-calculation.m"

A.5. VSP-CDP transform, trace averaging (Chapter 5)

File name: "ucalgary_2019_gordonferrebus_adriana _a5-vspcdp-trace_averaging.m"